

Nuclear spinodal fragmentation

Philippe Chomaz^a, Maria Colonna^b, Jørgen Randrup^{c,*}

^a*GANIL (DSM-CEA/IN2P3-CNRS), B.P. 5027, F-14076 Caen Cédex 5, France*

^b*Laboratori Nazionali del Sud, Via S. Sofia 44, I-95123 Catania, Italy*

^c*Nuclear Science Division, Lawrence Berkeley National Laboratory, University of California, Berkeley, CA 94720, USA*

Accepted 22 September 2003

editor: G.E. Brown

Abstract

Spinodal multifragmentation in nuclear physics is reviewed. Considering first spinodal instability within the general framework of thermodynamics, we discuss the intimate relationship between first-order phase-transitions and convexity anomalies in the thermodynamic potentials, clarify the relationship between mechanical and chemical instability in two-component systems, and also address finite systems. Then we analyze the onset of spinodal fragmentation by various linear-response methods. Using the Landau theory of collective modes in bulk matter as a starting point, we first review the application of mean-field methods for the identification of the unstable collective modes and the determination of their structure and the associated dispersion relations yielding their growth rates. Subsequently, the corresponding results for finite nuclei are addressed and, within the random-phase approximation, we establish the connection between unstable modes in dilute systems and giant resonances in hot nuclei. Then we turn to the temporal evolution of the unstable systems, discussing first how the dynamics changes its character from being initially linear towards being chaotic and then considering the growth of initially agitated instabilities within the framework of one-body dynamics. We review especially the body of work relating to the Boltzmann–Langevin model, in which the stochastic part of the residual two-body collisions provides a well-defined noise that may agitate the collective modes. We seek to assess the utility of various approximate treatments, including brownian one-body dynamics, and discuss the many possible refinements of the basic treatment. After these primarily formal or idealized studies, we turn to the applications to nuclear multifragmentation and review the various investigations of whether the bulk of the collision zone becomes spinodally unstable. Fragmentation studies with both many-body and stochastic one-body models are discussed and we address the emerging topic of isospin fractionation. We then make contact with experimental data which indicates that the spinodal region is being entered under suitable conditions and we discuss in particular recent results on multifragment size correlations that appear to present signals of spinodal fragmentation. It is demonstrated how various aspects of the data can be understood both qualitatively and quantitatively within the stochastic one-body framework, thus strongly suggesting that nuclear

* Corresponding author.

E-mail address: randrup@lbl.gov (J. Randrup).

spinodal fragmentation indeed occurs. We finally outline perspectives for further advances on the topic and make connections to current progress on related issues.

© 2003 Published by Elsevier B.V.

PACS: 24.10.Cn; 24.60.–k; 05.60.–k

Contents

1. Introduction	266
2. Spinodal instability in thermodynamics	268
2.1. General features of thermodynamic stability	268
2.1.1. Phase coexistence and spinodal instability	270
2.2. Uniform matter	272
2.2.1. Van der Waals fluid	273
2.2.2. Nuclear matter	274
2.2.3. Spinodal instability in classical many-body systems	276
2.3. Two-component systems	277
2.3.1. Mechanical and chemical stability in asymmetric nuclear matter	279
2.3.2. Two-component nuclear matter	281
2.4. Finite systems	285
2.4.1. Isochore canonical ensembles	287
2.4.2. Spinodal instability in molecular dynamics	288
2.4.3. Experimental evidence and perspectives	290
2.5. Concluding remarks about thermodynamics	290
3. Onset of spinodal fragmentation	292
3.1. Nuclear matter	293
3.1.1. Hydrodynamical instabilities in classical fluids	294
3.1.2. Collective motion in Fermi fluids	295
3.1.3. The unstable response of Fermi liquids	297
3.1.4. Linear response in semi-classical approaches	300
3.1.5. Refined analysis of the linear-response treatment	305
3.1.6. Role of the damping mechanism	306
3.1.7. Evolving systems	307
3.1.8. Linear response in quantum approaches	308
3.1.9. Instabilities in asymmetric nuclear matter	310
3.2. Finite nuclei	314
3.2.1. Thomas–Fermi dynamics	314
3.2.2. Expanding nuclear systems	317
3.2.3. Diabatic effects	318
3.2.4. Conclusions from studies with fluid dynamics	321
3.2.5. Quantal description of instabilities	321
3.2.6. Concluding remarks about instabilities in finite systems	330
4. Dynamics of spinodal fragmentation	331
4.1. From the linear regime towards chaotic evolution	331
4.1.1. Non-linear effects	332
4.1.2. Chaos and collective motion	332
4.2. Exploratory dynamical simulations	337
4.2.1. Mean-field studies of fragmentation	338

4.2.2. Nuclear Boltzmann dynamics	339
4.3. Boltzmann–Langevin model	341
4.3.1. Basic features	342
4.3.2. Linearization of collective stochastic dynamics	343
4.3.3. Lattice simulations of Boltzmann–Langevin dynamics	347
4.3.4. Refinements	350
4.4. Approximate Boltzmann–Langevin dynamics	352
4.4.1. Reliability of one-body treatments	354
4.4.2. Brownian one-body dynamics	355
4.5. Concluding remarks about spinodal dynamics	356
5. Applications to nuclear fragmentation	357
5.1. Is the spinodal region reached in the calculations?	357
5.1.1. Entering the spinodal zone	357
5.1.2. Role of heating and compression in semi-classical expansion	360
5.1.3. Expansion and dissipation in TDHF simulations	362
5.1.4. Role of the fluctuations on the expansion dynamics	364
5.1.5. Investigations with many-body approaches	366
5.2. Fragmentation studies	369
5.2.1. Fragmentation with molecular dynamics	370
5.2.2. First stochastic one-body simulations	371
5.2.3. BOB simulations	373
5.3. Isospin dependence of spinodal fragmentation	376
5.3.1. Fragmentation of dilute isobars with $A = 197$	377
6. Confrontation with experimental data	382
6.1. Source characteristics: is the spinodal region reached?	382
6.1.1. Radial collective flow	382
6.1.2. Correlation between particles and fragments	383
6.1.3. Temperature of the emitting source	384
6.1.4. Negative specific heat	385
6.2. Comparison with the INDRA data	385
6.2.1. Fragment velocity correlations	389
6.2.2. Partition correlations	391
6.3. Discussion	392
7. Perspectives	394
Acknowledgements	396
Appendix A. Seyler–Blanchard model	397
A.1. Basics	397
A.2. Thermodynamics	398
A.2.1. Statistical weight	399
A.2.2. Hot nuclei	400
A.2.3. Multifragmentation	401
A.3. Landau parameters	401
A.3.1. Density ripples	402
A.4. Collective modes in unstable nuclear matter	403
Appendix B. Boltzmann–Langevin transport treatment	404
B.1. Expansion around the mean trajectory	407
B.2. Lattice simulation method	408
B.3. Simplified Boltzmann–Langevin model	411
B.3.1. Quality of the simplified model	412
B.3.2. Minimal model	412
B.4. Memory effects	414

B.5. Relativistic formulation	417
Appendix C. Analytical approximations	418
C.1. Fermi surface moments of higher degree	418
C.2. Angular averages	420
C.2.1. Legendre expansion	421
C.3. Overlap matrix and dual basis	422
C.4. Source terms	423
Appendix D. Expanding bulk matter	424
D.1. Comoving variables	424
D.2. Linear response	425
D.3. Discussion	427
Appendix E. Spinodal fragmentation in FMD	427
E.1. Static properties	428
E.2. Early fragmentation dynamics in dilute systems	429
E.2.1. AMD framework	430
E.2.2. FMD framework	431
E.3. Phase transitions in finite systems	431
E.4. Dynamical evolution of excited and dilute finite systems	432
E.5. Further developments of molecular dynamics	433
References	434

1. Introduction

Spinodal decomposition is intimately related to first-order phase transitions and the mechanism plays an important role in many areas of both pure and applied physics, including the inflationary stage of the early universe, the hadronization of a quark–gluon plasma, and binary fluids or solids (such as alloys or glasses). Spinodal decomposition may also play a role in nuclear physics as a mechanism for multifragmentation, the breakup of an agitated nuclear system (usually produced in a collision between two heavy nuclei) into several massive fragments.

Nuclear multifragmentation has been studied extensively over the past two decades. A review of the topic was given about 10 years ago [1] and a more recent impression of this vigorous and diverse field can be gained from Ref. [2], for example. The phenomenon offers the prospect of providing unique experimental information about the equation of state as well as other equilibrium and non-equilibrium properties of nuclear matter far from its ordinary state [3,4]. Yet, the basic physics underlying the multifragmentation process has proven to be rather elusive, as a variety of models based on different mechanisms have been able to reproduce many aspects of the data to a comparable degree. Recently an overview of the various microscopic approaches to fragmentation of nuclei and phase transitions in nuclear matter was presented in Ref. [5], while the occurrence of critical phenomena in nuclear fragmentation was reviewed in Ref. [6]. A few recent perspectives on the topic can be found in Refs. [7–9].

However, an accumulating amount of experimental evidence suggests that spinodal decomposition plays a central role for multifragmentation, in a suitable range of bombarding energies for which an expanding composite system is formed. The bulk of the matter might then acquire densities and temperatures that correspond to spinodal instability and clusterization would ensue as the system seeks to separate into the corresponding coexisting liquid and gas phases. It therefore appears timely to review our understanding of spinodal nuclear fragmentation.

Before embarking on this task, we wish to stress that spinodal decomposition is but one particular mechanism for multifragmentation and that many alternative scenarios have been advocated. While it is not within the scope of the present review to discuss those, we do wish to mention a few alternative scenarios. For example, one may treat multifragment production as a generalization of either sequential fragment emission from a compound nucleus [10] or the transition-state description of binary fission [11]. Such scenarios assume that multifragmentation is a fully equilibrated process and there is thus no need for evoking any instabilities. Alternatively, it has been suggested that multifragmentation happens on a very short time scale at either high or low density. The former scenario receives some support from molecular-dynamics simulations in which it is possible to recognize preformed fragments already during the early stage of high compression, far outside the liquid–gas coexistence region [12]. The low-density scenario is visualized as a rapid transition to an assembly of massive clusters in statistical equilibrium [13], a picture that is supported by the fact that many features of the nuclear multifragmentation data can be well reproduced by purely statistical event generators, such as FREESCO [14–16], MMMC [17,18], and SMM [19].

In fact, most observed features of nuclear multifragmentation display a large degree of equilibration. For example, the fragment size distribution can to a large degree be understood in a rather universal manner as a result of a percolation process [20,21] as well as a manifestation of Fisher condensation [21,22]. Obviously, to the degree that the quantities measured exhibit such universal features, they cannot provide information about the specific dynamical process underlying the particular fragmentation phenomenon. Therefore, as we shall keep in mind throughout this review, it is of key importance to identify observable signals that are unique to a specific fragmentation mechanism, such as spinodal decomposition.

The presentation is organized as follows. Within a general thermodynamic framework, we discuss in Section 2 how spinodal instability is intimately related to the occurrence of a first-order phase transition, as signalled by a convex anomaly in the thermodynamic potential. The onset of the associated spinodal decomposition is then discussed in Section 3, where the early stage of the phase separation is elucidated by analyzing the linear response of matter within the phase region of spinodal instability. The collective dynamics may then be described by simple feed-back equations and the associated dispersion relation identifies the modes that are amplified most rapidly and which therefore will tend to become dominant in the course of time.

The theoretical tools for studying the further increasingly complex evolution are discussed in Section 4 and we show how the key physics is naturally contained within the Boltzmann-Langevin treatment, in which the stochastic outcome of individual two-body collisions between the constituent nucleons are propagated and amplified by the self-consistent effective one-body field. Subsequently, in Section 5, we review the applications of the various dynamical treatments to nuclear fragmentation. These applications suggest that the nuclear collision zone indeed enters the spinodal phase region, under suitable conditions of bombarding energy and impact parameter.

Finally, we address the confrontation of the theoretical expectations with the relevant experimental data. Especially important is the INDRA observation of a small but significant non-statistical component consisting of multifragmentation events in which the intermediate-mass fragments have very similar charges [23]. We conclude by briefly sketching the perspectives for further work on this evolving topic. Various useful and instructive details have been relegated to the appendices in order to facilitate the flow of the presentation.

2. Spinodal instability in thermodynamics

Spinodal instabilities are intimately related to phase equilibria and phase transitions. Although it consists of unstable states, the spinodal region of the phase diagram can be addressed by standard thermodynamics, as this first section illustrates. After first recalling the thermodynamical aspects of the instability problem, we discuss the key issues in nuclear spinodal decomposition, first in two-component matter and then in finite nuclear systems.

2.1. General features of thermodynamic stability

The usual discussion of phase transitions is carried out in the thermodynamical limit of bulk matter, in which the extensive variables are additive. This limit is well defined for saturating forces, such as the strong interaction which has a finite range. (The limit is also sensical when the Coulomb repulsion between protons is included, provided that a suitable counterbalancing negative charge density is added as well, as is done in studies of neutron stars.)

We give here a brief presentation of the key thermodynamical features and refer the reader to the standard textbooks for more thorough discussions (see, for example, Ref. [24]). Consider now such a thermodynamical system and let it be composed of a number of subsystems $\{i\}$, each of which by itself is in the thermodynamic limit. Let each such subsystem be characterized by a set of extensive variables, $\mathbf{X}_i = \{X_i^\ell\}$, where ℓ labels the specific attributes (such as the energy E , the particle number N , or the volume V). The values of the corresponding extensive variables for the combined system are then given by $\mathbf{X} = \sum_i \mathbf{X}_i$.

Let us first consider the case when the statistical ensemble is characterized by a definite value of \mathbf{X} . (This is the standard microcanonical situation occurring when the combined system is isolated from its surroundings so that $\{X^\ell\}$ are constants of motion.) The relative probability $P([\mathbf{X}_1, \mathbf{X}_2, \dots])$ that the system exhibits a specific partition $\{\mathbf{X}_i\}$ is then given by the product of the respective phase-space volumes W_i , each of which expresses the number of elementary states accessible in the subsystem i for the specified value of \mathbf{X}_i . Accordingly, the corresponding total entropy, $S([\mathbf{X}_1, \mathbf{X}_2, \dots])$, is given as the sum of the individual subsystem entropies,

$$S([\mathbf{X}_1, \mathbf{X}_2, \dots]) = \sum_i S_i(\mathbf{X}_i) , \quad (2.1)$$

where $S_i = \ln W_i$ is the entropy of the subsystem i . (We employ units in which the Boltzmann constant k is unity.) The stable thermodynamic equilibria can thus be determined by maximizing the entropy.

The first requirement for having a local maximum at $\mathbf{X}_i = \bar{\mathbf{X}}_i$ is that the entropy be stationary, i.e. the variation of the entropy must vanish,

$$0 \doteq \sum_i \delta S_i(\mathbf{X}_i = \bar{\mathbf{X}}_i) = \sum_{i\ell} \left(\frac{\partial S_i}{\partial X_i^\ell} \right)_{\mathbf{X}_i = \bar{\mathbf{X}}_i} \delta X_i^\ell = \sum_{i\ell} \lambda_i^\ell \delta X_i^\ell , \quad (2.2)$$

where we have introduced the conjugate variables $\lambda_i^\ell \equiv \partial S_i / \partial X_i^\ell$ which are intensive. Since the variations preserve the total value of \mathbf{X} , we must have $\delta \mathbf{X} = \sum_i \delta \mathbf{X}_i \doteq 0$ for each of the attributes ℓ , and then Eq. (2.2) can only be satisfied if all the corresponding intensive variables are equal,

$\lambda_i^\ell = \lambda_i^{\ell'}$. For example, for a thermodynamic system with given energy E , particle number N , and volume V , the intensive variables are

$$\lambda_i^E \equiv \frac{\partial S_i}{\partial E_i} = \frac{1}{T_i}, \quad \lambda_i^N \equiv \frac{\partial S_i}{\partial N_i} = -\frac{\mu_i}{T_i}, \quad \lambda_i^V \equiv \frac{\partial S_i}{\partial V_i} = \frac{P_i}{T_i}, \quad (2.3)$$

so all the subsystems must have the same values of the *temperature* T , the *chemical potential* μ , and the *pressure* P .

It is often more convenient to employ intensive variables for the characterization of a thermodynamic ensemble. (This is especially true when the system is not entirely isolated so some of its attributes fluctuate; for example, a system in contact with a heat reservoir has a fluctuating energy E whose average value is determined by the associated conjugate variable $\lambda^E = 1/T$, where T is the reservoir temperature.) The thermodynamic equilibria can then be obtained by maximizing a correspondingly constrained entropy S'

$$S_i(\mathbf{X}_i) \rightarrow S'_i(\mathbf{X}_i^\ell, \lambda^{\ell'}) \equiv S_i(\mathbf{X}_i) - \sum_{\ell'} \lambda^{\ell'} X_i^{\ell'}, \quad (2.4)$$

where the attributes ℓ' are those specified by their intensive variables $\lambda^{\ell'}$, while ℓ refer to all the others. The stationarity condition (2.2) then becomes $\delta S' = 0$. (It may be noted that the constrained entropy, being the logarithm of the ensemble partition sum, is simply the negative of the corresponding thermodynamic potential divided by the temperature.)

The stationary points identified by the above first-order variation of the entropy function $S([\mathbf{X}_1, \mathbf{X}_2, \dots])$ encompass both maxima and minima of the partitioning probability function $P([\mathbf{X}_1, \mathbf{X}_2, \dots])$. In order to ensure that a given extremum configuration be (locally) stable, one must insist that the entropy have a maximum, which in turn requires the second-order variation to be negative definite,

$$0 > \sum_i \delta^2 S'_i(\mathbf{X}_i = \bar{\mathbf{X}}_i) = \sum_{i, \ell'} \left(\frac{\partial^2 S'_i}{\partial X_i^{\ell'} \partial X_i^{\ell''}} \right)_{\mathbf{X}_i = \bar{\mathbf{X}}_i} \delta X_i^{\ell'} \delta X_i^{\ell''}. \quad (2.5)$$

This condition is met if and only if the curvature matrix $\partial^2 S'_i / \partial X_i^{\ell'} \partial X_i^{\ell''}$ has only negative eigenvalues.

We note that when all the normal curvatures are negative, then all the double derivatives (which are the entropy curvatures in the $X^{\ell'}$ directions) are negative as well, $\partial^2 S / \partial X^{\ell'^2} < 0$. This feature imposes constraints on the equations of state that relate the intensive and extensive variables since it implies $\partial \lambda^{\ell'} / \partial X^{\ell'} < 0$ (where we recall the definition $\lambda^{\ell'} \equiv \partial S / \partial X^{\ell'}$). This general feature is of particular interest for the *heat capacity* C , the *compressibility* κ , and the *chemical susceptibility* χ ,

$$EE : 0 > \frac{\partial \lambda^E}{\partial E} = -\frac{1}{T^2} \frac{\partial T}{\partial E} \Rightarrow C \equiv \frac{\partial E}{\partial T} > 0, \quad (2.6)$$

$$VV : 0 > \frac{\partial \lambda^V}{\partial V} = \frac{1}{T} \frac{\partial P}{\partial V} \Rightarrow \kappa^{-1} \equiv -V \frac{\partial P}{\partial V} > 0, \quad (2.7)$$

$$NN : 0 > \frac{\partial \lambda^N}{\partial N} = -\frac{1}{T} \frac{\partial \mu}{\partial N} \Rightarrow \chi^{-1} \equiv \frac{\partial \mu}{\partial N} > 0. \quad (2.8)$$

These relations express thermal, mechanical, and chemical stability, respectively, all of which must be present in thermodynamic equilibrium. If we employ the density $\rho = N/V$ as a state variable, we can see that in fact the last two conditions are intimately related. (In asymmetric nuclear matter there are two chemical potentials present and the situation is correspondingly more complex, see Section 2.3.)

It is important to recognize that the above conditions on the diagonal curvature terms are necessary but not sufficient stability conditions, since the principal directions of the curvature matrix need not be aligned with the adopted thermodynamic variables. Therefore, the condition for stability involves the entire curvature matrix, including off-diagonal terms. In particular, there may well be instabilities present even if all of the double derivatives are negative.

Generally, then, when the curvature matrix associated with a given stationary configuration is not negative definite the given stationary configuration is unstable. In that situation, there exist variations of the attributes $[X_1, X_2, \dots]$ away from their stationary values $[\bar{X}_1, \bar{X}_2, \dots]$ that cause the (constrained) entropy to increase (or the corresponding thermodynamic potential to decrease) and the system will seek to escape from the stationary configuration, rather than to return.

2.1.1. Phase coexistence and spinodal instability

Of particular relevance to the present review is the possible occurrence of *phase coexistence* and *spinodal instability*, two intimately related phenomena that arise when the entropy function $S(X)$ is locally convex. To bring out the key features as clearly as possible, we consider in the following only one single extensive attribute X . The convexity anomaly then occurs when $\partial^2 S / \partial X^2 > 0$ and it implies that the conjugate intensive thermodynamical variable, $\lambda(X) = \partial S / \partial X$, is globally non-monotonic. (For example, if X is the volume V then λ is related to the pressure P and convexity occurs if the compressibility is negative.) The situation, illustrated generally in Fig. 2.1, is further discussed below.

Consider now a system for which the entropy function $S(X)$ exhibits a convex region, as illustrated by the top curve in Fig. 2.1, with the curvature anomaly, $\partial^2 S / \partial X^2 > 0$, occurring for $X_{\min} < X < X_{\max}$. Due to the local convexity, there exists a common tangent to $S(X)$ between X_1 (below X_{\min}) and X_2 (above X_{\max}). Since thus $\lambda(X_1) = \lambda(X_2)$, *the two phases can coexist in thermodynamic equilibrium*. A linear interpolation along the common tangent then yields a globally concave envelope function, $\tilde{S}(X)$, lying above $S(X)$ for $X_1 < X < X_2$, thus signaling that the system is unstable against separation into the phases 1 and 2 throughout that region.

To understand this central feature in more detail, it is convenient to eliminate the trivial size dependence of the extensive variables. Towards this end, we may generally introduce reduced extensive variables, $x \equiv X/N$, where N is the number of particles. In particular, the entropy per particle is $\sigma = S/N$. The common division by N does not affect the conjugate variables since $\lambda \equiv \partial S / \partial X = \partial \sigma / \partial x$.

Let us now prepare a uniform thermodynamic system with a value of $x = X/N$ lying within the interval (x_1, x_2) . It has the total entropy $S = N\sigma(x)$. Alternatively, we may split this system into two thermodynamic subsystems for which the reduced extensive variables have the values x_1 and x_2 associated with the two coexisting stable phases. (As noted above, the corresponding intensive variables match, $\lambda(x_1) = \lambda(x_2)$, since the local tangent to $S(X)$ is common.) Let the respective particle numbers be N_1 and N_2 , respectively, with $N_1 + N_2 = N$. The resulting total entropy of the combined

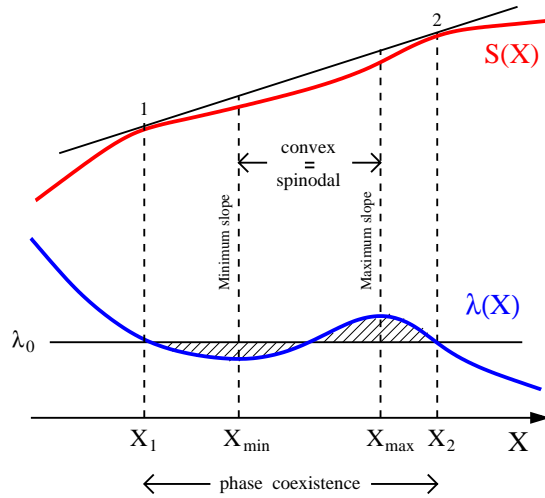


Fig. 2.1. Phase coexistence. The figure illustrates the relationship between entropy convexity, spinodal instability and phase coexistence. The entropy function $S(X)$ (top) is convex between the inflection points at X_{\min} and X_{\max} , at which the conjugate variable $\lambda(X) = \partial S / \partial X$ (bottom) has a local minimum or maximum, respectively. Through this region of spinodal instability, $\lambda(X)$ increases so the system is mechanically unstable. The region of phase coexistence extends from X_1 to X_2 , where the phases 1 and 2 are determined by the common tangent to $S(X)$ (which exists due to the local convexity); obviously, $X_1 < X_{\min}$ and $X_2 > X_{\max}$. Since the two slopes are the same, these two stable phases can coexist in thermodynamic equilibrium. Entropy can then be gained by separating the uniform system into these two phases, since the entropy of the corresponding mixed system, $\tilde{S}(X)$, moves along the common tangent as X is increased from X_1 to X_2 . Meanwhile $\tilde{\lambda}(X)$ maintains a constant value λ_0 which can be determined by the familiar Maxwell construction (2.11) requiring that the two hatched areas be equal.

mixed-phase system would then be

$$\tilde{S} = N_1 \sigma(x_1) + N_2 \sigma(x_2) = \frac{N_1}{N} S(X_1) + \frac{N_2}{N} S(X_2) > S. \quad (2.9)$$

This key feature is readily visualized by noting that \tilde{S} lies on the common tangent which is above S (see Fig. 2.1). Thus, the separation of the initial uniform state into the two coexisting phases maximizes the total entropy and such a mixed-phase configuration is therefore thermodynamically favored.

The above is true for any value of X between X_1 and X_2 . If the value of X is increased steadily through this interval, the relative preponderance of the two phases evolves correspondingly, with N_1 decreasing from N to zero as N_2 increases from zero to N . Their ratio follows immediately from the additivity of the extensive state variable, $X_1 + X_2 = X$,

$$\frac{N_1}{N_2} = \frac{x_2 - x}{x - x_1}. \quad (2.10)$$

The corresponding value of λ remains constant through this gradual transformation, as is evident from the fact that the system moves along the common tangent. This constant value, $\lambda_0 = d\tilde{S}/dX$,

can also be determined directly from the function $\lambda(X)$ by the familiar Maxwell construction,

$$\int_{X_1}^{X_2} dX (\lambda(X) - \lambda_0) \doteq 0, \quad (2.11)$$

which amounts to demanding that the area enclosed by $\lambda(X)$ below λ_0 be equal to the area enclosed above (the hatched areas on Fig. 2.1).

Because of the convexity in the entropy function $S(X)$, the function $\lambda(X)$ is invariably non-monotonic through the phase coexistence region, decreasing first to its (local) minimum at x_{\min} , then rising to its (local) maximum at x_{\max} , and finally decreasing again to its starting value. These two extrema delineate the *spinodal region*, within which $\lambda(X)$ is thus a steadily rising function, as the (local) slope of $\sigma(x)$ changes from its minimum to its maximum value. Thus, within the spinodal region, the system responds to an increase in volume by increasing its pressure, thus accelerating the disturbance. Equivalently, a local variation of the density will become amplified and the state may then spontaneously undergo a phase separation. It is this anomalous behavior that characterizes the spinodal region and, as the above discussion brings out, spinodal instability occurs whenever the entropy function exhibits local convexity.

In contrast to the local instability of the states inside the spinodal region, the remaining states within the coexistence region are locally stable (since the local curvature of $S(X)$ is negative). These states are thus globally metastable and are protected by a finite barrier against spontaneous phase separation.

These key features are also evident from the basic difference between concavity and convexity: When the system is situated within the convex region, entropy can be gained by transforming it into a mixture of two neighboring systems (on opposite sides). Thus, it is possible to transform the system in a continuous manner into a mixture of the two coexisting phases 1 and 2 with the entropy increasing steadily until it reaches its maximum possible value \tilde{S} when the transformation is complete and the system lies on the common tangent. On the other hand, when the system is situated in a concave region then any such local transformation into a mixture of neighboring states would result in an entropy decrease. Consequently, the transformation of the system into the mixture of the coexisting phases must necessarily involve a temporary reduction of the entropy and can thus not occur spontaneously.

2.2. Uniform matter

The previous discussion was not restricted to any specific case but considered the stability of general thermodynamic states by analyzing the curvature of the relevant thermodynamical potential. We shall now focus on the instabilities of uniform nuclear matter. Systems can be considered as being uniform with specific values of the thermodynamic quantities, such as energy density, particle density, and isospin density, if they are devoid of macroscopic correlations. (Throughout this review, we use the term “isospin” rather loosely to denote the neutron excess degree of freedom which is simply related to the third component of the isospin.) For macroscopic systems, this can be experimentally achieved by quenching the system sufficiently deep into the coexistence region of the phase space through a rapid variation of a state variable (as in the rapid cooling of binary alloys) or through the tuning of external control parameters. (In nuclear physics such experiments can be performed only on small systems and the associated complications will be addressed in Section 2.4.) In the

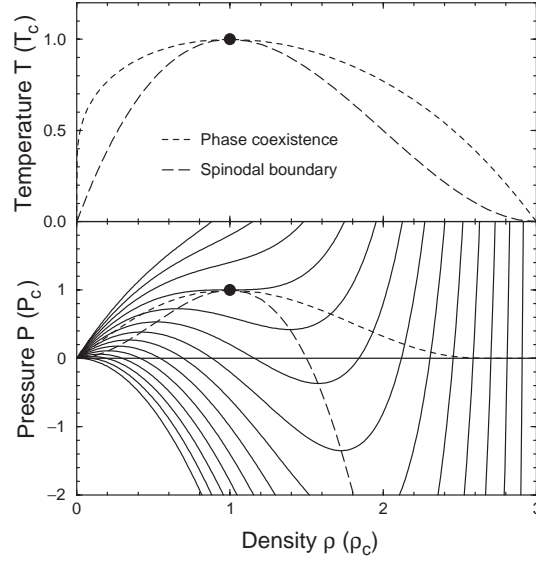


Fig. 2.2. Van der Waals equation of state. *Bottom panel:* The pressure P (in units of the critical pressure) as a function of the density ρ (in units of the critical density) for 14 equidistant temperatures $T=0-1.3$ (in units of the critical temperature) for a Van der Waals fluid as given in Eq. (2.12). The border of the spinodal zone is delineated by the long-dashed curve, which passes through the maxima and minima of $P(\rho)$; uniform matter situated below this curve is mechanically unstable. Also indicated is the phase coexistence line (short dashes) as obtained with the Maxwell construction. The critical point is indicated by the solid dot. *Top panel:* The corresponding (ρ, T) phase-plane representation of the spinodal boundary and the phase coexistence line.

present section, the general properties of uniform nuclear matter will be elucidated with the aid of various simple models. It is an important simplifying feature that mean-field approaches are excellent tools for describing the stability of such systems and that the observed spinodal instability is not an artefact of this approximation but a general property.

2.2.1. Van der Waals fluid

Perhaps the best known example of a system exhibiting spinodal instabilities is the Van der Waals fluid and it is well suited to illustrate the principal features. Since the state variables are $(T; N, V)$, the associated constrained entropy (2.4) is $S' = S - E/T$ and the appropriate thermodynamic potential is then the free energy $F(T; N, V) = -TS' = \bar{E} - TS = Vf(T, \rho)$.

The key quantity is the *equation of state* describing how the pressure in macroscopically uniform matter depends on the state variables,

$$P(T; N, V) = - \left(\frac{\partial F}{\partial V} \right)_{TN} = \frac{NT}{V - bN} - a \left(\frac{N}{V} \right)^2 = \frac{\rho T}{1 - b\rho} - a\rho^2, \quad (2.12)$$

where a is the strength of the mean-field attraction, while b governs the short-range repulsion. It is depicted in Fig. 2.2 (following the most common form of presentation, we use the density $\rho = N/V$ as the abscissa rather than the volume V employed above for pedagogical reasons). It is seen that when the temperature T exceeds a certain critical value, $T_c = 8a/27b$, the pressure rises steadily with

the density and we are faced with a normal thermodynamical situation in which there is precisely one thermodynamic state for each specified P and T .

By contrast, for subcritical temperatures ($0 < T < T_c$) the function $P(\rho)$ has a maximum followed by a minimum and the situation is thus similar to that discussed generally above (see Fig. 2.1). Then the specification of a pressure P below the critical value P_c , determines *three* possible densities. The smallest density, ρ_G , lies in the gas phase below the spinodal region, while the highest density, ρ_L , lies in the liquid phase above the spinodal region. The coexisting phase points can be determined by a Maxwell construction, $\int dV (P - P_0) = 0$, and they are shown in Fig. 2.2. While these thermodynamic states have positive compressibilities, the intermediate density is situated inside the spinodal zone and it has thus a negative compressibility and is, accordingly, mechanically unstable.

The region of spinodal instability is determined by the extrema of $P(\rho)$ and this boundary is also shown in the figure. As a general feature, the boundaries for phase coexistence and spinodal instability both start at the origin, $\rho = 0$, $T = 0$, $P = 0$. Equally generally, the coexistence region extends up to the ground-state density ρ_0 (which is equal to the maximum density of $3\rho_c$ for the Van-der-Waals fluid), while spinodal instability usually disappears well before that density is reached. However, for the somewhat pathological case of the Van-der-Waals fluid spinodal instability remains present at all densities.

2.2.2. Nuclear matter

Since nuclear forces have an attractive long-range part and a repulsive hard core, the nuclear system resembles the Van der Waals fluid. The thermodynamics of the (infinite) nuclear medium can be studied by omitting the Coulomb repulsion between the protons, leading to the concept of nuclear matter consisting of neutrons and uncharged protons (see, for example, Ref. [25]). Such idealized systems are useful for understanding the bulk properties of large nuclei. For the understanding of the structure of neutron star crusts it is important to include the Coulomb force which can be done by simultaneously introducing a compensating smooth negative charge density resulting from the electrons present.

A convenient framework for thermodynamic studies of nuclear matter is provided by mean-field treatments employing phenomenological effective interactions (which may, in principle, be derived through Brückner–Hartree–Fock regularization of the repulsive hard core [26]). The oldest and perhaps most commonly used effective interactions employed in nuclear physics are of the Skyrme type [27–29]. Such interactions are particularly convenient for studies of the equation of state [30,31]. In its simplest form, the isoscalar part of the effective two-body Skyrme interaction is a function of the local density $\rho(\mathbf{r})$,

$$V_{12} = \delta(\mathbf{r}_1 - \mathbf{r}_2) \left(t_0 + \frac{1}{6} t_3 \rho \left(\frac{\mathbf{r}_1 + \mathbf{r}_2}{2} \right)^\sigma \right), \quad (2.13)$$

where the parameters t_0, t_3, σ are fitted to nuclear properties at zero temperature. The first term represents the long-range attraction ($t_0 < 0$), while the second term provides a short-range repulsion ($t_3 > 0$), thus ensuring saturation at a certain density ρ_0 . The associated curvature of the energy, i.e. the nuclear compressibility, is governed by the parameter σ . The resulting equation of state is then akin to the Van der Waals form shown in Fig. 2.2 and a specific example is shown in Fig. 2.3 (left).

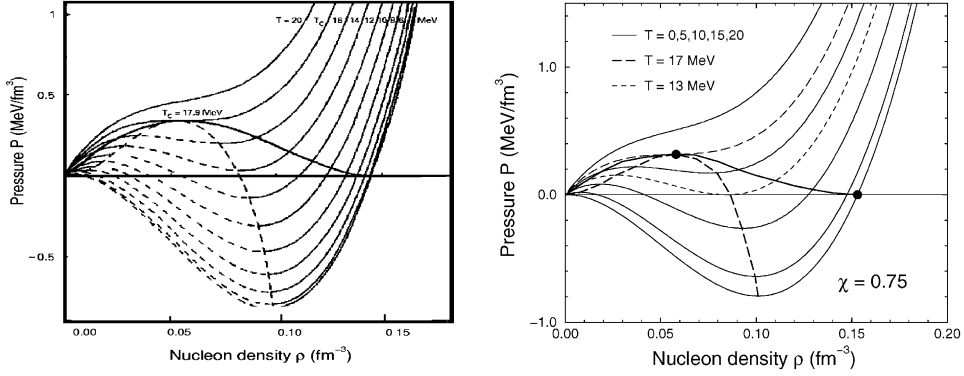


Fig. 2.3. Nuclear matter isotherms. Typical equations of state for nuclear matter obtained within a mean-field treatment using either a Hartree–Fock approach with an effective Skyrme force (*left*) (from Ref. [32]) or the Thomas–Fermi approximation with a modified Seyler–Blanchard force (*right*) (adapted from Ref. [35]). The pressure P is plotted as a function of the nucleon density ρ for temperatures in the range $T = 0$ –20 MeV. The spinodal boundary (dashed) and the coexistence curve (solid) are indicated.

The above prototype interaction (2.13) has two notable shortcomings, it has zero range and there is no medium effect on the nucleon mass, and numerous refinements have been made. A simple interaction that remedies both of these problems and leads to a good overall description of many macroscopic nuclear properties (such as sizes, masses, and barriers) is the Seyler and Blanchard interaction [33] as modified by Myers and Swiatecki [34] (see Appendix A for details),

$$V_{12} = -C \frac{e^{-r_{12}/a}}{r_{12}/a} \left[1 - \bar{\chi} \frac{p_{12}^2}{b^2} - \chi \frac{\kappa_s}{\rho_s} \left(\left(\frac{\rho(r_1)}{\rho_s} \right)^{2/3} + \left(\frac{\rho(r_2)}{\rho_s} \right)^{2/3} \right) \right]. \quad (2.14)$$

In addition to the original Seyler–Blanchard parameters a , b , and C , the parameter χ controls the balance between momentum and density dependence and thus allows an independent specification of the effective mass. The corresponding equation of state [35] is shown on the right in Fig. 2.3.

The similarity of the two equations of state displayed in Fig. 2.3 is typical of this general type of approach. Thus, for cold symmetric nuclear matter, the spinodal region extends up to about $\frac{2}{3} \rho_s$, while the critical density is roughly $\rho_c \approx \frac{1}{3} \rho_s$, with the corresponding critical temperature being $T_c \approx 14$ –18 MeV.

However, it should be noted that the mean-field approaches have certain inherent shortcomings. One is the fact that the associated Fermi-gas level density $g(\epsilon)$ significantly underestimates the level density of actual nuclear systems, thus yielding a correspondingly erroneous statistical weight; the use of a more realistic $g(\epsilon)$ will lead to a lower critical temperature [36]. Also notable is the inadequacy of mean-field treatments at the critical point (and for other second-order phase transitions), as reflected in incorrect values of the critical exponents. Fortunately, this local failure has little bearing on the rest of the phase diagram and the treatments may then be quite suitable for the study of first-order phase transitions, such as those underlying the spinodal instability. This will be illustrated below with exact molecular dynamics.

2.2.3. Spinodal instability in classical many-body systems

The above illustrations of spinodal phase separation in uniform matter have been made within the framework of mean-field treatments. In order to bring out the important fact that the spinodal phenomenon is not limited to this approximative framework, we recall here some relevant studies for classical many-particle systems for which exact numerical calculations can be performed.

Such treatments consider A particles within a box of volume V (for which periodic boundary conditions are usually imposed to eliminate surface effects). Infinite matter is then well approximated when the dimensions of the box are large in comparison with the interaction range. For a given model Hamiltonian function $H(\{\mathbf{r}_i\}, \{\mathbf{p}_i\})$, the temporal evolution of the microscopic state of the system, $(\{\mathbf{r}_i(t)\}, \{\mathbf{p}_i(t)\})$, is governed by the associated Hamilton equations of motion,

$$\dot{\mathbf{r}}_i = \frac{\partial H}{\partial \mathbf{p}_i} \quad \dot{\mathbf{p}}_i = -\frac{\partial H}{\partial \mathbf{r}_i}, \quad i = 1, \dots, A. \quad (2.15)$$

For any given dynamical state $(\{\mathbf{r}_i\}, \{\mathbf{p}_i\})$, it is then possible to extract an effective temperature [37]

$$T = \frac{1}{3A} \sum_i \mathbf{p}_i \cdot \frac{\partial H}{\partial \mathbf{p}_i} = \frac{1}{3A} \sum_i \mathbf{p}_i \cdot \dot{\mathbf{r}}_i. \quad (2.16)$$

Furthermore, a convenient expression for the stress tensor \mathbf{T} , which is directly related to the momentum transport, can be obtained by replacing the time average in the Virial Theorem by an instantaneous average over all the particles in the system [37],

$$3TV = \sum_i \left(\mathbf{p}_i \frac{\partial H}{\partial \mathbf{p}_i} - \frac{\partial H}{\partial \mathbf{r}_i} \mathbf{r}_i \right) = \sum_i (\mathbf{p}_i \dot{\mathbf{r}}_i - \mathbf{F}_i \mathbf{r}_i). \quad (2.17)$$

The effective pressure is then given by

$$P = \text{trc } \mathbf{T} = \rho \left(T + \frac{1}{A} \sum_{i < j} F_{ij} r_{ij} \right), \quad (2.18)$$

where $\rho = A/V$ is the density and $F_{ij} = -\partial H / \partial r_{ij}$ is the radial force between the particles i and j , with their separation being $r_{ij} = |\mathbf{r}_i - \mathbf{r}_j|$. These relations, which also hold for momentum-dependent interactions [37], make it possible to extract the location of the system in the $TP\rho$ phase diagram. (The accuracy can be improved indefinitely by averaging the result over an ever larger number of systems that have been initialized by a suitable statistical sampling, using for example the Metropolis method.)

A simple way to numerically investigate spinodal instability in such many-body systems is to first prepare the system at a density and temperature corresponding to a phase point (ρ, T) outside the spinodal region, where the system is stable and thus prefers to have a macroscopically uniform density $\rho = A/V$. Subsequently, the system is brought to a phase point of interest inside the unstable region by a sudden cooling and/or expansion which can be readily accomplished by rescaling the velocities and/or positions of the individual constituent particles. (Such quenching can also be carried out experimentally and is in fact routinely performed in various areas of physics, as well as in industry; a well-known example is the rapid supercooling of binary alloys—for an early review of phase separation experiments, see Ref. [38].)

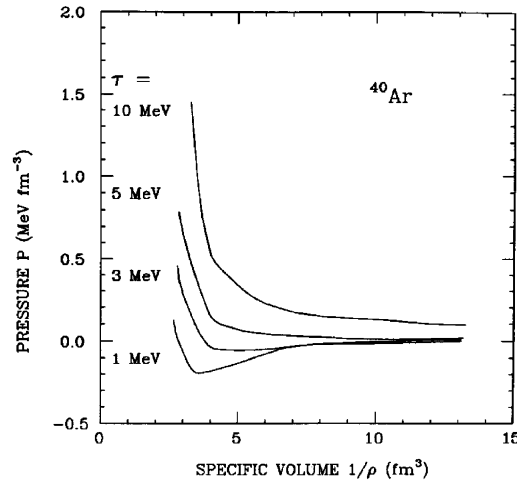


Fig. 2.4. Equation of state for ^{40}Ar . Isotherms of the pressure P versus the specific volume $v \equiv V/A = 1/\rho$ for a system of 20 (charged) protons and 20 neutrons which are constrained to be approximately uniformly distributed within a sphere of volume V , as obtained by means of quasi-classical molecular dynamics with a Pauli potential. (From Ref. [37].)

An early example in nuclear physics was the study by Dorso et al. [37] who considered approximately spherical configurations by means of a two-body interaction with three terms: the standard Coulomb repulsion between protons, a nuclear interaction of Lennard–Jones form, and a repulsive “Pauli” potential which depends on both the spatial separation and the difference in momentum and was intended to emulate the effect of the Pauli exclusion between fermions. Fig. 2.4 shows the resulting equation of state, displayed in the form of the general illustration in Fig. 2.1: the pressure plotted against the specific volume v for a given temperature T . It is evident that for temperatures below ≈ 3 MeV there is a density region where the compressibility is negative, $\kappa^{-1} = (-v\partial P/\partial v)^{-1}$, thus signaling the spinodal instability against phase separation.

A similar study was undertaken later on by Jacquot et al. [39] who employed a Lennard–Jones potential with a hard core for classical particles in a box with periodic boundary conditions. This force was also chosen so as to approximately reproduce the key nuclear features (size and binding). The resulting phase diagram is shown in Fig. 2.5, with the spinodal boundary delineated. It was demonstrated that the exact dynamics and thermodynamics are well reproduced by mean field approaches using the local density approximation with a Skyrme-type energy functional.

The above two examples serve to bring out the fact that spinodal instability is a general phenomenon in many-body systems, rather than merely an artifact of the mean-field approximation. Thus we may expect that the occurrence of a convex entropy function signals a preference for the system to undergo phase separation and that the mechanically unstable spinodal region is characterized by a negative compressibility modulus.

2.3. Two-component systems

The preceding discussion has been phrased as if the systems under consideration were composed of just a single particle species, nucleons. However, the nuclear medium contains two nucleonic species,

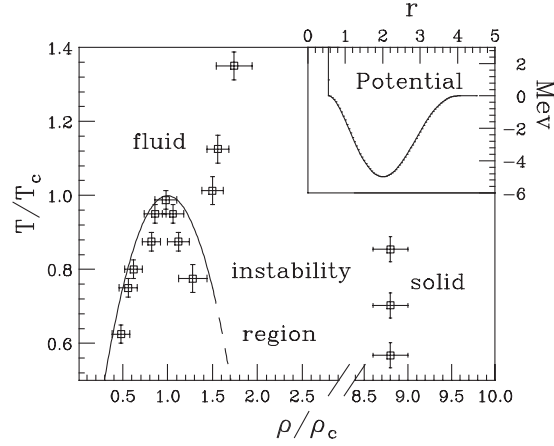


Fig. 2.5. Phase diagram from molecular dynamics. Phase diagram obtained in Ref. [39] for a system of classical particles having the interaction shown in the insert. The “data points” indicate the onset of instability as obtained by numerical simulation of the microscopic equations of motion. For low densities there is good agreement with the mean field spinodal boundary (the drawn curve), while the near vertical behavior at higher densities reflects the presence of a solid phase in a classical particle system, an artefact that is unimportant for the present discussion.

neutrons and protons, and the analysis therefore needs to be correspondingly two-dimensional. Instructive discussions of this situation have been made in Refs. [40–46].

In the two-component system, the particle number is represented by two observables that commute with the Hamiltonian \hat{H} , for example the baryon number \hat{A} and the charge number \hat{Z} . Alternatively, we may use the neutron and proton numbers $\hat{N}_n = \hat{A} - \hat{Z}$ and $\hat{N}_p = \hat{Z}$, thus preserving the symmetry between the two species. For systems characterized by temperature and particle number(s), it is convenient to consider the (Helmholtz) free energy,

$$F(T, V, N_p, N_n) = -T \log \text{Tr}[\delta(\hat{N}_p - N_p)\delta(\hat{N}_n - N_n)e^{-\hat{H}/T}] \asymp V f(T, \rho_p, \rho_n) . \quad (2.19)$$

The last expression pertains to the thermodynamical limit where F is proportional to the volume V , so we may consider the free energy density $f = F/V$ and use only the proton and neutrons densities as state variables, $\rho_n = N_n/V$ and $\rho_p = N_p/V$, in addition to the temperature T . The chemical potentials then follow,

$$\mu_n \equiv \frac{\partial F}{\partial N_n} = \frac{\partial f}{\partial \rho_n}, \quad \mu_p \equiv \frac{\partial F}{\partial N_p} = \frac{\partial f}{\partial \rho_p} . \quad (2.20)$$

Furthermore the stability condition (2.5) requires that the curvature matrix,

$$\mathbf{C} = \begin{pmatrix} \partial^2 f / \partial \rho_n \partial \rho_n & \partial^2 f / \partial \rho_p \partial \rho_n \\ \partial^2 f / \partial \rho_n \partial \rho_p & \partial^2 f / \partial \rho_p \partial \rho_p \end{pmatrix} = \begin{pmatrix} \partial \mu_n / \partial \rho_n & \partial \mu_n / \partial \rho_p \\ \partial \mu_p / \partial \rho_n & \partial \mu_p / \partial \rho_p \end{pmatrix} , \quad (2.21)$$

have only positive eigenvalues. For a 2×2 matrix this requirement amounts to

$$\det[\mathbf{C}] = c_- c_+ > 0 \quad \text{and} \quad \text{tr}[\mathbf{C}] = c_- + c_+ > 0 , \quad (2.22)$$

where c_- is the smallest eigenvalue and c_+ is the largest one.

Thus, if it is possible to calculate (or estimate) the free energy for uniform configurations (for example by use of the mean-field approximation or by quenching, as discussed above), then the above criterion (2.22) makes it possible to determine if a given uniform system is unstable against phase separation and, if so, the global equilibrium can be obtained by a Maxwell-type construction as that combination of the stable phases that minimizes the free energy at the specified values of the temperature, pressure, and chemical potentials.

The system is stable as long as both eigenvalues are positive and the spinodal boundary is reached when $\det[\mathbf{C}]$ turns from positive to negative. There is then one negative eigenvalue, $c_- < 0$, and the phase separation will initially proceed in the corresponding principal direction. Further into the spinodal region, the sum of eigenvalues may become negative, $\text{tr}[\mathbf{C}] < 0$, as the magnitude of the negative eigenvalue exceeds the positive eigenvalue, $|c_-| > c_+$. Finally, both eigenvalues may become negative. However, we need not discuss this case since it is not expected to occur in dilute nuclear matter.

2.3.1. Mechanical and chemical stability in asymmetric nuclear matter

In asymmetric matter, the variation of the pressure is given by $\delta P = \rho_n \delta \mu_n + \rho_p \delta \mu_p$. However, it is common to replace the individual densities ρ_n and ρ_p by the total density, $\rho = \rho_n + \rho_p$, and the proton concentration, $y = Z/A = \rho_p/(\rho_n + \rho_p)$. The usual discussion then proposes two corresponding criteria, usually referred to as “mechanical” and “chemical” instability conditions,

$$\text{“Mechanical”} : \left(\frac{\partial P}{\partial \rho} \right)_{T,y} < 0 , \quad (2.23)$$

$$\text{“Chemical”} : \left(\frac{\partial \mu_p}{\partial y} \right)_{T,P} < 0 . \quad (2.24)$$

However, this formulation of the instability problem is misleading because it might be taken to suggest that there are two independent instabilities: a mechanical instability conserving the proton concentration y and a chemical instability occurring at constant density ρ . Such an interpretation would not be correct. Not only do the chemical instabilities involve changes in the density and the mechanical instabilities produce changes in the proton concentration, but the two situations are in fact associated with one single instability.

The above “mechanical” and “chemical” instability conditions do not provide any directional information and the best way to understand the two-dimensional instability features is to recall the basic stability criterion, that the curvature matrix of the free energy in the ρ_n – ρ_p plane, \mathbf{C} , be positive definite. Thus, as pointed out above, one needs to consider its eigenvalues and eigenvectors. In the typical case, there is one negative eigenvalue, c_- , and the associated eigenvector, $(\delta \rho_p^-, \delta \rho_n^-)$, gives the direction of the instability. If $\delta \rho_p^- : \delta \rho_n^- = \rho_p : \rho_n$ then the instability preserves the ratio between protons and neutrons so it is a purely mechanical disturbance. Conversely, if $\delta \rho_p^- = -\delta \rho_n^-$ then the total density is constant and we are facing a pure chemical instability. Except for these two very special situations, a disturbance along the unstable eigendirection conserves neither ρ nor y , but has a mixed character with both chemical and mechanical contents. Nevertheless, if $\delta \rho_p^-$ and $\delta \rho_n^-$ have the same sign then protons and neutrons are affected similarly and the disturbance thus

has a predominantly isoscalar character, while it may be characterized as isovector-like if $\delta\rho_p^-$ and $\delta\rho_n^-$ have opposite signs [47].

It is also noteworthy that the two derivatives in the instability conditions (2.23) and (2.24) are intimately related [48],

$$\left(\frac{\partial\mu_p}{\partial y}\right)_{T,p} \left(\frac{\partial P}{\partial\rho}\right)_{T,y} = (1-y)\rho^2 |\mathbf{C}|. \quad (2.25)$$

Since the determinant $|\mathbf{C}|$ turns negative at the spinodal border, when the smallest eigenvalue passes through zero, the “chemical” instability condition (2.24) is always met first, irrespective of the actual direction of associated eigenvector. Furthermore, $(\partial P/\partial\rho)_{T,y}$ becomes negative only when the instability is strong enough to affect the curvature in the direction of constant y . When this happens (if there is only one negative eigenvalue, as is typically the case), then the above relation shows that $(\partial\mu_p/\partial y)_{T,p}$ must again become positive. Only in the case when both eigenvalues of \mathbf{C} are negative (which never happens in dilute nuclear matter) will both conditions (2.23) and (2.24) be violated. These features are illustrated below for a simple example of two independent fluids.

2.3.1.1. Instability analysis for two independent fluids The instabilities of a two-component system can be elucidated by the simple case of two independent (i.e. non-interacting) fluids. The curvature matrix is then diagonal,

$$\mathbf{C} = \begin{pmatrix} \partial_{\rho_p}\mu_p & 0 \\ 0 & \partial_{\rho_n}\mu_n \end{pmatrix}, \quad (2.26)$$

and so it is easy to derive the following expressions,

$$\left(\frac{\partial P}{\partial\rho}\right)_{Ty} = y \left(\frac{\partial P_p}{\partial\rho_p}\right)_T + (1-y) \left(\frac{\partial P_n}{\partial\rho_n}\right)_T, \quad (2.27)$$

$$\left(\frac{\partial P}{\partial\rho}\right)_{Ty} \left(\frac{\partial\mu_p}{\partial y}\right)_{TP} y = \left(\frac{\partial P_p}{\partial\rho_p}\right)_T \left(\frac{\partial P_n}{\partial\rho_n}\right)_T, \quad (2.28)$$

where the individual pressures are P_i , with $i = p, n$, and the spinodal region for the component i is where $\partial_{\rho_i}P_i = \rho_i\partial_{\rho_i}\mu_i$ is negative.

Consider now the situation when one component enters its spinodal region. One of the factors on the right in Eq. (2.28) has then turned negative but, since the other is still positive, it is evident from Eq. (2.27) that the total compressibility is still positive. Indeed, since Eq. (2.27) can be rewritten in terms of the compressibilities,

$$\frac{1}{\kappa} \equiv \rho \left(\frac{\partial P}{\partial\rho}\right)_{Ty} = \frac{1}{\kappa_p} + \frac{1}{\kappa_n}, \quad (2.29)$$

the total compressibility κ becomes negative only if the magnitude of the negative compressibility of the unstable component becomes smaller than the compressibility of the stable one. When this happens, the quantity $(\partial\mu_p/\partial y)_{TP}$, which turned negative simultaneously with the entry of the first component into the spinodal region, reverts to being positive (see Eq. (2.28)).

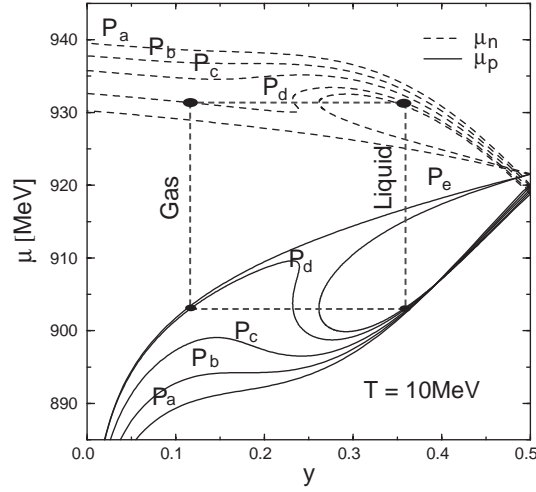


Fig. 2.6. Isobaric contours. Isobaric contours in the y – μ plane (with the specified pressure decreasing from a to e , with P_b being the critical pressure), as obtained with the relativistic mean-field approach for nuclear matter at $T = 10$ MeV. For subcritical pressures (contour c), both μ_n (dashed) and μ_p (solid) exhibit anomalous behavior (μ_n increases and μ_p decreases as the proton concentration y is increased) leading eventually to backbending (contour d), signaling the presence of spinodal instability. The boundary of the coexistence zone can be determined by demanding that the chemical potential for each species be equal in the liquid and the gas phases, for given values of the common pressure P and temperature T , as indicated by the rectangle which represent a two-dimensional extension of the Maxwell construction. (Adapted from Ref. [42].)

In this example we are clearly facing a single instability, namely the mechanical instability of one component, but an analysis in terms of Eqs. (2.23) and (2.24) would suggest that we pass from a “chemical” to a “mechanical” instability, since we first encounter $(\partial\mu_p/\partial\rho)_{TP} < 0$ and subsequently $(\partial P/\partial\rho)_{Ty} < 0$. Such an interpretation would be misleading, since the instability retains its direction along the same axis with only its magnitude changing. Thus, no special meaning should be attached to the two instability conditions (2.23) and (2.24); only the border of the instability is meaningful. Rather, to ascertain the character of an instability, one should consider the eigenvalues and the associated eigenvectors of the curvature matrix C .

2.3.2. Two-component nuclear matter

After the above general discussion, we now turn to the nuclear case. As a framework for our discussion, we shall employ the results obtained with the relativistic mean field by Serot et al. [42,49,50]. Other nuclear models yield qualitatively similar results, so the features are rather universal.

We start by considering the relationship between the proton concentration y and the chemical potentials μ_n and μ_p , for given values of temperature and pressure. This is illustrated in Fig. 2.6. As noted above, when the pressure is reduced below the critical value, it is the “chemical” stability condition which is first violated. This important general feature is brought out more clearly in Fig. 2.7 which shows the corresponding equation of state with the various boundary curves added. Entering from the one-phase region of the ρ – P phase plane, one first crosses the coexistence curve

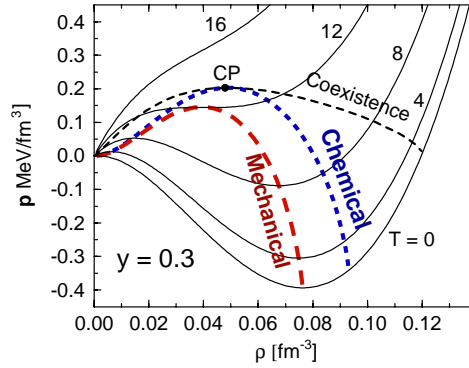


Fig. 2.7. Instability boundaries. The pressure as a function of the total density ρ in nuclear matter with a proton concentration of $y = 0.3$ for various temperatures T (in MeV), as obtained with the relativistic mean-field approach. The critical point (CP), the coexistence line, and the “mechanical” (2.23) and “chemical” (2.24) spinodal boundaries are indicated. (Adapted from Ref. [42].)

and subsequently the boundary for chemical instability determined by Eq. (2.24) (at the critical point these two coincide), while the so-called mechanical instability determined by Eq. (2.23) is encountered only deeper into the spinodal zone.

However, since relation (2.25) causes $\partial\mu_p/\partial y$ to change sign at the same time as the compressibility, the “mechanical” instability boundary does *not* represent the onset of a second instability. Rather, this artificial boundary marks only a quantitative modification of the instability properties, either an increase of the negative curvature or a rotation of the instability direction, but not a qualitative modification of the instability nature. As a consequence, one should not attach a strong significance to this “mechanical” spinodal line. This important point was noted already over fifteen years ago [47] (and has been further stressed recently [48,51]), but apparently it remains unrecognized in many discussions of asymmetric nuclear matter.

In order to achieve a deeper insight into the two-dimensional nature of the spinodal instability, one should determine the principal direction of the curvature matrix \mathbf{C} in the ρ_n – ρ_p density plane, as illustrated in Fig. 2.8. Using an effective interaction of either Skyrme or Gogny form, Margueron et al. [48] diagonalized the curvature matrix as a function of ρ_n and ρ_p . The figure shows a contour plot of the associated speed of sound c , where $c^2 = (1/18m)\rho c_-$. The outer contour, corresponding to $c = 0$, is then spinodal boundary, while the instability grows steadily stronger as one moves inside. This kind of plot brings out very clearly that we are facing a single instability. Furthermore, the direction of the corresponding eigenvectors are indicated along the contours. While they are generally directed neither along constant density nor along constant proton concentration, they do have a predominantly mechanical (isoscalar) character. Nevertheless, the result of the “mechanical” instability criterion (2.23) bears little resemblance to the actual results. One might also note that the instabilities have a chemical character as well, since they always seek to reduce rather than enlarge isosymmetry in the dense regions.

This local tendency toward the restoration of the isospin symmetry is also present in the global phase equilibrium, as we shall now illustrate. As already discussed in connection with Fig. 2.6, the coexistence curve and the conditions for phase equilibrium can be extracted from the various

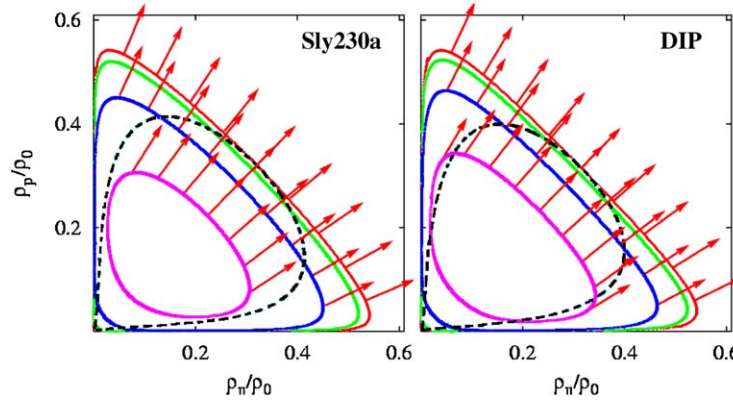


Fig. 2.8. Two-dimensional spinodal boundary. Spinodal instability in the ρ_n – ρ_p density plane as calculated with an effective interaction of either Skyrme (left) or Gogny (right) form. Each contour corresponds to a fixed value of the sound velocity $c = (\rho c_-/18m)^{1/2}$ (c_- is the smallest eigenvalue of the curvature matrix), the outer one being the spinodal boundary corresponding to $c = 0$. The direction of the corresponding eigenvectors are indicated along the contours. The result of the “mechanical” instability criterion (2.23) is also shown (dashed boundary). (From Ref. [48].)

isotherms. Thus, given the relationship between the chemical potentials and y for given temperature and pressure, the matching conditions for the chemical potentials, $\mu_n^L = \mu_n^G$ and $\mu_p^L = \mu_p^G$, makes it possible to determine the respective proton concentrations of the liquid and gas phase, y^G and y^L . In order to discuss in some detail how the phase transformation proceeds, we consider a system with an overall proton concentration of $y = 0.3$ which is held at a fixed temperature of $T = 10$ MeV as the pressure is gradually increased. This situation is illustrated in Fig. 2.9.

We may note that generally the gas phase of a neutron-rich system has a smaller proton concentration than the corresponding liquid phase. Indeed, when the gas phase has been reached (point D in the figure) its proton concentration is rather small, $y_D \approx 0.1$. This is a typical fractionation process, akin to the distillation of alcohol from water. In nuclear matter the liquid tries to get as close as possible to equal concentrations of neutrons and protons, since symmetric matter is energetically favorable, and the gas is then left with the excess. This mechanism, first noted in Ref. [14], can be an important signal of the occurrence of phase transitions. It was thoroughly investigated in a lattice gas model [52] and has been investigated experimentally through the study of isotopic ratios [53–57].

As we have seen, for a two-component system the pressure is *not* constant during the phase transformation. The underlying reason for this feature is that the coexisting gas and liquid phases have different chemical compositions which provides an additional degree of freedom. Furthermore, the relative abundances of the phases change as well. Therefore, the calculation of the phase transformation by use of the Gibbs criteria (the generalized Maxwell construction) requires knowledge of the isotherms for a range of concentrations y . The resulting equation of state is shown in Fig. 2.10.

As noted in Refs. [42,49,50], the phase transition is continuous. However, the continuity of the phase transformation as a function of the applied pressure should not be taken as evidence that the transition is of second order. In fact, any phase point inside the coexistence region is associated with

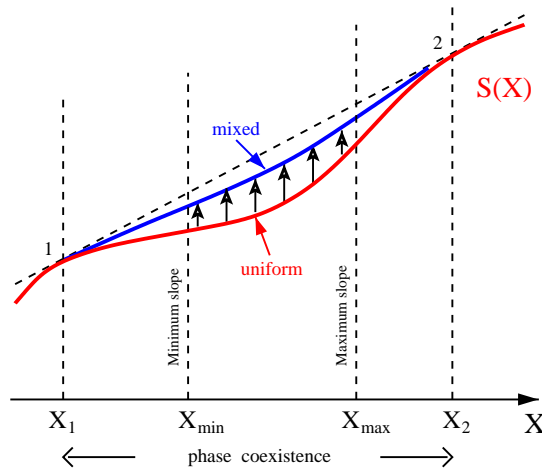


Fig. 2.11. Isolated finite system. When the entropy function for a uniform finite system (lower curve) has a local convexity region, the isolated system may gain entropy by reorganizing itself into a mixture of the two coexisting phases, but the resulting equilibrium entropy function (upper curve) will always lie below the common tangent (dashed line).

a first order phase transition. Indeed, the order of the phase transition does not depend on how the state has been reached but is an inherent state property determined by the topology of the surface of the thermodynamic potential. (The same situation occurs in the familiar water-vapor system: the phase transition is manifestly of first-order but the phase transformation is continuous if the volume is kept constant.) Thus it is possible to have at the same time continuous phase transformations and spinodal decomposition.

2.4. Finite systems

We have seen above that the concept of spinodal instability applies in general to macroscopically uniform systems that are suddenly brought deep into the coexistence region of their phase diagram. The principal characteristic of this out-of-equilibrium phenomenon is the instability against local disturbances of the order parameter. This instability occurs when the entropy function for the uniform system has a local convexity. Indeed, in the thermodynamical limit the entropy is additive and can thus be increased in the region of convexity by splitting the system into independent subsystems. The thermodynamical limit then guarantees the ensuing mixed-phase system acquires an entropy function that is nowhere concave (see Fig. 2.1).

For finite systems the above features are modified by the fact that the energy associated with the interface between the coexisting phases is no longer negligible. Then the energy is no longer additive. By the same token, the entropy of the combined system is not merely a sum of the individual subsystem entropies (but is somewhat smaller than that) and the Maxwell construction thus loses its validity. The situation is illustrated in Fig. 2.11. As for infinite systems, it is possible to prepare a finite system in a macroscopically uniform state and one may consider the corresponding entropy function $S(X)$. (One may, for example, think of X as controlling the geometrical size of the system through a scaling of the position \mathbf{r} .) When a convexity is present in $S(X)$, the uniform state

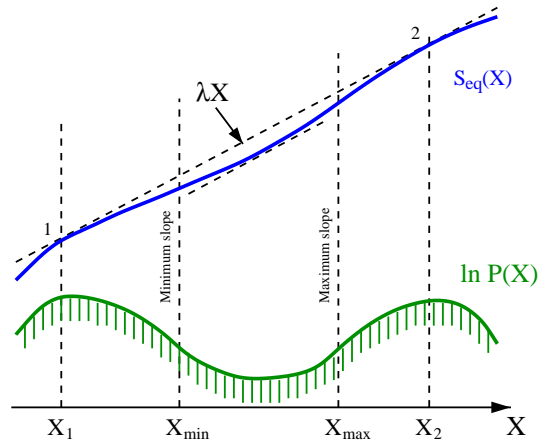


Fig. 2.12. Canonical ensemble of finite systems. When the finite system is brought into contact with a reservoir, it may explore the entire range of X values and the resulting bimodal statistical equilibrium distribution is given by $P(X) \sim \exp(S(X) - \lambda X)$. The figure shows the case when the Lagrange multiplier λ equals the slope of the common tangent. The two peaks in $P(X)$ have then the same height, its points of inversion coincide with those of $S(X)$, (so $\ln P(X)$ has positive curvature in between), and its minimum lies where the slope of $S(X)$ also equals λ .

is out of equilibrium as entropy can be gained by reorganizing it into a phase mixture. However, the resulting maximal entropy for the given value of X falls below the common tangent, due to the finite interface energy. Thus, the resulting equilibrium entropy function lies below the Maxwell line and, consequently, it will still exhibit a convexity.

The above considerations apply to a microcanonical situation, as the system considered is isolated, with a fixed value of X , and is initially out of thermodynamic equilibrium. If situated inside the region of convexity, the isolated system may then spontaneously undergo a spinodal decomposition into a mixture of two coexisting phases in an equilibrium state conditioned by the specified value of X . If now such a system is subsequently brought into contact with a reservoir, the value of X may fluctuate as the system now explores the entire phase space. The associated equilibrium distribution is $P(X) \sim \exp(S(X) - \lambda X)$, where λ is the Lagrange multiplier controlling the average. This situation is illustrated in Fig. 2.12. It is seen that when a convexity is present, the resulting X distribution acquires a bimodal character. When λ is adjusted so the two peaks in $P(X)$ have the same height (the common tangent to $S(X)$ has then the slope λ), the curvature of $\ln P(X)$ is positive throughout the region of entropy convexity and $P(X)$ has a minimum at the value of X corresponding to the intermediate coexisting unstable phase (where the slope of $S(X)$ equals that of the common tangent).

The fact that first-order phase transitions in finite systems can be associated with the occurrence of a curvature anomaly in the appropriate thermodynamic potential has been discussed in a considerable amount of recent work [18,58–71]. The entire coexistence region may be explored by varying the associated extensive state variables, which present the relevant order parameters. In the region of negative curvature, the system will acquire conditional stability when kept in isolation, while its instability will be revealed as a bimodal distribution of the order parameter when it is put into contact with a reservoir. Furthermore, the occurrence of a first-order phase-transitions is often accompanied

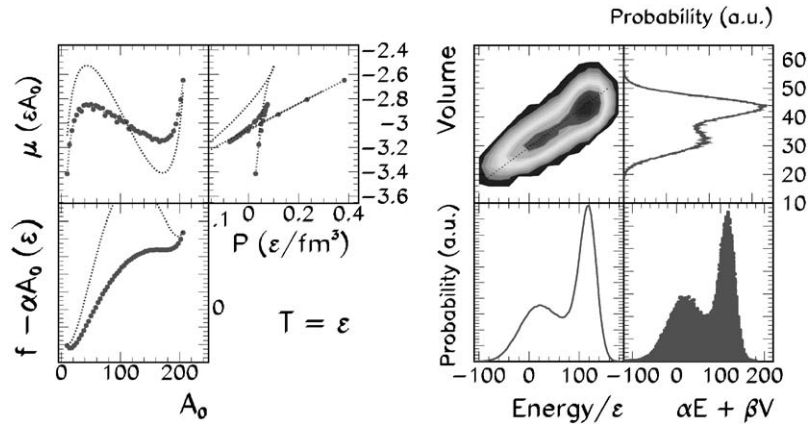


Fig. 2.13. Lattice gas. *Left panel:* The free energy (minus a linear term) of a canonical lattice gas in a fixed total volume as a function of the particle number (*bottom*) and its derivative, the chemical potential (*top left*). The concave intruder in the free energy produces a backbending of the chemical potential, thus leading to a negative chemical susceptibility. The pressure (*top right*), being the variation of the free energy with respect to the volume, exhibits a simultaneous anomaly reflecting a negative compressibility throughout the phase transition region. The mean-field result (dotted curve) associated with a uniform density is unstable against phase separation (solid points), as illustrated in Fig. 2.11. (Adapted from Ref. [62].) *Right panel:* Volume and energy distribution in the first-order phase-transition region (after the system has also been put into contact with a volume reservoir), with three associated projections: on the energy (*bottom left*), on the volume (*top right*) and on the line which connect the two maxima which can be seen as the best order parameter (*bottom right*). The convex intruder in the probability distribution (which is responsible for the observed bimodality) corresponds to a convex intruder in the corresponding entropy. Therefore it signals the occurrence of negative specific heat and compressibility. (From Ref. [64].)

by a plateau-like behavior of the caloric curve, or even a “backbending” corresponding to a negative specific heat. However, since the caloric curve is affected by the specific dependence of the volume on the excitation energy it may not provide direct information on the character of the phase transition [63,72,73].

2.4.1. Isochore canonical ensembles

Let us first illustrate the general definition of a first-order phase transition as the occurrence of a curvature anomaly of the thermodynamical potential as a function of one order parameter. For the liquid–gas phase transition, the density can be taken as an order parameter. Since the density is related to both particle number and volume, one may consider an ensemble in which these two extensive quantities are state variables. This is the case, for example, for the canonical lattice gas in a constant volume where a phase transition is signaled by a concavity anomaly in the free energy $F = -T \ln Z = E - TS$ (which follows from the partition sum $Z(T, V, N)$), as shown in Refs. [62,65] and illustrated in Fig. 2.13 (*left*). For the chemical equation of state, $\mu = \partial_N F$, the concavity anomaly appears as a back bending of the chemical potential μ as a function of the particle number N . This back bending implies that the chemical susceptibility $\chi^{-1} = \partial_N \mu$ has a negative branch. Furthermore, the mechanical equation of state, $P = \partial_V F$, exhibits a similar back-bending behavior as a function of the density, thus leading to a negative compressibility. It should be stressed that these two anomalies are found for a finite system in an equilibrium characterized by a fixed particle number and volume.

These features can be further elucidated by imagining that the finite system in equilibrium is brought into contact with a reservoir for particles (or volume). Then any arbitrarily small mismatch between the intensive variables (chemical potential or pressure) will become amplified, since the negative chemical susceptibility (or compressibility) will cause a change of particle number (or volume) that will further increase the difference. The finite system will then evolve away from the anomalous region of negative curvature and approach a stable equilibrium state that has again the same value of the intensive variable as the reservoir but with a normal curvature. In this sense, the original finite system finds itself in an unstable equilibrium configuration and it will therefore seek to escape from the spinodal region when offered an opportunity in the form of a suitable perturbation.

To further illustrate this point, let us now consider the liquid–gas phase transition in a system of N particles for which the volume is not fixed but may fluctuate. In such a case, we can define an observable \hat{V} as a measure of the volume of the system and we can characterize a statistical ensemble of realizations of this system by its average volume $\langle \hat{V} \rangle$. As usual in statistical physics, one may then introduce a corresponding Lagrange multiplier λ_v (which has dimension of a pressure divided by a temperature).

As shown in Fig. 2.13 (right), in such an isochore canonical ensemble it is possible to define the distribution $P_{\beta\lambda_v}(E, V) = \bar{W}(E, V) Z_{\beta\lambda_v}^{-1} e^{-\beta E - \lambda_v V}$, which contains the complete information since the events are sorted according to the two thermodynamical variables E and V . It leads to the density of states, which is simply the exponential of the entropy, $\bar{W}(E, V) = \exp(\bar{S}(E, V))$. One can see that in the first-order phase transition region the probability distribution is bimodal, as expected since the entropy presents a convex intruder. Moreover, for a fixed λ_v , there exists a temperature for which the two maxima have equal height, corresponding again to the Maxwell construction. It is clear from the figure that for such a system in contact with a reservoir (of energy and volume in the present case) the anomalous concavity region tends to become depopulated, since the probability distribution displays a minimum, and this region can thus be characterized as unstable. Nevertheless, contrary to the thermodynamical limit, the probability density remains finite throughout the unstable region.

The joint distribution of energy and volume and at its two projections show that the system has simultaneously a negative heat capacity and a negative compressibility. Thus, in liquid–gas phase transitions, spinodal instability is intimately related to the occurrence of negative specific heat.

2.4.2. Spinodal instability in molecular dynamics

The clustering caused by the spinodal instability of dilute nuclear matter was studied by Peilert et al. [74] who performed canonical Metropolis simulations with a quasi-classical many-body model. For this purpose, the QMD model [75], which includes two- and three-body Skyrme-type interactions as well as a finite-range Yukawa force, was augmented with a momentum-dependent Pauli-potential [76] that serves to keep the nucleons apart in phase space, $V_P \sim \sum_{ij} \exp(-r_{ij}^2/2q_0^2 - p_{ij}^2/2p_0^2)$. Furthermore, since both finite nuclei and infinite nuclear matter were considered, the Coulomb interaction was screened, using a suitably large range.

Fig. 2.14 illustrates how the dilute matter prefers to cluster, the effect becoming increasingly pronounced as the volume is increased. The associated gain in energy can be considerable for temperatures below ≈ 8 MeV, as is illustrated in Fig. 2.15. As the authors pointed out, it is important to take this phenomenon into account when seeking to determine the nuclear equation of state from data. However, due to the irregular and varied appearance of the clustered system, the inclusion of

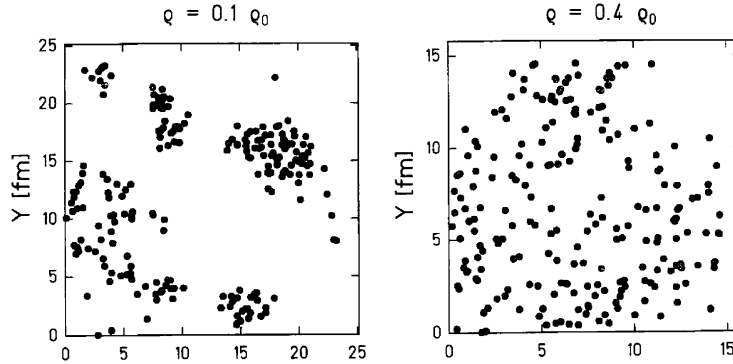


Fig. 2.14. Clustered matter. Typical manifestations of nuclear matter at two densities inside the spinodal region of the phase diagram, as obtained with quasi-classical molecular dynamics (the positions of 254 nucleons are projected onto the xy plane). (From Ref. [74].)

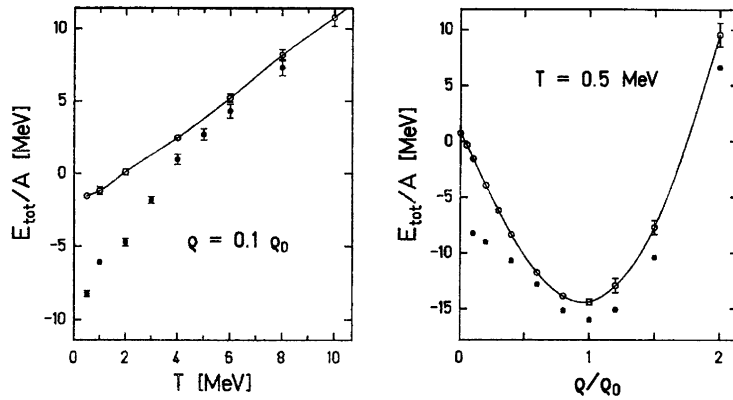


Fig. 2.15. Clusterization energy. The average energy per nucleon as obtained for either random positions (higher values) or a canonical (Metropolis) ensemble (lower values), for either a fixed density as a function of temperature (*left*) or for a fixed temperature as a function of density (*right*), as obtained with quasi-classical molecular dynamics. (From Ref. [74].)

the subsaturation clustering into calculations of the nuclear equation of state poses a considerable challenge which has not yet been overcome.

An instructive numerical experiment has been performed in Ref. [77] within classical molecular dynamics. The particles interact through a Lennard–Jones type potential, $V(r) = (r^{-8} - r^{-4})\theta(r - R_{\max})$, and are prepared at a given density and temperature within a fixed box (with periodic boundaries). They are then evolved until they have equilibrated, at which time the pressure and the temperature are extracted. The resulting equation of state (isotherms of the pressure versus density) is shown on the left in Fig. 2.16.

Although the statistics is rather poor, it can be clearly seen that there is a region where $\partial P / \partial \rho$ is negative. It is thus possible to identify a spinodal region and the associated liquid–gas co-existence region. The critical temperature can also be extracted as the temperature of the isotherm having an inflection point.

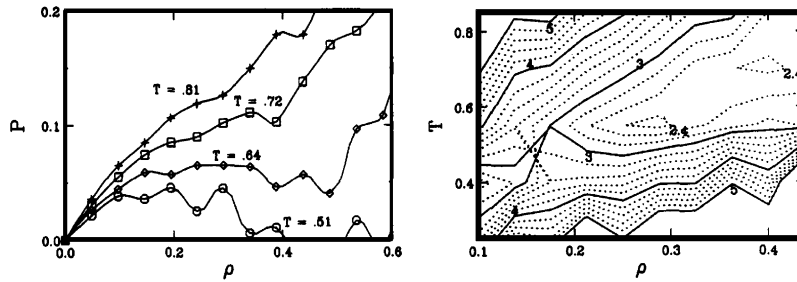


Fig. 2.16. Spinodal instability in classical molecular dynamics. *Left panel:* The equation of state (isotherms of the pressure P versus density ρ) obtained for a system of 512 Lennard-Jones particles in a box with periodic boundary conditions. *Right panel:* Contour plot in the T - ρ plane of the power τ characterizing the equilibrium mass distribution of the clusters formed within the spinodal region. (From Ref. [77].)

When the system is prepared inside the liquid-gas coexistence region it becomes clumpy and an associated “fragment” mass distribution can be extracted. Its density and temperature dependence was also studied in Ref. [77] and it was found that the mass distribution in the range $4 < A < 30$ exhibits a power falloff characterized by the exponent τ shown on the right in Fig. 2.16. Large values of τ indicates that the mass distribution is evaporation-like (U-shaped) (at small T) or vaporization-like (at high T). The lowest value of τ was obtained near the critical point, $\tau_{\min} \approx 2.2$.

The occurrence of critical behavior inside the coexistence region is a generic result for systems with a very small number of constituents. It has been shown in Ref. [62] that for a lattice-gas simulation the fragment distribution presents a critical behavior with power laws and scaling not only at the critical point but at all densities along a line passing by the critical point but diving deeply inside the coexistence and even the spinodal region. This is illustrated in Fig. 2.17.

2.4.3. Experimental evidence and perspectives

Both bimodal energy distributions and negative microcanonical heat capacities have been recently reported for open finite systems undergoing a phase transition. In the case of nuclear multifragmentation the heat capacity has been reconstructed using partial energy fluctuations [78]. The first results, obtained for peripheral strongly-damped Au+Au collisions [79], were followed by results for central “fusion-like” processes [80–82] and for pion-induced reactions [83]. The same general phenomenon has been reported recently in another field of physics: metallic cluster melting [84], where the canonical distribution of events was demonstrated to be bimodal. It should be noted that all these results were obtained for open systems in which the volume may fluctuate and the observed heat capacity is then related to C_P . Using the relation between C_P , C_V and κ_T , one can see that when C_P diverges then κ_T approaches zero, which demonstrates the equivalence between the negative heat capacity region and the mechanical spinodal region.

2.5. Concluding remarks about thermodynamics

In this first section, we have seen that spinodal instability of a system is a general feature that reflects the particular structure of the associated phase diagram. Generally, spinodal instability is associated with a convex anomaly of the entropy function. In macroscopically uniform systems,

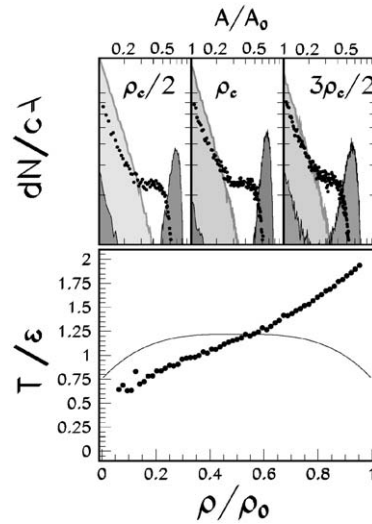


Fig. 2.17. Critical fragment distribution. *Top*: Fragment distributions at various densities and temperatures in a lattice gas. At each density, a typical U-shaped distribution emerges below a critical temperature (dark histograms) with both light fragments and heavy residues, while only small fragments remain above (light histograms). Around the critical temperature the distribution resembles a power law (dots). *Bottom*: The density dependence of the corresponding critical temperature (dots) and the boundary of the coexistence region (light curve). The critical-temperature curve intersects the coexistence boundary close to its top (the thermodynamic critical point, but critical behavior appears both above (along the so-called Kertész line) and below (inside the coexistence region)). (Adapted from Ref. [62].)

the entropy can then be increased by infinitesimal fluctuations of the local order parameter and the system decomposes itself into two coexisting phases in equilibrium, thereby eliminating the convexity.

In an isolated finite system, such a spontaneous transformation may not be possible and the system may establish a conditional equilibrium inside the anomalous region. However, if such a system is brought into contact with a suitable reservoir, it will explore the entire range of the order parameter which will then acquire a bimodal equilibrium distribution exhibiting a minimum in the unstable concave region.

In the nuclear case, where two interacting components are present, protons and neutrons, the discussion of spinodal instability is more complicated because of the presence of two independent chemical potentials, μ_p and μ_n . Although it has some intuitive appeal to discuss the phenomenon in terms of separate “mechanical” and “chemical” instabilities (representing changes in the nucleon density or the proton concentration, respectively), such an approach can be misleading since those are in fact associated with a single instability. Indeed, the relevant variables are determined by the corresponding normal modes, as obtained by diagonalizing the curvature matrix of the thermodynamic potential, and they generally involve changes in both total density and concentration. We have seen that the direction of the unstable normal mode is predominantly isoscalar (i.e. of mechanical character), which shows that the underlying mechanism is in fact a liquid–gas phase transition rather than a chemical (i.e. isovector) separation of protons from neutrons (so it is not a ferromagnetic phase transition in the isospin space). Nevertheless, a spinodal decomposition of the nuclear system

generally induces isospin fractionation, since the high-density (liquid) phase is closer to symmetric matter than its low-density (gas) partner phase.

3. Onset of spinodal fragmentation

In the previous section, we have discussed the concept of spinodal instability within the framework of thermodynamics, where it appears when a uniform system in equilibrium loses stability against phase separation. Since these systems are unstable, they will evolve in time and a dynamical point of view must therefore be adopted. We generally wish to investigate the fate of systems that have been prepared in an unseparated configuration situated within the region of spinodal instability. This can typically be achieved by first preparing the system in a suitable equilibrium configuration, such as hot uniform matter, and then making the system unstable by performing a quench, a sudden reduction of the temperature or/and the density.

A basic theoretical framework for treating spinodal decomposition was developed by Hillard, Cahn, and coworkers [85–91]. Further important developments were made by Langer et al. [92,93] and a good overall discussion of the kinetics of first-order phase transitions can be found in Ref. [94]. In order to bring out the main features, we start by considering the phenomenological Landau–Ginzburg model [92,95] within which the time evolution of the density $\rho(\mathbf{r})$ is governed by a simple diffusion equation,

$$\frac{\partial}{\partial t} \rho(\mathbf{r}, t) = v \nabla^2 \frac{\delta F[\rho(\mathbf{r}, t)]}{\delta \rho(\mathbf{r}, t)} . \quad (3.1)$$

Here the free energy $F[\rho(\mathbf{r})]$, which is a functional of the density $\rho(\mathbf{r})$, may be expressed in a simple approximate form,

$$F[\rho(\mathbf{r})] = \int d\mathbf{r} [f(\rho(\mathbf{r})) + \frac{1}{2} c (\nabla \rho(\mathbf{r}))^2] , \quad (3.2)$$

where $f(\rho)$ is the free-energy density for matter with a uniform density ρ and where the gradient term seeks to account for the finite range of the interaction. The pressure is given by $P = \rho^2 \partial_\rho \phi$, where $\phi = f/\rho$ is the free energy per particle in the uniform system, and the compressibility modulus is $\kappa^{-1} = \rho \partial_\rho P = \rho^2 \partial_\rho^2 f$.

The onset of spinodal decomposition can then be studied by linearization of the time-dependent Ginzburg–Landau equation (3.1). One thus considers small variations of the density around a uniform value, $\delta \rho(\mathbf{r}, t) = \rho(\mathbf{r}, t) - \rho_0$, and find

$$\frac{\partial}{\partial t} \delta \rho(\mathbf{r}, t) = v \nabla^2 \left[\left(\frac{\partial^2 f}{\partial \rho^2} \right)_{\rho=\rho_0} - c \nabla^2 \right] \delta \rho(\mathbf{r}, t) . \quad (3.3)$$

For plane-wave disturbances, $\delta \rho(\mathbf{r}, t) \sim \exp(i\mathbf{k} \cdot \mathbf{r} - i\omega_k t)$, the dispersion relation for the associated frequency ω_k can then be obtained,

$$\omega_k = -ivk^2 \left[\frac{1}{\kappa \rho^2} + ck^2 \right] . \quad (3.4)$$

The system is situated inside the spinodal region when the compressibility is negative, $\kappa < 0$, and a mode \mathbf{k} is then unstable if its wave number is below a maximum value, $k < k_{\max}$, where $\kappa \rho^2 k_{\max}^2 c = -1$. For these modes, the frequency is imaginary, $\omega_k = \pm i\gamma_k$, so the disturbance evolves exponentially, $\rho_k \sim \exp(\pm \gamma_k t)$. The growth rate tends to zero at the two boundaries, $\gamma_k \rightarrow 0$ for $k \rightarrow 0$ and $k \rightarrow k_{\max}$, and it thus attains a maximum value at a certain preferred wave number, k_0 , which in the simple Landau–Ginzburg model is given by half the maximum value, $k_0 = \frac{1}{2} k_{\max}$. It may therefore be expected that density irregularities with wave numbers near k_0 will come to dominate the spatial pattern of the spinodal decomposition. The corresponding characteristic wave length, $\lambda_0 = 2\pi\rho_0\sqrt{-c\kappa}$, is determined by the ratio of the compressibility modulus κ^{-1} and the parameter c which reflects the finite range of the interaction. If the system is sufficiently dilute, the result of the spinodal decomposition will be the transformation of the unstable uniform system into an assembly of fragments. It then follows from the above analysis that the fragments should exhibit a corresponding preferential size, $A_f \approx \lambda_0^3 \rho_0$.

Those characteristics, the amplification of small fluctuations with growth rates that exhibit a preference for a certain length, are generic properties of spinodal decomposition. In macroscopic systems, such as binary alloys, this phenomenon has long been known and is now a standard part of text books on statistical physics (see Ref. [95], for example). Its relevance to nuclear multifragmentation was first pointed out by Bertsch and Siemens [3] over 20 years ago.

However, although the general features discussed above will also be present in the spinodal decomposition of nuclei, phenomenological descriptions of the above type are clearly inadequate for the treatment of the nuclear problem. Of particular importance are the following features:

1. Nuclear matter is Fermi liquid with specific quantum properties. Furthermore, the uncertainty principle plays a strong role in nuclear physics because of the relatively small size of nuclei. Moreover, up to several MeV of excitation, specific nuclear structure such as shell effects may play a role, as we will see in the complete RPA treatment of the nuclear instabilities.
2. Nuclei are not large in comparison with the range of the strong interaction, so surface effects are significant and any description must have a correspondingly fine spatial resolution. In addition, nuclei are charged and the long-range Coulomb repulsion renders the thermodynamical limit problematic.
3. The time scales for the macroscopic nuclear dynamics occurring in heavy-ion collisions are fairly short and the system is typically out of local equilibrium. The transport description must therefore be correspondingly detailed.
4. Linear treatments apply only to the early development of instabilities. Once the density disturbances grow large the dynamics becomes non-linear and a more complete treatment is required. Moreover, the phenomenological treatment does not concern itself with how the system has become unstable or how the disturbances originated. These important questions will be addressed in the next section.

In the present section, we will focus on the early growth of the disturbances.

3.1. Nuclear matter

To make the connection with thermodynamics, we first consider spinodal instability in bulk matter. As we shall see in this section, and in contrast to the time-dependent Ginzburg–Landau

approach which only treats the diffusion of the density fluctuation, the density fluctuations generally propagate and thus form sound waves. Since nucleons are fermions, the density fluctuations should be investigated in Fermi-liquid theory. Then the sound properties are strongly affected, since only particles near the Fermi surface participate in the collective motion. However, before embarking on the specific description of Fermi liquids, let us first recall what can be expected for a classical fluid.

We shall see in this section that spinodal instabilities in infinite matter can be seen as ordinary sound waves whose speed has turned imaginary upon entry into the spinodal region. At sufficiently long wave lengths, where the situation is the simplest since only the bulk properties and the Coulomb force play a role, the speed of sound ultimately approaches zero. In the opposite extreme of small wave numbers the speed of sound also tends to zero, due to the finite range of the interaction. Thus there is a length scale for which the growth rate has a maximum, as is characteristic of spinodal decomposition.

3.1.1. Hydrodynamical instabilities in classical fluids

Let us first consider the dynamics of density fluctuations in a classical fluid. The evolution of a fluid element caused by the pressure gradients is governed by the Navier–Stokes equation,

$$\frac{d}{dt}\rho\mathbf{v} \equiv \frac{\partial}{\partial t}\rho\mathbf{v} + \mathbf{v} \cdot \nabla\rho\mathbf{v} = \nabla P, \quad (3.5)$$

while the continuity equation, which expresses the conservation of matter, yields

$$\frac{\partial}{\partial t}\rho + \nabla \cdot \rho\mathbf{v} = 0. \quad (3.6)$$

If we linearize around the initial uniform density ρ_0 , $\delta\rho(\mathbf{r},t) = \rho(\mathbf{r},t) - \rho_0$, the first equation becomes $\rho_0\partial\mathbf{v}/\partial t = \nabla P$, while the second reduces to $\partial\delta\rho/\partial t = \rho_0\nabla \cdot \mathbf{v}$. With a corresponding linearization of the pressure, $P(\mathbf{r},t) = P_0 + (\partial P/\partial\rho)_0\delta\rho(\mathbf{r},t)$, these two equations lead to a single closed equation for the density disturbance,

$$\frac{\partial^2}{\partial t^2}\delta\rho(\mathbf{r},t) = \nabla^2 P = \left(\frac{\partial P}{\partial\rho}\right)_{\rho=\rho_0} \nabla^2\delta\rho(\mathbf{r},t). \quad (3.7)$$

Taking the Fourier transform and introducing the speed of sound $v_s = (-\rho m \kappa)^{1/2}$, where $\kappa^{-1} = \rho\partial_\rho P$ is the compressibility modulus, we obtain the dispersion relation,

$$\omega_k^2 = v_s^2 k^2 \quad \text{or} \quad k^2 = \rho m \kappa \omega_k^2. \quad (3.8)$$

This expression brings out the fact that the dynamics of the sound waves is directly related to the thermodynamics. In a perfect gas, $P = \rho T$, the compressibility is always positive and the speed of sound is always real. In this regime, called *first sound*, the density fluctuations propagate. The situation remains similar after the increase of the pressure caused by hard collisions has been taken into account.

However, the attractive long-range part of the interaction tends to reduce the pressure. (In the Van der Waals fluid, this effect is emulated by the attractive term containing the parameter a .) Then a new type of sound arises, *zero sound*, for which the propagation is due to the attractive tail of the interaction. This attractive part is responsible also for the condensation of a gas into a liquid,

a phenomenon associated with the occurrence of a negative compressibility. The speed of sound is then imaginary and the system is unstable against density undulations. It should be noted that in the nuclear case the fermionic nature of the nucleons modifies the above discussion because the exclusion principle suppresses collisions, thus reinforcing the role of the mean field, and reduces the number of active particles to those near the Fermi surface, thus affecting the propagation of waves.

3.1.2. Collective motion in Fermi fluids

In the standard treatment, the fluid dynamical equations are deduced from the Boltzmann equation by taking the zeroth and the first moments of the local momentum distribution. This approach is also possible for Fermi fluids. However, as an alternative treatment, we shall discuss here the derivation of the fluid dynamics from a variational approach [96,26], which will allow us to derive equations for collective modes, thus simplifying the extraction of the region of instability.

In the variational formulation of quantum fluid dynamics, the starting point is the action integral, $I = \int dt \langle \Psi | i\hbar \partial/\partial t - \hat{H} | \Psi \rangle$, from which the many-body Schrödinger equation can be obtained. The expectation value of the Hamiltonian, $\langle \Psi | \hat{H} | \Psi \rangle$, is calculated by making a specific ansatz for the many-body wave function,

$$\Psi(\mathbf{r}_1, \mathbf{r}_2, \dots, \mathbf{r}_A; t) = \Phi(\mathbf{r}_1, \mathbf{r}_2, \dots, \mathbf{r}_A; t) e^{(i/\hbar) \mathcal{S}(\mathbf{r}_1, \mathbf{r}_2, \dots, \mathbf{r}_A; t)}, \quad (3.9)$$

where the amplitude $\Phi(t)$ and the phase $\mathcal{S}(t)$ are real functions of the positions. With the assumption that the phase is additive, $\mathcal{S}(t) = \sum_{n=1}^A S(\mathbf{r}_n, t)$, and that $\Phi(t)$ is a Slater determinant characterized by its one-body density ρ , it is possible to express the action [26,97],

$$I = \int_{t_1}^{t_2} dt \left[E[\rho] + \int d^3\mathbf{r} \left(S(\mathbf{r}) \frac{\partial}{\partial t} \rho(\mathbf{r}) - \frac{\rho(\mathbf{r})}{2m^*(\mathbf{r})} \nabla S(\mathbf{r}) \cdot \nabla S(\mathbf{r}) \right) \right], \quad (3.10)$$

where $m^*(\mathbf{r})$ is the effective nucleon mass and $E[\rho]$ is the energy functional. A local density approximation is often performed so that $E[\rho] = \int d^3\mathbf{r} E(\rho(\mathbf{r}))$, where $E(\rho)$ is the energy density of bulk matter at the density ρ . (Such a local approximation is used for the kinetic energy in the Thomas–Fermi treatment and for the interaction energy in Skyrme-type models.)

Within these approximations, the density $\rho(\mathbf{r})$ plays the role of the coordinate while the phase $S(\mathbf{r})$ is the conjugate momentum. The requirement of stationarity under variations in ρ then leads to the continuity equation,

$$\frac{\partial}{\partial t} \rho(\mathbf{r}) + \nabla \cdot (\mathbf{u}(\mathbf{r}) \rho(\mathbf{r})) = 0, \quad (3.11)$$

with the velocity field being $\mathbf{u} = (1/m^*) \nabla S$. Thus the phase function $S(\mathbf{r})$ may be interpreted as a velocity potential and the Lagrange equation for $S(\mathbf{r})$ then yields an Euler-type equation for the velocity field $\mathbf{u}(\mathbf{r}, t)$.

Small-amplitude collective motion can now be studied by linearizing the above continuity equation around a given reference state having the uniform density ρ_0 . Thus, for a given collective mode v , the velocity potential may be parametrized as $S(\mathbf{r}, t) = \dot{q}_v(t) S_v(\mathbf{r})$, where q_v is the collective amplitude. The corresponding distortion of the density is given by $\delta\rho(\mathbf{r}, t) = q_v(t) \delta\rho_v(\mathbf{r})$, where the specific density distortion can be obtained from the continuity equation (3.11), $\delta\rho_v = -\rho_0 \nabla \cdot ((1/m^*) \nabla S_v)$.

The expectation value of the Hamiltonian then assumes a normal form,

$$\langle \psi | H | \psi \rangle = E_0 + \frac{1}{2} M_v \dot{q}_v^2 + \frac{1}{2} C_v q_v^2, \quad (3.12)$$

where E_0 is the energy of the equilibrium state. Furthermore, the inertia and stiffness coefficients for the mode are

$$M_v = \int d^3 \mathbf{r} \frac{\rho_0}{m^*(\mathbf{r})} \nabla S_v(\mathbf{r}) \cdot \nabla S_v(\mathbf{r}) > 0, \quad (3.13)$$

$$C_v = \int d^3 \mathbf{r} \int d^3 \mathbf{r}' \left(\frac{\delta^2 E[\rho]}{\delta \rho(\mathbf{r}) \delta \rho(\mathbf{r}')} \right)_0 \delta \rho_v(\mathbf{r}') \delta \rho_v(\mathbf{r}), \quad (3.14)$$

and the collective frequency ω_v is then given by $\omega_v^2 = C_v/M_v$. When C_v becomes negative the collective mode turns unstable, $\omega_v = \pm i\gamma_v$, where γ_v is the growth rate of the amplitude q_v .

We finally note that all the input quantities for the above treatment are fixed by the standard parameters of the considered interaction, so in that sense the analysis is parameter free. However, we wish to stress that the reduction of the density dependence of the kinetic term to the diagonal part $\rho(\mathbf{r})$ neglects the deformation of the Fermi surface which might be important for the collective motion [96,98].

3.1.2.1. Nuclear matter. After the above general discussion, we now turn to the study of collective motion in nuclear matter. Thus the reference configuration has a uniform density ρ_0 and the distortion can be expanded on plane waves. Accordingly, we may characterize the collective mode by its wave vector \mathbf{k} and the associated velocity potential becomes

$$S_{\mathbf{k}}(\mathbf{r}) = \frac{1}{2} (e^{i\mathbf{k} \cdot \mathbf{r}} + h.c.) = \cos \mathbf{k} \cdot \mathbf{r}. \quad (3.15)$$

The corresponding distortion in density then is determined by the continuity equation (3.11), $\delta \rho_{\mathbf{k}}(\mathbf{r}, t) = 2M_{\mathbf{k}} \cos \mathbf{k} \cdot \mathbf{r}$, where the collective inertia is $M_{\mathbf{k}} = (\rho_0/2m^*)k^2$. The restoring force, $C_{\mathbf{k}}/M_{\mathbf{k}}^2$, is simply related to the Fourier transform of the effective interaction $V(r, r') = \delta^2 E / \delta \rho(\mathbf{r}) \delta \rho(\mathbf{r}')$ and since the Skyrme interaction is local with a quadratic momentum dependence it is a simple polynomial, $C_{\mathbf{k}}/M_{\mathbf{k}}^2 = (A + Bk^2)$ where A and B depend on the specific Skyrme interaction employed. The frequencies of the collective modes are thus given by the dispersion relation,

$$\omega_{\mathbf{k}}^2 = \frac{\rho_0}{2m^*} (A + Bk^2) k^2. \quad (3.16)$$

The first term is the compressibility, $A = \partial P / \partial \rho$. When this quantity is negative, the sound velocity $v_c = (A\rho_0/2m^*)^{1/2}$ is imaginary and we are within the spinodal zone where the disturbances evolve exponentially. For small values of k (gentle undulations), the growth rate is linear, $\gamma_k \approx |v_s|k$. As k is increased the quadratic term gains significance, as the non-local effects become important. It generally counteracts the first term and causes to growth rate drop to zero at $k_{\max} = (-A/B)^{1/2}$. The maximum growth rate, γ_0 , occurs for $k_0 = k_{\max}/\sqrt{2}$. As in the linear Ginzburg–Landau model, the problem is thus characterized by two quantities: the magnitude of the sound velocity $|v_c|$, which is the initial slope of $\gamma_k(k)$, and the typical length scale $\lambda_0 = 2\pi/k_0$ giving the wave length of the most strongly amplified modes.

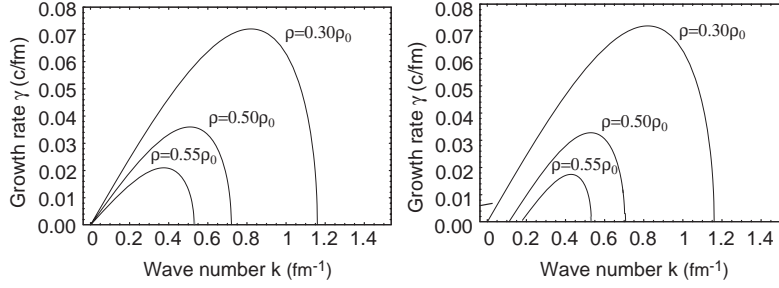


Fig. 3.1. Dispersion relation for unstable sound waves in nuclear matter. The growth rate $\gamma_k = \text{Im}(\omega_k)$ of unstable modes as a function of their wave number k , as obtained either without (left) or with (right) the Coulomb interaction. (From Ref. [99].)

3.1.2.2. Coulomb interaction. Up to now we have only considered the nuclear attraction, since it is the source of the condensation phenomenon. However, protons are charged so the Coulomb interaction must also be taken into account. Using the Hartree–Fock expression, with the exchange term evaluated in the local-density approximation, we may write the Coulomb energy density as [100]

$$e_C(\mathbf{r}) = \frac{1}{2} e^2 \rho_p(\mathbf{r}) \int d^3\mathbf{r}' \frac{\rho_p(\mathbf{r}')}{|\mathbf{r}' - \mathbf{r}|} - \frac{3}{4} e^2 \left(\frac{3}{\pi} \right)^{1/3} \rho_p(\mathbf{r})^{4/3}, \quad (3.17)$$

where $\rho_p(\mathbf{r})$ is the proton density. Of course, the Coulomb energy diverges in infinite matter, so it must be counterbalanced by a suitable negative background charge density. Alternatively, one may employ a simple screening by modulating the first term by the factor $\exp(-|\mathbf{r}' - \mathbf{r}|/a)$. When the screening length a is large compared to the nuclear radius it should not affect the properties of finite nuclei while making the matter calculation possible (the quantitative reliability of the results can be checked by changing a).

Since the restoring force in infinite matter is the Fourier transform of the interaction, the inclusion of the screened Coulomb energy density adds repulsive term having a Lorentzian shape, $[C_k/M_k^2]_C \sim a^2/(a^2 + k^2)$. This term is positive and thus reduces the growth rate. It is important for long wave lengths $k \ll \lambda$, but becomes negligible for small λ , as illustrated in Fig. 3.1. For wave lengths of the order of the nuclear radius, the reduction of the growth rate induced by the Coulomb interaction appears to be insignificant. Thus, for the length scales accessible in nuclear systems, the Coulomb interaction induces only a small reduction of the spinodal growth rate. These results agree well with those of obtained by Fabbri and Matera [101] with the linearized Vlasov equation (which will be discussed in Section 3.1.9).

3.1.3. The unstable response of Fermi liquids

We now discuss how the fermionic nature of the nucleons can be taken into account in a more detailed manner. The propagation of density waves in Fermi liquids has been considered already a long time ago, in particular by Landau [102,103].

With a view towards nuclear systems formed in heavy-ion collisions, Pethick and Ravenhall studied the growth of instabilities within the spinodal region of a normal Fermi liquid [104]. Restricting their considerations to wave lengths that are long compared with both the interparticle spacing and the

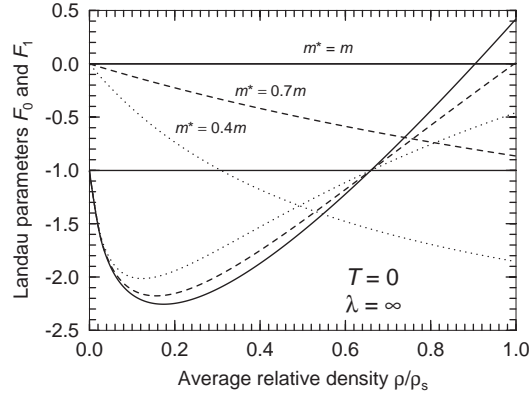


Fig. 3.2. Landau parameters. The standard Landau parameters F_0 (bottom) and F_1 (top), as functions of the density (in units of the saturation density ρ_s), as obtained with the Seyler–Blanchard model (described in Appendix A) for various degrees of momentum dependence as characterized by m^* , the value of the effective nucleon mass at saturation.

(strong) interaction range, as well as to frequencies and temperatures that are low compared with the Fermi kinetic energy, the authors carried out their study within the framework of Landau Fermi-liquid theory. Simple analytic results emerge in the opposite extremes when residual collisions are either very frequent or very rare, as we shall now briefly recall.

When the collision time is short on the macroscopic time scale and the mean free path is short on the macroscopic length scale, the hydrodynamical limit is approached and, as we have seen in Section 3.1.1, the dispersion relation is simple, $\omega_k^2 = v_s^2 k^2$ where v_s is the speed of sound, $v_s^2 = (1/m)\partial_\rho P \sim 1 + F_0$. For conditions under which v_s^2 becomes negative ($F_0 < -1$), the modes have imaginary frequencies. Their amplitudes then evolve exponentially with growth rates given by

$$\gamma_k^\infty = -i\omega_k = -\frac{\hbar}{t_k} = \left(-\frac{1}{3} \frac{m^*}{m} (1 + F_0)\right)^{1/2} kV_F, \quad (3.18)$$

where the effective mass is $m^* = (1 + F_1/3)m$. The quantities F_0 and F_1 are the standard Landau parameters characterizing the medium. They are illustrated for nuclear matter in Fig. 3.2 and are discussed further below and in Appendix A.

The opposite extreme occurs when the residual collisions occur only rarely, so the collision rate is small on the macroscopic time scale and the mean free path is large on the macroscopic length scale. In nuclear physics, this dilute limit occurs at low excitations where the Pauli principle suppresses direct collisions and thus renders the optical potential purely real. One may then employ the Landau kinetic equation for a disturbance in the quasiparticle phase-space density $\delta f(\mathbf{r}, \mathbf{p}, t)$,

$$\frac{\partial}{\partial t} \delta f(\mathbf{r}, \mathbf{p}) + \mathbf{v} \cdot \nabla \delta f(\mathbf{r}, \mathbf{p}) - \frac{\partial f_0(\mathbf{p})}{\partial \epsilon} \mathbf{v} \cdot \nabla \left(\delta U(\mathbf{r}) + \sum_{\mathbf{p}'} F_{\mathbf{p}\mathbf{p}'}(\mathbf{r}) \delta f(\mathbf{r}, \mathbf{p}') \right) = 0. \quad (3.19)$$

An analysis of the pole structure for various values of F_0 then yields the dispersion relation for the corresponding physical scenarios. For example, in the stable regime the collective modes are of zero sound form when $F_0 + (m/m^*)F_1 > 0$. We note that this approach assumes that

$f(\mathbf{p} + \frac{1}{2}\mathbf{q}) - f(\mathbf{p} - \frac{1}{2}\mathbf{q}) \approx \mathbf{v} \cdot \mathbf{q} \partial f(\mathbf{p}) / \partial \epsilon$. This semi-classical approximation may not be accurate at the low densities where spinodal instabilities appear [105], as will be discussed in Section 3.1.8.

The modes are unstable when $F_0 < -1$. When F_0 is only slightly below threshold, the growth rate is linear in F_0 ,

$$F_0 \approx -1 : \gamma_k \approx -\frac{2}{\pi}(1 + F_0)kV_F . \quad (3.20)$$

It increases as F_0 grows increasingly negative and approaches another simple form,

$$F_0 \ll -1 : \gamma_k \approx \left(-\frac{1}{3} \frac{m^*}{m} \left(\frac{9}{5} + F_0 \right) \right)^{1/2} kV_F , \quad (3.21)$$

which is seen to be smaller than the hydrodynamic growth rate γ_k^∞ given in (3.18).

In the intermediate regime, $-1 < F_0 < 0$, the hydrodynamical limit yields undamped oscillations while the collisionless limit leads to Landau damping. This particular regime can play an important role in nuclear collisions, since F_0 is expected to change from the positive values characteristic of hot compressed matter to values below -1 inside the spinodal region, as the collision evolves.

Adopting the relaxation-time approximation for the collision integral, the authors of Ref. [106] bridge the above opposite limits where the mean free path is either very short (hydrodynamics) or very long (Knudsen scenario) and for which analytic results may be derived. In this manner it is possible to achieve a better understanding of the somewhat counterintuitive result that the collisions tend to increase the growth rates. The key reason is that the collisions act to reduce the distortions of the Fermi surface (except for the monopole and dipole which are fixed by the continuity equation, thus reducing the stiffness and facilitating the growth of the instabilities. This effect is further examined in Section 3.1.6 and shown to be relatively small.

In a subsequent study within the same framework, Heiselberg et al. [107] calculated the density response and derived the dispersion relation in hot Fermi liquids, including in particular modes that are unstable with respect to density waves.

3.1.3.1. Growth factors. In a more quantitative study, Heiselberg et al. [106] treated the instabilities with Landau's kinetic equation. Ignoring the small effect of dissipation and employing the relaxation-time approximation, they obtained the growth rate for density ripples of a given wave number k , $\gamma_k(\rho, T) = -\text{Im} \omega_k(\rho, T)$, in the manner described above.

In order to estimate the factor by which a given unstable mode k can grow, uniform nuclear matter was prepared at a given point in the phase plane and its subsequent phase evolution was then determined, $(\rho(t), T(t))$ (assuming that there is no dissipation). If the total energy is negative, the phase point oscillates around the equilibrium density while a steady expansion results when the energy is positive. In either case, the growth rate was integrated over the time spent inside the spinodal region, yielding $G_k = \int \gamma_k(\rho(t), T(t)) dt$. The factor by which the amplitude of the mode k is expected to grow is then given approximately by e^{G_k} . By employing the thermal equilibrium fluctuation of the mode for the initial density fluctuation, it was possible to subsequently obtain an estimate of the absolute magnitude of the resulting density undulation. This analysis suggested that fragmentation may be induced for growth factors in the range of $G \approx 1$ –3. The resulting regions of initial phase conditions are shown in Fig. 3.3.

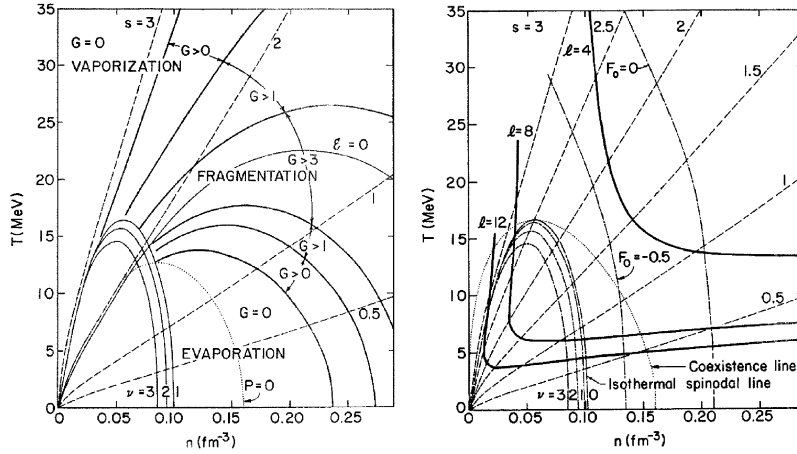


Fig. 3.3. Growth factors. Contours of initial conditions in symmetric nuclear matter for which the largest growth exponent G for the most rapidly growing mode falls within a specified range. The zero-pressure line ($P = 0$), which gives the saturation density as a function of temperature T , is shown together with adiabats, selected instability lines, and the zero-energy contour ($\mathcal{E} = 0$). (From Ref. [106].)

In this type of description, the dynamical phase trajectory depends on the equation of state over a broad range of densities, whereas the spinodal growth rates depend only on the equation of state in a limited subsaturation regime where it is relatively well known. Therefore, as the authors of Ref. [106] point out, experimental information on the high-density part of the equation of state can be obtained if the initial conditions can be extracted from the data. As it happens, for the cases of actual interest, conditions are close to the collisionless limit. It would therefore appear that the adiabatic spinodal line, which is relevant for instabilities in the hydrodynamic limit, plays no role in the present context. (This was confirmed by the molecular-dynamics studies by Lopez et al. [108,109] to be discussed in Section 5.1.5.)

3.1.4. Linear response in semi-classical approaches

After the above general discussion, we now turn towards more specific aspects of instabilities in nuclear systems. The analytic structure of the energy of nuclear matter in the subsaturation metastable region was studied by Friman et al. [110], who obtained the imaginary part of the energy as a non-perturbative sum of ring diagrams.

For the present review, it is particularly interesting to consider the pure Vlasov approach [111–113], in which the residual collisions are entirely neglected. We thus assume that the individual nucleon is governed by an effective Hamiltonian of the form $h(\mathbf{r}, \mathbf{p}) = p^2/2m + U[\rho](\mathbf{r})$. (We ignore for simplicity the possible medium modification of the mass; this more general case is described in Appendix A.) The propagation of a small disturbance in uniform matter, $\delta f(\mathbf{r}, \mathbf{p}, t) = f(\mathbf{r}, \mathbf{p}, t) - f_0(\mathbf{p}, t)$ is then obtained by linearizing the Vlasov equation $Df/dt = 0$,

$$\frac{\partial}{\partial t} \delta f + \frac{\mathbf{p}}{m} \cdot \frac{\partial}{\partial \mathbf{r}} \delta f - \frac{\partial f_0}{\partial \mathbf{p}} \cdot \left(\frac{\partial}{\partial \rho} U \frac{\partial}{\partial \mathbf{r}} \delta \rho \right) = 0. \quad (3.22)$$

Here

$$\delta\rho(\mathbf{r}, t) = g \int \frac{d^3\mathbf{p}}{h^3} \delta f(\mathbf{r}, \mathbf{p}, t) \quad (3.23)$$

is the associated density disturbance, with g being the (four-fold) spin–isospin degeneracy. Performing a Fourier expansion on plane waves,

$$\delta f(\mathbf{r}, \mathbf{p}, t) = \sum_{\mathbf{k}} f_{\mathbf{k}}(\mathbf{p}, t) e^{i\mathbf{k}\cdot\mathbf{r}}, \quad (3.24)$$

we find that the different wave numbers \mathbf{k} are decoupled in uniform matter. Thus, for each value of \mathbf{k} , collective solutions of the form $f_{\mathbf{k}}(\mathbf{p}, t) = f_{\mathbf{k}}(\mathbf{p})e^{-i\omega_{\mathbf{k}}t}$ are determined by the transform of the Vlasov equation (3.22),

$$(-\omega_{\mathbf{k}} + \mathbf{v} \cdot \mathbf{k})f_{\mathbf{k}}(\mathbf{p}) = \mathbf{v} \cdot \mathbf{k} \frac{\partial f_0}{\partial \epsilon} \frac{\partial U}{\partial \rho} \rho_{\mathbf{k}}, \quad (3.25)$$

where $\mathbf{v} = \partial h / \partial \mathbf{p} = \mathbf{p}/m$ is the nucleon velocity, leading directly to the corresponding dispersion equation,

$$0 = \varepsilon(\omega_{\mathbf{k}}) \equiv 1 - \left(g \int \frac{d^3\mathbf{p}}{h^3} \frac{\mathbf{v} \cdot \mathbf{k}}{\mathbf{v} \cdot \mathbf{k} - \omega_{\mathbf{k}}} \frac{\partial f_0}{\partial \epsilon} \right) \frac{\partial U}{\partial \rho} \quad (3.26)$$

$$= 1 - \left(g \int \frac{d^3\mathbf{p}}{h^3} \frac{(\mathbf{v} \cdot \mathbf{k})^2}{(\mathbf{v} \cdot \mathbf{k})^2 - \omega_{\mathbf{k}}^2} \frac{\partial f_0}{\partial \epsilon} \right) \frac{\partial U}{\partial \rho}. \quad (3.27)$$

The solutions to the dispersion equation are thus the roots of the susceptibility $\varepsilon(\omega)$. The second relation follows by eliminating odd terms in the integrand and it shows that the solutions come in real or imaginary pairs of opposite sign. Introducing the sound speed in units of the Fermi speed V_F , $s_{\mathbf{k}} \equiv \omega_{\mathbf{k}}/kV_F$, the dispersion equation (3.27) becomes independent of k . Thus, the speed of sound, $v_s = \omega_{\mathbf{k}}/k = s_{\mathbf{k}}V_F$, is the same for all wave numbers \mathbf{k} . Contact with the Landau treatment can be made by means of the relation $\partial_{\rho}U \approx \frac{2}{3}\epsilon_F F_0/\rho$ (see Appendix A).

3.1.4.1. Zero temperature. In order to elucidate the collective dynamics described by the dispersion relation (3.27), we first look for real solutions at zero temperature, $T = 0$. The momentum integral is then restricted to the Fermi surface (since $\partial_{\epsilon}f_0 = -\delta(\epsilon - \epsilon_F)$) so it reduces to an elementary angular average (see Appendix C), yielding

$$\frac{s}{2} \ln \left(\frac{s+1}{s-1} \right) = 1 + \frac{1}{F_0}. \quad (3.28)$$

This dispersion relation is completely analogous to the one obtained in Fermi liquid theory [102,103,114] and it has real solutions with $s^2 > 1$ when $F_0 > 0$. These disturbances thus propagate with a speed that exceeds V_F . The corresponding roots are shown in Fig. 3.4 as functions of F_0 .

It is equally simple to look for imaginary solutions, $s = \pm i\gamma$, with $\gamma > 0$. The corresponding dispersion equation,

$$\gamma \arctan \frac{1}{\gamma} = 1 + \frac{1}{F_0}, \quad (3.29)$$

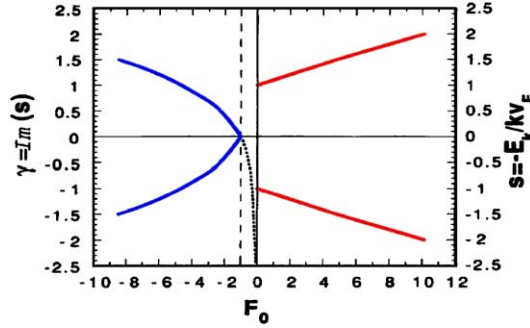


Fig. 3.4. Dispersion relation in nuclear matter at zero temperature. Roots (solid curves) of the dispersion relation (3.27) as a function of the Landau parameter F_0 for both stable ($F_0 > 0$) and unstable ($F_0 < -1$) modes, together with the analytical continuation (dotted curve) into the zero-sound regime ($-1 < F_0 < 0$). (From Ref. [113].)

has the desired solutions for $F_0 < -1$ and they correspond to exponential growth and decay, respectively. Since the derivative of the pressure is given by

$$\frac{\partial P}{\partial \rho} = \left(\frac{\partial U}{\partial \rho} + \frac{2\epsilon_F}{3\rho} \right) \rho = \frac{2}{3} \frac{\epsilon_F}{\rho} (1 + F_0) \rho, \quad (3.30)$$

it is readily seen that the condition $F_0 < -1$ corresponds to the usual stability condition $\partial_\rho P < 0$. Thus, the analysis of the density dynamics yields the same conditions as the thermodynamical analysis of Section 2.

We note that on the positive half of the imaginary axis, $s = i\gamma$ with $\gamma > 0$), the dispersion equation (3.29) is equivalent to

$$\gamma \left(\frac{\pi}{2} - \arctan \gamma \right) = 1 + \frac{1}{F_0}. \quad (3.31)$$

If this relation is analytically continued into the negative half of the imaginary axis ($\gamma < 0$), we may obtain a solution also when $-1 < F_0 < 0$. While this root is not a solution of the dispersion equation Eq. (3.26), it does provide a means for understanding the response of the system in this intermediate regime $-1 < F_0 < 0$. Since these solutions have $\gamma < 0$ they act as a damping, the phenomenon is usually called *Landau damping* and occurs when the interaction (as measured by F_0) is not attractive enough to produce an instability.

3.1.4.2. Finite range. The above analysis has been carried out for the idealized case when the interaction is local so that the potential depends only on the density at the specified position, $U[\rho](\mathbf{r}) = U(\rho(\mathbf{r}))$. To be realistic, one must take account of the finite interaction range and $\partial_\rho U$ should then be replaced by the appropriate Fourier component which we denote by $(\partial_\rho U)_k$. This is most easily seen by imagining that the potential is obtained through a convolution of the density by a suitable kernel. For example, if the kernel is of Gaussian form, $\sim \exp(-r^2/2a^2)$, then $(\partial_\rho U)_k = \partial_\rho U \exp(-\frac{1}{2}k^2a^2)$ and the Landau parameter acquires a k dependence, $F_0(k) = F_0 \exp(-\frac{1}{2}k^2a^2)$. Studies using finite-range Gogny forces have been carried out by Ventura et al. [115,116].

In order to give a quantitative impression of this finite-range effect, we show in Fig. 3.5 (left) how the function $F_0(\rho)$ depends on the wave length of perturbation. It is seen that $F_0(\rho)$ steadily moves

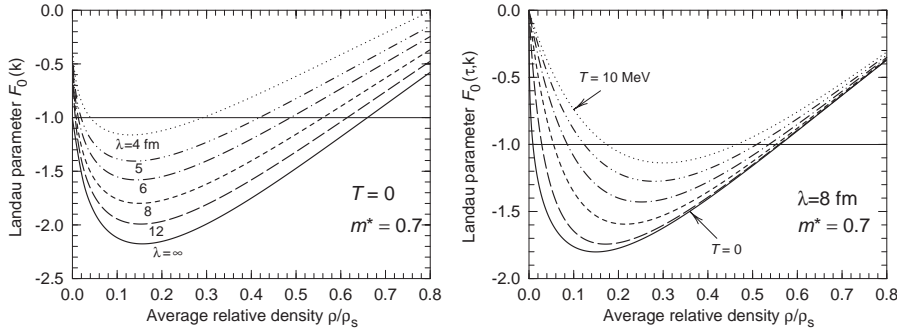


Fig. 3.5. Dependence of F_0 on wave length and temperature. The effective Landau parameter $F_0(k, T)$ is displayed as a function of the density ρ (relative to the saturation density ρ_s) for either various wave lengths λ at $T = 0$ (left) or for various temperatures T for the wave length $\lambda = 8$ fm (right). The results were obtained with the Seyler–Blanchard model for an effective mass of $m^* \approx 0.7m$ (see Appendix A).

upwards as k is increased. Thus, for fixed thermodynamic conditions (ρ and T) inside the spinodal region, the finite range of the force generally reduces the magnitude of F_0 and hence stabilizes the system. While the effect is negligible for long wave lengths, it may be significant for the most rapidly amplified wave lengths which are of nuclear dimensions and therefore are of practical interest.

It follows that spinodal instability occurs only for perturbations having a sufficiently long wave length, $\lambda > \lambda_{\min}$, while the Landau regime, $-1 < F_0 < 0$, contains more rapid undulations. For the Gaussian form of the interaction (see above), the minimum wave length for which spinodal instability is encountered is determined by $\lambda_{\min}^2 = 4\pi a^2 \ln(1/|F_0(0)|)$, while a kernel of Yukawa form, $\sim 1/(1 + a^2 k^2)$, would yield $\lambda_{\min}^2 = 2\pi a^2 / |1 + F_0(0)|$.

3.1.4.3. Finite temperature. The above type of analysis can readily be extended to finite temperatures as well. Fig. 3.5 illustrates how F_0 depends on the temperature T for a given wave length $\lambda = 8$ fm, which is in the range of the most rapidly amplified values (see below). As T is increased, F_0 generally moves towards positive values, thus shrinking the unstable region and reducing the growth rates (see below). The dependence of the spinodal boundary in the ρ – T plane on the wave length $\lambda = 2\pi/k$ is illustrated in Fig. 3.6 (left). The thermodynamic spinodal boundary corresponds to the limit of infinitely long wave lengths, $\lambda = \infty$. As the wave length of the mode is decreased, the corresponding spinodal boundary shrinks steadily and finally, for sufficiently short wave lengths (below $\lambda \approx 3.5$ fm), any perturbation is spinodally stable.

Further insight into the spinodal instabilities can be gained from Fig. 3.6 (right) which, for the particular wave length $\lambda = 2\pi/k = 8$ fm, shows the dependence of the growth times t_k on density and temperature in the form of a contour plot. The corresponding spinodal boundary corresponds to $t_k = \infty$ and lies well inside the thermodynamics boundary determined by $t_{k=0} = \infty$. The region within which the growth rate exceeds a certain value shrinks steadily towards a point on the ρ axis which thus identifies the condition for fastest growth of perturbations of the specified wave length. In the present case, $\lambda = 8$ fm, the shortest growth time is about 0.6×10^{-22} s ≈ 20 fm/c and it occurs for a density of about $0.25\rho_s$ (and $T = 0$).

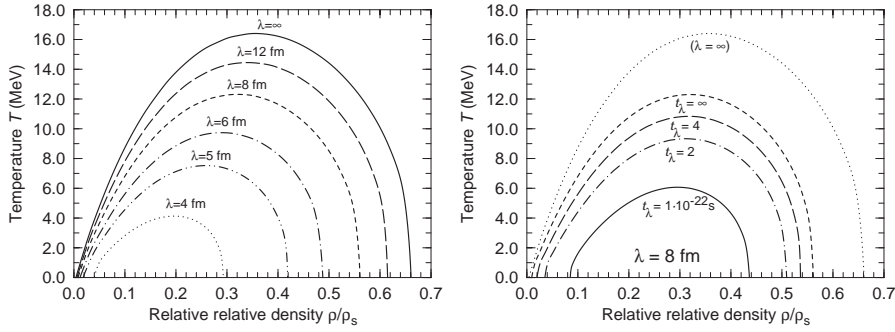


Fig. 3.6. Spinodal boundaries. *Left panel*: Spinodal boundaries in the ρ - T phase plane for density undulations with a specified wave length λ . The thermodynamic spinodal boundary corresponds to $\lambda = \infty$. *Right panel*: Contours of the growth times t_λ for a specified wave length $\lambda = 8$ fm, with the thermodynamic spinodal boundary indicated as well. [These results have been obtained with the Seyler–Blanchard model described in Appendix A (using $\chi = 0.75$).

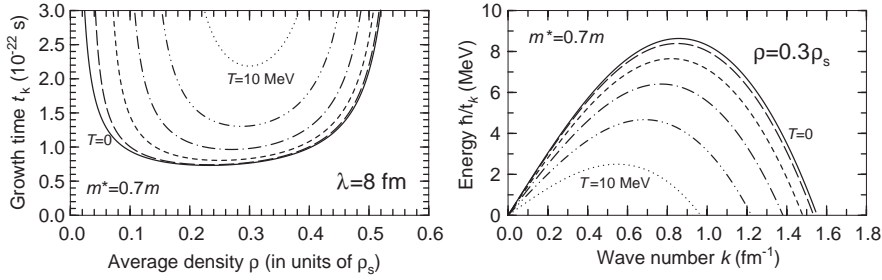


Fig. 3.7. Dependence of growth rates on density, temperature and wave length. *Left panel*: The collective growth time t_k for modes with a wavelength of $\lambda = 8$ fm, for various temperatures T as a function of the density ρ . *Right panel*: The characteristic energy $E_k = \hbar/t_k$ for various temperatures T , as a function of the wave number k in matter at the density $\rho = 0.3\rho_s$. (Adapted from Ref. [117].)

More typically, for systems produced in a nuclear collision at intermediate energy, the temperature is several MeV, so the optimal situation does not occur dynamically. Taking as an example $T = 5$ MeV and $\rho = 0.4\rho_s$, which could likely occur, we see that spinodal instability may occur for $\lambda > 5$ fm and that disturbances with $\lambda = 8$ fm have a characteristic time of $t_k \approx 10^{-22}$ s ≈ 30 fm/ c .

Finally, we illustrate the resulting growth rates in Fig. 3.7. The left panel shows the density dependence of the growth time t_k for modes of wave length $\lambda = 8$ fm, which is close to the most rapidly amplified value. For each temperature below critical, the growth rate rises from zero at the gas-like spinodal boundary as the density is increased, reaches a maximum value, and then drops to zero at the liquid-like spinodal boundary. At moderate temperatures, the growth rate changes little with density. The right panel shows the dependence of the growth rate on the wave number k at the density $\rho = 0.3\rho_s$, which lies in center of the spinodal region. In such a plot, for each given temperature T , the growth rate rises linearly from the origin, exhibits a maximum that depends inversely on T , and then drops to zero at the appropriate maximum value. It should be noticed that there is little temperature dependence below a few MeV.

The model dependence of the instability growth time was investigated by Idier et al. [118] who studied the evolution of instabilities in nuclear matter using a large variety of interactions within the framework of a pseudo-particle treatment. The decomposition times were found to be in the range of 60–200 fm/c. Hence, in addition to the expected strong dependence on density and temperature, the growth times were shown to also depend significantly on the interaction itself. Therefore, it is important to use realistic forces and in particular realistic ranges (or momentum dependence) in order to have reliable results.

It is important to recognize that the numerical method used to produce a smooth density may increase the effective range of the force, so the effective interaction should be appropriately adapted to ensure that the numerical implementation has the specified properties. Thus, the range of the force should be reduced in order to compensate for the finite lattice spacing and it is important to verify that the numerically obtained dispersion relation in fact correspond to the analytically expected one.

3.1.5. Refined analysis of the linear-response treatment

The above linear response treatment has been reconsidered by Božek [119] who demonstrated that the standard solution (3.25) based on the Fourier time resolution of the linearized Vlasov equation (3.22) is incomplete when an initial perturbation at $t = 0$ is employed. The additional contributions (see below) are usually damped and may be neglected at large times, but their presence early on is essential to recover the correct initial density perturbation. Because of the principal importance of this analysis, we briefly summarize the main points below.

Consider a density perturbation with the wave number \mathbf{k} and denote its initial support by $g_{\mathbf{k}}(\mathbf{p}) = \delta f_{\mathbf{k}}(\mathbf{p}, t=0)$. Because the system is thus initialized at $t=0$, the Fourier resolution should include only positive times. This restriction introduces an additional step function in the integrand which produces an additional term in the Fourier resolution of the time derivative. (The usual treatment presented above, in which the Fourier integral extends over all times, may thus be understood as propagating an infinitesimal perturbation introduced at $t=-\infty$.) With the additional term, the transformed Vlasov equation (3.25) is modified,

$$(-\omega_{\mathbf{k}} + \mathbf{v} \cdot \mathbf{k})f_{\mathbf{k}}(\mathbf{p}) - \mathbf{v} \cdot \mathbf{k} \frac{\partial f_0}{\partial \epsilon} \frac{\partial U}{\partial \rho} \rho_{\mathbf{k}} = i g_{\mathbf{k}}(\mathbf{p}) . \quad (3.32)$$

The solution may be written as an integral in the plane of the complex frequency,

$$\delta \rho_{\mathbf{k}}(t) = -i \int_{-\infty+i\epsilon}^{\infty+i\epsilon} \frac{d\omega}{2\pi} G_{\mathbf{k}}(\omega) \varepsilon_{\mathbf{k}}(\omega) e^{-i\omega t} , \quad (3.33)$$

where $\varepsilon_{\mathbf{k}}(\omega)$ is the susceptibility defined in Eq. (3.26) and where

$$G_{\mathbf{k}}(\epsilon) = \int \frac{d^3\mathbf{p}}{(2\pi)^3} \frac{g_{\mathbf{k}}(\mathbf{p})}{\mathbf{k} \cdot \mathbf{v} - \omega} . \quad (3.34)$$

In the standard treatment, the integration of (3.33) retains only the two pole contributions from the zeros of the susceptibility, $\varepsilon_{\mathbf{k}}(\omega^{\pm}) = 0$, which are the solutions of the dispersion equation. These contributions yield

$$\delta \rho_{\mathbf{k}}^{\text{pole}}(t) = -\frac{G_{\mathbf{k}}(\omega^+)}{\partial_{\omega} \varepsilon_{\mathbf{k}}(\omega^+)} e^{-i\omega^+ t} - \frac{G_{\mathbf{k}}(\omega^-)}{\partial_{\omega} \varepsilon_{\mathbf{k}}(\omega^-)} e^{-i\omega^- t} . \quad (3.35)$$

In the spinodal region, where the roots ω^\pm are imaginary, $\delta\rho_k^{\text{pole}}(t)$ represents the growing and decaying collective solutions. However, Božek pointed out that the zeros of the susceptibility $\varepsilon_k(\omega^\pm) = 0$ are not the only singularities to be considered, since the susceptibility has a cut on the real ω axis leading to an additional contribution,

$$\delta\rho_k^{\text{cut}}(t) = -i \int_{-\infty}^{\infty} \frac{d\omega}{2\pi} \left(\frac{G_k(\omega + i\epsilon)}{\varepsilon_k(\omega + i\epsilon)} - \frac{G_k(\omega - i\epsilon)}{\varepsilon_k(\omega - i\epsilon)} \right) e^{-i\omega t} . \quad (3.36)$$

The standard solution $\delta\rho_k^{\text{pole}}(t)$ having only growing and decreasing components, differs at $t=0$ from the specified initial condition and one needs to include the additional contribution $\delta\rho_k^{\text{cut}}(t)$. When this additional contribution to $\delta\rho_k(t)$ is included, the decaying component falls off more rapidly, especially for small values of the growth rate. Thus, the unstable modes gain earlier prominence, while the long term effect can be expressed as a renormalization of the overlap between the initial perturbation and the unstable mode.

Rather than Fourier resolving the time-dependent equation of motion, many studies employ an expansion over a complete set of normal modes in order to propagate the disturbance. Clearly, if a truly complete set of normal modes is used, then the results are not affected by the present discussion. However, if only the collective states are considered, as is most often the case, then the initial fluctuation cannot be fully represented and the problem remains present.

3.1.6. Role of the damping mechanism

If we add the collision integral to the Vlasov equation, i.e. we have an additional damping due to nucleon–nucleon collisions. For example, in the Boltzmann equation of motion, the average effect of the residual two-body collisions, $\bar{I}[f]$, is to provide a dissipative term in the evolution of the phase-space density $f(\mathbf{r}, \mathbf{p}, t)$. In so far as this term can be treated in the relaxation-time approximation, it is fairly straightforward to include its effect in the above treatment, as already discussed in Ref. [104]. In the relaxation-time approximation, the collision term takes the form $\bar{I}[f] = -(f - \tilde{f})/t_0$, where t_0 is the local relaxation time and $\tilde{f}(\mathbf{r}, \mathbf{p})$ is the local equilibrium density. The former can be estimated as [120]

$$t_0^{-1} \approx \pi^2 \frac{T^2}{\epsilon_F^2} V_F \sigma_0 \rho_0 \left[1 + \pi^2 \frac{T^2}{\epsilon_F^2} \right]^{-1} , \quad (3.37)$$

where $\sigma_0 \approx 4 \text{ fm}^2$ is the nucleon–nucleon scattering cross section and T is the temperature. The local equilibrium density \tilde{f} differs from the initial density f_0 due to the change in the local density, $\delta\rho(\mathbf{r})$, and the presence of a local current density $\mathbf{j}(\mathbf{r})$. Exploiting the continuity equation, we obtain the relation $m\omega' \rho_k = \mathbf{k} \cdot \mathbf{j}$, and then find, in the limit of small temperatures $T \ll \epsilon_F$ [104],

$$\tilde{f} \approx f_0 - \frac{2}{3} \frac{\epsilon_F}{\rho_0} \left(1 + 3 \frac{\omega'}{k^2 V_F^2} \mathbf{k} \cdot \mathbf{v} \right) \frac{\partial f_0}{\partial \epsilon} \delta\rho . \quad (3.38)$$

Accordingly, the equation for the Fourier component $f_k(\mathbf{p})$ becomes

$$\left(\omega'_k - \mathbf{k} \cdot \mathbf{v} + \frac{i}{t_0} \right) f_k = - \left[\mathbf{k} \cdot \mathbf{v} + \frac{i}{t_0} \frac{2\epsilon_F}{3\rho_0} \left(1 + 3 \frac{\omega'_k}{k^2 V_F^2} \mathbf{k} \cdot \mathbf{v} \right) \right] \frac{\partial f_0}{\partial \epsilon} \rho_k . \quad (3.39)$$

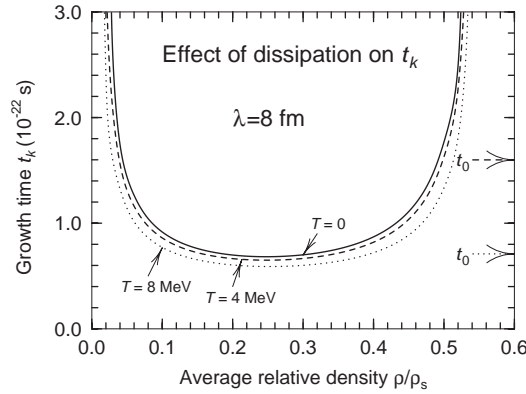


Fig. 3.8. Effect of dissipation. The effect on the growth times t_k caused by including the dissipative BUU collision term in the relaxation-time approximation, for modes having a wave length $\lambda = 8$ fm in nuclear matter with an average density $\rho = 0.3\rho_s$. In deriving the modified dispersion relation, the temperature has been assumed to be small, for simplicity, and the strength of the dissipative term has been calculated from the simple approximation (3.37) using $T = 0$ (solid), 4 MeV (dashed), and 8 MeV (dotted), leading to the relaxation times t_0 indicated by the arrows on the right. (From [117].)

The form of the eigenfunctions $f_k(\mathbf{p})$ then immediately follows and the eigenfrequencies ω'_k are determined by the corresponding modified dispersion equation.

Within the spinodal region, the addition of the dissipative term changes the eigenfrequencies, but they remain purely imaginary, $\omega'_k = i/t'_k$. This is illustrated in Fig. 3.8 for a typical scenario having $\rho = 0.3\rho_s$ and $\lambda = 8$ fm. The figure shows the growth times t'_k calculated in the above manner for various strengths of the dissipative term, as governed by the relaxation time t_0 . This quantity depends mostly on temperature (see Eq. (3.37)) and the results for $\tau = 0, 4, 8$ MeV are displayed; the corresponding values of the relaxation time t_0 are indicated on the right. Perhaps somewhat counterintuitively, the inclusion of the damping term increases the growth rate [104,117], but the effect is negligible as long as t_0 is larger than the undamped growth time t_k . This is because the damping reduces the distortions of the Fermi surface which tend to stabilize the mode; this feature is also manifested by the hydrodynamic growth rates being larger than the collisionless ones. For the fastest modes, the growth times are reduced by only about 10% for $T = 6$ MeV, which is near the upper limit of applicability of the analytical approximations employed in subsequent developments. Therefore, it is justified to ignore the effect of the average collision term. Of course, when high accuracy is called for, the dissipation-induced shifts in the characteristic times should be included, and the finite temperature should be taken into account.

3.1.7. Evolving systems

Spinodal instability is an out-of-equilibrium concept. Up to now we have discussed this phenomenon in the context of uniform systems having an equilibrated kinetic energy distribution. Since spinodal instability may be derived within transport theory, the treatment can be extended to more general situations. In fact, spinodal instability may be more generally defined as a collective instability of the density distribution relative to any (static or dynamic) state.

3.1.7.1. Counterstreaming matter. With a view towards the conditions created early on in energetic nuclear collisions, Larionov et al. [121] considered the development of instabilities of spinodal and two-flow types arising in collisions of two slabs of nuclear matter using the Vlasov equation with a self-consistent nuclear potential. The expansion of the matter formed following the collision of the slabs leads to a strong longitudinal contraction of the Fermi surface which in turn increases the growth rate for the unstable longitudinal modes after the system has entered the region of spinodal instability. Instabilities occurring at the initial counter-streaming collision stage was also investigated in an approximate manner. The principal conclusion was that the development of spinodal instability is significantly enhanced if the initial counter-streaming form of the distribution function is still maintained at the expansion stage.

The occurrence of instabilities in matter with an anisotropic momentum distribution has long been known in electromagnetic plasma physics [122] and the mechanism may induce color filamentation in the quark-gluon plasma created in a high-energy nuclear collision [123–125].

3.1.7.2. Spinodal modes in expanding bulk matter. The growth of spinodal modes in expanding nuclear matter has been studied within a Vlasov framework in Ref. [126], as described in Appendix D, and very recently in Ref. [127]. As a main result, it appears that the effect of the expansion can be accounted for by employing time-averaged inertial and Landau parameters, as well as a decreasing range for the interaction. While the effective values of the key quantities determining the dominant collective modes in the fragmentation pattern are thus modified by the expansion dynamics, as one would intuitively expect, the essential characteristics of the spinodal instabilities are preserved in expanding systems and thus the associated fragmentation follows the same phenomenology as in static matter.

3.1.8. Linear response in quantum approaches

The above derivations have been performed within a semi-classical description of spinodal instabilities in nuclear matter. It turns out that the fastest growing collective modes, which are those that will become predominant, have wave numbers comparable to those of nucleons at the Fermi surface. For example, for densities $\rho \approx 0.3\rho_0$ and typical temperatures $T = 4\text{--}5$ MeV, the wave numbers of the fastest growing modes are in the order of $k \approx 0.8 \text{ fm}^{-1}$, while the Fermi wave number for the same density is $k_F \approx 1.0 \text{ fm}^{-1}$. This suggests that the quantal effects associated with the mean-field evolution can influence the growth of spinodal instabilities. Therefore, the time-dependent Hartree–Fock equation for the single-particle density matrix $\hat{\rho}(t)$ provides a more suitable framework for studying the dynamics of density fluctuations in nuclear systems than the semi-classical Vlasov treatment [105],

$$i \frac{\partial \hat{\rho}(t)}{\partial t} - [\hat{h}[\hat{\rho}], \hat{\rho}(t)] = 0 . \quad (3.40)$$

This equation describes the mean-field evolution in terms of an effective one-body Hamiltonian $\hat{h}[\hat{\rho}] = -(1/2m)\hat{\nabla}^2 + \hat{U}[\hat{\rho}]$. A perturbation $\delta\hat{\rho}$ of the single-particle density matrix away from the finite-temperature equilibrium characterized by $\hat{\rho}_0$ is propagated by the linearized TDHF equation,

$$i \frac{\partial \delta\hat{\rho}}{\partial t} - [\hat{h}_0, \delta\hat{\rho}] - [\delta\hat{U}, \hat{\rho}_0] = 0 , \quad (3.41)$$

where h_0 is the mean-field Hamiltonian at the equilibrium state and δU denotes the fluctuating part of the one-body mean field. This response treatment provides a quantal framework for describing the early evolution of the spinodal instabilities in a finite nuclear system, as we will see later.

In the context of the present review, we are interested in the quantal effects on the growth of instabilities in nuclear matter. Furthermore, we assume that the mean-field Hamiltonian in the equilibrium state, \hat{h}_0 , is uniform so hence the equilibrium single-particle density matrix is diagonal in the momentum representation, $\langle \mathbf{p} | \hat{\rho}_0 | \mathbf{p}' \rangle = \delta(\mathbf{p} - \mathbf{p}') \rho_0(\mathbf{p})$, where $\rho_0(\mathbf{p})$ is a finite-temperature Fermi–Dirac function. Carrying out a Fourier transform with respect to time, the mean-field part of the linearized TDHF equation in the plane wave representation becomes

$$(\omega - \epsilon_{p_1} + \epsilon_{p_1}) \delta \rho(\mathbf{p}_1, \mathbf{p}_2; \omega) = \delta U(\mathbf{p}_1, \mathbf{p}_2; \omega) [\rho_0(\mathbf{p}_1) - \rho_0(\mathbf{p}_2)] , \quad (3.42)$$

where $\delta \rho(\mathbf{p}_1, \mathbf{p}_2; \omega)$ denotes the Fourier transform of the fluctuating part of the single-particle density matrix,

$$\delta \rho(\mathbf{p}_1, \mathbf{p}_2; \omega) = \int dt e^{i\omega t} \langle \mathbf{p}_1 | \delta \hat{\rho}(t) | \mathbf{p}_2 \rangle , \quad (3.43)$$

and analogously for $\delta U(\mathbf{p}_1, \mathbf{p}_2; \omega)$. The situation is relatively simple when the effective mean field is generated from the local density $\rho(\mathbf{r})$ by convolution with a finite-range kernel $g(\mathbf{r})$, $U[\rho] = g * \tilde{U}$, where $\tilde{U}(\rho(\mathbf{r}))$ is a function of the local density. Then the disturbance of the mean field can be expressed as

$$\delta U(\mathbf{p} + \tfrac{1}{2}\mathbf{k}, \mathbf{p} - \tfrac{1}{2}\mathbf{k}; \omega) = \frac{\partial U_k(\rho)}{\partial \rho} \delta \rho(\mathbf{k}, \omega) , \quad (3.44)$$

where $U_k(\rho) = g(k) \tilde{U}(\rho)$ is the Fourier transform of $U[\rho](\mathbf{r})$ and $\delta \rho(\mathbf{k}, \omega)$ is the Fourier transform of the local density disturbance in space and time,

$$\delta \rho(\mathbf{k}, \omega) = \int d^3\mathbf{r} dt e^{i(\omega t - \mathbf{k} \cdot \mathbf{r})} \delta \rho(\mathbf{r}, t) = \int \frac{d^3\mathbf{p}}{(2\pi)^3} \delta \rho(\mathbf{p} + \tfrac{1}{2}\mathbf{k}, \mathbf{p} - \tfrac{1}{2}\mathbf{k}; \omega) . \quad (3.45)$$

Insertion of Eqs. (3.42) and (3.44) into Eq. (3.45) then yields a quantal dispersion equation for the frequency of the collective mode over the wave number \mathbf{k} ,

$$1 = \frac{\partial U_k(\rho)}{\partial \rho} \int \frac{d^3\mathbf{p}}{(2\pi)^3} \frac{\rho_0(\mathbf{p}) - \rho_0(\mathbf{p} - \mathbf{k})}{\omega - \epsilon_{\mathbf{p}-\mathbf{k}} + \epsilon_{\mathbf{k}}} . \quad (3.46)$$

The roots appear in opposite pairs. They are real for the stable modes and imaginary for the unstable ones, for which we may then write $\omega_k = \pm i/t_k$, where $t_k > 0$ is the characteristic growth time of the mode \mathbf{k} . When the background distribution is isotropic, $\rho_0(\mathbf{p}) = \rho_0(p)$, as is most often the case, the eigenfrequencies depend only on the magnitude k . Furthermore, at zero temperature the momentum integral in the dispersion equation can be evaluated exactly,

$$\frac{1}{F_0(k)} + \frac{1}{2} = \frac{1}{8s_0} \left\{ [(s + s_0)^2 - 1] \ln \frac{s + s_0 + 1}{s + s_0 - 1} - [(s - s_0)^2 - 1] \ln \frac{s - s_0 + 1}{s - s_0 - 1} \right\} , \quad (3.47)$$

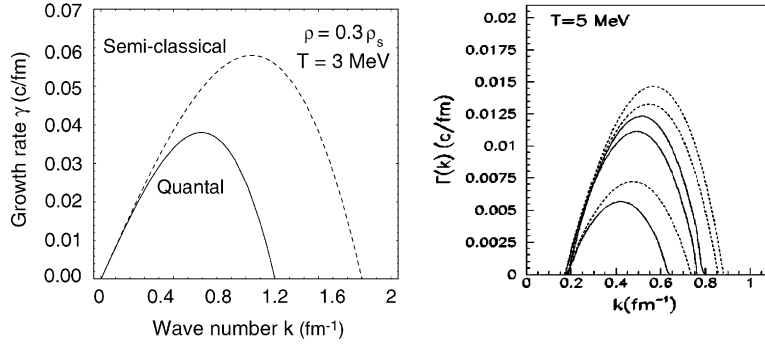


Fig. 3.9. Quantal versus semi-classical dispersion relation. Comparison between the semiclassical dispersion relation (3.27) (dashed curves) and its quantal form (3.46) (solid), as obtained with a finite-range interaction. The growth rate is shown as a function of the wave number for two phase points well inside the spinodal region. *Left panel:* Symmetric nuclear matter for $\rho_0 = 0.3\rho_s$ and $T = 3$ MeV. (Adapted from [105].) *Right panel:* Three degrees of isospin asymmetry, $I = 0, 0.3, 0.6$ (from top), for $\rho_0 = 0.4\rho_s$ and $T = 5$ MeV. (From Ref. [101].)

where $s = \omega_k/kV_F$ and $s_0 = k/2k_F$. For small wave numbers, $k \ll k_F$, this expression reduces to the semi-classical zero-temperature dispersion equation (3.28). However, for large k the quantal dispersion relation differs from the semi-classical one.

At finite temperatures, the dispersion equations (3.46) and (3.27) may be solved numerically. As an illustration, Fig. 3.9 shows the growth rates obtained with a finite-range interaction that has been adjusted to reproduce the ground-state properties of finite nuclei [128]. It can be seen that the quantal treatment modifies the dispersion relation substantially, with the most rapidly amplified wave length being increased from $\lambda_0 \approx 5.5$ to 8.5 fm.

It is interesting to note that the effect of the quantal treatment is similar to the effect of increasing the interaction range in the semi-classical treatment. This can be intuitively understood by recalling the Heisenberg uncertainty principle, which states that in order to maintain a spatial resolution of λ the system must exhibit a momentum dispersion of $\Delta p = \hbar/k = h/\lambda$. The associated energy cost, which amounts to $\Delta E = \hbar^2 k^2/2m = h^2/2m\lambda^2$, will act as a k -dependent potential energy, thus constituting an additional finite-range effect. Therefore, for unstable systems, quantal effects can be included by a suitable redefinition of the interaction range.

3.1.9. Instabilities in asymmetric nuclear matter

As discussed in Section 2, the nuclear case is more complicated than the usual Fermi liquid because of the simultaneous presence of two components, neutrons and protons. A two-component system can readily be investigated within semi-classical mean-field transport framework, which then provides two coupled Vlasov equations for the individual phase-space densities $f_q(\mathbf{r}, \mathbf{p}, t)$ [44,101,129–131],

$$\frac{\partial f_q(\mathbf{r}, \mathbf{p}, t)}{\partial t} + \frac{\mathbf{p}}{m} \cdot \frac{\partial f_q}{\partial \mathbf{r}} - \frac{\partial U(\mathbf{r}, t)}{\partial \mathbf{r}} \cdot \frac{\partial f_q}{\partial \mathbf{p}} = 0, \quad q = p, n. \quad (3.48)$$

In the simplest treatment, the momentum dependence is neglected (so the effective nucleon mass equals the free value) and one employs a local mean-field potential $U_q(\mathbf{r}, t)$ with a Skyrme-like

form [130],

$$U_q = A \left(\frac{\rho}{\rho_0} \right) + B \left(\frac{\rho}{\rho_0} \right)^{\alpha+1} + C \left(\frac{\rho'}{\rho_0} \right) \tau_q + \frac{1}{2} \frac{dC(\rho)}{d\rho} \frac{(\rho')^2}{\rho_0} - D \triangle \rho + D' \tau_q \triangle \rho', \quad (3.49)$$

where $\rho \equiv \rho_n + \rho_p$ and $\rho' \equiv \rho_n - \rho_p$. Furthermore, the sign of the isospin is $\tau_q = +1(-1)$ for $q = n(p)$. The parameters A , B , α , and D can be adjusted to reproduce the saturation properties of symmetric nuclear matter as well as the nuclear surface energy [132–134]. The finite range of the isovector interaction is governed by the coefficient $D' \approx \frac{1}{3}D$, which is usually chosen according to Ref. [135], yielding a value close to that used in the SKM* interaction [136].

We may now discuss the linear response of the coupled Vlasov equations (3.48). Thus we consider small periodic perturbations, $\delta f_q(\mathbf{r}, \mathbf{p}, t) \sim \exp(-i\omega t)$, relative to the stationary Fermi–Dirac distributions, $f_q^{(0)}(\mathbf{p}) = 1/[\exp((\epsilon_q - \mu_q)/T) + 1]$, where $\epsilon_q = p^2/(2m) + U_q^{(0)}$ and μ_q denote the energy and chemical potential of type- q nucleons. Linearizing Eq. (3.48), we then find

$$-i\omega \delta f_q + \frac{\mathbf{p}}{m} \cdot \frac{\partial \delta f_q}{\partial \mathbf{r}} - \frac{\partial U_q^{(0)}}{\partial \mathbf{r}} \cdot \frac{\partial \delta f_q}{\partial \mathbf{p}} - \frac{\partial \delta U_q}{\partial \mathbf{r}} \cdot \frac{\partial f_q^{(0)}}{\partial \mathbf{p}} = 0, \quad (3.50)$$

where $\delta U_q(\mathbf{r})$ is the time-dependent part of the mean-field potential.

Since we are in matter, $\nabla U_q^{(0)} = \mathbf{0}$ and $\delta f_q \sim \exp(-i\omega t + i\mathbf{k} \cdot \mathbf{r})$ in Eq. (3.50). Following the standard Landau procedure [104,130], we can then derive the following coupled equations for the proton and neutron density disturbances,

$$[1 + F_0^{nn} \chi_n] \delta \rho_n + [F_0^{np} \chi_n] \delta \rho_p = 0, \quad (3.51)$$

$$[F_0^{pn} \chi_p] \delta \rho_n + [1 + F_0^{pp} \chi_p] \delta \rho_p = 0, \quad (3.52)$$

where $\mathbf{v} = \mathbf{p}/m$ is the nucleon velocity and

$$\chi_q(\omega, \mathbf{k}) = \frac{2}{N_q(T)} \int \frac{d^3 \mathbf{p}}{h^3} \frac{\mathbf{k} \cdot \mathbf{v}}{\omega + i0 - \mathbf{k} \cdot \mathbf{v}} \frac{\partial f_q^{(0)}}{\partial \epsilon_p^q}, \quad (3.53)$$

is the long-wave limit of the Lindhard function [104]. Furthermore, the thermally averaged level density is

$$N_q(T) = -2 \int \frac{d^3 \mathbf{p}}{h^3} \frac{\partial f_q^{(0)}}{\partial \epsilon_p^q} \approx N_q(0) \left[1 - \frac{\pi^2}{12} \left(\frac{T}{\epsilon_F^q} \right)^2 \right], \quad (3.54)$$

where the Fermi momentum for the specie q is given by $p_F^q = (3\pi^2 \rho_q)^{1/3} \hbar$ and the corresponding Fermi energy is $\epsilon_F^q = (p_F^q)^2/2m$. The zero-temperature single-particle level density for the species q is then $N_q(0) = m p_F^q/(\pi^2 \hbar^3)$. Finally, the quantities

$$F_0^{q_1 q_2}(k) = N_{q_1}(T) \frac{\delta U_{q_1}}{\delta \rho_{q_2}}, \quad q_1, q_2 = n, p \quad (3.55)$$

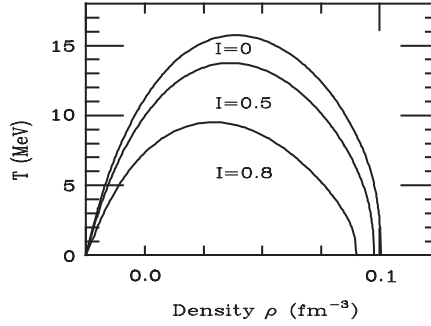


Fig. 3.10. Spinodal boundaries for various asymmetries. Spinodal boundaries in the ρ – T plane for different isospin asymmetries I , as obtained by solving the dispersion equation (3.57). (From Ref. [44].)

represent the generalization of the usual Landau parameter $F_0(k)$ to a multi-component system. For the particular choice of potential given by Eq. (3.49), these parameters are readily obtained,

$$F_0^{q_1 q_2}(k) = N_{q_1}(T) \left[\frac{A}{\rho_0} + (\alpha + 1)B \frac{\rho^\alpha}{\rho_0^{\alpha+1}} + Dk^2 + \left(\frac{C}{\rho_0} - D'k^2 \right) \tau_{q_1} \tau_{q_2} + \frac{dC}{d\rho} \frac{\rho'}{\rho_0} (\tau_{q_1} + \tau_{q_2}) + \frac{d^2 C}{d\rho^2} \frac{\rho'^2}{2\rho_0} \right]. \quad (3.56)$$

The eigenfrequencies are the roots of the determinant of the coupled equations (3.51)–(3.52), so the dispersion equation is

$$(1 + F_0^{nn} \chi_n)(1 + F_0^{pp} \chi_p) - F_0^{np} F_0^{pn} \chi_n \chi_p = 0. \quad (3.57)$$

Since the present focus is on the unstable modes, the Lindhard function Eq. (3.53) is evaluated for $\omega = i\gamma$ where $\gamma > 0$ is the growth rate of the mode, yielding [104]

$$\chi_q(s_q) = 1 - s_q \arctan \frac{1}{s_q}, \quad (3.58)$$

where $s_q = \gamma/(kv_F^q)$. The resulting thermodynamic spinodal boundary can be obtained by solving the dispersion equation (3.57) for $k = 0$ and the result is illustrated in Fig. 3.10. For each value of the nuclear matter asymmetry $I = \rho'/\rho$, the region under the boundary curve is unstable and we have

$$(1 + F_0^{nn})(1 + F_0^{pp}) - F_0^{np} F_0^{pn} < 0. \quad (3.59)$$

Furthermore, for each phase point (ρ, T) inside the thermodynamic instability region there exists a wave number k for which the associated spinodal boundary passes through that point. The asymmetry leads to shrinking of the spinodal region, reducing both the critical temperature and the critical density [42]. This is a quite general effect arising from the fact that the effective neutron–proton interaction is attractive while the interaction between like nucleons is repulsive [129], thus strengthening the symmetry term in the equation of state for asymmetric nuclear matter and thereby making the instability region smaller.

For distortions with a finite wave length, $k > 0$, the dispersion equation Eq. (3.57) can be solved for specified values of the temperature T and the densities ρ_p and ρ_n (usually given in terms of

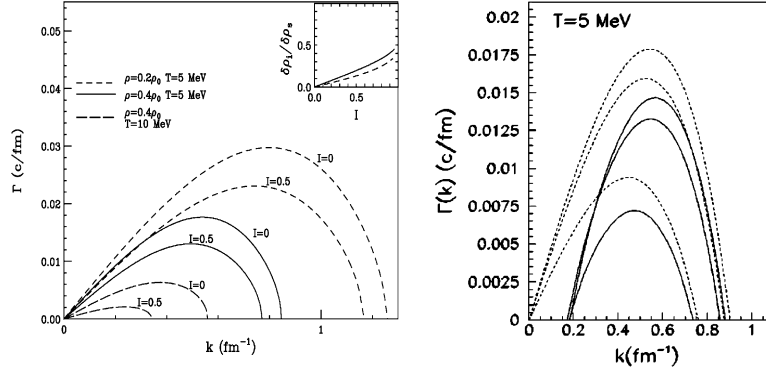


Fig. 3.11. Growth rates in asymmetric nuclear matter. Growth rates in two-component nuclear matter as functions of the wave vector k , calculated from the dispersion relation (3.57). *Left panel*: Three phase points inside the spinodal region for two asymmetries of the initial uniform system, $I \equiv \rho'/\rho$. The insert shows the asymmetry of the perturbation, $\delta I \equiv \delta\rho'/\delta\rho$, as a function of I for the most unstable mode, in the case where $\rho = 0.25\rho_0$ and $T = 5$ MeV. (From Ref. [44].) *Right panel*: Three degrees of asymmetry, $I = 0, 0.3, 0.6$ (from top) at $T = 5$ MeV and $\rho_0 = 0.4\rho_s$, calculated either with (solid) or without (dashed) the Coulomb interaction. (From Ref. [101].)

the total density ρ and the isospin asymmetry I . The effect of the asymmetry on the growth rate γ_k is illustrated in Fig. 3.11. The appearance of γ_k for symmetric matter is as expected from our earlier discussion: The growth rate exhibits a maximum and then drops off as a result of the finite interaction range. From the left panel it can be seen that the region of instability shrinks when the relative density ρ/ρ_s is increased from 0.2 to 0.4 and it then shrinks further when the temperature T is increased from 5 to 10 MeV. As both panels bear out, an increase in the isospin asymmetry generally reduces the growth rate, as one would expect already from the shrinkage of the instability region shown in Fig. 3.10. However, while the effect is significant, it is not large in the region of most rapid growth, where it amounts to around $\approx 30\%$.

It should be noted that the overall reduction of the growth rate is accompanied by a shift of the maximum towards longer wave lengths. While this effect appears to be only slight at the lower temperature, it is considerable at the higher temperature (where the system is closer to the spinodal boundary) and one may expect a corresponding increase in the size of the resulting (pre)fragments.

It is also interesting to note the effect of the Coulomb interaction, which was also considered in the study by Fabbri and Matera [101]. In general, as seen from the right panel of Fig. 3.11, the Coulomb force stabilizes the modes. In particular, perturbations with a wave length above $\lambda_{\max} \approx 30$ fm become stable, a value that is rather long on the nuclear scale. Thus, the main Coulomb effect amounts to an overall reduction (by about $\approx 25\%$) in the growth rates of the most relevant modes.

Further understanding of the spinodal decomposition process in a two-component system can be achieved by studying the chemical composition of the evolving instability. For any given k inside the associated spinodal region, a solution of Eqs. (3.51)–(3.52) yields the corresponding unstable eigenvector $(\delta\rho_p, \delta\rho_n)$ (as already discussed in Section 2.3.1, only one of the two eigenmodes is unstable in dilute nuclear matter). One may then consider the associated asymmetry δI , i.e. the ratio of $\Delta\delta\rho = \delta\rho_n - \delta\rho_p$ and $\delta\rho = \delta\rho_n + \delta\rho_p$, which generally deviates from the corresponding ratio $I = \Delta\rho_0/\rho_0$ in the original uniform system. As is illustrated in the insert of Fig. 3.11 for the most

unstable mode in the case of $\rho = 0.25\rho_s$ and $T = 5$ MeV, the asymmetry of the eigenmode is smaller than the original asymmetry (one obtains $\delta I \approx 0.5I$). This chemical effect arises from the fact that the symmetry energy per nucleon increases with density, in the dilute density region considered here, and it therefore grows stronger with increasing total density. An important consequence of this general feature is that the growth of an unstable mode produces high-density regions (liquid phase) that are more symmetric and low-density regions (gas phase) that are less symmetric. Hence, the spinodal fragmentation causes a collective migration of protons from low-density regions to high-density regions (and a reverse migration of neutrons). (This isospin fractionation effect was already discussed in connection with the liquid–gas phase transition in two-component systems in Section 2.3.)

As already stressed in Section 2, the spinodal decomposition occurring in asymmetric nuclear matter at low density arises from a single instability having both mechanical and chemical features. The calculations reported by Li et al. [137] are particularly instructive in this regard, as they show very clearly that the instabilities behave similarly throughout over the spinodal region, irrespective of whether they are being characterized as mechanical or chemical.

In conclusion, we note that the fast spinodal decomposition mechanism in neutron-rich matter leads to a mixture of intermediate-mass fragments that are more symmetric than the overall system and a gas of light fragments with an enhanced neutron excess. This general expectation appears to be borne out by recent fragmentation experiments with neutron-rich nuclei [53,54,138], where the light fragments were found to be very neutron-rich. However, it is important to recognize that this feature is expected already on statistical grounds [14]. Thus, the results suggest that the spinodal fragmentation mechanism tends to drive the system towards an assembly of fragments that are in equilibrium with regard to their neutron and proton contents (often referred to as *chemical* equilibrium), as we shall discuss further in Section 5.3.

3.2. Finite nuclei

The above treatments of spinodal instability in nuclear matter can be adapted to the more realistic problem posed by finite nuclei.

3.2.1. Thomas–Fermi dynamics

The growth of instabilities of finite nuclear systems at low densities has been investigated by a number of authors [139–143]. Common to these approaches is the adoption of a suitable energy functional $E[\rho]$ yielding the energy of the nuclear system in the geometry specified by the matter density $\rho(\mathbf{r})$, at a certain temperature T . For simplicity, a Skyrme form is usually employed, with a gradient term to account for the finite interaction range. (Appendix A gives the energy functional for the finite-range Seyler–Blanchard interaction.)

For a fluid dynamical treatment of small distortions around a spherical density $\rho_0(\mathbf{r})$, it suffices to perform a multipole expansion of the velocity potential. Thus one may consider the linear response to distortions of an elementary form,

$$S(\mathbf{r}, t) = \dot{q}_{kLM} j_L(kr) \bar{Y}_{LM}(\hat{\mathbf{r}}) = \dot{q}_{kLM} S_{kLM}(\mathbf{r}) . \quad (3.60)$$

Here $\bar{Y}_{LM} = [Y_{LM} + Y_{LM}^*]/[2(1 + \delta_{M0})]^{1/2}$ are the real spherical harmonics and the radial form factor $j_L(kr)$ is assumed to be a Bessel function.

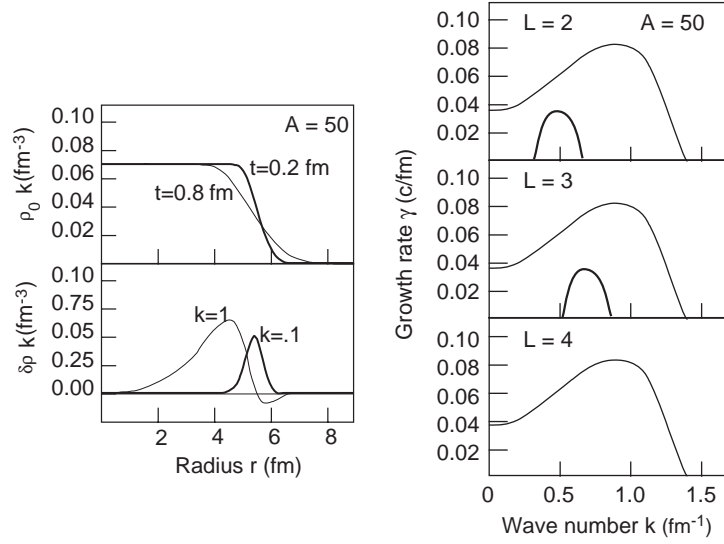


Fig. 3.12. Dilute spherical nucleus. *Left panel:* The density profile of a dilute spherical nucleus containing $A=50$ nucleons, as obtained by either scaling the equilibrium density (thin curve marked $t = 0.8 \text{ fm}$) or by minimizing the energy with respect to the thickness parameter t (thick curve marked $t = 0.2 \text{ fm}$) (top), together with the corresponding octupole transition densities for two values of the radial wave number k (bottom). *Right panel:* The corresponding dispersion relation for three multiplicities L , for either the scaled profile (thin curves) or the optimized profile (thick curves). (From Ref. [99].)

From this point, the various approaches differ in their treatment of the nuclear surface. Let us first discuss Ref. [140] which is using a realistic shape for the nuclear density profile of Wood–Saxon form, $\rho_0(r) = \rho_c/[1 + \exp(r - R)/t]$. The central density ρ_c is chosen well inside the spinodal zone and the radius $R = \lambda R_A$ is then fixed by the nucleon number A . Two cases were considered for the surface profile: (1) a simple scaling of the surface thickness parameter t in proportion to the expansion factor λ and (2) a minimization of the energy E_0 with respect to t . Fig. 3.12 (left, top) shows the resulting density profiles $\rho_0(r)$ for $A = 50$.

Given the profile, the continuity equation yields the transition density,

$$\delta\rho_{kLM}(\mathbf{r}, t) = q_{kLM} \nabla \cdot \left(\frac{\rho_0}{m^*} \nabla S_{kLM} \right). \quad (3.61)$$

It should be noted that the wave number k is a continuous variable, contrary to the sharp-surface approximation. For large wave numbers, $kR > 1$, the velocity field (3.60) approximates those of the bulk instabilities, while the opposite limit, $kR < 1$, describes surface modes. Fig. 3.12 (left, bottom) shows the radial part of the transition density $\delta\rho_L(r)$ for $A = 50$, and for $L = 3$ and for radial wave numbers $k = 1.0 \text{ fm}^{-1}$ (volume modes) and $k = 0.1 \text{ fm}^{-1}$ (surface mode).

By proceeding as described in Section 3.1.2, it is straightforward to compute the inertial coefficient M_L and the stiffness C_L . If the kinetic term is expressed by the usual Fermi integrals, the resulting dispersion relation is neglecting the contribution arising from the deformation of the Fermi surface [96,98,105]. The validity of this approximation can be ascertained in the case of infinite matter by comparing the fluid dynamical calculations with the result of the semi-classical

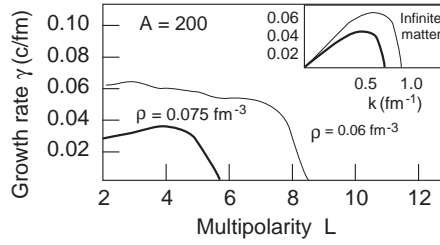


Fig. 3.13. Dispersion relations. Fastest growth rates for unstable modes in dilute spheres as functions of the multipolarity L , obtained with the optimized surface profiles for central densities ρ_0 of either 0.075 fm^{-3} (thick curves) or 0.060 fm^{-3} (thin curves). The insert shows the corresponding dispersion relation in uniform matter. (From Ref. [140].)

RPA dispersion relation which includes effects due to distortion of the Fermi surface. It can be seen that the fluid dynamical calculations provide a good approximation, within about 10–20%, for the semi-classical dispersion relation in the unstable zone. However, it is well known that in the case of high-frequency surface vibrations at normal density, such as the giant-quadrupole mode, the dominant contribution to the restoring force arises from the deformation of the Fermi surface. At lower densities, this effect is still important and tends to stabilize the surface modes, but it does not affect the volume instabilities appreciably. Consequently, well inside the spinodal region, where the instabilities are dominated by the unstable volume modes, the effect of the deformation of the Fermi surface is expected to be small. We will discuss in the next subsection recent fluid dynamics approaches which consider the relaxation toward a spherical Fermi distribution [141–143] and then we shall consider quantal RPA solutions which naturally include the deformation of the Fermi sphere.

Fig. 3.12 (right) shows the growth rates $t_k^{-1} = |\omega_k|$ for three multiplicities for a source having $A = 50$ nucleons expanded to about one third of saturation, $\rho_0 = 0.06 \text{ fm}^{-3}$. (For the system with the optimized surface thickness, only the modes with $L = 2$ and $L = 3$ are unstable.) The fact that the growth rate exhibits a maximum at a finite k demonstrates the volume nature of the instability. It is interesting to note that the scaled system is generally more unstable than the optimized one. In fact, when the surface profile has been optimized, the surface modes occurring for $k \rightarrow 0$ are stable. Thus the properties of the surface modes, including their possible instability, depend upon the details of the nucleus surface.

Naturally, larger systems have more unstable modes. For example, for $A = 200$ the most unstable modes have a radial wave number in the range of $k_0 \approx 0.7\text{--}1.0 \text{ fm}^{-1}$ and a corresponding typical growth rate of $t_0 \approx 0.05\text{--}0.06 \text{ c/fm}$, as illustrated in Fig. 3.13. As seen from this figure, the growth rates of the most unstable modes of the finite system are nearly the same for different multiplicities up to a maximum multipolarity L_{max} and they are only slightly reduced compared to the bulk instability. However, large multiplicities are suppressed. This result suggests that the unstable spherical system can develop into fragmentation channels of different multiplicity (hence IMF multiplicity) with nearly equal probability (apart from the factor $2L + 1$), with the production of small fragments being inhibited. These findings are in agreement with the recent results obtained from Boltzmann–Langevin simulations [144–146] to be discussed in Section 5.2.2. This behavior of the finite system is qualitatively different from the development of instabilities in nuclear matter, in which the most unstable mode is characterized by a single characteristic length corresponding to the

optimal wave number k_0 . For finite systems, the limited size is the most important restriction, in effect limiting the magnitude of the multipolarity L . However, once the condition on L , the radial wave numbers tries to adjust itself to the optimum value obtained for infinite nuclear matter.

It should be noted that the Coulomb potential (included in the calculation) has, in general, a very small effect on the growth rates of the unstable collective modes, except close to the border of the spinodal zone, where it stabilizes unstable modes of very long wave-length.

3.2.2. Expanding nuclear systems

For an irrotational and non-viscous fluid [147], it was demonstrated that the dynamical evolution of density waves in an expanding nuclear system differs markedly from their evolution in an expanded but static system. In particular, statically stable modes may become dynamically unstable, thus in effect enlarging the spinodal region. This general effect of expansion on the stability of density waves was confirmed in a further study that took account of both finite size and non-linearities [148]. That study also demonstrated that the fraction of expansion trajectories that lead to multifragmentation changes from zero to one only gradually as the initial conditions are changed from the stable to the unstable region of the ρ – T phase diagram.

The expansion of a spherical nucleus was also considered by Csernai et al. [149]. Imposing an overall scaling expansion, they studied in particular the properties of bubble instabilities, both by analytical means and by numerical solution of the Vlasov equation with a self-consistent finite-range interaction. On this basis, they investigated the dependence of the spinodal multifragmentation phenomenon on such quantities as the rate of expansion, the radius and diffuseness of the bubble, and the nuclear forces as manifested in compressibility and interaction range.

As we shall discuss later (Section 5), numerical simulations of an expanding nuclear system with either the Vlasov equation or the nuclear Boltzmann equation often yield hollow unstable configurations [150–153]. The properties of such systems can be investigated within the method described above by employing a monopole distortion of the form $\delta\rho(r) = -\nabla \cdot (\rho_0 \nabla j_0(kr))$, with its amplitude q_0 chosen to produce the desired central depletion. Proceeding in this manner for a system with a central depletion of about 30%, the authors of Ref. [140] have shown that the hollow configuration is slightly more unstable than the uniformly diluted system. However, this effect is sufficiently small to render the bulk instabilities robust against variations in the profile.

The Vlasov equation can be considered as a more suitable framework for studying the early development of instabilities in nuclei. Indeed, important effects, such as the deformation of the Fermi sphere, are automatically taken into account within such a framework. Moreover the effect of two-body collisions can be included by solving the BUU equation, which includes the average effects of the two-body collisions. In such a context, the early dynamical behavior of dilute finite nuclei has been studied numerically [144–146]. It appears that the early fragmentation process is dominated by relatively few unstable modes and by the lack of light-cluster production, due to the suppression of short wave length perturbation. The maximum multipolarity L that can be accommodated by a finite system is found to dependent on the range of the effective interaction used and on the size of the system considered. The details of the effective interactions also influence the instability growth rates. A detailed discussion of the features of the early fragmentation pattern in spinodal decomposition of nuclei can be found in Section 5.

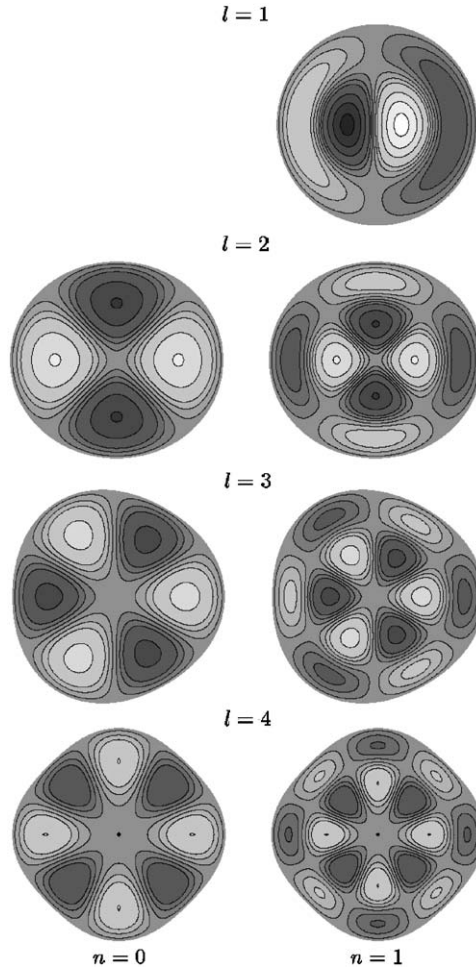


Fig. 3.14. Density distortions of a sphere. Density distributions in a sharp sphere (cut across the (x, y) plane) for the lowest collective modes having $n = 0$ and $n = 1$ (left and right column, respectively) and multipolarities $L = 1 - 4$ (from top to bottom). The grey color in the centers and at the borders correspond to the density in the initial undistorted sphere, while the darker (lighter) shades indicate larger (smaller) densities. (From Ref. [142].)

3.2.3. Diabatic effects

The studies described above rely on the assumption that the local momentum distribution maintains a Fermi–Dirac form throughout, as would be true in the adiabatic limit of very slow macroscopic motion. Since this is hardly realistic, it is important to study the effect of diabatic evolution in which the macroscopic motion brings the microscopic degrees of freedom out of equilibrium. This phenomenon has been studied within the framework of Fermi fluid dynamics [141–143], as we shall now briefly recall. These studies employ sharp boundary conditions, so that the radial wave number k is discrete and can then be replaced by the node number n . Fig. 3.14 shows the density distributions associated with perturbations of the form $\delta\rho_{nLL}(\mathbf{r}, t)$.

Let us for simplicity consider only one mode and let us include damping in the relaxation-time approximation. The fluid dynamics can then be recast into the simple form of a damped oscillator [142],

$$M\ddot{q} + C' \int_0^t dt' e^{-(t-t')/t_{\text{relax}}} \dot{q}(t') + Cq = 0, \quad (3.62)$$

with the inertia M and the stiffness C being computed as above, i.e. neglecting the contribution from the deformation of the Fermi sphere. (So C represents the adiabatic stiffness coefficient.)

The finite relaxation time produces the additional restoring term proportional to C' , which will eventually be damped out. Using the diabatic single-particle basis $\{|\alpha\rangle\}$ associated with the occupation number n_α and the energy ε_α , we obtain

$$C' = - \sum_\alpha \frac{\partial \varepsilon_\alpha}{\partial q} \frac{\partial \tilde{n}_\alpha}{\partial q}, \quad C = \sum_\alpha \frac{\partial}{\partial q} \left(\frac{\partial \varepsilon_\alpha}{\partial q} \tilde{n}_\alpha \right) = \sum_\alpha \frac{\partial^2 \varepsilon_\alpha}{\partial q^2} \tilde{n}_\alpha - C', \quad (3.63)$$

where \tilde{n}_α is the local equilibrium occupation number. (The commutator terms arising from the energy or the occupation number are neglected but, as has been often discussed, these non-diagonal terms may be important and should be investigated.) The various terms in the coefficients C and C' can easily be understood, since the first one in C is the restoring force caused only by the energy variation at constant occupation, while C' is the modification of this energy due to the variation of both the single-particle energies and the occupation numbers.

Considering early times, $t \ll t_{\text{relax}}$, we obtain the dispersion relation,

$$-M\omega^2 + C' \frac{\omega}{\omega + i/\tau} + C = 0. \quad (3.64)$$

The authors of Ref. [142] consider a Skyrme-type effective interactions, so that they can explicitly derive all terms of the above equation. First, they split the energy into its various components,

$$e[\rho] = \frac{\hbar^2}{2m^*} \kappa[\hat{\rho}] + e_V[\rho] + e_W[\rho] + e_C[\rho] + e_S[\rho], \quad (3.65)$$

where $\kappa[\hat{\rho}]$ represents the kinetic energy density, e_V is the volume term related to the momentum-independent part of the interaction (the parameters t_0, t_3, x_0 , and x_3 in the Skyrme force), while e_W is the Weizsäcker term related to density gradients due to the interaction range (associated with the density-dependent terms proportional to t_1, t_2, x_1 , and x). When the kinetic energy is treated semi-classically, then the Weizsäcker term can also include quantal corrections proportional to the Laplacian of the density [141]. The Coulomb energy is $e_C[\rho]$ (was already discussed for infinite matter). The last term $e_S[\rho]$ is new and takes account of the surface around the nucleus. All these different terms will directly contribute to the restoring force.

As an example, let us consider the adiabatic limit of an infinitely small relaxation time, $t_{\text{relax}} \rightarrow 0$. Then the dispersion relation simply leads to $\omega^2 = C/M$. Since C is directly related to the energy, the above decomposition can be used to analyze how the mode frequency depends on the various parts. These are illustrated in Fig. 3.15 (left), and one can see that indeed the origin of the instability is the volume term, which is reduced by the kinetic and the finite-range. Since a finite wave number

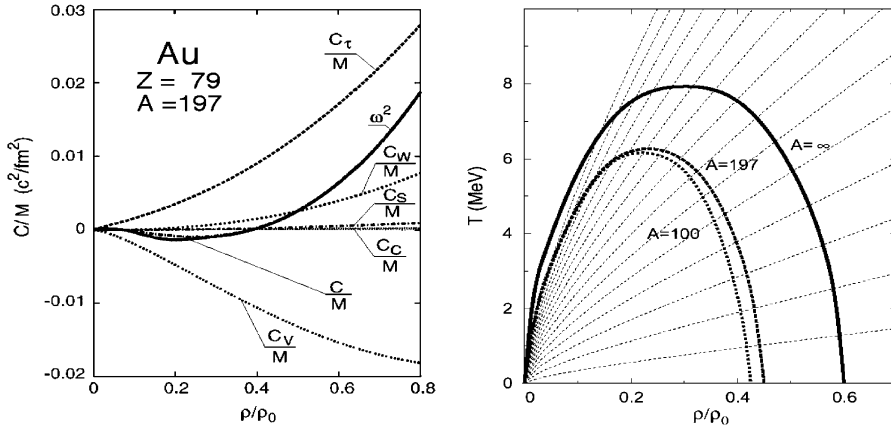


Fig. 3.15. Fermi fluid dynamics. Fermi fluid dynamics for nuclear droplets obtained with the SkM* Skyrme force. *Left panel*: Various contributions to the restoring force for a quadrupole mode ($L=2$) with no node ($n=0$) in a Au nucleus. Also shown is the square of the frequency, which differs slightly from C/M because of coupling to higher node numbers. *Right panel*: Adiabatic spinodal boundaries in the ρ – T phase plane for various nucleon numbers A . The dashed lines follow isentropic expansions. (From Ref. [142].)

is needed to fit at least one oscillation inside the drop, the finite-range (Weizsäcker) reduces the degree of instability in the finite system.

As already discussed in connection with infinite matter, it was pointed out in Ref. [141] that the Weizsäcker term leads to a k^2 correction in the sound speed, thus explaining the high- k suppression in the dispersion relation. All the other contributions, including Coulomb effects, are almost negligible. Only near the spinodal boarder might they become a more important, since the other terms tend to zero.

The spinodal regions obtained with this adiabatic approximation are shown in Fig. 3.15 (right). It can be seen that indeed the spinodal region is reduced (mainly by the Weizsäcker term) as compared with infinite matter. It should be noted that the above treatment yields so-called adiabatic spinodal which is already much reduced relative to the isothermal spinodal. This feature arises from the specific approximations made. In fact, the system is supposed to remain on an adiabat (see the constant entropy lines in Fig. 3.15 (right)), so it can only explore instabilities along this line. Therefore, the curvature anomaly of the thermodynamical potential has to lie on this line for spinodal instability to occur. This restriction leads to a reduction of the instability region. However, on this adiabat the density fluctuations induce a temperature variation so that the system will become inhomogeneous in temperature. A more complete treatment should then also solve the heat propagation coupled to the collective dynamics. Considering the smallness of the typical most unstable wave length and of the nuclear dimension in most cases, the heat propagation cannot be safely neglected. In fact, it is probable that during the typical instability time thermalization of the density irregularities will occur. In such a case, the present local adiabatic treatment will not be valid. Rather, if the thermalization is fast, the isothermal spinodal will determine the sound propagation.

3.2.4. Conclusions from studies with fluid dynamics

In the fluid dynamic approaches it is possible to study many aspects of the instabilities, such as the competition between bulk and surface, the deformation of the Fermi sphere, and the most unstable wave length and multipolarity. However, since rather drastic approximations have been made in order to bring the problem onto a Fermi droplet form, caution should be exercised when interpreting the results. In the following, we shall point out when results from more refined methods appear to conflict with conclusions drawn from the simplified models described above.

The following lessons from fluid-dynamical studies appear to be robust and should not be modified in more complete treatments:

- The Coulomb force has little influence on the instabilities.
- The bulk instabilities are not very sensitive to the nuclear shape but the possible surface instabilities are (for example, a very diffuse density may induce surface instabilities and lead to hollow configurations). However, as we shall see, a full quantal treatment of the problem reduces the role of surface instabilities significantly.
- The main effect of the finite size is the shrinkage of the spinodal region, caused primarily by the limitation in which wave lengths can be fitted inside the nucleus.
- The radial structure of modes with various L favors a zero-node transition density, since the associated k is already sufficiently large and larger node numbers are suppressed.
- The role of the damping is two-fold. On the one hand it slows down the collective motion, but on the other hand it allows the system to explore more unstable configurations by rearranging the single-particle occupations. Therefore, we may expect that it will enlarge the instability region but at the same time slow down the growth. However, this is still an open question which calls for a complete quantal calculation of the unstable response, including the effects of non-diagonal terms arising from the non-commutation of density and energy.

Finally, we saw that the suppression of large wave numbers imposes a maximum multipolarity of the instabilities but that the semi-classical treatment render the allowed L about equally unstable. This feature will be strongly modified by the introduction of quantal effects, since a specific collective mode must be built out of transitions between different single-particle states. Then the specific single-particle structure will directly influence the stability of the collective states. In particular, we shall see that the low-lying collective 3^- state is always the first to become unstable in a quantum treatment, while it is more often the quadrupole mode that becomes unstable first in a fluid dynamic approximation.

3.2.5. Quantal description of instabilities

In finite dilute systems quantal effects are expected to have an even more important role, relative to what is obtained in nuclear matter. Indeed, in addition to the matter properties, the presence of boundary conditions introduces shell effects which will not subside until the temperature is comparable to the shell gaps (i.e. several MeV). Moreover, the nuclear response and so the instability are strongly influenced by approximate symmetries of the single-particle states, such as those arising from the similarity between the nuclear mean-field and the harmonic-oscillator potentials.

In this section, we extend the quantal RPA treatment presented in the nuclear matter Section 3.1.4 in order to investigate the early evolution of the unstable collective modes for such

finite nuclei that may be formed in nuclear collisions. In the first part, in order to make contact with the semi-classical treatments discussed above, we calculate the growth rates of the unstable collective modes by solving a quantal dispersion equation. In the second part we will solve the complete RPA directly, thus going beyond the approximations that make it possible to recast the quantal RPA into a simple dispersion equation. We will also address the question of isospin fractionation in finite systems.

3.2.5.1. RPA equations. In order to study systems out of equilibrium, such as those produced in nuclear reactions, the initial density $\rho_0 = \rho(t=0)$ can always be seen as the solution of a constrained Hartree–Fock equation

$$[h[\rho_0] - \lambda \hat{Q}, \rho_0] = 0, \quad (3.66)$$

where \hat{Q} is a suitable constraining operator for preparing the system in the desired state (e.g. expanded) and λ is the associated Lagrange multiplier. The stability of such a state against density perturbations is more conveniently studied in the “comoving frame”, by introducing the associated boost transformation [154], e.g.

$$\rho'(t) \equiv e^{(i/\hbar)\lambda\hat{Q}t} \rho(t) e^{-(i/\hbar)\lambda\hat{Q}t}. \quad (3.67)$$

The TDHF equation is then correspondingly modified,

$$i\hbar \frac{\partial}{\partial t} \rho'(t) = [h'(t) - \lambda \hat{Q}, \rho'(t)], \quad (3.68)$$

where h' is the boosted mean-field Hamiltonian.

In order to investigate the early evolution of instabilities, we study a perturbation $\delta\rho'(t)$ around the reference solution, $\rho'_0(t)$, of the TDHF equation (3.68), with the initial condition $\rho_0(0)$ determined by the constrained Hartree–Fock equation (3.66). The evolution of $\delta\hat{\rho}(t)$ is determined by the linearized TDHF equation in the comoving frame,

$$i\hbar \frac{\partial}{\partial t} \delta\rho' = [h'_0(t) - \lambda Q', \delta\rho'] + [\delta U'(t), \rho'_0(t)] = \mathcal{M}(t) \cdot \delta\rho'(t), \quad (3.69)$$

where $h'_0(t)$ is the comoving mean-field Hamiltonian and $\delta U'(t)$ represents the distortion of the mean-field potential in the comoving reference system. Furthermore, $\mathcal{M}(t)$ denotes the instantaneous RPA matrix. The formal solution of this equation can be expressed as

$$\delta\rho'(t) = \mathcal{U}(t) \cdot \delta\rho(0), \quad (3.70)$$

where $\mathcal{U}(t) = \mathcal{T}(\exp[-(i/\hbar) \int_0^t dt' \mathcal{M}(t')])$ denotes the linearized evolution operator with \mathcal{T} being the time ordering operator. However the construction of $\mathcal{U}(t)$ is generally a very difficult task. Usually, only the early evolution of the instabilities in the vicinity of the initial state ρ_0 is considered and so the RPA problem associated with $\mathcal{M}(0)$ is solved. We will go beyond this approximation in the next section, where also large-amplitude motion will be discussed. Performing a Fourier transform with respect to time, the RPA equation becomes

$$(\hbar\omega_v - \epsilon_i + \epsilon_j) \langle i | \delta\rho_v | j \rangle = (\rho_j - \rho_i) \langle i | \delta U_v | j \rangle, \quad (3.71)$$

where ρ_i and ϵ_i are the occupation number and the energy associated with the constrained Hartree–Fock state $|i\rangle$, respectively. The temperature dependence enters into the calculations through the occupation number ρ_i , which is assumed to be given by the Fermi–Dirac function in terms of the single-particle energies ϵ_i .

The RPA equation (3.71) can be solved using standard techniques [154,26], but to provide a better insight into the problem of instabilities, let us first recast it into an approximate dispersion relation.

3.2.5.2. RPA dispersion relation. The RPA problem can be highly simplified if we can guess a parametrization of the transition density associated with the collective mode under study. As far as spinodal instability is concerned, as in the fluid dynamics approaches, we can use the multipole expansion of sound waves to modulate the spherical reference density $\rho_0(r)$,

$$\delta\rho_v(\mathbf{r}) = \langle \mathbf{r} | \delta\rho_v | \mathbf{r} \rangle = \alpha_v j_L(kr) \rho_0(r) \bar{Y}_{LM}(\theta, \phi) , \quad (3.72)$$

where α_v is the amplitude of the collective excitation. Inversion of this relation yields an expression for the amplitude,

$$\alpha_v = K_L \int d^3\mathbf{r} F_L(r) \delta\rho_v(\mathbf{r}) , \quad (3.73)$$

where $F_L(\mathbf{r}) = F_L(r) \bar{Y}_{LM}(\theta, \phi)$, with $F_L(r)$ being a smooth profile function that is not orthogonal to the collective transition density $j_L(kr) \rho_0(r)$. The normalization factor K_L , which is then finite, is determined by

$$\frac{1}{K_L} = \int d^3\mathbf{r} F_L(\mathbf{r}) j_L(kr) \rho_0(r) \bar{Y}_{LM}(\theta, \phi) . \quad (3.74)$$

A dispersion relation for the frequencies of the collective modes can be deduced from the self-consistency condition that is obtained by inserting the solution of the RPA equation (3.71) for $\delta\rho_v$,

$$\delta\rho_v = \sum_{i,j} |i\rangle \langle i | \delta\rho_v | j \rangle \langle j| = \sum_{i,j} |i\rangle \langle i | \delta U_v | j \rangle \langle j| \frac{\rho_j - \rho_i}{\hbar\omega_v - \epsilon_i + \epsilon_j} , \quad (3.75)$$

into the right-hand side of Eq. (3.73), in order to factorize the collective amplitude $\alpha_L(\omega)$. This gives

$$\frac{1}{K_L} = \sum_{i,j} \frac{\langle i | \partial U / \partial \alpha_v | j \rangle \langle j | F_L | i \rangle}{\hbar\omega_v - \epsilon_i + \epsilon_j} , \quad (3.76)$$

where the transition field δU_v is written in terms of the collective amplitude α_v as $\delta U_v = \alpha_v \partial U / \partial \alpha_v$. In principle, this dispersion equation holds for any choice of $F_L(r)$, provided that parametrization (3.72) is a good approximation for the density distortions in a multipole mode. Usually one selects $F_L(\mathbf{r}) = \partial U / \partial \alpha_v$ because it yields a symmetric dispersion equation,

$$\frac{1}{K_L} = \sum_{i,j} \frac{|\langle i | \partial U / \partial \alpha_v | j \rangle|^2}{\hbar\omega_v - \epsilon_i + \epsilon_j} (\rho_j - \rho_i) . \quad (3.77)$$

It is instructive to note that this dispersion equation is equivalent to the RPA result for a separable interaction with the coupling constant given by the normalization factor K_L ,

$$V(\mathbf{r}, \mathbf{r}') = \frac{1}{2} K_L F_L(\mathbf{r}) F_L(\mathbf{r}') . \quad (3.78)$$

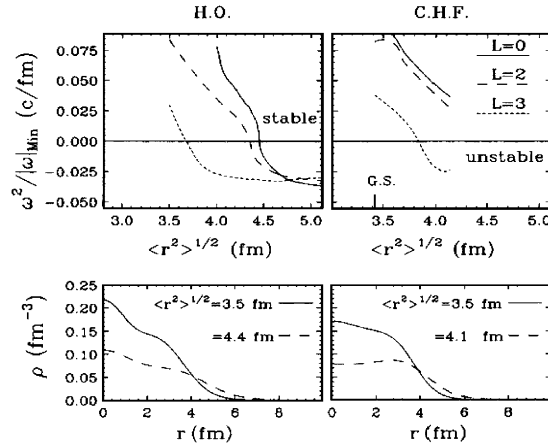


Fig. 3.16. RPA results for $A = 40$. Spherical systems with 40 nucleons treated in the harmonic-oscillator representation (*left*) or the constrained Hartree–Fock representation (*right*) at zero-temperature. *Bottom panels*: The density profiles $\rho(r)$. *Top panels*: Minimum values of $\omega_L^2/|\omega_L|$ for modes with $L = 0, 2, 3$ as a function of the root-mean-square size $\langle r^2 \rangle^{1/2}$. (From Ref. [155].)

The dispersion equation (3.77) makes it possible to determine the frequencies ω_v associated with the collective modes of the nucleus. For a spherically symmetric system, collective frequencies depend on the multipole L and the radial wave number k . In the unstable region, the collective frequencies are imaginary, $\omega_v \equiv \omega_L(k) = \pm i/t_L(k)$. In the calculations reported in Ref. [155], a Skyrme-like parametrization for the effective mean-field potential was used.

In order to solve the dispersion equation (3.77), first we need to determine the single-particle representation of the constrained Hartree–Fock problem (CHF). However, it is difficult to guess a suitable form of a constraining operator $\hat{Q}(r)$ that will yield the single-particle representation for a wide range of densities in the unstable region. An operator of Gaussian form $\hat{Q}(r) = r^2 \exp(-r/r_0)$ provides a reasonable constraint for preparing the system at low densities. However, in the spinodal region, as soon as the monopole mode $L = 0$ is unstable, the CHF calculations can not be carried out. For this reason, we take here a more schematic approach and solve the dispersion relation by employing the harmonic-oscillator wave functions and the wave functions of a Wood–Saxon-like potential, instead of the CHF wave functions (see Ref. [155] for more details). We present calculations carried out for systems containing $A = 40$ and 140 nucleons by including 100 and 120 orbitals, respectively. For the Skyrme force we have used $\sigma = 1$, $t_0 = 1000 \text{ MeV fm}^3$, and $t_3 = 1500 \text{ MeV fm}^6$ [155]. This force gives a saturation density of $\rho_s = 0.16 \text{ fm}^{-3}$ and a stiff compressibility of $K = 350 \text{ MeV}$. The range parameter $c = -126 \text{ MeV fm}^5$ is the same as in the corresponding term in the Skyrme-III force.

The results for $A = 40$ are illustrated in Fig. 3.16. Bottom panels show the density profiles of obtained in either the harmonic-oscillator representation or the Hartree–Fock representation with a Gaussian constraint. The density profiles are shown in the bottom panels, while the top panels show minimum value of the $\omega_L^2/|\omega_L|$ for various multiplicities, plotted as a function of the root-mean-square size of the system, $R_{\text{RMS}} = \langle r^2 \rangle^{1/2}$. The mutual agreement between the two treatments is rather good. As the size is increased, the collective modes grow steadily softer

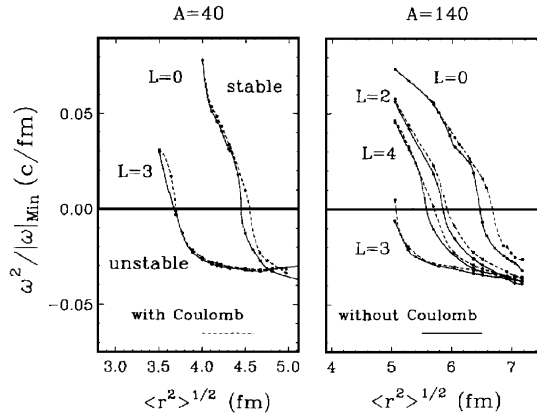


Fig. 3.17. Coulomb effect on RPA modes. Minimum values of $\omega_L^2/|\omega_L|$ for collective modes of various multipolarity L in spherical systems with either $A = 40$ (left) or $A = 140$ (right) as a function of the root-mean-square size. Calculated in the harmonic-oscillator representation without (solid) and with (dashed) the Coulomb force. (From Ref. [155].)

and they turn unstable when ω_L^2 becomes negative. For the octupole mode, this occurs at $R_{\text{RMS}} \approx 3.7$ fm.

As reported in Ref. [155], the radial wave numbers associated with the most unstable modes calculated in the harmonic oscillator representation display a crossover from a surface (small k) to a volume character (large k) at $R_{\text{RMS}} \approx 4.0$ – 4.5 fm for all modes. Thus, while the different multipolarities become unstable at different degrees of dilution, they all tend to change acquire a volume character at the same point of dilution. This this feature appears to be governed by the overall geometry of the configuration (the decisive property presumably being the ratio between the surface thickness and the overall bulk radius).

The effect of the Coulomb force is illustrated in Fig. 3.17 for the most important multipolarities. The Coulomb force decreases the degree of spinodal instability, but the effect is generally seen to be relatively small. Furthermore, as one would expect, it increases with the number of nucleons.

To illustrate the dependence on temperature, results for $T = 0$ and 3 MeV are compared in Fig. 3.18 for the same two values of A . As generally expected, a hot system is spinodally more stable. Furthermore, the hotter the system the lower the density at which it turns unstable. This behavior is similar to that exhibited by spinodal instabilities in uniform matter.

In the bottom panel of Fig. 3.19, the dispersion relations for various multipolarities are plotted as a function of the radial wave number k for $A = 40$ and 140, as obtained for a temperature $T = 3$ MeV in both the harmonic-oscillator and the Woods–Saxon representations. The density profiles are also displayed. As can be seen, the dispersion relation is not very sensitive to the differences in initial conditions, except for the lowest unstable mode. In both cases the growth rates for large values of the radial wave number are suppressed due to quantal and surface effects, reflecting the fact that the system admits only one radial oscillation in the unstable modes. In the case of $A = 40$, the calculations show that the system is unstable only against quadrupole and octupole deformations. In particular, in the calculations with the Woods–Saxon representation the octupole is the dominant unstable mode. This is consistent with the CHF calculations presented in Fig. 3.16, in which the first mode to become unstable is the low-lying octupole mode. In the larger system ($A = 140$), several multiple

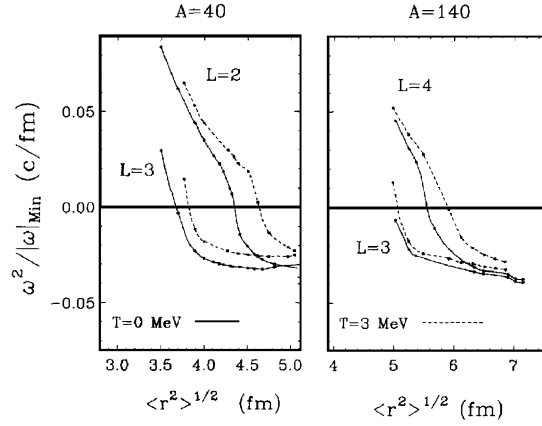


Fig. 3.18. Temperature dependence of RPA modes. Minimum values of $\omega_L^2/|\omega_L|$ for collective modes of various multipolarity L in spherical systems with either $A = 40$ (left) or $A = 140$ (right) as a function of the root-mean-square size. Calculated in the harmonic-oscillator representation for either $T = 0$ (dashed) or $T = 3$ MeV (solid). (From Ref. [155].)

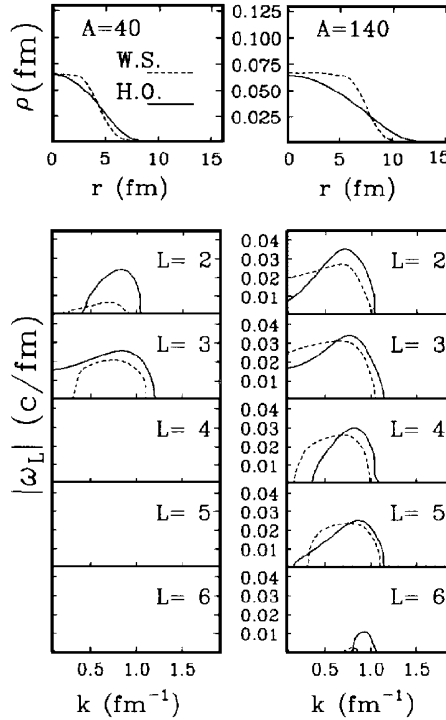


Fig. 3.19. RPA for various multiplicities. RPA results at $T = 3$ MeV obtained in either the harmonic-oscillator representation (solid) or the Woods–Saxon representation (dashed) for dilute spherical nuclei with $A = 40$ (left) and $A = 140$ (right), Top panels: Density profiles $\rho(r)$. Bottom panels: The growth rates $|\omega_L|$ for various multiplicities L as functions of the radial wave number k . (From Ref. [155].)

modes up to $L=5$ become unstable but, due to quantal and surface effects, modes with L larger than 5 are strongly suppressed. The unstable modes are predominantly volume modes, with the associated wave numbers in the range of $k = 0.6\text{--}0.9 \text{ fm}^{-1}$. In fact, as noted above for low temperatures, when the system expands into the region of spinodal instability, some of the unstable modes first appear as surface instabilities with small radial wave numbers. However, at higher temperatures ($T \approx 3 \text{ MeV}$), the instabilities associated with surface fluctuations are suppressed and the local instabilities of the mean-field trajectories are dominated by the volume modes.

It is important to note that the maximum value of the growth rate, $\gamma_L(k_0)$, is nearly independent of the multipole order for $L = 2\text{--}5$, indicating that these modes are amplified at comparable rates. Therefore, provided that they are equally agitated by the fluctuation source, they grow equally prominent in the fragmentation pattern, apart from the geometrical weight $2L + 1$. These results are in agreement with the fluid-dynamic calculations of spinodal instabilities (see above). It is also interesting to note that the maximum of the growth rate for a typical multipole mode in a finite source is comparable to what is obtained in nuclear matter [155].

3.2.5.3. Full RPA calculations for dilute nuclei. A more accurate treatment can be found in Ref. [51], where a fully self-consistent comoving solution of the finite-temperature RPA problem is given. We shall briefly summarize this approach here.

In terms of the RPA functions $\rho_v^{ij} = \langle i | \rho_v | j \rangle$ and the residual interaction $V_{il,kj} = \langle i | \partial U / \partial \rho_{lk} | j \rangle$, the RPA equation (3.71) takes on its standard form,

$$\omega_v \rho_v^{ij} = (\epsilon_i - \epsilon_j) \rho_v^{ij} + \sum_{kl} (n_j - n_i) V_{il,kj} \rho_v^{kl}. \quad (3.79)$$

Given an initial density matrix ρ_0 , this equation can be directly diagonalized. To mimic conditions observed in dynamical simulations, ρ_0 can be taken as a self-similar scaling of a hot Hartree–Fock density. Then, the Hartree–Fock equation is first solved for the ground state, $[h_{\text{HF}}, \rho_{\text{HF}}] = 0$, yielding the single-particle wave functions $|\varphi_i\rangle$ and the associated energies ϵ_i . Subsequently, a finite-temperature density matrix is introduced as $\rho_{\text{HF}}(T) = [1 + \exp(h_{\text{HF}} - \epsilon_F(T))/T]^{-1}$, where $\epsilon_F(T)$ is the Fermi level adjusted to the fixed particle number A . Then one applies a scaling transformation, $R(\alpha)$, which stretches the wave functions in the radial direction by the dilution factor α , $\langle r | R(\alpha) \varphi \rangle = \alpha^{-1/3} \langle r | \varphi \rangle$, and the density matrix for hot and dilute system is finally given as $\rho_0(\alpha, T) = R(\alpha) \rho_{\text{HF}}(\alpha^2 T) R^\dagger(\alpha)$. The corresponding constrained Hamiltonian is thus $\bar{h}_0(\alpha) = \alpha^2 R(\alpha) h_{\text{HF}} R^\dagger(\alpha)$, so that the constraint can be identified as $-\lambda Q_\alpha = \bar{h}_0(\alpha) - h[\rho_0(\alpha, T)]$. By construction, $\bar{h}_0(\alpha)$ and $\rho_0(\alpha, T)$ commute, since they can be diagonalized simultaneously. The eigenstates of the constrained Hamiltonian are given by $|i\rangle' = R(\alpha) |\varphi_i\rangle$ and the corresponding energies and occupation numbers are $\epsilon_i' = \alpha^{-2} \epsilon_i$ and $n_i' = [1 + \exp((\epsilon_i - \epsilon_F(\alpha^2 T))/\alpha^2 T)]^{-1}$, respectively.

In Ref. [51], such Hartree–Fock calculations have been performed for Ca and Sn isotopes in the coordinate representation using the Skyrme force SLy4 [156,157]. The particle states were obtained by diagonalizing the Hamiltonian in a large harmonic-oscillator representation that includes 12 major shells for Ca and 15 for Sn. Then the RPA equation (3.79) was solved by a direct diagonalization using a discrete two-quasi-particle representation.

The top panel of Fig. 3.20 shows the isoscalar strength function calculated for ^{40}Ca as a function of the dilution parameter α . We observe that the frequencies associated with the dominant modes decrease as dilution becomes larger. At a critical dilution they cross through zero and become

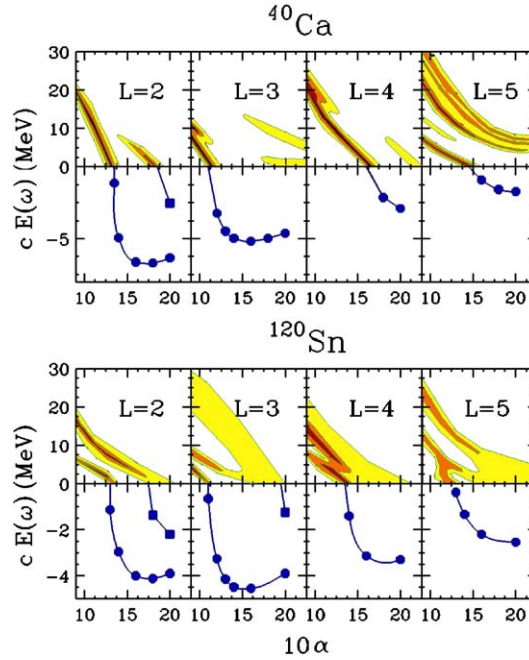


Fig. 3.20. Isoscalar strength functions. For ^{40}Ca and ^{120}Sn are shown contour plots of the isoscalar strength functions associated with the multipolarity $L = 2-5$ (top panels) and minus the growth rates for unstable modes, $-|\omega_v|$ (bottom panels), as functions of the dilution parameter α . (From Ref. [51].)

imaginary. The (negative of) the associated growth rates $|\omega_v|$ are included in the figure. It can be seen that when several branches of the strength function exist, each one may develop towards instability. Consequently, for sufficiently large degrees of dilution, there may be more than one unstable mode with a given multipolarity (see $L = 2$ for Ca and $L = 2, 3$ for Sn).

At moderate dilutions, $\alpha \approx 1.2$, only the octupole mode is unstable. In general, density fluctuations with odd multipolarity become unstable at smaller degrees of dilution than those of even multipolarity. This is a genuine quantum effect: the majority of the particles have to jump only one major shell in order to produce an odd natural-parity particle–hole excitation, while twice this energy is required for an even one. In nuclei at normal density this makes the 3^- a strongly collective state at low energy and this state is the first to turn unstable as the system is diluted.

The second important feature is that distortions of large multipolarity are hardly becoming unstable. This is due to finite-range and quantum effects that prevent break-up into the correspondingly small fragments. As a consequence, the fastest growth time, $t_{\min} \approx 28 \text{ fm}/c$, occurs for $L = 2$ at a dilution of $\alpha = 1.8$. However, deep inside the instability region the octupole mode is almost as unstable as the quadrupole. The figure shows clearly that only a small dilution suffices to bring the system well inside the spinodal region, where then the mean-field treatment should be as valid as at normal density.

Results of similar calculations performed for ^{120}Sn are shown in the bottom part of Fig. 3.20. Also in this case is the octupole mode the first to turn unstable, which happens at $\alpha \approx 1.1$. Moreover, large multipoles are more unstable in ^{120}Sn than in ^{40}Ca . This should be expected since L must

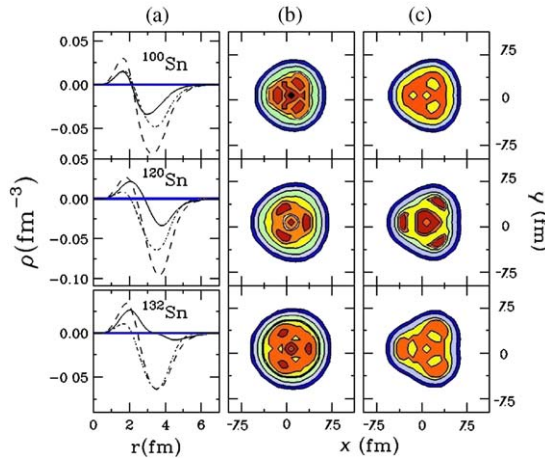


Fig. 3.21. Full RPA calculations for unstable octupole modes in Sn isotopes. Results for unstable octupole modes in Sn isotopes obtained with the full RPA calculation: (a) radial dependence of the form factor at the dilution $\alpha = 1.5$ for neutrons (solid), protons (dotted), and nucleons (dashed); (b) contour plots of the perturbed neutron density; (c) contour plots of the perturbed proton density. (From Ref. [51].)

increase in proportion to R in order to maintain the wave length of the associated density undulation at a constant value.

The behavior of charge-asymmetric systems has also been investigated. In order to gain a deeper insight into the instability properties, it is useful to study the behavior of the RPA solution in coordinate space and consider $\rho_n(\mathbf{r})$ and $\rho_p(\mathbf{r})$ separately. For different Sn isotopes, Fig. 3.21 shows the radial dependence of the form factor associated with the unstable octupole mode at the dilution $\alpha = 1.5$, both for neutrons and protons separately for the sum. Contour plots of the perturbed neutron and proton densities are also shown. We observe that neutrons and protons move mostly in phase, which demonstrates that unstable modes have mostly an isoscalar character. Moreover, the collective modes try to restore the isospin symmetry in the dense phase. In fact, in neutron-rich systems (e.g. ^{132}Sn), protons oscillate even more than neutrons as a means for forming more symmetric fragments and thus reduce the symmetry energy. This effect is related to the isospin fractionation that occurs in unstable asymmetric nuclear matter, as discussed above.

Moreover, proton oscillations are located at the surface of the system, which helps to minimize the repulsive Coulomb energy. However, in the full treatment, the surface and volume instabilities do not appear to be in competition but combine to a unique mode. However, the RPA approach is a local diabatic approach which considers only particle–hole excitations around a given state. If the instability needs a larger rearrangement of the single-particle states, TDHF and RPA approaches will miss it. So this problem would certainly deserve more study.

The RPA studies at finite temperature and dilutions define the border of the instability region for different unstable modes. In order to draw a more usual phase diagram, the dilution factor can be replaced by a density, $\rho = \rho_0/\alpha^3$. Fig. 3.22 shows the resulting phase diagrams for octupole instabilities in Ca and Sn isotopes. Also shown are the boundaries corresponding to a specified growth time t_L . The size of the instability region generally increases with A but it still remains

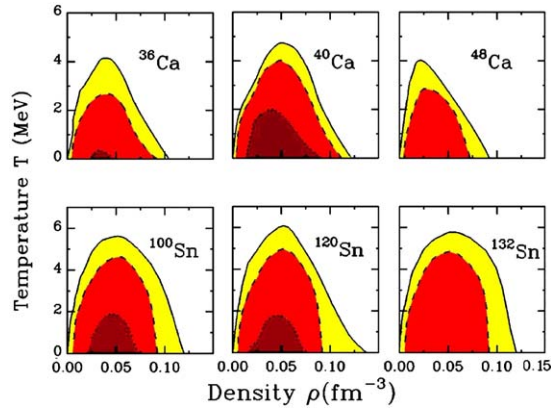


Fig. 3.22. Border of the instability region. Boundaries of the instability region (*solid curves*) associated with $L=3$ collective modes in Ca and Sn isotopes. Also delineated are phase points having the same growth time t_L equal to either 100 fm/c (*dashed*) or 50 fm/c (*dots*). (From Ref. [51].)

significantly smaller than that for nuclear matter. For example, the limiting temperatures for Ca and Sn are about 4.5 and 6 MeV, respectively, while it is about 16 MeV in symmetric nuclear matter. Moreover, more asymmetric systems are spinodally more stable. For example, in spite of its larger mass, ^{132}Sn is more stable than ^{120}Sn . This behavior is also in agreement with the nuclear matter calculations, which indicate that the instability region shrinks in asymmetric nuclear matter [47].

3.2.6. Concluding remarks about instabilities in finite systems

In this section, we have discussed in detail various aspects of the spinodal instabilities in nuclei and we have seen that the essential features of spinodal instability are not strongly affected by the finiteness of the systems.

First we showed that the suppression of large wave numbers to quantal corrections and the finite size of the range of nuclear forces is manifested in finite nuclei by the fact that only low multipoles are unstable and that the radial form factor of the instability does not have any node. Because of the fact that the wave length of the instability should fit into the nuclear radius, the spinodal region is reduced compared with the infinite system. Another important factor is the quantum nature of the nucleons. In particular the parity sequence of the various single-particles orbital implies that at moderate temperature the first mode to grow unstable is the low-lying 3^- collective state. All those effects may have experimental consequences, such as the possible importance of ternary fission in the onset of multifragmentation.

The various calculations have also shown that when the system is sufficiently well inside the spinodal region the various unstable modes of different L have very similar growth rates, so that one might expect that the various multi-IMF channels become populated in a fairly democratic fashion. This feature may lead to a scale invariant fluctuation distribution over a broad range of multipolarities, something that could be investigated experimentally. Furthermore, the various calculations suggest that the Coulomb force plays a marginal role. By contrast, the isospin degree of freedom is important. Since the instabilities are essentially of isoscalar nature, they try to form liquid drops close to β stability.

With regard to the competition between surface and volume modes, full RPA calculations have shown that this phenomenon is merely an artefact of the considered approximation. Indeed, in general only a single mode turns unstable and it is a mix of surface and volume transitions, with the volume character gaining in relative prominence as the system grows. It should also be noted that mean-field approaches do not allow a fast rearrangement of many single-particle orbitals and may therefore miss some instabilities. In the case of the opening of such many-particle many-hole channels the dissipation may help the system to explore the new degrees of freedom. More work is needed on this point, in particular in the framework of extended quantal mean-field approaches.

Finally, all the approaches discussed in this section are restricted to small-amplitude motion. Moreover, they do not address the origin of the irregularities that from the seeds for amplification by the dynamics. Thus, in order to achieve a complete understanding of an instability, one would need to go beyond these limitations and study the source of the fluctuations and propagate them to large amplitudes. This is the subject of the next section.

4. Dynamics of spinodal fragmentation

Spinodal fragmentation may occur when the bulk of the evolving nuclear system enters the phase region of spinodal instability. Irregularities in the density are then amplified and, if given sufficient time, this mechanism may cause the system to break up into separate fragments. In the previous section, we focussed on the understanding of the involved instabilities in the linear regime of small amplitudes. In the present section, we go beyond the small-amplitude regime, allowing us to consider the actual formation of fragments. We will thus discuss the conceptual framework and the calculational tools for treating and analyzing spinodal multifragmentation. In particular, the non-linear regime of the dynamics will be carefully investigated and the seeds for the fragment formation elucidated.

4.1. From the linear regime towards chaotic evolution

The above discussion of spinodal multifragmentation is based on the basic physical picture advanced in Ref. [106] which utilizes a simple linear analysis of the instabilities. However, a more accurate treatment may affect the results in important ways, especially for finite nuclear systems. In particular, the presence of the self-consistent one-body field renders the mean-field equations non-linear and the ensuing dynamics is therefore expected to exhibit features characteristic of chaotic processes [158,159].

At the early stage the unstable modes are independent and their amplitudes evolve exponentially. As the disturbances increase in magnitude, the modes become progressively coupled and the evolution grows correspondingly complicated as the non-linearities gain importance. Concurrently, the overall growth of the density irregularities is being attenuated due to the fact that the density must remain within zero and (in practice) the saturation density. The system then acquires a lumpy appearance and may be roughly described as an assembly of prefragments (into which the system would split if it were free to expand). Subsequently, over a longer time scale, this lumpy structure will proceed to equilibrate. This process consists predominantly in the fusion of the smaller prefragments into ever larger ones, as the system seeks to organize itself into the two coexisting liquid and gas

phases, leading ultimately towards a few large fragments surrounded by a dilute gas of very light clusters.

It is an important feature of the systems formed in nuclear collisions that they are generally endowed with an overall expansion which will then cause the evolution of the “prefragment gas” to be truncated before phase coexistence has been reached, thus effectively providing a snapshot of the non-equilibrium dynamics.

4.1.1. *Non-linear effects*

The emergence of a non-linear behavior was studied for a spherical nucleus by Donangelo et al. [160]. Analyzing the instability growth, they demonstrated that higher-order terms have a stabilizing effect, thus effectively shrinking the spinodal region.

Non-linear evolution cannot be described as merely a quantitative modification of linear dynamics but has a qualitatively different phenomenology. In particular, nuclei can be considered as soliton solutions of the non-linear mean-field dynamics. The problem of dynamical instability and clusterization in the breakup of nuclear systems was discussed from such a perspective by Kartavenko et al. [161]. Noting that the existence of solitary waves is essentially determined by the interplay between non-linearity and dispersion, the authors showed that the non-linear terms are associated with the volume (i.e. spinodal instability), while the dispersion terms arise from the surface (i.e. Rayleigh–Taylor instability). Within the illustrative framework of a simple one-dimensional three-level system, it was then found that clusterization may appear in the form of stable solutions (solitons) that are formed as a result of a mutual compensation between the two types of instability.

4.1.2. *Chaos and collective motion*

Generally, the presence of non-linearities makes the nuclear mean-field dynamics a candidate for chaotic behavior. The occurrence of chaos would be of great importance since it might provide a justification for the apparent success of statistical approaches in the description of multifragmentation events [162]. Accordingly, the possibility of disorder and chaos in nuclear fragmentation has been discussed by many authors [17,19,163–174]. Chaos may be especially expected for spinodal fragmentation since the density irregularities acquire large amplitudes. However, the studies in Refs. [112,113,126,145,175–177] suggest that spinodal decomposition, simulated through full mean-field calculations, is significantly influenced by the regular regime of amplified unstable collective modes. In order to elucidate this central issue, considerable effort has been devoted to the understanding of the dynamical character of the nuclear Vlasov dynamics in the presence of instabilities [162,172,173,175,178–184].

The analysis of chaos in presence of instabilities is a delicate task. In particular, the extraction of the Lyapunov exponent, a standard diagnostic tool in chaos studies, is complicated by the fact that trajectories exhibit an exponential divergence already in the early regular regime. In order to separate the linear regime from the chaotic dynamics, Jacquot et al. [184] have introduced new methods that have also been applied (and extended) by Baldo et al. [182,183]. These studies have confirmed that any initial disturbance evolves through a regular stage, which is well described by the linear analysis and persists up to $\delta\rho \approx \frac{1}{2}\rho_0$, before reaching the ultimate irregular (possibly chaotic) stage [184]. Because of their instructive value, we recall these results in some detail below.

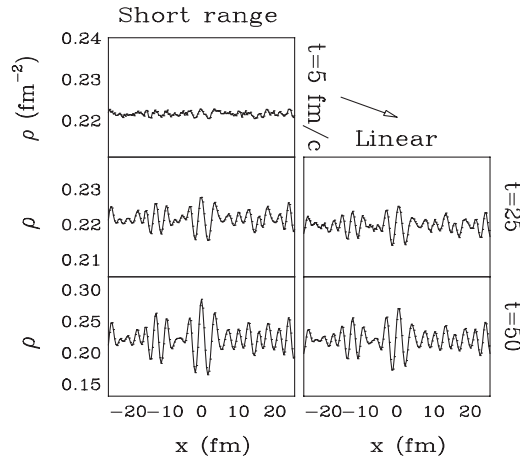


Fig. 4.1. Non-linear versus linearized dynamics. Snapshots of the density, $\rho(x)$ as obtained by either the complete (non-linear) dynamical Vlasov evolution (*left*) or the corresponding linearized approximation (*right*), starting from a random perturbation around an average of $\rho_0 = 0.4\rho_s$. (From Ref. [184].)

The studies in Ref. [184] have been performed in two spatial dimensions, with the potential being always averaged along the y direction, so that the evolution occurs only along the x axis. In order to avoid numerical noise, which may interfere with the chaos analysis, the Vlasov equation has been solved on a spatial lattice (rather than with the more common pseudo-particle method), using the code developed in Ref. [178]. Most studies have employed a zero-range interaction [162,172,178,180,182,183], but since this leads to an indefinite growth of the dispersion relation, Ref. [184] employed a finite-range interaction yielding a more realistic dispersion relation.

4.1.2.1. Vlasov dynamics of randomly initialized fluctuations. In the study by Jacquot et al. [184], an ensemble of initial configurations was prepared by perturbing a constant density located well inside the spinodal region, $\rho_0 = 0.4\rho_s$, and the resulting exact Vlasov evolution was then compared with the linear dynamics where each unstable mode evolves independently in an exponential manner. In this comparison, care was taken to match the interaction-range employed in the linear analysis to the effective range resulting from the finite lattice width used in the full calculation. For a typical trajectory, Fig. 4.1 shows the resulting evolution of the density profile, $\rho(x, t)$, for the two treatments. The two evolutions are almost identical, thus demonstrating the regularity of the early unstable dynamics and the quantitative validity of the linear treatment.

Insofar as the dynamics can be described as a simple exponential evolution of the unstable collective modes, an initial density $\rho(x, 0)$, with vanishing time derivative, $\dot{\rho}(x, 0) = 0$, will evolve as follows,

$$\rho(x, t) = \sum_k \rho_k(x) \cosh \gamma_k t, \quad (4.1)$$

where each individual term approaches a pure exponential once t exceeds the corresponding characteristic time $t_k = \hbar/\gamma_k$. Thus, the density will become increasingly dominated by the fastest-growing mode k_0 . Once the local density amplitude grows comparable to the saturation value ρ_s , the dynamics

begins to deviate progressively from the linear behavior, as it ceases to be regular, and this might indicate the onset of chaos. However, a more careful analysis is needed to investigate this aspect.

4.1.2.2. Time correlation and the onset of chaos. A standard method for analyzing complex dynamics is to study the relation between the initial value of a given degree of freedom and its value at a later time. At the early, linear stage of the evolution the relevant degrees of freedom are the normal modes characterized by the wave number k . The associated amplitudes can be obtained by a Fourier analysis of the density, $A_k^{(n)}(t) = L^{-1/2} \int_0^L dx e^{-ikx} \rho^{(n)}(x, t)$, where n labels an individual dynamical history (an “event”), and its square provides a suitable measure of the agitation of the mode,

$$C_k^{(n)}(t) \equiv |A_k^{(n)}(t)|^2 = \int_0^L dx_{12} \rho^{(n)}(x_1) e^{-ikx_{12}} \rho^{(n)}(x_2) . \quad (4.2)$$

The corresponding ensemble average, $C_k = \prec C_k^{(n)} \succ$ is simply the Fourier transform of the density–density correlation function $C(x_{12}) \equiv \prec \rho^{(n)}(x_1) \rho^{(n)}(x_2) \succ$,

$$C_k \equiv \prec |A_k^{(n)}(t)|^2 \succ = \int_0^L dx_{12} e^{-ikx_{12}} C(x_{12}) . \quad (4.3)$$

The onset of chaos can then be quantitatively analyzed by considering the evolution of the dimensionless amplification coefficient $\alpha_k^{(n)}(t) \equiv C_k^{(n)}(t)/C_k^{(n)}(0)$, which is initially unity. Furthermore, its ensemble dispersion, $\Delta\alpha_k(t)$, remains vanishing within the linear regime, so this quantity presents a suitable diagnostic tool. Thus, as long as $\Delta\alpha_k(t)$ remains small (compared to unity) the system is dominated by the regular amplification dynamics. Conversely, when it exceeds unity the correlation with the initial state is lost and the chaotic regime has been reached.

The results of such an analysis are illustrated in Fig. 4.2. From the left panels, which display a sample of individual histories, one may see how the modes grow exponentially during the early evolution, at the particular rate γ_k , but then start diverging strongly. The early exponential growth is also evident from the center panel showing the ensemble average amplification coefficient $\bar{\alpha}_k$. During this stage, the associated ensemble dispersions $\Delta\alpha_k$ remain very small. It can be seen that the most rapidly amplified mode (the fifth one having $k_0 \approx 0.6 \text{ fm}^{-1}$) maintains a regular behavior throughout the time period considered, which amounts to about five times its growth time $t_0 \approx 40 \text{ fm}/c$, while the slower modes lose their regularity, and the sooner so the smaller their growth rate γ_k . It thus appears that the most unstable collective modes are fairly robust against chaos and remain only weakly coupled to the other degrees of freedom.

The regularity of the first stage of spinodal decomposition was also found in Refs. [182–184] from studies of the two-time correlation function. Such a gradual onset of chaos in the presence of robust (unstable) zero-sound modes is reminiscent of the survival of (stable) collective motion at high temperature, as in the case of the hot Giant Dipole Resonance [185,186], and it illustrates the general feature that fully regular and fully chaotic regimes are merely two extremes and generally one should expect to encounter an intermediate situation, the weaker modes becoming chaotic sooner than those that are more robust.

4.1.2.3. Lyapunov exponents. With the above results in mind, one may acquire a deeper insight by studying the Lyapunov exponents associated with the spinodal mean-field dynamics, as has been

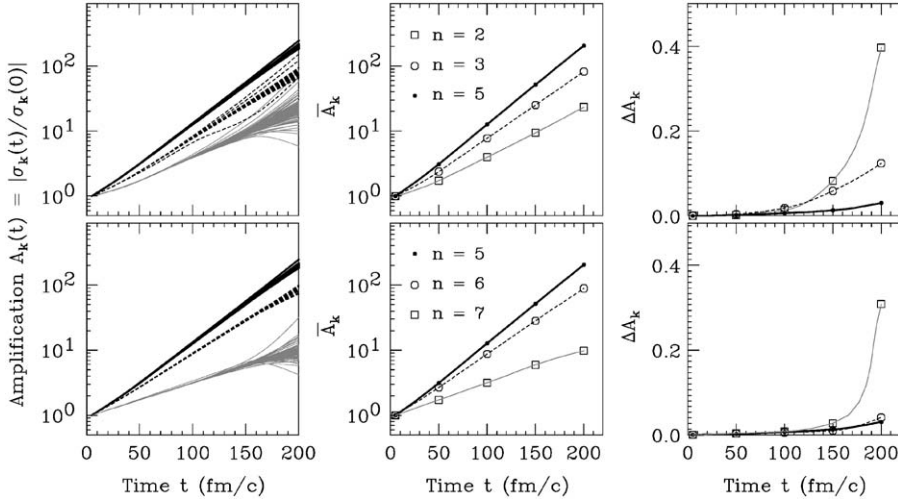


Fig. 4.2. Mode amplification. The evolution of the amplification coefficients extracted in Ref. [184] for two-dimensional matter with a finite-range interaction for various modes, labeled by their node number n . In the upper panel the thick lines correspond to $n = 5$ (the fastest-growing mode), the dashed lines to $n = 3$ and the thin grey lines to $n = 2$; in the lower panel the thick lines correspond to $n = 5$, the dashed lines to $n = 6$ and the thin grey lines to $n = 7$. The left panels present a sample of 100 events, $\{\alpha_n^{(i)}(t)\}$, the central panels show the corresponding ensemble averages, $\bar{\alpha}_n(t)$ and the right panels show the ensemble dispersions, $\Delta\alpha_n(t)$.

reported in Refs. [180,172,187]. The Lyapunov exponents provide a measure of the rate of trajectory divergence. As a general measure of the distance between two trajectories, one may utilize the difference in the spatial densities [180,172],

$$d_{12}(t) = \frac{1}{L} \int_0^L dx |\rho^{(1)}(x, t) - \rho^{(2)}(x, t)| = \frac{1}{N} \sum_{c=1}^N |\rho_c^{(1)}(t) - \rho_c^{(2)}(t)|, \quad (4.4)$$

where N is the number of lattice cells c along the x axis. Then it is possible to define a time-dependent Lyapunov exponent as [180,172],

$$\Lambda(t) = \left(\frac{1}{t} \ln \frac{d_{12}(t)}{d_{12}(0)} \right)_{d_{12}(0) \rightarrow 0}, \quad (4.5)$$

where the two initial densities contain white noise and one must consider the limit where their difference tends to zero (see also Ref. [175]). The Lyapunov exponent thus extracted during the first stage of the dynamics is compared in Fig. 4.3 with the expectation based on the linear response approximation. It can be seen that the Lyapunov exponent coincides with the maximum growth rate, γ_0 , over the entire range of temperatures and densities considered.

This result can readily be understood on the basis of the discussion in Section 4.1.2.2. Indeed, since the regularly amplified evolution will become dominated by the exponential growth of the most unstable modes (those having growth rates near the largest value γ_0), the distance between two given trajectories has then the same time dependence, $d_{12}(t) \sim \exp(\gamma_0 t)$, once $\gamma_0 t \gg 1$, and so the Lyapunov exponent becomes $\Lambda \rightsquigarrow (1/t) \ln \exp(\gamma_0 t) = \gamma_0$. Thus, insofar as the first stage of the

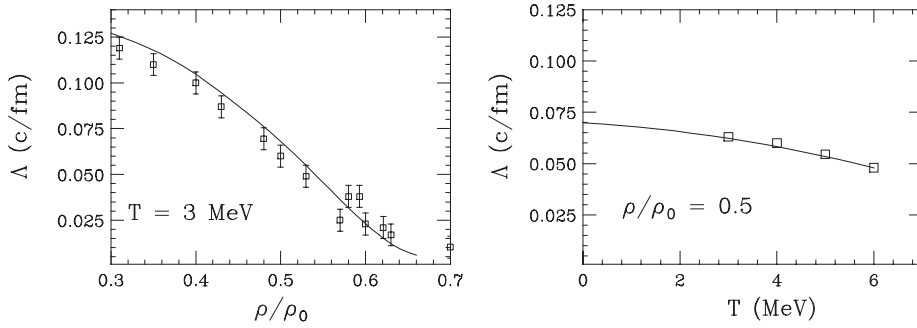


Fig. 4.3. Lyapunov exponents. Lyapunov exponents (squares) extracted with Eq. (4.5), as a function of density ρ (left) and temperature T (right), together with the largest growth rate of the linear response, γ_0 , as obtained from the associated dispersion relation (curves). (From Ref. [180].)

spinodal decomposition is dominated by the regular amplification of the most unstable modes, the associated Lyapunov exponent should equal the largest imaginary RPA frequency.

It is therefore evident, as discussed in Ref. [184], that the Lyapunov exponents cannot be used to signal the presence of chaos. Rather, in order to investigate the post-linear chaotic regime, it is necessary to employ more intricate measures, such as the one discussed in Section 4.1.2.2.

4.1.2.4. Fragment formation and chaos. As discussed above, the early stage of spinodal decomposition is dominated by an almost regular amplification of the most unstable modes and is well described by a linear response analysis. This first stage holds up to rather large density fluctuations of the order of $\delta\rho \approx \frac{1}{2}\rho_0$. Chaos then occurs only subsequently, after the amplification of the most unstable modes has saturated, when the local density has largely moved out of the spinodal region and become close to either the associated liquid density, $\rho_L \approx \rho_s$, or the coexisting gas density $\rho_G \ll \rho_s$. Thus, at this point, the density is very lumpy, as prefragments have already been formed, and it is tempting to associate the onset of chaos with the start of the coalescence stage.

The coalescence process is driven by the preference of the system to reorganize itself into the two coexisting liquid and gas phases. Since this mechanism increases the fragment sizes, the small- k amplitudes are increased and become comparable to those of the most unstable spinodal modes k_0 that initially dominated the evolution. On the other hand, the high- k components, which are not populated much by the spinodal instability, tend to become further depleted by the coalescence.

The above observations imply that even at large times, when disorder is present, the dynamics is not yet fully chaotic, in the sense that a hierarchy is kept between the various modes as a memory of the instabilities present during the early stage of the fragmentation. These findings may have important consequences since they show that if the fragmentation process is fast enough (such as in the case of open expanding systems) the phase space cannot become fully populated in a statistical manner. In particular, spinodal decomposition does not lead to a population of the small-size region of the primary fragment distribution. Furthermore, the fragment-size distribution contains a large-mass tail arising from mode beating, large-wavelength instabilities, and the late-stage coalescence.

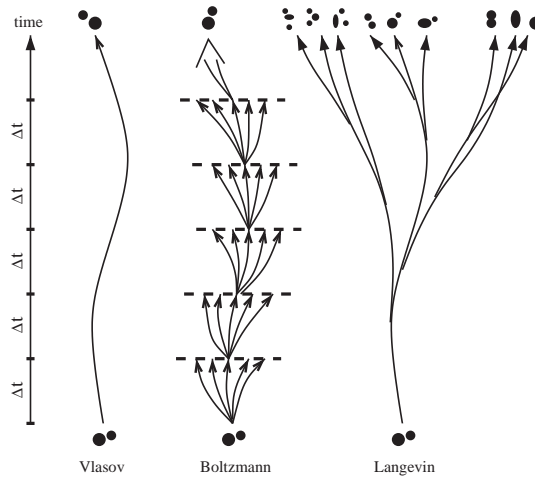


Fig. 4.4. Characterization of dynamical models. The various semi-classical treatments of microscopic nuclear dynamics can be characterized by the manner in which the single-particle phase-space density is being propagated from one time step to the next. In the Vlasov treatment, the particles experience only the self-consistent effective field, leading to a single dynamical history $f(\mathbf{r}, \mathbf{p}, t)$. At the Boltzmann level, the various possible outcomes of the residual collisions are being averaged at each step, leading then to a different but still single dynamical trajectory. Finally, the Boltzmann–Langevin model allows the various stochastic collision outcomes to develop independently, thus leading to a continual trajectory branching and a corresponding ensemble of histories.

4.2. Exploratory dynamical simulations

The recognition of the key role played by instabilities in the dynamics of nuclear fragmentation has led to a variety of model studies and we start this section with a brief discussion of several different microscopic dynamical simulations that illustrate some of the key features of the spinodal fragmentation phenomenon. An early guide to the various microscopic models for intermediate-energy nuclear collisions was presented in Ref. [188]. The various models discussed here are all deterministic in principle and the fluctuations in the outcome arise solely from the use of a sample of different initial conditions or from numerical noise associated with the specific implementation of the deterministic equations. Subsequently, we will discuss how this lack of dynamical fluctuations can be remedied by introducing stochastic approaches. However, as far as the fragment formation is concerned, the investigation of systems with fluctuating initial conditions is of key importance.

In order to elucidate the key characteristics of the various models, let us consider the class of models that describes the nuclear system at the level of the reduced one-body phase-space density, $f(\mathbf{r}, \mathbf{p}, t)$. (There is, in principle, one such entity for each spin–isospin component of each particle specie considered but we ignore this straightforward complexity here.) It is instructive to group the various dynamical treatments according to the level of refinement to which they take account of the residual interactions, as illustrated in Fig. 4.4. Within the semi-classical framework, the equation of motion can be expressed on the following form,

$$\dot{f} \equiv \frac{\partial}{\partial t} f - \{h[f], f\} = K[f] = \bar{K}[f] + \delta K[f], \quad (4.6)$$

where the left side describes the collisionless propagation of the individual particles in their common self-consistent one-body field, while the right side expresses the effect of the residual binary collisions.

At the simplest level, the *Vlasov* treatment, the nucleons feel only the common effective one-body field, described by the self-consistent one-body Hamiltonian $h[f](\mathbf{r}, \mathbf{p})$. The total time derivative then vanishes, $\dot{f} = 0$. The corresponding quantal version of this level of approximation is the time-dependent Hartree–Fock treatment.

The effect of residual interaction among the nucleons (and any other hadronic species considered) is included on the right-hand side as a collision term, $K[f](\mathbf{r}, \mathbf{p})$. This term has a stochastic character. (For example, the distance a particle travels in the medium before colliding is stochastic, as is the resulting scattering angle.) The next level of refinement includes only the *average* part of the collision term, $\bar{K}[f](\mathbf{r}, \mathbf{p})$, along the lines introduced by Boltzmann. Usually, in nuclear systems, the quantum statistics are taken into account by adding suitable Fermi blocking or Bose enhancement factors in the single-particle final states. This refinement was first made for electronic gases by Nordheim [189] and Uehling and Uhlenbeck [190]. It was adapted to uniform gases of nucleons, pions, and Δ resonances about 25 years ago [191] and was subsequently augmented by the mean field [192] to provide a description of collisions between finite nuclei. The resulting *nuclear Boltzmann equation* exists in many implementations that differ with respect to both the physics input (such as the types of constituents included, the form of their effective Hamiltonian, and their differential interaction cross sections) and the numerical methods employed (whether of pseudo-particle or lattice type) and various names have been employed in the literature, including BUU (for Boltzmann–Uehling–Uhlenbeck), VUU (for Vlasov–Uehling–Uhlenbeck), and Landau–Vlasov. It is important to recognize that these models have still a deterministic character, since only the average outcome of each residual collision is being pursued dynamically. Ensembles of final states may be obtained by propagating suitable ensembles of initial configurations.

The highest level of refinement, the nuclear *Boltzmann–Langevin* treatment, includes also the *stochastic* part of the collision term, $\delta K[f](\mathbf{r}, \mathbf{p})$. This leads to a continual splitting of the dynamical trajectories, as all possible outcomes of the residual collisions are being allowed to develop independently, each one with its own self-consistent field. Thus, even a single initial state, as specified by the one-body phase-space density $f(\mathbf{r}, \mathbf{p}, 0)$, leads to an entire ensemble of different dynamical histories.

4.2.1. Mean-field studies of fragmentation

Let us first recall the early work by Knoll et al. [193–195]. In that approach, the system is represented as a statistical ensemble of Slater determinants whose initial ensemble average yields the initial one-body density matrix. Each of these pure states is then propagated by standard self-consistent Hartree–Fock dynamics using a Skyrme-type interaction with proper saturation properties (in fact this exploratory study neglects the antisymmetrization and thus employed simple Hartree product wave functions, being then entirely analogous to the semi-classical Vlasov treatment). As a consequence, the fluctuations inherent in the initial one-body field are propagated self-consistently, thus enabling the system to explore any symmetry-violating instabilities of the type leading to fragmentation.

Although the authors of Refs. [193,195] made no analysis of the specific instabilities, whether spinodal or of another character, their results do illustrate the importance of considering an ensemble of dynamical evolutions when instabilities are present, as initially very similar states may then develop

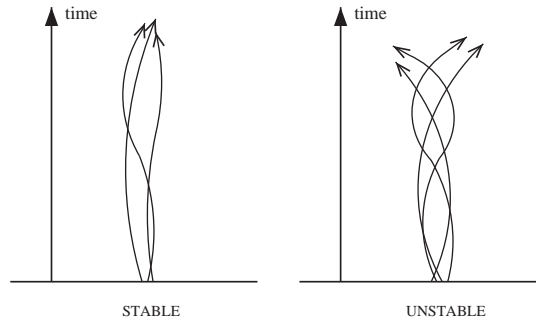


Fig. 4.5. Ensemble propagation. These sketches illustrate the effect of propagating an ensemble of macroscopically similar initial states, each one experiencing an independent self-consistent dynamical evolution. When the system is stable, the trajectories remain closely bundled throughout and the states are macroscopically similar (*left panel*), while instabilities lead to divergences that result in distinct trajectory bundles describing qualitatively different final states (*right panel*).

into qualitatively different final configurations. It should be noted that in this type of approach, the only stochastic element enters when the initial states are selected; from there on, the evolutions are fully deterministic, as each initial state evolves in its own self-consistent one-body field. The approach can be considered as an extension of the familiar finite-temperature TDHF treatment which propagates a single one-body density matrix representing the entire ensemble of trajectories in the single common (ensemble averaged) one-body field and which is therefore expected to be accurate only when the ensemble consists of macroscopically similar configurations.

This latter feature is illustrated in Fig. 4.5, which shows that the trajectories for an ensemble of macroscopically similar initial configurations remain closely bundled when the system is stable and they may thus be well approximated by a single average trajectory, whereas instabilities may split the ensemble into several subensembles that represent macroscopically different channels.

4.2.2. Nuclear Boltzmann dynamics

The nuclear Boltzmann model was used by Batko et al. [150] to study the role of instability growth for fragment formation in expanding nuclear geometries. They considered the development of initially compressed or heated spherical nuclei. On the basis of the nuclear BUU model, it was found that a heavy nucleus initially compressed to 2–3 times normal density expands to a bubble-like quasi-stationary unstable configuration that then has time to coalesce into massive bound fragments. This spontaneous breaking of the spherical symmetry is due to the numerical implementation of the semi-classical transport. Indeed, Batko et al. used the pseudo-particle method which is inherently endowed with numerical noise because of the associated irregular coverage of the phase space. Such noise breaks the macroscopic symmetries and may thus trigger the formation of clusters. It was demonstrated that the character of the outcome depends on the employed number of pseudo-particles per nucleon \mathcal{N} , a purely numerical parameter in the model: The larger the value of \mathcal{N} , the smaller the numerical fluctuations in the density distribution and, consequently, the better the initial spherical symmetry is preserved, thus requiring longer time for the instabilities to grow, ultimately allowing the bulk of the system to recontract without fragmenting (provided that the initial compression is sufficiently modest).

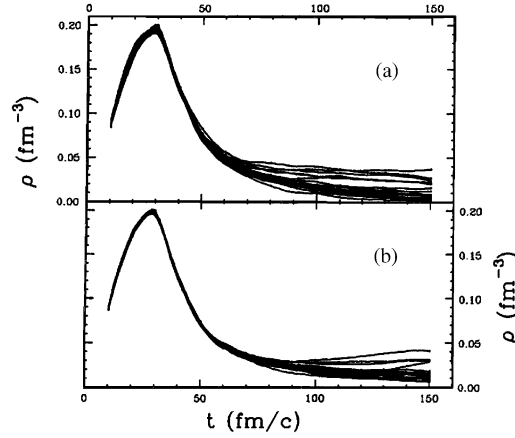


Fig. 4.6. Effect of instabilities on the trajectory bundle. The central density ρ as a function of time for 70 MeV/A Ca + Ca for bundles of dynamical trajectories resulting from different initial placings of \mathcal{N} pseudo-particles per nucleon, with either $\mathcal{N} = 40$ (a) or $\mathcal{N} = 100$ (b). (From Ref. [196].)

That study suggests the existence of a specific nuclear multifragmentation process by which an initially compressed system disassembles into several massive fragments. The characteristic feature is a decomposition leading to an unstable structure whose global evolution is sufficiently slow to allow the instabilities to manifest themselves, resulting in a clusterization of the structure into disjoint prefragments. In this calculation the instabilities are continually triggered by the numerical noise, whereas the symmetry breaking in the treatments discussed in Section 4.2.1 has arisen from the irregularity of the initial configuration.

This novel multifragmentation process displays an intricate interplay between the time scale for the global expansion dynamics and those for the triggering and amplification of the various unstable modes and it was noted that its qualitative identification and quantitative exploration could provide important new experimental information on nuclear dynamics.

The occurrence of instabilities along the dynamical evolution of nuclear reactions and the sensitivity of the final outcome to the number of pseudo-particles employed was subsequently investigated by Colonna et al. [196]. For an ensemble of similarly prepared collision systems, such as 70 MeV/ N $^{40}\text{Ca} + ^{40}\text{Ca}$, the authors of extracted the central nucleon density as a function of time and studied the resulting bundle of curves. As illustrated in Fig. 4.6, at early times the curves are all very similar, but they then rather suddenly start to exhibit a growing divergence. This general behavior is interpreted as follows: early on the systems remain well away from any instabilities and they therefore all have very similar evolutions, while they diverge after entering the region of instability, where clusterization is triggered. The rate of the trajectory divergence (the growth of the bundle width) is related to the growth time of the instabilities present. While it is rather robust against modifications of the numerical implementation, thus confirming that the effect reflects an inherent property of the system, the actual magnitude of the bundle width depends significantly on the number of pseudo-particles used, i.e. on the level of numerical noise. Further studies have elucidated the competition between the expansion of the system and the spinodal growth of the fluctuations [197].

In order to better understand such spinodal multifragmentation and its interplay with the global dynamics, it is important to compare the growth times for the dominant unstable modes with the other relevant time scales. In the linear regime the growth times vary from 30 to 200 fm/c or more, as discussed in the previous section, and in the next section we will compare this time scale with that of the global dynamics of the system. However, it is important to recognize that the growth rates are not the only important quantities, since a given instability will develop only if it is being triggered. So the magnitude and spectral distribution of the irregularities provide the seeds of the spinodal decomposition and are thus important, as we shall see below.

4.3. Boltzmann–Langevin model

An essential shortcoming of the nuclear Boltzmann model is the fact that the propagation of the one-body density is, in principle, entirely deterministic. This lack of stochasticity precludes the spontaneous appearance of fluctuations and thus renders the description inadequate when bifurcations and instabilities are encountered in the dynamics. The principal differences between the various types of dynamical model were illustrated in Fig. 4.4.

The description of nuclear dynamics by means of stochastic models has become a rich and vigorous field which was reviewed several years ago by Abe et al. [198]. In the present review, we seek to include only those contributions that have specific relevance to the developments of the models used to treat spinodal multifragmentation.

An important early advance was made by Bixon and Zwanzig [199] who extended the theory of hydrodynamical fluctuations to non-equilibrium scenarios by deriving a Boltzmann–Langevin equation in which the stochastic behavior of the fluid arises from the fluctuating force incorporated into the standard Boltzmann equation. The characteristics of this force can then be explicitly related to the collision kernel and, furthermore, it was shown that the Boltzmann–Langevin equation yields a correct description near equilibrium, where it reproduces the standard hydrodynamical results for the fluctuations in pressure and heat current (a review is given in Ref. [200]).

The application of this approach to nuclear dynamics was pioneered by Ayik [201] who derived the statistical properties of the residual interaction by the general projection technique of quantum statistics. Subsequently, Ayik and Gregoire [202,203] applied that general scheme to the particular case when the residual interaction is approximated by the Uehling–Uhlenbeck collision term. This approach considers the evolution of the one-body density as a generalized Langevin process akin to the motion of a Brownian particle, with the appropriate dynamical variable being the entire one-body density $f(\mathbf{r}, \mathbf{p})$ in place of the momentum of the Brownian particle.

From the same starting point, Randrup and Remaud [204] derived the equivalent Fokker–Planck transport equation for the distribution of one-body densities, $\phi[f]$, and they presented expressions for the associated transport coefficient functionals. This type of treatment was subsequently developed further by Chomaz et al. [178,179] in connection with the development of a lattice simulation method for the solution of the Boltzmann–Langevin transport equation.

A more formal derivation of the Boltzmann–Langevin equation was undertaken by Reinhard et al. [205] using Green’s function techniques in the real-time path formalism, the key point being to allow the free Green’s function to contain two-body correlations, thus providing a source of stochasticity. This study also presents a careful discussion of time scales and order counting and, in particular, it is shown that the derivation requires the fluctuating part of the residual interaction to be weak and

that the associated collisions must complete before essential changes can occur in the mean field. It may be interesting to note that the Boltzmann–Langevin equation can alternatively be derived from the stochastic time-dependent Hartree–Fock equation of motion by averaging over subensembles with small fluctuations [206,207].

4.3.1. Basic features

As noted above, the Boltzmann–Langevin (BL) equation of motion for the reduced one-body phase-space density can be written on compact form as $\dot{f} = K$, see Eq. (4.6). The left-hand side represents the collisionless propagation of $f(\mathbf{r}, \mathbf{p})$ in its self-consistent mean field described by the effective single-particle hamiltonian $h(\mathbf{r}, \mathbf{p})$; this part of the problem was discussed in Section 3 and need not concern us here. The right-hand side of the Boltzmann–Langevin equation represents the effect of the residual interaction. In the present context it is associated with the two-body collisions between the constituent nucleons. The collision term, $K(\mathbf{r}, \mathbf{p})$, can be decomposed into two parts. The first part, $\bar{K}(\mathbf{r}, \mathbf{p})$, is the familiar collision term entering in the nuclear Boltzmann equation; it represents the average effect of the residual collisions and is thus deterministic in character. The remainder, $\delta K(\mathbf{r}, \mathbf{p})$, is a qualitatively new term which fluctuates in a stochastic manner. In the simple physical scenario where the residual interaction can be considered as binary collisions that are well localized in space and time, the average part is given by the familiar Uehling–Uhlenbeck modification of the Boltzmann collision term [189,190],

$$\bar{K}(\mathbf{r}, \mathbf{p}_1) = g \sum_{234} W(12; 34) [\bar{f}_1 \bar{f}_2 f_3 f_4 - f_1 f_2 \bar{f}_3 \bar{f}_4] , \quad (4.7)$$

where f_i is a short-hand notation for $f(\mathbf{r}, \mathbf{p}_i, t)$ and $\bar{f} \equiv 1 - f$ is the associated Fermi blocking factor. For simplicity, we consider here only spin and isospin saturated systems and the associated spin–isospin degeneracy factor is then $g = 4$. The basic transition rate is simply related to the differential cross section for the corresponding two-body scattering process,

$$W(12; 34) = v_{12} \left(\frac{d\sigma}{d\Omega} \right)_{12 \rightarrow 34} \delta(\mathbf{p}_1 + \mathbf{p}_2 - \mathbf{p}_3 - \mathbf{p}_4) , \quad (4.8)$$

with $v_{12} \equiv |\mathbf{v}_1 - \mathbf{v}_2|$, and it thus has corresponding symmetry properties,

$$W(12; 34) = W(21; 34) = W(34; 12) . \quad (4.9)$$

Since it arises from the same elementary two-body processes, the stochastic part of the collision term is fully determined by the basic transition rate as well, a manifestation of the fluctuation–dissipation theorem. With the collisions assumed to be local in space and time, the correlation function for the fluctuating part of the collision term is of the following form,

$$\prec \delta K(\mathbf{r}, \mathbf{p}, t) \delta K(\mathbf{r}', \mathbf{p}', t') \succ = C(\mathbf{p}, \mathbf{p}', \mathbf{r}, t) \delta(\mathbf{r} - \mathbf{r}') \delta(t - t') , \quad (4.10)$$

where $\prec \cdot \succ$ denotes the average with respect to the ensemble of possible trajectories resulting from the current one-body density f . Furthermore, for elastic scattering, the correlation kernel is given

by [202]

$$C(\mathbf{p}_a, \mathbf{p}_b, \mathbf{r}, t) = \delta_{ab} \sum_{234} W(a2; 34) F(a2; 34) + \sum_{34} [W(ab; 34) F(ab; 34) - 2W(a3; b4) F(a3; b4)] , \quad (4.11)$$

with the short-hand notations $\delta_{ab} \equiv h^3 \delta(\mathbf{p}_a - \mathbf{p}_b)$ and $F(12; 34) \equiv f_1 f_2 \bar{f}_3 \bar{f}_4 + \bar{f}_1 \bar{f}_2 f_3 f_4$. The symmetry properties (4.9) of the transition rate ensure that the following sum rules hold,

$$\sum_1 C(\mathbf{p}_1, \mathbf{p}_2, \mathbf{r}, t) \mathbf{p}_1 = \sum_2 C(\mathbf{p}_1, \mathbf{p}_2, \mathbf{r}, t) \mathbf{p}_1 = 0 , \quad (4.12)$$

$$\sum_1 C(\mathbf{p}_1, \mathbf{p}_2, \mathbf{r}, t) \mathbf{p}_1 = \sum_2 C(\mathbf{p}_1, \mathbf{p}_2, \mathbf{r}, t) \mathbf{p}_2 = \mathbf{0} , \quad (4.13)$$

$$\sum_1 C(\mathbf{p}_1, \mathbf{p}_2, \mathbf{r}, t) \epsilon_1 = \sum_2 C(\mathbf{p}_1, \mathbf{p}_2, \mathbf{r}, t) \epsilon_2 = 0 , \quad (4.14)$$

where $\epsilon_i = p_i^2/2m$ is the kinetic energy for a specified momentum. These sum rules express the fact that each of the elementary binary collisions conserves particle number, momentum, and energy, respectively.

4.3.2. Linearization of collective stochastic dynamics

The study of the small-amplitude response in stochastic one-body theories can yield considerable insight into the dynamics of the collective modes. The present discussion is based on the original treatment given in Ref. [112] and the subsequent further analysis in Ref. [208].

We thus wish to study the evolution of small amplitude deviations from the average phase-space trajectory, $f(\mathbf{s}, t) = f_0(\mathbf{s}, t) + \delta f(\mathbf{s}, t)$, where \mathbf{s} denotes the phase-space point (\mathbf{r}, \mathbf{p}) for D spatial dimensions, with $d\mathbf{s} = h^{-D} d^D \mathbf{r} d^D \mathbf{p}$ being the associated dimensionless volume element. The reference density $f_0(\mathbf{s})$ satisfies the non-fluctuating Boltzmann equation, $\partial f_0 / \partial t = \{h[f_0], f_0\} + \bar{K}[f_0]$. To leading order, the deviation $\delta f(\mathbf{s})$ then follows the linearized equation of motion,

$$\frac{\partial}{\partial t} \delta f = -i\mathcal{M}[f_0] \delta f + \delta K[f_0] , \quad (4.15)$$

where $\delta K[f_0]$ represents the fluctuating part of the collision term and where the extended RPA matrix \mathcal{M} is defined by $-i\mathcal{M}[f_0] \delta f = \{h[f_0], \delta f\} + \{h[\delta f], f_0\} + \bar{K}[\delta f]$. Any general disturbance can be expanded on the eigenvectors f_v of the associated RPA matrix operator,

$$\delta f(\mathbf{s}, t) = \sum_v A_v(t) f_v(\mathbf{s}) . \quad (4.16)$$

Here $f_v(\mathbf{s})$ solves the equation $\mathcal{M} f_v = \omega_v f_v$, where the frequency ω_v is in general complex, $\omega_v = E_v - i\Gamma_v$. When the mode is stable, Γ_v is positive and represents the damping width due to the action of the collision term. Conversely, when the mean-field treatment renders the mode unstable, its frequency is purely imaginary.

Substitution of expansion (4.16) into the linearized equation (4.15) yields the following solution for the amplitude A_v ,

$$A_v(t) = e^{-i\omega_v t} \left(A_v(0) + \int_0^t dt' B_v(t') e^{i\omega_v t'} \right), \quad (4.17)$$

where $A_v(0)$ is the initial amplitude of the disturbance,

$$A_v(0) = \sum_{\mu} O_{v\mu} \langle f_{\mu}; \delta f(0) \rangle, \quad (4.18)$$

with $\langle g; h \rangle \equiv \int ds g(s)^* h(s)$ being the scalar product in the one-body density Liouville space. In Eq. (4.17), the noise term B_v is the projection of the fluctuating term $\delta K(s, t)$ onto the particular eigenmode,

$$B_v(t) = \sum_{\mu} O_{v\mu} \langle f_{\mu}; \delta K(t) \rangle, \quad (4.19)$$

with O being the inverse of the overlap matrix, $(O^{-1})_{v\mu} = \langle f_v; f_{\mu} \rangle$. Since the fluctuations are (assumed to be) Markovian, the noise correlation is local,

$$\prec B_v(t) B_{\mu}(t')^* \succ = 2\mathcal{D}_{v\mu} \delta(t - t'), \quad (4.20)$$

where the diffusion coefficient in the eigenmode representation is

$$\mathcal{D}_{v\mu} = \sum_{v'\mu'} O_{vv'} \Delta_{v'\mu'} O_{\mu'\mu}, \quad (4.21)$$

with $\Delta_{v\mu}$ being its matrix elements with respect to the eigenmodes,

$$\begin{aligned} \Delta_{v\mu} &= \langle f_v; Df_{\mu} \rangle = \int ds \int ds' f_v(s)^* D(s; s') f_{\mu}(s') \\ &= \frac{1}{2} \int dv_{12;34} \{ f_v(1)^* [f_{\mu}(1) + f_{\mu}(2) - 2f_{\mu}(1')] \\ &\quad + f_v(1')^* [f_{\mu}(1') + f_{\mu}(2') - 2f_{\mu}(1)] \}. \end{aligned} \quad (4.22)$$

In the last relation, $\Delta_{v\mu}$ has been expressed directly in terms of the basic two-body collision processes. Note that in equilibrium the two terms in the integrand are equal, since detailed balance ensures that then $dv_{12;34} = dv_{34;12}$.

With the above quantities defined, it is now possible to express the general temporal correlation function for the amplitudes of the disturbance,

$$\begin{aligned} \sigma_{v\mu}(t_1, t_2) &\equiv \prec A_v(t_1) A_{\mu}(t_2) \succ \\ &= e^{-i\omega_v t_1 + i\omega_{\mu}^* t_2} \left(\sigma_{v\mu}(0, 0) + \int_0^{t_{<}} dt 2\mathcal{D}_{v\mu}(t) e^{i(\omega_v - \omega_{\mu}^*)t} \right), \end{aligned} \quad (4.23)$$

where the upper limit is the earliest of the two specified times, $t_{<} = \min(t_1, t_2)$.

When one of the time arguments vanishes, $\sigma_{v\mu}(t, 0) = \exp(-i\omega_v t) \sigma_{v\mu}(0, 0)$, the information carried concerns the eigenfrequencies only. In particular, the correlation function for $f(s)$ can be

expressed as

$$\begin{aligned}\sigma_f(t) &\equiv \sigma(s, s', t) = \prec f_v(s, t) f_\mu(s', t) \succ \\ &= \sum_{v\mu} f_v(s, t) \sigma_{v\mu}(t, 0) f_\mu(s', t) = \sum_{v\mu} e^{-iE_v t/\hbar - \Gamma_v t/\hbar} f_v(s) \sigma_{v\mu}(0, 0) f_\mu(s') .\end{aligned}\quad (4.24)$$

Thus, for stable systems σ_f attenuates in time due to the collisional damping of the modes, while for unstable systems σ_f will soon become dominated by the exponential growth of the unstable modes. The expression also displays the Landau damping (which is due to the beating of close frequencies) and, if the collisional damping is sufficiently small, the Poincaré recurrence phenomenon.

Of special interest is the equal-time correlation function, $\sigma_{v\mu}(t) \equiv \sigma_{v\mu}(t, t)$, which satisfies a simple feedback equation of motion (the *Lalime* equation [112]),

$$\frac{d}{dt} \sigma_{v\mu} = -i\omega_{v\mu} \sigma_{v\mu} + 2\mathcal{D}_{v\mu} , \quad (4.25)$$

with $\omega_{v\mu} \equiv \omega_v - \omega_\mu^*$. Thus, when the noise term $\mathcal{D}_{v\mu}$ is constant in time, we have

$$\sigma_{v\mu}(t) = -i \frac{2\mathcal{D}_{v\mu}}{\omega_{v\mu}} (1 - e^{-i\omega_{v\mu} t}) + \sigma_{v\mu}(0) e^{-i\omega_{v\mu} t} . \quad (4.26)$$

The diagonal fluctuations (the variances) then evolve as follows (with $D_v^{\text{var}} \equiv D_{vv}$),

$$\sigma_{vv}(t) = \begin{cases} \mathcal{D}_v^{\text{var}} t_v (1 - e^{-2t/t_v}) + \sigma_{vv}(0) e^{-2t/t_v} \rightarrow 2\mathcal{D}_v^{\text{var}} t_v, \\ \mathcal{D}_v^{\text{var}} t_v (e^{2t/t_v} - 1) + \sigma_{vv}(0) e^{2t/t_v} \rightarrow (2\mathcal{D}_v^{\text{var}} t_v + \sigma_{vv}(0)) e^{2t/t_v} \end{cases} \quad (4.27)$$

for stable ($\Gamma_v > 0$) and unstable ($\Gamma_v < 0$) modes, respectively, and their behavior is characterized by the time constant $t_v = \hbar/|\Gamma_v|$. In the former case, the equilibrium variance equals the amount of fluctuation generated by the source over a time interval equal to the relaxation time t_v (and it thus independent of the initial situation, as it should be). In the latter case, the asymptotic behavior amounts to an exponential amplification of the initial fluctuations *plus* the amount of fluctuation generated by the source over a time interval equal to the growth time t_v .

While the above developments are quite general, we now focus on unstable matter prepared with a phase-space density that is uniform in position and rotationally invariant in momentum. The reference system described by f_0 is then stationary in time and uniform in space and, accordingly, the eigenmodes are of plane-wave form, $f_k^v(\mathbf{r}, \mathbf{p}) = f_k^v(\mathbf{p}) \exp(i\mathbf{k} \cdot \mathbf{r})$, so we need consider only one wave number \mathbf{k} at a time.

Although the eigenfunctions $\{f_k^v(\mathbf{p})\}$ form a complete set in momentum space, they are *not* mutually orthogonal and it is useful to introduce the matrix $o_k^{v\mu}$ as the inverse of their overlap matrix,

$$(o_k^{-1})^{v\mu} = \langle f_k^v; f_k^\mu \rangle = \int d\mathbf{p} f_k^v(\mathbf{p})^* f_k^\mu(\mathbf{p}) . \quad (4.28)$$

It depends only on the magnitude $k=|\mathbf{k}|$ due to the rotational invariance. The amplitudes in expansion (4.16) of the disturbance $f_k(\mathbf{r}, \mathbf{p})$ are then given by

$$A_k^v(t) = \sum_\mu o_k^{v\mu} \langle f_k^\mu; f_k(t) \rangle = \langle q_k^\mu; f_k(t) \rangle , \quad (4.29)$$

where the functions $\{q_k^v(\mathbf{p})\}$ constitute the dual basis, $\langle q_k^v; f_k^\mu \rangle = \delta_{v\mu}$. (They are given explicitly as $q_k^v(\mathbf{p}) = Q_k^v(\mathbf{p}) / \langle Q_k^v; f_k^\mu \rangle$, where $Q_k^v(\mathbf{p}) = 1/(\mathbf{k} \cdot \mathbf{v} - \omega_v^*)$.) Furthermore, the noise term (4.21) is simply the projection of the basic diffusion coefficient onto the dual basis,

$$\mathcal{D}_k^{v\mu} = \langle q_k^v; Dq_k^\mu \rangle = \sum_{v'\mu'} o_k^{vv'} \langle f_k^{v'}; Df_k^{\mu'} \rangle o_k^{\mu'\mu} . \quad (4.30)$$

When the system is situated within the spinodal boundary associated with the magnitude k of the considered wave number, it has two modes with imaginary frequency, $\omega = \pm i/t_k$, exhibiting exponential growth and decay, respectively. Since the amplified mode grows dominant at times exceeding t_k , it may suffice to retain only the two collective modes in the treatment. This approximation (which was made in the original analysis [112]) amounts to replacing the full matrix $o^{v\mu}$ by the 2×2 matrix $\tilde{o}^{v\mu}$ involving only the two collective modes, $f_k^\pm(\mathbf{p})$. This approximation receives some support from the linear-response analysis made by Božek [119] (see Section 3.1.4) which revealed that there are two distinct contributions, one coming from the zeroes of the susceptibility, i.e. from the collective states, and a second related to the singularity of the susceptibility, i.e. the non-collective states. The fact that the former is dominant at large t supports suggests that it may suffice to retain only the collective modes. When this approximation is adopted, the expansion of the disturbance with the wave number \mathbf{k} contains then only the two collective terms,

$$f_k(\mathbf{p}, t) = A_k^+(t) f_k^+(\mathbf{p}) + A_k^-(t) f_k^-(\mathbf{p}) . \quad (4.31)$$

and the correlations between the amplitudes, $\sigma_k^{\kappa\kappa'}(t) \equiv \prec A_k^\kappa(t) A_k^{\kappa'}(t) \succ$, evolve as follows,

$$\frac{d}{dt} \sigma_k^{++} = 2\mathcal{D}_k^{++} + \frac{2}{t_k} \sigma_k^{++}; \quad \sigma_k^{++}(t) = \mathcal{D}_k^{++} t_k (e^{2t/t_k} - 1) , \quad (4.32)$$

$$\frac{d}{dt} \sigma_k^{+-} = 2\mathcal{D}_k^{+-}; \quad \sigma_k^{+-}(t) = 2\mathcal{D}_k^{+-} t , \quad (4.33)$$

$$\frac{d}{dt} \sigma_k^{--} = 2\mathcal{D}_k^{--} - \frac{2}{t_k} \sigma_k^{++}; \quad \sigma_k^{--}(t) = \mathcal{D}_k^{--} t_k (1 - e^{-2t/t_k}) , \quad (4.34)$$

where it should be noted that $\mathcal{D}_k^{++} = \mathcal{D}_k^{--}$ and $\mathcal{D}_k^{+-} = \mathcal{D}_k^{-+}$.

A comparison of the approximate treatment, which includes only the collective modes, with the result of performing a full projection onto the dual basis, Eq. (4.30), was carried out in Ref. [208] on the basis of a realistic interaction [35]. The result for the most important source term, \mathcal{D}_k^{++} , is shown in Fig. 4.7. As it turns out, the two treatments yield very similar results, except for an overall larger magnitude of the full treatment. For the most rapidly amplified mode, having a wave length of $\lambda_0 \approx 8$ fm, the approximate source term is about 30% below the exact result.

In order to compare the two methods with regard to their predictions for the density fluctuations, we consider the Fourier component of the density variance,

$$\begin{aligned} \sigma_k(t) &\equiv \prec |\rho_k|^2 \succ = \int d^3 r_{12} e^{-i\mathbf{k} \cdot \mathbf{r}_{12}} \prec \delta\rho(\mathbf{r}_1) \delta\rho(\mathbf{r}_2) \succ \\ &\approx \sigma_k^{++}(t) + \sigma_k^{--}(t) + 2\sigma_k^{+-}(t) = 2\mathcal{D}_k^{++} t_k \sinh \frac{2t}{t_k} + 4\mathcal{D}_k^{+-} t , \end{aligned} \quad (4.35)$$

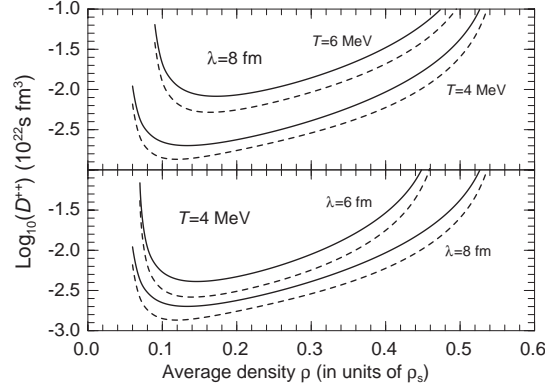


Fig. 4.7. Comparison of source terms. The noise term \mathcal{D}_k^{++} for the amplified collective mode having a wave length $\lambda 2\pi/k$, in nuclear matter prepared with a uniform density ρ and with a specified temperature T , using either the complete dual basis (solid) or its collective truncation (dashed). The calculations have been done with the approximate formulas developed in Ref. [117]. The lower panel considers the typical temperature $T = 4$ MeV and illustrates the dependence on the wave length λ , while the upper panel keeps the wave length fixed at $\lambda = 2\pi/k = 8$ fm, near which the most rapid amplification occurs, and illustrates the temperature dependence.

where only the two collective modes have been considered and it has been used that $\mathcal{D}_k^{++} = \mathcal{D}_k^-$ and $\mathcal{D}_k^{+-} = \mathcal{D}_k^{-+}$.

At the spinodal boundary, where the collective frequency tends to zero, the two collective modes become identical. Within the approximate projection method, both \mathcal{D}_k^{++} and \mathcal{D}_k^{+-} then diverge, but, as it happens, $\mathcal{D}_k^{++} + \mathcal{D}_k^{+-} \approx t_k^{-1}$ as $t_k \rightarrow \infty$. So the resulting density variance σ_k tends to zero at the boundary, which is physically reasonable. By contrast, with the exact projection method the mixed source term remains regular as the boundary is approached and so it cannot cancel the divergence of the diagonal term. The density variance then diverges at the boundary where $t_k \rightarrow \infty$, a physically unreasonable result. (The failure of the exact projection near the spinodal boundary results from the fact that it is expected to be accurate only at late times, $t \gg t_k$, but this situation is never reached at the boundary where $t_k \rightarrow \infty$.) It would obviously be of interest to cure this problem, so that the exact projection method would be reliable also near the spinodal boundary and, in general, in all cases where t_k diverges.

The results obtained for σ_k with the two methods are compared in Fig. 4.8. It may be noted that σ_k is a rather flat function of k at the very early times, $t < t_{k_0}$, before the amplification of the instabilities has manifested itself. This feature reflects the fact that the modes are being agitated almost equally by the Langevin fluctuation term δK , which thus has the character of white noise. At later times, $t > t_{k_0}$, this democratic behavior is changing, as those modes that have the shortest amplification time grow progressively dominant, making σ_k ever more narrowly peaked around k_0 .

4.3.3. Lattice simulations of Boltzmann–Langevin dynamics

The dynamical evolution of unstable nuclear matter has been elucidated by lattice simulations of the Boltzmann–Langevin dynamics [162,181]. In this method the stochastic part of the collision number is simulated directly on a lattice in phase space. The mean-field evolution is treated by a standard matrix technique. So far calculations have been made only in two dimensions due to the

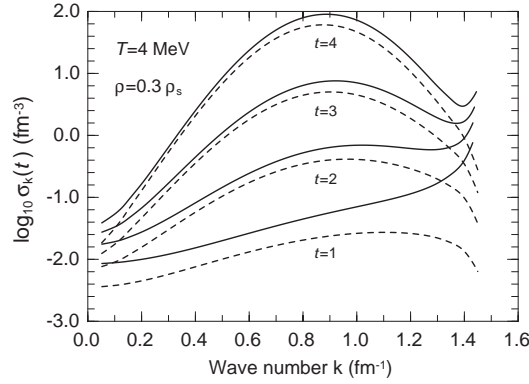


Fig. 4.8. Dependence of density fluctuations on wave number. The variance of the density fluctuations associated with the collective modes, σ_k , after a given time $t = 1, 2, 3, 4 \times 10^{-22}$ s has elapsed, as a function of the wave number $k = 2\pi/\lambda$, for the density $\rho = 0.3\rho_s$ at the temperature $T = 4$ MeV, using either the complete dual basis (solid) or its collective truncation (dashed), as in Fig. 4.7. (From Ref. [208].)

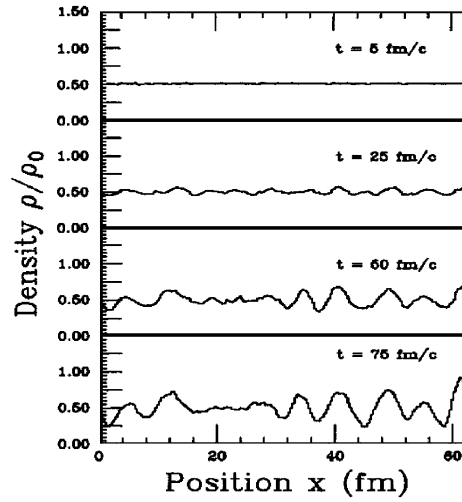


Fig. 4.9. Evolution of the density profile in a box. An initially uniform 2D system at half the saturation density, $\rho = \frac{1}{2}\rho_s$, and with a temperature of $T = 3$ MeV, is evolved with the Boltzmann–Langevin lattice method (see text) and examined at four subsequent times t . *Left panel*: The density profile associated with one particular dynamical history. *Right panel*: The variance σ_k as a function of the mode number $K = kL/2\pi$, extracted from an ensemble of histories. (Adapted from Ref. [176].)

heavy numerical effort required. We summarize here the studies reported in Ref. [162], in which the system is confined within a square, with periodic boundary conditions imposed. Furthermore, in order to simplify the analysis, the fluctuations along the y direction are averaged out so that only the evolution along the x direction is interesting.

Fig. 4.9 (*left*) shows the time evolution of the spatial density for a system initialized at half the saturation density, $\rho = \frac{1}{2}\rho_s$, with a temperature of $T = 3$ MeV. The various stages from the

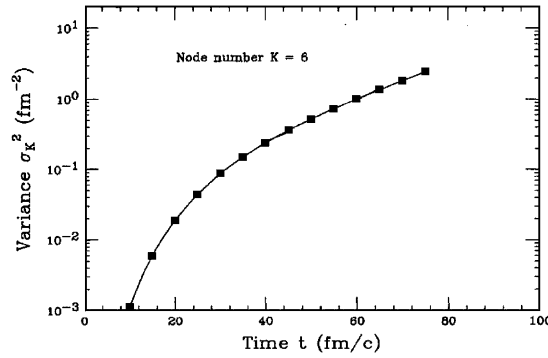


Fig. 4.10. Growth of the most unstable mode. The time evolution of the most unstable mode, k_0 , as given by $\sigma_{k_0}(t)$, the Fourier component of the spatial correlation function, as a function of the time elapsed since starting from a uniform system having $\rho = \frac{1}{2}\rho_s$ and $T = 3$ MeV. (Adapted from Ref. [176].)

uniform density towards clusterization are reflected in the snapshots shown in the figure: Since the collision term only produces rearrangements in the local momentum distribution and ρ therefore remains rather uniform early on (first frame). The initial uniformity of the spatial density is then destroyed as these rearrangements are being propagated; the resulting density fluctuations have an irregular appearance, in reflection of the random nature of the momentum rearrangements (second frame). The subsequent self-consistent response by the effective field then starts the amplification process and the magnitude of the density undulations grow, with the most favored wave lengths gaining prominence (third frame). The system then acquires a clusterized appearance, in which the size distribution of the prefragments is not statistical but rather reflects the most rapidly growing modes (fourth frame). (Because of the fixed size of the box, the further development towards multifragmentation is hindered and the density fluctuations will ultimately reflect the corresponding statistical equilibrium.)

As noted in Eq. (4.35), the strength distribution of the density fluctuations, $\sigma_k(t)$, is simply related to the Fourier components of the spatial density and it can thus be readily extracted from a (suitably large) sample of histories. The result is shown in Fig. 4.9 (right). (The higher harmonics seen at the earliest time, when the undulations are very small, result from the finite lattice employed and are numerically unimportant.) It can be seen that the dynamical evolution leads to a predominance of the most unstable modes, causing $\sigma_k(t)$ to have a peaked character. It is an important result of the study in Ref. [176] that an alternative treatment based on the pseudo-particle treatment leads to a very similar result for $\sigma_k(t)$, thus ensuring that the observed features are not artifacts of the particular numerical method.

Further insight into the features of the behavior of the system can be gained by considering the time evolution of the fastest growing mode, $\sigma_{k_0}(t)$, displayed in Fig. 4.10. we expect that the evolution of this quantity should be approximately described by Eq. (4.35), obtained by a linear-response treatment. Thus, at asymptotic times, $t \gg t_0$, we expect that $\sigma_k(t) \approx \mathcal{D}_k^{++} t_0 \exp(2t/t_0)$ and we may then extract the key quantities \mathcal{D}_k^{++} and t_0 from the behavior: On a logarithmic plot, the slope of a linear fit is $2/t_0$ and its value at $t = 0$ is $\ln(\mathcal{D}_k^{++} t_0)$. This procedure yields values in very good agreement with those obtained from the exact projection method for \mathcal{D}_k^{++} and the dispersion relation

for t_k . So one may conclude that the early fragmentation dynamics is dominated by the growth of few important unstable modes, whose characteristics (amplitude and growth time) agree with those derived by a linear response analysis. This feature completes the discussion in Section 4.1, as it confirms the persistence of the regular behavior up to large amplitudes and the associated lateness of the entry into the non-linear (and possibly chaotic) regime.

4.3.4. Refinements

In order to bring out the key features, the above discussion has been carried out within the simplest framework, in which the system is described in terms of a semi-classical phase-space density subject to a collision kernel that is local in space and time. Numerous studies of more refined treatments have been carried out, as will now be briefly summarized.

4.3.4.1. Memory and quantum effects. In the one-body transport treatment discussed so far, the collision term is assumed to be local in both space and time, in accordance with Boltzmann's original treatment. This simplification is usually justified by the fact that the interaction range, as measured by the residual scattering cross section $\sigma_{NN} \approx 4 \text{ fm}^2$, is relatively small on the scale of a typical nuclear system, and the duration of a two-body collision is short on the time scale characteristic of the macroscopic evolution of the system. The resulting collective motion has then a classical character, as is the case also in TDHF. However, when the system possesses fast collective modes whose characteristic energies are not small in comparison with the temperature, quantum effects are important and the treatment needs to be appropriately improved.

Quantum effects on the stochastic dynamics in nuclear matter were considered by Kiderlen and Hofmann [111] within Landau theory. Using the quantal fluctuation–dissipation theorem, suitably generalized to unstable modes, they deduced the properties of the stochastic force and found sizable quantum effects both inside and outside the spinodal regime. Further work on the nuclear fluctuation dynamics has been carried out by Kiderlen [209].

When the collision term has a non-Markovian form, then the evolution of the single-particle density matrix depends on the (recent) past. This problem was addressed by Ayik [210] who derived a transport equation for the single-particle phase-space density by performing a statistical averaging of the Boltzmann–Langevin equation. In analogy with Brownian motion, the fluctuating part of the collision term gives rise to a memory time in the collision kernel which, in turn, leads to a dissipative coupling between collective modes and single-particle degrees of freedom. This approach was adapted by Ayik and Randrup [211] to nuclear matter inside the spinodal zone, as is briefly recalled in Appendix B.4.

The key result is that the usual source terms $\mathring{D}_k^{vv'}$ responsible for the agitation of the unstable collective modes in nuclear matter may be replaced by effective coefficients of the form $\mathcal{D}_k^{vv'}(t) = \mathring{D}_k^{vv'} \chi_k^{vv'}(t)$. The *Lalime* equation (4.25) governing the collective correlation coefficients is then modified accordingly,

$$\frac{d}{dt} \sigma_k^{vv'}(t) = 2\mathring{D}_k^{vv'} \chi_k^{vv'}(t) + \frac{v + v'}{t_k} \sigma_k^{vv'}(t) . \quad (4.36)$$

It follows that the solutions can be expressed on a simple form,

$$\sigma_k^{vv'}(t) = \overset{\circ}{\sigma}_k^{vv'}(t) \bar{\chi}_k^{vv'}(t), \quad (4.37)$$

where $\overset{\circ}{\sigma}_k^{vv'}(t)$ is the solution for the Markovian case. The memory effect is thus expressed by means of the renormalization coefficients $\bar{\chi}_k^{vv'}(t)$ which in turn can be obtained as suitable time averages of the collective correlation functions (see Appendix B.4). These correction factors ultimately attain constant values and the evolution is then similar to what the standard treatment would give, except for the time-independent renormalization of the source terms. But this limiting simplicity emerges only relatively slowly, particularly for the mixed factor, as is evident from Fig. B.7.

Although the analysis in Ref. [211] was carried out for the idealized scenario of initially uniform nuclear matter, the conclusions are expected to hold for more complicated dynamical scenarios, such as may be encountered in nuclear collisions. Since the correction factors can deviate significantly from unity, particularly in the domain where the fastest growth occurs, it appears necessary to refine the treatment to take account of the memory time in an appropriate manner, if quantitatively reliable results are to be obtained from numerical simulations based on the Boltzmann–Langevin model, especially when instabilities are present.

4.3.4.2. Collective quantum fluctuations. The development of density fluctuations associated with collective modes in the presence of expansion was studied by Wen et al. [212] by means of classical and quantal transport equations. Considering a quadrupole giant resonance or an low-lying octupole vibration, the authors study the dynamical symmetry breaking as the global expansion drives the mode from its usual stable state towards instability. The time evolution of the collective variable Q is then determined by either classical Langevin dynamics or a quantal transport model containing initial quantal fluctuations.

It is found that the final fluctuations of Q arise primarily from the amplification of the initial fluctuations during the unstable stage. Since the growth rates are the same in the two treatments, the quantum treatment yields larger final fluctuations due to the contribution from the initial quantum fluctuations which add to the (common) statistical fluctuations. This feature is particularly important at low temperatures where the quantum fluctuations may exceed the statistical fluctuations. In this situation, their inclusion in the treatment will enhance the symmetry breaking.

These results suggest that, as a first approximation, it may be possible to mimic the quantum fluctuations in a classical approach by a suitably tuned artificial increase of the initial temperature, as it is well known in the purely harmonic case. Clearly, though, there is a need for developing a quantum Langevin treatment that quantizes the collective motion. Such an approach would go beyond the Stochastic TDHF framework which does not quantize the collective degrees of freedom.

4.3.4.3. Relativistic treatment. Nuclear spinodal fragmentation occurs at energies that are sufficiently low to permit the use of non-relativistic kinematics and, moreover, to justify the neglect of mesonic degrees of freedom. For applications of the Boltzmann–Langevin model to nuclear collisions at higher energies, it is of interest to recast the treatment in a proper relativistic form. This undertaking is briefly reviewed in Appendix B.5.

4.4. Approximate Boltzmann–Langevin dynamics

The numerical implementation of the exact Boltzmann–Langevin dynamics has been feasible only in 2D, so the introduction of approximate treatments is essential to deal with realistic 3D problems. However, typically, such attempts introduce the fluctuations by fiat in a manner that is inconsistent with the general relaxation properties of the one-body density, as expressed through the fluctuation–dissipation theorem. We discuss here in turn those various approaches.

An attempt to introduce spontaneous fluctuations in a practically realizable manner was made by Bauer et al. [213]. Their method can be implemented relatively easily into standard BUU codes that use the pseudo-particle method of solution and it consists essentially in forcing similar two-body collisions to occur for neighboring pseudo-particles so that effectively two entire nucleons are involved in each particular collision event. Employing an idealized two-dimensional nucleon gas as a test case, Chapelle et al. [214] examined this intuitively appealing method. They found that it is able to produce fluctuations of the correct general magnitude, provided that a suitable coarse graining of the phase space is performed, and that these display some of the correlation features expected from the basic characteristics of the two-body collision process. These features can be improved by suitable tuning of the phase-space metric (the concept of a distance in phase space is required for the selection of the “neighboring” pseudo-particles). However, for any tuning, the detailed momentum dependence of the variance in phase space occupancy deviates significantly from what is dictated by quantum statistics. Therefore this simple prescription may be unsuitable for problems in which these properties are important.

On a more formal basis, Ayik and Gregoire [215] proposed an approximate method for numerical implementation of the Boltzmann–Langevin theory. The method reduces the Boltzmann–Langevin equation for the microscopic one-body phase-space density $f(\mathbf{r}, \mathbf{p})$ to stochastic equations for a set of macroscopic variables, namely the local or global quadrupole moment of the momentum distribution. A random change of the quadrupole moment is then made at each time step and a suitable stretching of $f(\mathbf{r}, \mathbf{p})$ is performed subsequently in order to reconstruct the entire phase-space density. This method was also examined by in Ref. [214] and, although several variations of the proposed scheme were examined, it was generally found that the results were far from satisfactory, since the resulting correlations associated with the fluctuating one-body density will tend to reflect the symmetries and other characteristics of the employed reconstruction procedure rather than those of the underlying physical fluctuations. Therefore this method appears unsuitable for calculating quantities that depend sensitively on the details of the momentum distribution.

For the purpose of addressing catastrophic phenomena in nuclear dynamics, such as multifragmentation, Colonna et al. [176] explored the possibility of simulating the stochastic part of the collision integral in the Boltzmann–Langevin model by the numerical noise $\sigma_k(0)$ associated with the finite number of pseudo-particles \mathcal{N} employed in the ordinary BUU treatment. This idea is based on the observation that for large times, $t \gg t_k$, the fluctuation of density undulations of a given wave number k is given by $\sigma_k^2(t) = D_k t_k e^{2t/t_v}$ in the Boltzmann–Langevin treatment, whereas it is $\sigma_k^2(t) = (D_k t_k / \mathcal{N} + \sigma_k(0)) e^{2t/t_v}$ in the BUU pseudo-particle treatment. Since $\sigma_k(0)$ also scales as $1/\mathcal{N}$, the matching of those two asymptotic fluctuations yields a relation determining the value of \mathcal{N} . For idealized two-dimensional matter, which presents a suitable test case, as it is here

practical to simulate the Boltzmann–Langevin equation directly, they demonstrated that \mathcal{N} can be adjusted so that the corresponding BUU calculation yields a good reproduction of the spontaneous clusterization occurring inside the spinodal region. This approximate method may therefore provide a relatively easy way to introduce meaningful fluctuations in simulations of unstable nuclear dynamics. This method was subsequently extended to 3D nuclear matter, allowing the direct extraction of the growth times t_k of the unstable modes and the associated diffusion coefficients D_k [113].

Guarnera et al. [145] studied the spinodal fragmentation of a hot and dilute nucleus by first expanding the system into a spinodally unstable configuration and then adding a stochastic density fluctuation that is carefully tuned to reflect the degree of fluctuation in the most unstable mode, as determined by the corresponding linear-response analysis of the unstable sphere. They found that the early clusterization appears to be dominated by unstable modes whose spatial structure is similar to the fastest growing spinodal modes in infinite matter at similar density and temperature. They followed the development of the instabilities until multifragmentation had occurred and then made an analysis of the resulting fragment size distribution. As expected from the fact that only a few modes dominate, the clusterization pattern has a large degree of regularity which in turn favors breakup into nearly fragments of nearly equal size, with a corresponding paucity of small clusters.

Subsequently, Colonna et al. [216] introduced a method that roughly approximates the Boltzmann–Langevin model by adding a suitable noise to the collision term in the usual BUU treatment. The noise employed corresponds to the thermal fluctuation in the local phase-space occupancy, $\sigma_f^2(\mathbf{r}, \mathbf{p}) = f(1 - f)$, where $f(\mathbf{r}, \mathbf{p})$ is the local Fermi–Dirac equilibrium distribution. By performing such a local momentum redistribution at suitable intervals in the course of the evolution, the inherently stochastic nature of the two-body collision processes is mimicked. The method has the advantage that it is readily tractable and it applies equally well to both stable and unstable parts of the phase diagram.

Recently a different approach was taken by Matera and Dellafiore [217] who applied white noise to a Vlasov system. The noise term was determined self-consistently by invoking the fluctuation–dissipation theorem and, within the linear approximation, the time evolution of the density fluctuations was found to be given by the same closed form as was found in Ref. [112]. The authors showed that while a white-noise form of the stochastic field is in general *not* consistent with the fluctuation–dissipation theorem, it may provide a good approximation when the free response function is sufficiently peaked.

It is important to note that all of the methods described above employ an *ad hoc* procedure to generate fluctuations. Therefore the microscopic structure in phase space of the produced correlations is typically very different from the prediction of the Boltzmann Langevin theory. However, as stressed first in Ref. [176], in situations where the dynamics is dominated by only a few modes (such as the fastest growing spinodal modes) it may suffice to require equivalence with the exact Boltzmann–Langevin approach for only those few degrees of freedom. As a consequence, several approaches have carefully designed the fluctuation source so as to mimic the effects of the stochastic Boltzmann–Langevin term on the dynamics of the most unstable modes [113,145,176]. In such a way the dynamics of the spinodal decomposition can be simulated. The comparison with exact many-body dynamics presented in the next section illustrates the power of such instability projected stochastic approaches.

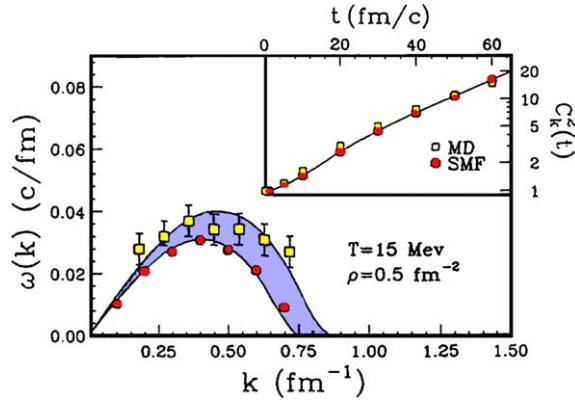


Fig. 4.11. One-body versus many-body: dispersion relation. The dispersion relation extracted from either the many-body (molecular-dynamics) calculation (open squares) or the stochastically initialized one-body (BUU) simulation (solid dots). The linear-response result for the one-body treatment is shown by the shaded area covering the range of uncertainty in the one-body parameters. The insert shows the corresponding temporal growth of the most unstable mode k_0 , as measured by the corresponding correlation strength, σ_{k_0} . (From Ref. [39].)

4.4.1. Reliability of one-body treatments

The quantitative reliability of one-body treatments of spinodal fragmentation was examined by Jacquot et al. [39]. Considering a two-dimensional gas of classical particles subject to a Lennard–Jones interaction, which presents a many-body problem that can be solved exactly by direct numerical solution of the equations of motion, the authors compared these exact results to those obtained by using the approximate one-body method introduced in Ref. [145]. The mean-field dynamics was derived from a local-density approximation of the energy functional using a Skyrme-type parametrization, adjusted so as to approximately reproduce the features of the many-body model. The collision cross section is taken as coming from the repulsive hard core in the inter-particle potential.

The approximate Boltzmann–Langevin treatment was tested against the exact many-body model for two-dimensional uniform matter inside the phase region of spinodal instability. The emerging filamentation patterns exhibited a large degree of qualitative similarity. In order to make the comparison more quantitative, the dispersion relations were extracted from the early dynamical evolutions and they are shown in Fig. 4.11 together with the linear-response result for the one-body model. The two dynamical treatments are seen to yield the same dispersion relation to within about 10% and the corresponding wave numbers for the most rapidly growing density undulations are $k_0 = 0.399$ and 0.359 fm^{-1} , respectively. As shown in the insert, the temporal evolution of the corresponding correlation strength for the most rapidly amplified mode, $\sigma_{k_0}(t)$, are very similar.

It was also found that, well inside the spinodal region, the exact early fragmentation follows closely the growth of the most unstable collective modes as obtained by a linear-response analysis of the associated mean-field propagation. The good correspondence between the exact many-body result and the approximate one-body treatment is illustrated in Fig. 4.12, which shows two snapshots of the correlation strength distributions σ_k . They are very similar, especially for the most rapidly growing modes that ultimately dominate the fragmentation pattern. Moreover, it was shown that the

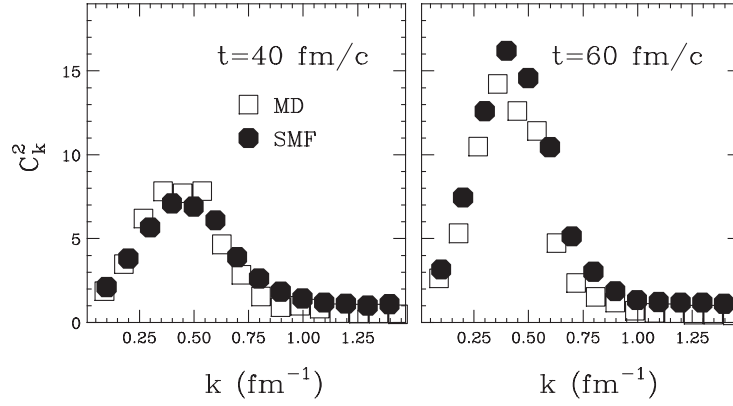


Fig. 4.12. One-body versus many-body: density fluctuations. The spectral distribution of the spatial correlation function, as measured by the variance σ_k of modes with wave number k , for either the many-body (molecular-dynamics) calculation (open squares) or the stochastically initialized one-body (BUU) simulation (solid dots), as extracted at two successive times for a sample of ten events. (From Ref. [39].)

fragmentation pattern obtained with the exact many-body model can be reproduced by the one-body treatment even at late when the system exhibits large many-body correlations.

This study thus brings out the fact that one-body treatments, when endowed with a suitable degree of stochasticity, may be quantitatively useful for studies of catastrophic dynamics, such as may occur when first-order phase-transitions are present.

4.4.2. Brownian one-body dynamics

A novel method for introducing fluctuations in one-body dynamics was proposed by Chomaz et al. [144]. It consists of employing a brownian force in the kinetic equations and it was therefore denoted as the *brownian one-body* (BOB) treatment.

The basic idea the method is to replace the actual stochastic collision term δK by a suitable brownian force $\delta \mathbf{F}$ (with $\langle \delta \mathbf{F} \rangle = 0$) in such a manner that the novel equation of motion is obtained by making the following replacement in the Boltzmann–Langevin equation (4.6),

$$\delta K[f] \rightarrow \delta \tilde{K}[f] = -\delta \mathbf{F} \cdot \frac{\partial f}{\partial \mathbf{p}}. \quad (4.38)$$

In order to ensure that the resulting brownian one-body dynamics mimic the BL evolution, the stochastic force $\delta \mathbf{F}$ is assumed to be local in space and time. Moreover, since nuclear matter is isotropic, the force may also be taken to have rotational invariance. Its correlation function can then be written as follows,

$$\langle \delta \mathbf{F}(\mathbf{r}_1) \delta \mathbf{F}(\mathbf{r}_2) \rangle = 2\tilde{D}_0(\mathbf{r}) \mathbf{I} \delta(\mathbf{r}_{12}) \delta(t_{12}), \quad (4.39)$$

where \mathbf{I} is the unit tensor in position space. The resulting dynamics is then qualitatively similar to that resulting from the Boltzmann–Langevin equation, but the associated diffusion coefficient for the evolution of the phase-space density $f(\mathbf{s})$ is modified,

$$2\tilde{D}(\mathbf{s}_1; \mathbf{s}_2) = 2\tilde{D}_0(\mathbf{r}) \frac{\partial f(\mathbf{s}_1)}{\partial \mathbf{p}_1} \cdot \frac{\partial f(\mathbf{s}_2)}{\partial \mathbf{p}_2} \delta(\mathbf{r}_{12}). \quad (4.40)$$

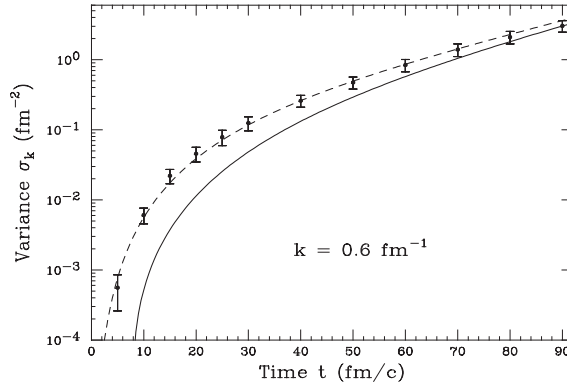


Fig. 4.13. Test of the brownian one-body simulation method. The evolution of the strength σ_{k_0} of the most unstable mode ($k_0 = 0.6 \text{ fm}^{-1}$) in idealized two-dimensional nuclear matter, prepared at half the saturation density with $T = 3 \text{ MeV}$: The expected BL result taking into account the actual growth time t_{k_0} obtained in the BUU pseudo-particle propagation (solid curve), the actual result of the BOB dynamics (points), and the result of the corresponding linearized BOB dynamics (dashed curve). (From Ref. [144].)

The local strength, as given by the coefficient $\tilde{D}_0(r)$, is determined by the demand that the dynamics of the fastest unstable modes be as given by the Boltzmann–Langevin theory, in uniform with a density given by the local value $\rho(r)$. This amounts to requiring that the projection $\tilde{\mathcal{D}}_k^{++}$ be equal to \mathcal{D}_k^{++} (see Section 4.3.2). There are thus no adjustable parameters involved in the BOB approximation.

The brownian one-body simulation method was tested in Ref. [144] by considering the evolution of the density variance for the most unstable mode, σ_{k_0} , in idealized two-dimensional nuclear matter prepared at half the saturation density with a temperature of $T = 3 \text{ MeV}$, as illustrated in Fig. 4.13. As can be seen, the BOB results are very well reproduced by the analytical linear-response treatment of the Boltzmann–Langevin model, using the actual growth time t_{k_0} as extracted from a sample of pseudo-particle simulations. In the course of time, the growth obtained with the brownian one-body dynamics exhibits an exponential approach to that reference evolution. Moreover, the numerical BOB results are well reproduced by the corresponding linear-response prediction (using the extracted actual growth time t_{k_0}). Finally, it was found that the evolutions of neighboring modes are similarly well approached [146]. Thus, the BOB method does indeed emulate the corresponding Boltzmann–Langevin dynamics fairly well and it thus appears that it may provide a practical quantitative means for addressing catastrophic nuclear processes.

4.5. Concluding remarks about spinodal dynamics

It has been elucidated how the inclusion of fluctuations is essential in the dynamical description of the evolution of unstable systems, such as those undergoing spinodal fragmentation. We have discussed the Boltzmann–Langevin treatment which presents the natural extension of the deterministic nuclear Boltzmann. The fluctuations then arise from the stochastic part of the two-body collision integral and there are thus no new adjustable parameters introduced.

Furthermore, we have described powerful approximate tools that make it possible to address multifragmentation processes in realistic 3D systems, such as nuclei. We wish to particularly note

the brownian one-body (BOB) model which is an approximation to the full Boltzmann–Langevin treatment that involves no adjustable parameters, thus making it practical to carry out essentially parameter-free numerical transport simulations of nuclear reactions.

The quantitative utility of this kind of model is well illustrated by the recent detailed study by Matera et al. [127] who considered spinodal decomposition of expanding nuclear matter with a BOB-type model, constraining the stochastic field by the fluctuation–dissipation theorem for the expanding system. The spinodal growth rates, the evolution of the density–density correlation function and the emerging liquid domains were determined. Furthermore, the fragment-size distribution were found to agree well with data and the associated critical exponents were extracted.

In the currently tractable treatments, the fluctuations are introduced at the semi-classical level. However, as we have discussed, quantal effects appear to be of quantitative importance in the evolution of unstable nuclear systems. Hence it would be of interest to go beyond the semi-classical level and develop a suitable quantal transport treatment where such features as quantum fluctuations and memory effects are included.

5. Applications to nuclear fragmentation

In recent years many experimental and theoretical efforts have been devoted to the study of reaction mechanisms in nuclear collisions at intermediate energies and, in particular, to the understanding of the observed copious production of intermediate-mass fragments (IMF), one of the most challenging issues in the field. Insofar as the phenomenon of spinodal multifragmentation can be directly related to the properties of nuclear matter around and below the saturation density, those studies have a direct bearing on the experimental observability of the nuclear liquid–gas phase transition.

In order to make such a connection, it must first be established that the bulk of the involved system in fact enters the phase region of spinodal instability. This is the topic of the first part of this section. Subsequently we address the resulting multifragmentation and we make contact with the data in the next section.

5.1. *Is the spinodal region reached in the calculations?*

In order to ascertain whether nuclear multifragmentation, as observed in nuclear reactions, can in fact be related to the spinodal decomposition, it is necessary to carry out numerical studies of the collision dynamics and we review below various key results in this regard.

5.1.1. *Entering the spinodal zone*

Over the past decades, many calculations have predicted that the systems formed in nuclear collisions may expand to reach dilute configurations containing spinodal instabilities. Using a microscopic quasi-particle transport model, Boal [218] sought to determine the temperature and density regions in which the nuclear liquid–gas phase transition is expected to occur. He found that the mechanical instability region should be easily accessible and that the associated change in entropy appears to be in agreement with that observed experimentally. Further studies of multifragmentation with this microscopic many-body model have been made by Boal and Glosli [219,220].

On a more macroscopic level, Schultz et al. [221] considered the isentropic expansion of a blob of nuclear matter towards the two-phase instability region under two extreme conditions: instantaneous development of the phase transition and spinodal decomposition. They found as well that the experimentally observed entropy values support the onset of a liquid–gas phase transition. Papp and Nörenberg [222] investigated the path of hot nuclei towards multifragmentation by considering an expanding and evaporating spherical source. Assuming that the expansion is isentropic, they demonstrated that the initial compression and temperature needed for entering the spinodal region depend significantly on the stiffness of the equation of state.

For well over a decade, quantitatively useful simulations of nuclear collisions have been made on the basis of semi-classical mean-field treatments that include the average effect of the residual two-body collisions, as discussed in Section 4.2. A particularly thorough and instructive study was carried out by Morawetz [223] who was able to locate instabilities and points of phase transition in the dynamical system. He found an early surface-dominated instability and a later volume-dominated spinodal instability. While the latter occurs only if the incident energy is around the Fermi energy, the former occurs over a much wider range of scenarios.

Such studies are carried out with the so-called BUU, BNV or Landau–Vlasov equation of motion for the one-body phase-space density $f(\mathbf{r}, \mathbf{p}, t)$. It may be considered as a semi-classical approximation to TDHF theory with Pauli-suppressed residual collisions included and it describes the average evolution and generally yields a satisfactory description of the reaction mechanisms in the regimes of low and intermediate energy. However, as discussed in Section 4, this kind of treatment is inadequate for processes exhibiting bifurcations, such as nuclear fragmentation processes, where a small fluctuation in the spatial density may be amplified, thus producing an irreversible divergence of the possible trajectories, as a variety of qualitatively different density configurations may develop. In such cases, the average trajectory is no longer physically informative and it becomes necessary to treat an entire ensemble, which is most conveniently done by stochastic methods. This general limitation notwithstanding, the average trajectory may still be used as a tool for identifying the onset of instabilities, using various stability criteria [223–225] or the sudden growth of a suitable observable as an indicator (see Ref. [196]). (Of course, once instabilities are encountered, the subsequent average evolution of the system is no longer reliable and must be replaced by a suitable stochastic treatment.)

Such BUU-like simulations have been used as exploratory calculations for studying the spinodal crossing and a suitable illustration is provided by the study of the central reactions La+Al and La+Cu at 55 MeV/*A* carried out by Colonna et al. [226] using a soft equation of state. In order to make comparison with experiment possible, any compound nuclei remaining after the BUU simulation should be subjected to a “afterburner” producing statistical particle and fragment emission. As it turns out, the incomplete fusion residues produced in the La+Al reaction yield evaporation products in good agreement with the data [227], while the calculations fail to produce the abundant IMF emission observed for the energetic La+Cu reaction. This result suggests that the fragments produced in the latter case do not come from an evaporative process.

To understand this sudden transition to an apparently prompt fragmentation process, the authors inspected the time evolution of the density and excitation energy in the participant zone, and analyzed them in a thermodynamic framework making use of the nuclear matter equation of state. The central nucleon density ρ was extracted and the corresponding thermal excitation energy per nucleon was then assumed to be of the form $\epsilon^* = \epsilon_{\text{kin}} - \frac{3}{5}\epsilon_F(\rho)$, where $\epsilon_F(\rho)$ is the local Fermi energy and ϵ_{kin}

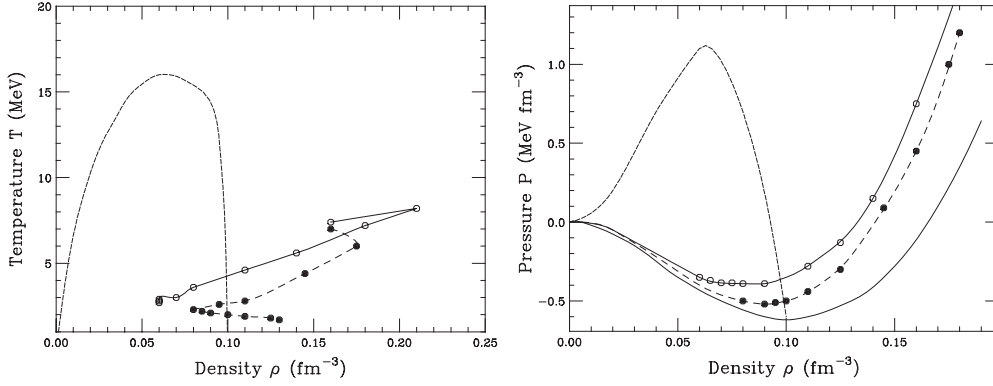


Fig. 5.1. Phase trajectories for 55 MeV/A La on Al and Cu. Dynamical trajectories in the ρ - T (left) and ρ - P (right) phase planes for the reactions 55 MeV/A La on Al (solid dots) and Cu (open dots) at an impact parameter of 1 fm. The density ρ , temperature T and the pressure P have been extracted in the interaction zone at time intervals of 10 fm/c. The short-dashed curve delineates the spinodal region. The ρ - P plot includes the pressure evaluated at a constant entropy of $S = 0.6$ (dashed), $S = 1.0$ (solid) or $S = 0$ (bottom curve). (Adapted from Ref. [226].)

is the kinetic energy per nucleon computed from the actual momentum distribution. The temperature was then extracted by use of the Fermi gas model, $T^2 = \epsilon^*/a$, with the level density parameter being $a(\rho) = \pi^2/4\epsilon_F$, and the corresponding entropy per nucleon is calculated as $s(\rho) = 2aT = 2(\epsilon^*a)^{1/2}$. These approximate relations are accurate for $T \ll \epsilon_F$, as was the case for this analysis where $\epsilon^* = 1$ –4 MeV. It should be noted, though, that these idealized relations employ the free nucleon mass m rather than the effective mass $m^* \approx 0.6 m$ which would change the values significantly.

The resulting dynamical evolution of these thermodynamic quantities display several instructive features, as shown in Fig. 5.1 (left). While the central density for the La+Al reaction experiences an oscillatory behavior, with the formation of one excited compound system, the La+Cu reaction has more available energy and it therefore exhibits a larger initial compression and the subsequent dilution then suffices to bring the system well within the region of spinodal instability, resulting in prompt disassembly. The extracted entropy values remain remarkably constant, $s \approx 0.6$ and $s \approx 1.0$, respectively. Fig. 5.1 (right) shows the corresponding evolutions in the ρ - P plane, with the pressure P being obtained from the equation of state given by the dynamical model, using the extracted temperature and density. It is clearly seen how the systems evolve isentropically. Even though the La + Al system enters the spinodal region temporarily, it reexpands out of the region before any fragmentation can occur, contrary to La + Cu.

The occurrence of volume instabilities may also be revealed by the time evolution of suitable collective variables related to the density. Of particular interest is the monopole moment Q , where $Q^2 = \langle r^2 \rangle$, as studied by Cussol et al. [228]. Using the extracted local density $\rho(\mathbf{r}, t)$ and $\mathbf{j}(\mathbf{r}, t)$, these authors extracted the monopole inertial-mass parameter B , and the stiffness C ,

$$\frac{1}{2} B(t) \left(\frac{d}{dt} Q(t) \right)^2 = E_{\text{coll}}(t) = \frac{m}{2} \int d^3r \frac{\mathbf{j}(\mathbf{r}, t)^2}{\rho(\mathbf{r}, t)}, \quad (5.1)$$

$$C(t) = \frac{d^2}{dQ^2} E_{\text{intr}}(t) = -\frac{d^2}{dQ^2} E_{\text{coll}}(t), \quad (5.2)$$

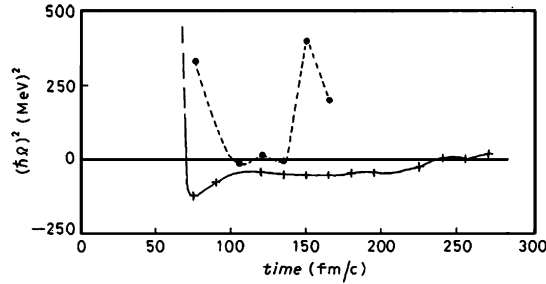


Fig. 5.2. Evolution of the monopole mode. The time dependence of the square of the monopole oscillation frequency Ω for the reaction $^{40}\text{Ar} + ^{50}\text{Ti}$ ($b = 0$) at 44 MeV/A (solid curve) and 20 MeV/A (dashed curve). Negative values of Ω^2 reveal an excursion into the spinodal region. (From Ref. [228].)

since the total energy $E_{\text{tot}} = E_{\text{coll}} + E_{\text{intr}}$ is conserved, so the collective frequency can be obtained, $\Omega^2 = C/B$. The evolution of this quantity is shown in Fig. 5.2 for the reaction $^{40}\text{Ar} + ^{50}\text{Ti}$ at two energies, as obtained with the BUU treatment using a soft equation of state. It is seen that while 20 MeV/A leads to compound formation with an oscillatory behavior of Q , the higher beam energy brings the system well into the unstable region characterized by $\Omega^2 < 0$. Since these results depend sensitively on the equation of state employed [229,229a], the analysis of the onset of multifragmentation may provide important information on the stiffness of the nuclear equation of state in regions far from normal density.

Employing a relativistic transport calculation, Fuchs et al. [230] investigated thermodynamic properties and instability conditions in intermediate-energy heavy-ion reactions. The thermodynamic variables (density, pressure and temperature) are calculated directly from the phase-space distribution. Instabilities are spotted using the criterion that the effective compressibility becomes negative. Thus, in the case of semi-central Au+Au reactions at 600 MeV/nucleon, clear indications of instability are found in the center of the spectator matter, with conditions of density and temperature that are consistent with experimental determinations.

As the above exposition illustrates, the possible entry of the system into an unstable region can be quantitatively ascertained already on the basis of average dynamics described by mean-field dynamical models.

5.1.2. Role of heating and compression in semi-classical expansion

In nuclear reactions, the expansion required for the system to enter the spinodal region may occur as a result of the initial compression and/or the thermal pressure. Therefore, we discuss here in some detail the role of heating and compression on the prospects for a nuclear system to enter the spinodal region, an issue of great relevance to fragmentation studies.

A detailed study of the dynamical evolution of compressed and/or heated spherical nuclear systems, within the framework of the BUU model, was carried out by Batko and Randrup [150]. As stressed before, the BUU model yields a mean-trajectory description and as such it should preserve the initial symmetries of the system. However, in most existing numerical implementations, the discretization introduces irregularities that act as a numerical noise which may thus be amplified when the system becomes unstable. In order to preserve the overall spherical symmetry even in the presence of

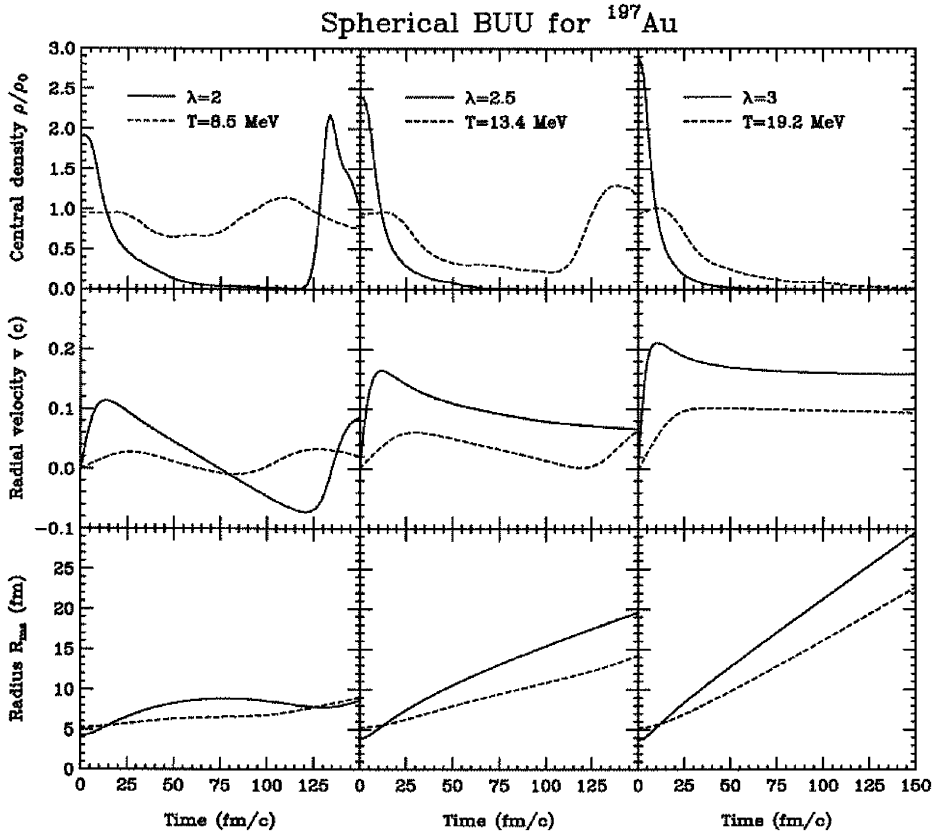


Fig. 5.3. Collective flow for ^{197}Au with spherical *BUU*. The degree of compression in the central cell ρ/ρ_s (upper row), the average radial velocity $v = \langle \mathbf{v} \cdot \mathbf{r} \rangle$ (middle row), and the root-mean-square radius $R_{\text{rms}} = \langle r^2 \rangle^{1/2}$ (lower row) as functions of time, for ^{197}Au , calculated by imposing spherical symmetry in the *BUU* code. The results corresponding to three different initial values of the compression parameter λ and the temperature T are indicated by the solid and dashed curves, respectively. (From Ref. [150].)

such instabilities, the authors enforced an angular average of the mean field at each time step, thus obtaining a more reliable approximation to the true average solution. As a main result of this study, it was found that, under suitable conditions, the nucleus expands into a hollow, quasi-stationary unstable configuration that evolves sufficiently slowly to enable the instabilities to develop.

Here we review calculations performed for ^{197}Au nuclei that have been excited to a certain degree either by uniform compression or by a corresponding degree of heating. The resulting evolutions are illustrated in Fig. 5.3. At relatively moderate initial compressions ($\lambda \equiv \rho/\rho_s = 2$), the nucleus exhibits an oscillatory motion, while slowly radiating its excess excitation away by emission of individual pseudo-particles. The oscillatory character of the motion is clearly reflected in the periodic fall and rise of the central density, as well as in the periodic behavior of the radial velocity. Oscillations are less evident in the rms radius R_{rms} , due to the significant and steadily growing contribution from the emitted particles. The continual loss of energy carried off by the emitted particles appears to be the main source of the damping of the collective radial motion.

As the initial compression λ is increased, the oscillatory period grows longer and the rate of particle emission increases. At some point, the initial compression exceeds a critical value and the system keeps expanding steadily. This qualitative change in behavior occurs for $\lambda \approx 2.5$, corresponds roughly to the compression where the monopole mode becomes unstable.

At the dilute turning point, the density profile becomes drastically distorted into a bubble-like configuration with the local density and temperature corresponding to a phase point well within the spinodal region of mechanical instability, as illustrated in Fig. 5.4. This configuration is quasi-stationary for $\lambda \approx 2.5$, with the time spent under these unstable conditions being as large as 100 fm/c, which exceeds the growth times for density irregularities (see Section 3). Therefore, if density irregularities are introduced, the system will undergo a spontaneous transformation leading to condensation of the dilute matter in the shell into a number of prefragments. Thus, on the basis of such studies, one is led to the expectation that compression may be an effective agency for expanding the system into an unstable configuration.

It is instructive also to examine the alternative scenario in which the same degree of initial agitation has been achieved by thermal excitation (also shown in Fig. 5.4). The resulting hot systems generally exhibit an evaporation-like behavior, radiating pseudo-particles while gradually shrinking and cooling. Thus, the thermal initialization appears to be much less effective in generating collective radial motion. (However, it should be noted that this feature may well be an artifact of semi-classical approaches, since quantum mean-field treatments render heating almost as effective as compression in driving the system to low density [231], as we discuss below.)

We finally emphasize the important fact that the possible entry of the system into the unstable zone is a feature determined by the average dynamics and thus it can be studied within the framework of mean-field treatments. On the other hand, the subsequent evolution within the unstable region is highly dependent on the details of both the physical model and the numerical implementation, as we shall discuss in more detail in Section 5.2.

5.1.3. Expansion and dissipation in TDHF simulations

The above type of analysis is based on a semi-classical mean-field treatment and therefore the extracted results, such as the value of the critical compression λ , may change quantitatively if a more quantal approach is employed. In order to investigate this issue, Lacroix et al. [231] performed TDHF simulations for finite nuclei prepared under extreme conditions of temperature and pressure together with the corresponding semi-classical approximation, the Vlasov dynamics. (Both of these treatments neglect the residual two-body collisions included in the study discussed above.) They found that the differences in the results are primarily due to the wave nature of the nucleons which generally renders the system less dissipative, so that the initial compression required for achieving a given degree of density oscillation is lower in TDHF than in the Vlasov treatment.

The faster expansion towards lower densities obtained with TDHF simulations stems primarily from the slower damping and cooling processes. In particular, while a unbound nucleon would be emitted when described as a particle, its description as a wave in TDHF allows it to be partly reflected at the surface, thus reducing the particle evaporation rate and increasing the pressure on the nuclear surface. The replacement of particles by waves in effect then converts evaporation into expansion.

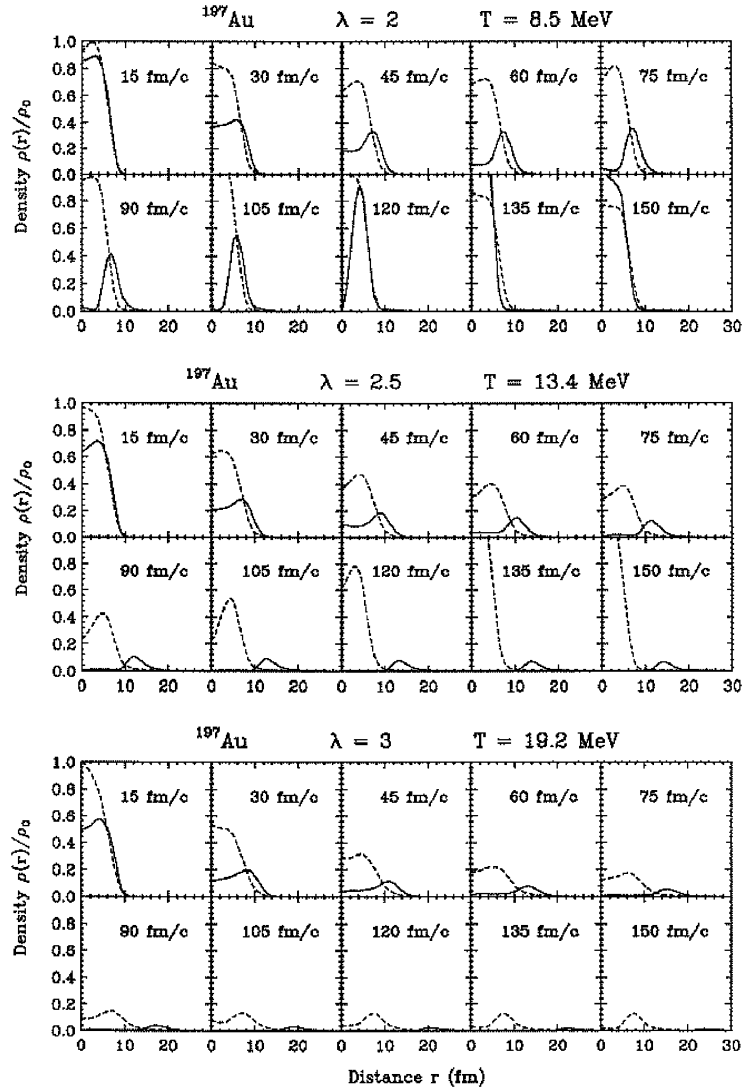


Fig. 5.4. Density profile for ^{197}Au with spherical BUU. Time evolution of the nuclear density profile for ^{197}Au obtained by imposing spherical symmetry in the BUU code. The three sets of figures display results obtained from different compressed (solid curves) and thermal (dashed curves) initializations, corresponding to pairs of values of the temperature T and the compression parameter $\lambda = \rho/\rho_s$ that yield the same excitation energy. (From Ref. [150].)

The difference in the evaporation process affects not only the amplitude of the monopole motion but it also changes the size of the remaining residual nucleus. As we have noted, the evaporation in TDHF is reduced by reflections from the surface, so a large part of the system may survive the expansion stage and reach the low density region. By contrast, the fast evaporation in the classical treatment removes more particles and radial momentum, so the residue is smaller and cannot expand as much.

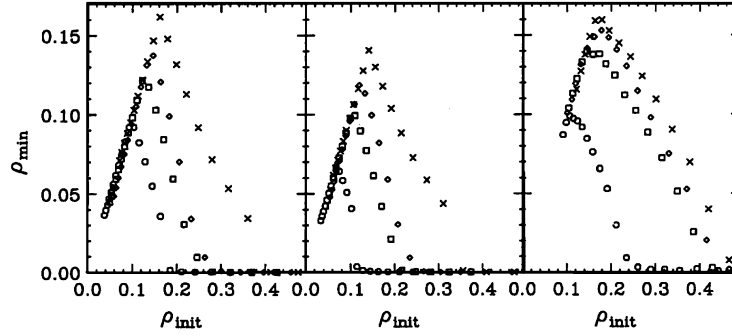


Fig. 5.5. TDHF versus Vlasov expansion. The central density at the time of maximum dilution (the turning point in the monopole motion), ρ_{\min} , as a function of the initial central density ρ_{init} , for a ^{40}Ca nucleus at various initial temperatures, either in TDHF (left and center) and the corresponding Vlasov treatment (right). The initial excitations correspond to the following values of the entropy per nucleon σ : 0 (crosses), 1.1 (diamonds), 2.35 (squares) and 3.28 (circles) which correspond to $T = 0, 5, 10$ and 15 MeV for the uncompressed heated nuclei. (From Ref. [231].)

A quantitative illustration of the differences between TDHF and Vlasov is shown in Fig. 5.5. It presents the correlation between the initial compression ρ_{init} and the resulting minimum density ρ_{\min} , as obtained in either TDHF calculations, without (*left*) and with (*center*) gradient terms in the effective interaction, or semi-classically (*right*). It is evident that TDHF yields a larger degree of expansion. For example, for an entropy per nucleon of $\sigma \approx 2.35$ (corresponding to $T=10$ MeV for the uncompressed heated nucleus) a small compression of $\rho/\rho_s = 1.3$ suffices in the quantum dynamics since the thermal pressure is the essential agency for producing a very considerable expansion, $\rho_{\min}/\rho_s = 0.1$. By contrast, in the semi-classical dynamics the essential agency for expansion is the compression which should exceed about double density, $\rho/\rho_s = 2$, to achieve an equivalent degree of dilution.

In summary, when the wave mechanical nature of the nucleon is taken into account, as in TDHF, both compression and heat are as effective in bringing a larger part of the system to lower density, as a larger part of the initial excitation energy is converted into dilution. In particular, even a system starting at saturation density may expand into the spinodal region if sufficiently hot.

5.1.4. Role of the fluctuations on the expansion dynamics

When instabilities are encountered in dynamical simulations, irregularities may be drastically amplified. Thus, an ensemble of initially very similar systems, each with its own individual small deviations from the ensemble average (arising from the initial fluctuations or/and from some stochasticity on top of the deterministic dynamics), may display a relatively sudden branching into qualitatively different subensembles, thus rendering the overall average phase-space density meaningless (see Fig. 4.4). Therefore, when the instabilities are present, it is essential to acquire a good understanding of the fluctuation sources and to the development of appropriate treatments is required for reaching reliable conclusions on even the average dynamics.

A detailed study of the disassembly of finite nuclei was performed by Guarnera et al. [145] using the simplified approach developed in Refs. [113,176] (see discussion in Section 4). They evolved central collisions of Xe and Sn at 50 MeV/A with the BUU model until instabilities were

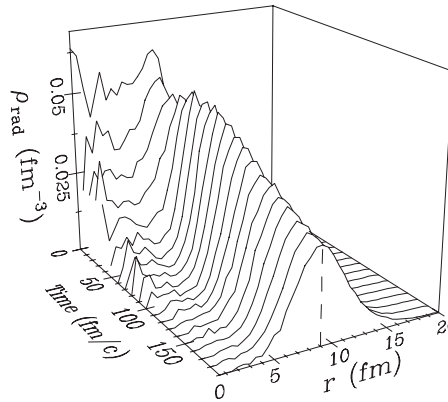


Fig. 5.6. Evolution of the radial density profile. Time evolution of the radial density profile for a hot and expanding nuclear system (with 210 nucleons) initialized inside the spinodal region. (From Ref. [145].)

encountered, leading typically to a relatively heavy compound system ($A \approx 200$) with the bulk conditions being inside the spinodal region ($\rho \approx \frac{1}{2}\rho_0$) and $T \approx 3$ MeV. This system was then endowed with a self-similar radial expansion as occurring in the average dynamics (reaching a maximum speed of $v \approx 0.1c$ at the surface) and a noise that was carefully tuned to reproduce the complete Boltzmann–Langevin dynamics for the most unstable mode in nuclear matter at the considered density and temperature, k_0 . (The magnitude of the introduced irregularity is derived from the linearized Langevin dynamics.)

In agreement with the calculations performed within the BUU model [150] (described in Section 4.2.2), the matter concentrates at the surface of the system, as shown in Fig. 5.6. This leads to the formation of bubble-like configurations when the initial source is spherical (as in the case considered), or torus-like fragmenting systems when the source happens to be flatter (see Ref. [151] for an early exploration of this phenomenon). In either case, the formation of a hollow structure is favored and even stabilized by the fragmentation of the system.

The results obtained with this simplified dynamics are important because they show that the instabilities are helping the system to remain in the low-density region long enough to permit the instabilities to fully develop. Indeed, the development of density fluctuations results in a reduction of the restoring force associated with the monopole breathing mode. This slows down the recontraction of the system, thus allowing more time for the instabilities to develop. This important feature deserves a more refined analysis of the time scales involved in the fragmentation dynamics.

The main disadvantage of the simple method of Ref. [145] is that it introduces noise only at the initial time and thus does not take account of the fluctuations arising from the stochastic nature of the dynamical evolution. A significant improvement of this shortcoming is provided by the brownian one-body (BOB) dynamics model [144,146] which provides a both simple and powerful approximate calculational tool. (We recall that the BOB dynamics introduces noise in the one-body field whenever the local phase conditions correspond to spinodal instability, with the noise being adjusted so that it would produce the same growth rate as the full Boltzmann–Langevin model for the most unstable mode in nuclear matter prepared at that local density and temperature.) A good illustration is provided by the disassembly of a gold nucleus having been prepared in a suitably compressed configuration.

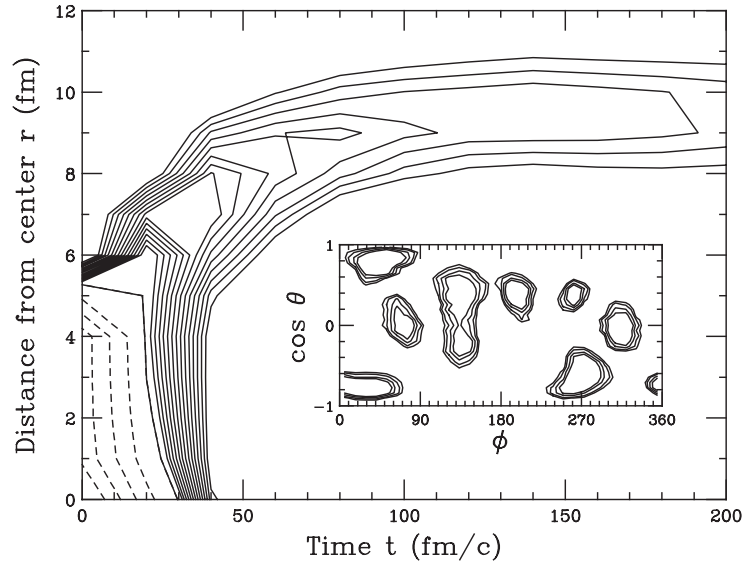


Fig. 5.7. Evolution of the density profile. Contour plot of the evolving radial density profile, as obtained with the BOB treatment of a compressed gold nucleus. The density contours are separated by $\Delta\rho = 0.005 \text{ fm}^{-3}$ and dashed contours are employed in the regions of compression. The insert shows the angular distribution of the fragments formed in a typical event. (From Ref. [146].)

This system is also close to the one discussed above ($A \approx 200$) and can be considered as an approximate realization of configurations obtained along the path of central nuclear collisions at intermediate energy.

The resulting evolution of the radial density profile (averaged over many stochastic trajectories) is shown in Fig. 5.7. As in the pure mean-trajectory dynamics [150], if the gold nucleus is initially compressed to twice the normal density it will expand into a quasi-stationary hollow configuration that is unstable against multifragmentation. It is an important feature of the BOB treatment that the strength of the stochastic force is larger than the numerical noise. The results are therefore no longer sensitive to the latter and thus this non-physical source of fluctuation may be neglected. This resulting robustness of the calculated results is obviously a great advantage of the treatment.

After the formation of a hollow configuration, the matter in the shell condenses into a number of prefragments as shown in the insert of Fig. 5.7. This condensation reduces the restoring force so the system is prevented from relapsing into a single compound nucleus. The stochastic approaches are thus essential to correctly predict the evolution of the system as soon as an instability has been encountered.

5.1.5. Investigations with many-body approaches

In the previous sections the dynamical evolutions of highly excited systems have been discussed within mean-field approaches (including stochastic mean-field models), and it was showed that the spinodal region of the nuclear matter phase diagram is indeed reached under suitable conditions. We have also seen that the development of the instabilities weakens the overall restoring force and thus helps to keep the system within the instability region. To investigate the generality of these key

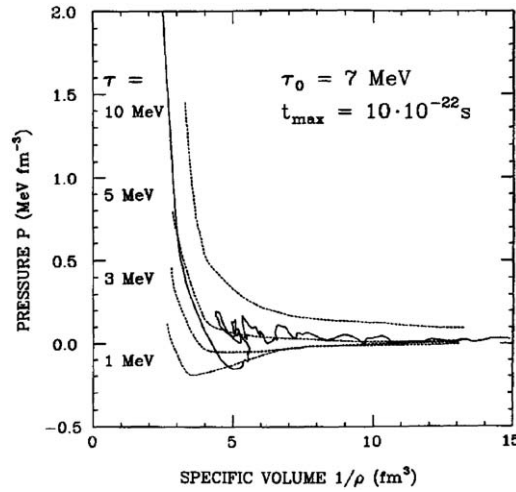


Fig. 5.8. Phase evolution of ^{40}Ar . The evolution in the P - v phase plane of an ensemble of systems prepared at double density, with the temperature $T = 10$ MeV. The dynamical trajectory joins points at time intervals of 3 fm/c. (From Ref. [37].)

features, it is interesting to perform the same kind of study for scenarios where exact calculations can be carried out. While this cannot yet be done for nuclear systems, it is quite feasible for classical particle systems.

Nuclear spinodal fragmentation was studied with molecular dynamics by López et al. [108,109]. Making comparison with Cahn's theory, they found that isothermal spinodal decomposition plays a dominant role in the breakup, while neither nucleation of bubbles in the two-phase region nor adiabatic spinodal decomposition contribute to the fragment production, consistent with the results of Ref. [106].

The phase evolution of a fragmenting nucleus was studied by Dorso and Randrup [37] who applied a quasi-classical simulation model to systems that have been compressed and heated. Systems consisting of 80 "nucleons" were prepared in states corresponding to a compression by a factor 2, with respect to the saturation density, and several initial temperatures T_0 . It was observed that at low temperature the temporal evolution is fairly slow and the system remains essentially as a single entity. On the other hand, at high temperature the system quickly explodes into individual particles and loosely bound clusters, with the spatial density acquiring a filamentary character. As already stressed above, this corresponds to the situation where the competition between the radial flow (resulting from the compression and thermal pressure) and the cohesion (resulting from the inter-particle attraction) results in the break-up of the systems into several clusters.

The behavior of the pressure P as a function of the specific volume $v = 1/\rho$ along the trajectory of the system (20 events were considered) is depicted in Fig. 5.8, for the initial conditions ($T = 10$ MeV) that lead to the disassembly of the system. As a reference, the isothermal curves of pressure with respect to density are also represented. It can be observed that the trajectory crosses into the spinodal region. Moreover, it should be noted that the emergence of bound clusters is reflected in the fact that the extracted dynamical pressure falls below the coldest isotherm of the P - v diagram.

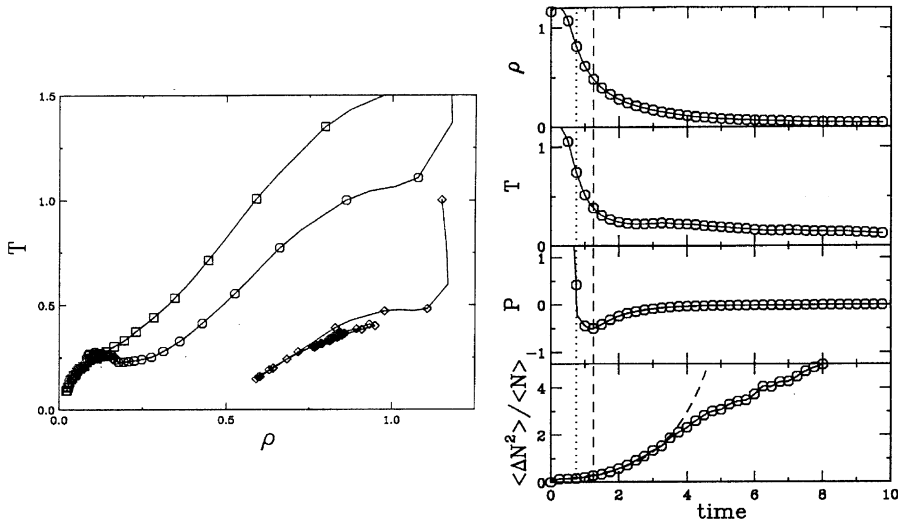


Fig. 5.9. Fragmentation of a hot drop. The time evolution of a hot spherical assembly of N interacting particles. *Left*: Trajectories followed the T – ρ phase plane for the three energies considered and $N=251$ (see text). *Right*: Time evolution of pressure, density, temperature and multiplicity fluctuations obtained in the case yielding maximum IMF production ($N=485$). (From Ref. [77].)

More recently, Belkacem et al. [232] performed molecular-dynamics calculations indicating that a hot spherical drop may expand into the spinodal region and disassemble into many fragments. For the specific two-body force employed, the trajectory yielding the maximum production of intermediate-mass fragments enters the coexistence region close to the critical point.

Furthermore, Pratt et al. [77] have studied the disassembly of a system of particles interacting with a Lennard–Jones type saturating force. They are initially confined within a spherical container at the saturation density and their momenta are sampled micro-canonically to yield a given kinetic energy. The hot systems were then allowed to expand according to the classical equations of motion and the phase path followed by the system was extracted.

The dynamical trajectories followed by the system in the T – ρ phase plane are shown in Fig. 5.9 (*left*) for the three energies considered and the results are similar to what is observed in mean-field calculations (see e.g. Ref. [150]). At low excitation the system expands only slightly and then retracts to saturation density after evaporating some light fragments, while the system explodes into many small fragments at high excitation. At a suitable intermediate excitations a balance is reached where the drop expands but neither explodes nor retracts. Rather, the matter attains a metastable configuration where the collective velocity and the pressure are both near zero, see Fig. 5.9 (*right*). This situation yields a maximum number of intermediate-mass fragments. It should also be noted that the T – ρ trajectory penetrates deeply into the spinodal region, where the liquid and gas phases can coexist, and the fragment formation can be interpreted as a manifestation of the associated phase separation.

The occurrence of fragmentation is signalled by the relative variance particles near the center of mass of the system, $\langle (\Delta N)^2 \rangle / \langle N \rangle$, which measures the degree of spatial clustering relative to random

particle positions. This quantity exhibits an accelerating growth to values significantly in excess of one while the system is inside the spinodal region, as shown in Fig. 5.9 (right).

Based on the various simulations, we may conclude that many initial conditions, from systems formed in nuclear collision to hot or compressed nuclei, evolve in such a manner that their bulk regions enter the spinodal region. From there on those approaches that do not correctly take account of the fluctuations and their dynamics cannot be trusted. It appears that the fragmentation dynamics, which can be regarded as the development of large-scale many-body correlations, reduces the restoring force acting to bring the system back to a single compound nucleus near saturation. As a consequence, the system may remain longer in the spinodal region thereby allowing the instabilities to develop sufficiently for fragmentation to occur. We now turn to the more detailed discussion of the implications of such a spinodal decomposition on the properties of the fragmentation pattern.

5.2. Fragmentation studies

Many studies have been directed towards fragment formation in nuclear collisions. Already in 1987, Sneppen and Vinet [224], using both Vlasov and BUU one-body dynamics, observed that the expansion of nuclear systems is generally followed by the formation of fragments. Still based on BUU-like studies, Moretto et al. [233] found that the head-on collision of two Mo nuclei at typically 60 MeV/A would lead to relatively thin oblate disks which would then cluster as a result of Rayleigh–Taylor type instabilities. Gross et al. [163] considered the central collision of two Mo nuclei at 55 MeV/A and reported that condensation into fragments occurs throughout the entire spherical volume, once the system has expanded sufficiently. (Subsequently, a more detailed study was carried out [225].) Bauer et al. [151] considered Nb+Nb at 60 MeV/A and observed the development of a transient bubble-like configuration that subsequently turns into a toroidal structure, before breaking up into fragments. The formation of ring-shaped systems, that break up into fragments, was also observed in the BUU simulations of Pb + Pb collisions at 50 MeV/A carried out by Norbeck et al. [152]. Borderie et al. [153] studied central collisions between very heavy nuclei around 30 MeV/A and found Coulomb instabilities, which also lead to the formation of unstable bubble configurations. Finally, the influence of the employed equation of state on the spatial geometry of the fragmenting system was discussed by Xu et al. [234], who found that a stiff equation of state leads to the prompt formation of several nearly equal fragments positioned in a ring-like structure, due to the formation of metastable toroids. By contrast, a soft equation of state produces a prompt condensation into several nearly equal fragments isotropically distributed on the surface of a metastable bubble.

However, in all of those scenarios, the resulting fragmentation pattern depends sensitively not only on physical quantities, such as the equation of state or the dissipation, but also on the specific numerical implementation of the one-body dynamics (especially the number of pseudo-particles per nucleon, \mathcal{N}). So the fragmentation geometries predicted by BUU-like approaches are not reliable. This can be understood as an inherent feature of deterministic dynamics which cannot explore the various possible branchings of the trajectory and should therefore generally not lead to the multifragmentation. However, the discretization required for the numerical treatment of the deterministic model in effect presents a source of noise and this agency may break the imposed macroscopic symmetries, thus providing seeds for amplification by any instabilities encountered in the course of the evolution.

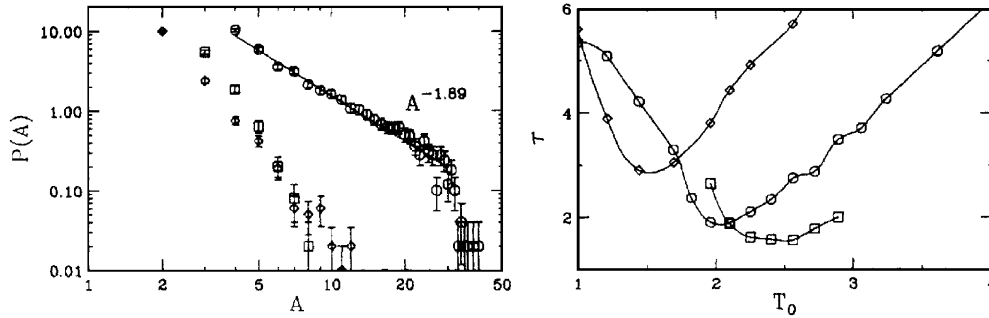


Fig. 5.10. Mass distributions from molecular dynamics. *Left panel*: Fragment size distributions for three initial temperatures: $T_0 = 1.44$ (diamonds), $T_0 = 2.10$ (circles) and $T_0 = 4.0$ (squares), for $N = 251$ particles. *Right panel*: Fitted value of τ as a function of the initial temperature T_0 $N = 93$ (diamonds), $N = 251$ (circles) and $N = 485$ (squares). (From Ref. [77].)

As we have already remarked above, when instabilities are encountered by the system, a reliable description of its further evolution requires a treatment containing the appropriate *physical* fluctuations. This is the case when fragments are produced at some stage of the reaction. In Section 4, we have presented stochastic mean-field approaches and we have shown that they provide a good basis for the understanding of unstable dynamics. We will review the application of those approaches to the problem of the fragment formation in this section. A different type of treatment that is suitable for fragmentation processes is stochastically initialized molecular dynamics where the different break-up channels can be explored by different members of the ensemble of many-body states considered. While the utility of such approaches for providing insight into the collision dynamics has already been illustrated repeatedly, the quantitative validity of classical molecular dynamics in nuclear physics is still being debated. Moreover, the role of the specific spinodal decomposition mechanism has not yet been completely elucidated, as will be discussed in Appendix E.

5.2.1. Fragmentation with molecular dynamics

The fragmentation of a hot spherical drop with classical molecular dynamics was studied by Pratt et al. [77], who found that the IMF production is enhanced for trajectories that lead the system inside the spinodal region (see above). In the case of maximal IMF yield, the corresponding mass distribution is quite broad, and a power-law fit, $P(A) \sim A^{-\tau}$, yields $\tau = 1.89$ (the value expected at the critical point is 2.2). The maximum IMF production occurs at larger temperatures for larger systems and their mass distribution is also broader, as illustrated in Fig. 5.10.

The final mass distribution differs from what would result in the fragmentation of an equilibrated system having the density and temperature reached in the dynamical evolution. Those “equilibrium” mass distributions (discussed in Section 2.4.2) are characterized by a power τ that appears to be larger (see Fig. 2.16), i.e. the equilibrium partitions contain fewer intermediate-mass fragments than those obtained in the actual fast dynamics. Hence one can speculate that the IMF excess (relative to equilibrium), as signalled by a small τ , might signal the disassembly of systems that have penetrated deeply into the spinodal region. Other molecular-dynamics studies [232] find explosion-like evolutions that yields a mass distribution represented by a power of $\tau \approx 2.2$. However, these systems fragment

close to the critical point rather than deep inside the spinodal region, so the scenarios may not be comparable.

It is interesting to note that a power behavior, with the value τ significantly below 2.2 have been found experimentally for systems which, according to the mean-field calculations, are expected to reach the nuclear spinodal region. This feature certainly deserves a more systematic study, from point of view of general physics as well as in the nuclear context.

The utility of modeling nuclear dynamics by means of classical many-particle systems is far from obvious because of their fundamental differences in especially two respects: Since they are quantum particles, the nucleons cannot be sharply localized in phase space, and since they are fermions, they are subject to the Pauli exclusion principle. Consequently, over the past 20 years, various extensions of the standard molecular approximation have been proposed in order to partially remedy these problems. The simplest introduce various forms of momentum-dependent forces that serve to mimic the effect of the Pauli phase-space exclusion [37,76,235–237]. The Time-Dependent Cluster model forms a more elaborate treatment using classical Euler–Lagrange equations of motion and is particularly aimed at collisions with light nuclei [238–240].

Several multifragmentation studies have been performed within the so-called quantum molecular dynamics (QMD) approaches [74,75,241–244] which attempt to take account of the wave-mechanical nature of the nucleons by representing them by Gaussian wave packets (with the particle dynamics being is still purely classical). In these studies, the reactions have a binary character, even for central events, and the fragments are formed early on and pass through the reaction zone without being destroyed [245].

At a more refined level, the basic anti-symmetry of the wave function is taken into account by representing the A -body state as a Slater determinant of Gaussians with a complex width that is either kept constant, Anti-Symmetrized Molecular dynamics [246], or allowed to evolve dynamically, Fermionic molecular dynamics (FMD) [247,248]. A set of coupled classical equations of motion then result for the wave packet centroids (and, for FMD, their width).

Since these approaches provide a good description of many features, especially the properties of nuclear matter and the structure of light fragments, it is of great interest to employ this framework for studying the fragmentation dynamics and, in particular, for investigating whether spinodal decomposition occurs. For such an undertaking, it is important to calculate the phase diagram and identify the associated spinodal instabilities. Some recent studies along that line will be discussed in Appendix E.

5.2.2. First stochastic one-body simulations

Among the first studies based on stochastic one-body approaches were the efforts to study fragment production by means of momentum-space quadrupole fluctuations [249–252]. But, as already discussed in Section 4.4, it was shown in Ref. [214] that this schematic treatment of the fluctuation may be unsuitable for quantitative calculations. In particular, for central collisions of ^{40}Ca and ^{40}Ca at 90 MeV/ A , this method predicts that a sizable fraction of the available energy is released from the system by fast pre-equilibrium nucleon emission, and the explosion of the system is caused by a rapid but cold expansion. However, since the appearance of the fast nucleons could be an artifact of the approximation used to implement the fluctuations, the resulting description may not be reliable.

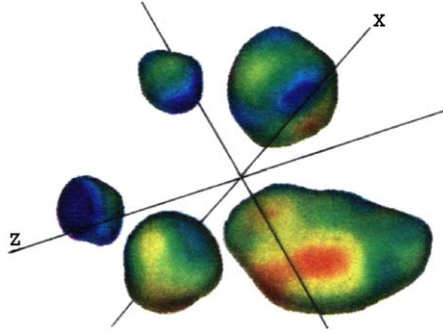


Fig. 5.11. Final fragmentation configuration. A typical configuration after the formation of the primary fragments in the collision of Xe+Sn at 50 MeV/A studied in Ref. [145] with the simplified Boltzmann–Langevin dynamics developed in Refs. [176,113]. The drawing has been rescaled according to the distance from the viewer in order to provide a three-dimensional impression. (From Ref. [254].)

Guarnera et al. [145,253] have applied the simplified approach using a stochastic initialization proposed in Refs. [113,176,177] to the disassembly of nuclear systems that have been brought inside the spinodal region in the course of a collision. The spherical system studied is intended to approximate the compound systems formed in central collisions of Xe+Sn at 50 MeV/A (see the previous section), which provides an expanding heavy system starting at half normal density with a moderate temperature. As discussed above, the spinodal instabilities lead to the formation of a hollow structure which subsequently condenses into large fragments. A typical final fragment configuration is illustrated in Fig. 5.11. It shows that five fragments of approximately equal size have been formed at the periphery of the system, while there is no production of small clusters. A more quantitative analysis of these features is given below.

For spherical systems, the collective modes have the form $f(r)Y_{LM}(\hat{r})$ and, insofar as the bulk region resembles nuclear matter, the radial part can be obtained from the expansion of a plane wave on spherical Bessel functions, $f(\mathbf{r}) \approx j_L(kr)$. One may therefore perform a multipole analysis of the density fluctuations $\delta\rho^{(n)}(\mathbf{r})$ and consider

$$\sigma_L(k, t) = \sum_M \prec \left| \int d^3\mathbf{r} j_L(kr) Y_{LM}^*(\hat{r}) \delta\rho^{(n)}(\mathbf{r}, t) \right|^2 \succ, \quad (5.3)$$

which provides the multipole strength distribution of the spatial correlation function given by $\sigma\mathbf{r}(12) = \prec \delta\rho^{(n)}(\mathbf{r}_1)\delta\rho^{(n)}(\mathbf{r}_2) \succ$. For each multipolarity L , the growth rate depends on the radial wave number k . Its optimal value is determined by the requirement that the radial density profile fit within the system, so it is given by $k_L \approx x_L/R$, where R is the radius of the sphere and x_L is the argument for which $j_L(x)$ has its first maximum. Fig. 5.12a shows the corresponding multipole strength distribution, $\sigma_L(k_L)$, at the time $t = 100$ fm/c when the fragments are formed. The dominant mode has $L \approx 5$ for which the distance between bulges, $\lambda \approx 2\pi R/L \approx 10$ fm. For this multipolarity, Fig. 5.12b shows the dependence on wave number (in terms of the reduced variable $k_{\text{red}} \equiv k/x_L$) and the strong preference for the indicated optimal value k_L) is clearly seen. This wave length admits only one radial undulation, so, consequently, the fragments appear around the center of the system thus making the global matter distribution hollow. It should

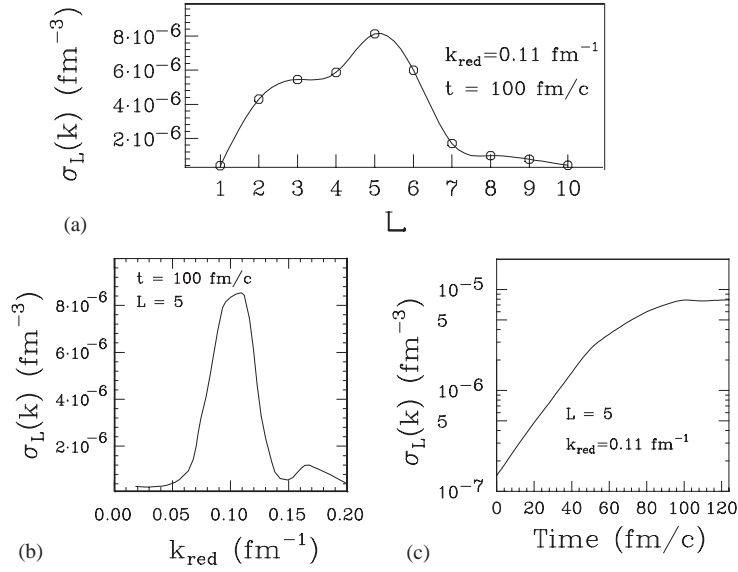


Fig. 5.12. Fragmentation of a compressed sphere. An initially compressed sphere is evolved with the BOB model and the following quantities are extracted from a sample of 400 events: (a) the dependence of $\sigma_L(k)$ on L for $k_{\text{red}} = 0.11 \text{ fm}^{-1}$ and $t = 100 \text{ fm}/c$; (b) the dependence of $\sigma_L(k)$ on k for $L = 5$ and $t = 100 \text{ fm}/c$; (c) and the time evolution of $\sigma_L(k, t)$ for $L = 5$ and $k_{\text{red}} = 0.11 \text{ fm}^{-1}$. (From Ref. [145].)

also be noted that the optimal wave length, $\lambda \approx 10 \text{ fm}$, is close to the value in nuclear matter (see Fig. 3.7).

Finally, Fig. 5.12c shows the time evolution of $\sigma_5(k)$. The initial growth appears to be exponential, with a characteristic growth time of $t_L \approx 35 \text{ fm}/c$. This is close to the fastest growth time found in RPA calculations (where $t_0 \approx 30 \text{ fm}/c$ for $\lambda_0 \approx 10 \text{ fm}$ [105,155]). This growth rate and the initial amplitude of the irregularities together determine the fragment formation time, which in the present case is $\approx 100 \text{ fm}/c$.

In summary, as a key result, it is found that spinodal instability leads to a characteristic time scale for the fragmentation process and a typical size of the resulting fragments. For infinite matter, we have discussed how the finite range of the interaction, which is related to the cost in surface energy of the fragments formed, is responsible for the suppression of instabilities with a short wavelength, thus ensuring the existence of a most favored wave length, $\lambda_0 \approx 10 \text{ fm}$. In the spherical system this feature translates into a suppression of high-multipolarity distortions, leading to a preferred value of $L_0 \approx 5$ in heavy systems.

5.2.3. BOB simulations

The results presented above demonstrate the important fact that multifragmentation processes can be described within the framework of stochastic one-body treatments. Therefore it is interesting to discuss the corresponding results of the more accurate BOB treatment [144,146] (see Section 4.4.2). As brought out by the average dynamics discussed earlier, the expanding system forms a hollow structure that condenses into a number of fairly similar prefragments. Since the matter distribution

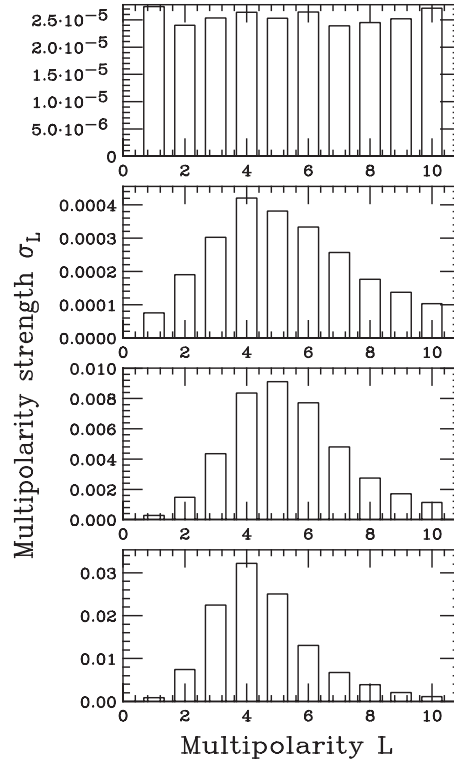


Fig. 5.13. Multipolarity strength distribution. The multipolarity strength distribution σ_L as obtained with BOB at successive times during the evolution of the expanding Au system. (From Ref. [146].)

is concentrated near a spherical surface and the radial structure of the density irregularities was examined already within the simple model, it suffices to analyze the density fluctuations in terms of spherical harmonics.

Fig. 5.13 shows the multipolarity strength distribution σ_L , extracted at successive times during the evolution, and the time dependence of the most dominant modes is shown in Fig. 5.14 (left). Since the physical noise is approximately white [120], the different multiplicities are about equally agitated at early times. During the early expansion stage, the nuclear bulk is above the critical density for spinodal decomposition, but the expanding surface region is unstable, as the dilute matter seeks to increase its binding. This leads to an amplification of the surface irregularities and determines the initial growth of the multipolarity strengths observed in Fig. 5.13. As the bulk of the system subsequently descends into the region of spinodal instability, the unstable bulk modes are amplified as well. It should be noted that, as already pointed out, the monopole mode ($L=0$) is agitated from the outset, while the higher multiplicities are agitated by the stochastic force only when the local spinodal instability occurs. Once the system becomes dilute, a rapid growth of the monopole mode is favored and a hollow configuration develops promptly. Meanwhile, the various multipoles are being agitated by the brownian force and amplified by the one-body field, so the associated amplitudes start to grow, with the most unstable modes increasing most rapidly. Once the hollow configuration

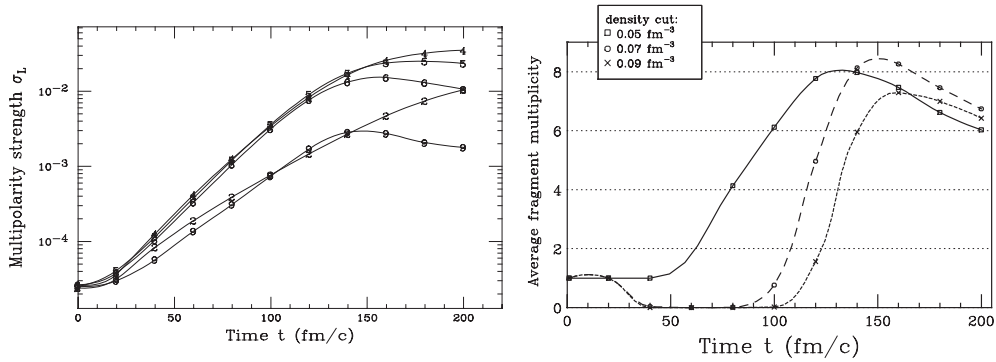


Fig. 5.14. Spinodal fragmentation dynamics in Au. *Left panel*: The time evolution of the multipolarity strength σ_L of the unstable modes having $L = 2-6$ for the expanding Au system. *Right panel*: The associated time evolution of the average fragment multiplicity obtained by using various values of the density cut-off ρ_{cut} , as indicated. (From Ref. [146].)

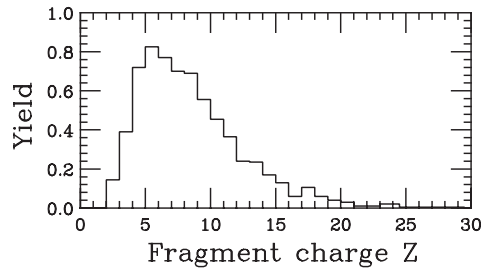


Fig. 5.15. Fragment charge distribution. The fragment charge distribution resulting from the fragmentation of initially compressed gold nuclei, as extracted from the density pattern after the condensation has occurred, using a density cut-off of $\rho_{\text{cut}} = 0.05 \text{ fm}^{-3}$. (From Ref. [146].)

has been formed, there is little change in the strength distribution, except for a continued overall growth, as the amplified irregularities relatively rapidly condense into a number of intermediate-mass fragments. The multiplicity and the characteristics of the fragments obtained are determined primarily by the dominant multipolarities.

Similarly to what was seen in Fig. 5.12c, the early exponential growth characteristic of unstable modes is apparent, and the eventual leveling off at the time when the fragments are fully formed is observed. The final multipole strength is concentrated around $L \approx 4$, so that elementary geometrical considerations suggest a final fragment multiplicity of $N \approx 6$ [146].

It is possible to identify distinct prefragments at each time step during the evolution by employing a density cut-off ρ_{cut} . Fig. 5.14 (right) shows the resulting prefragment multiplicity as a function of time. The results obtained with the three different cut-off values ρ_{cut} converge at $t \approx 150 \text{ fm/c}$ when the condensation is completed. Fig. 5.15 displays the resulting final fragment charge distribution extracted at $t = 200 \text{ fm/c}$ with the lowest cut-off value, $\rho_{\text{cut}} = 0.05 \text{ fm}^{-3}$. The distribution is rather broad, with a concentration near carbon-like fragments.

The emergence of these primary fragments is a reflection of the fact that certain unstable multipoles dominate the dynamics. Also, as is evident from the multipolarity strength distribution, the dynamics

effectively suppresses the development of high multiplicities, thereby preventing the formation of very small primary fragments. However, the mass distribution is broad, reflecting the competition between several unstable modes and the importance of non-linear dynamics, such as coalescence effects among the prefragments.

Since the wavelengths and the growth times of the most important modes are not very dependent on the particular density and temperature achieved inside the spinodal region, the resulting fragment mass decreases with the dilution of the system. The resulting fragment sizes thus effectively depend on the expansion velocity at the stage when the fragments are formed. Thus, as illustrated using the simple model of Ref. [145], larger fragments are obtained for systems that expand only slowly.

We finally stress that we have discussed only the formation of prefragments. Since these are still excited, their subsequent de-excitation must be taken into consideration before any comparison to experimental data would be meaningful. For example, the de-excitation generally produces an abundance of very light fragments ($Z \leq 2$) and reduces the mass of the primary fragments. It is therefore important to carefully ascertain whether the final fragmentation pattern retains a significant memory of the original spinodal fragmentation dynamics. For example, the light-fragment population, which is suppressed in the primary IMF yield, is largely being replenished as a result of evaporation, so that no low- Z hole is apparent in the final yield curve.

As shown by these simulations, the presence of spinodal decomposition is signalled by the formation of nearly equal-sized fragments, due to the dominance of a few collective unstable modes in the linear regime. Therefore, one may search for events that keep the memory of this early configuration, typical of spinodal decomposition, even after the secondary decay. With this aim, one may employ the correlation analysis proposed by Moretto et al. [255] which reveals the presence of such events even if they are only relatively few. It basically consists of producing a two-dimensional histogram (occasionally called a LEGO plot) in terms of the extracted mean and dispersion of the IMF charge distribution, $\langle Z \rangle$ and ΔZ .

Fig. 5.16 presents the results of such an analysis made for the BOB simulations of central Xe + Sn collisions at 32 MeV/A [256]. It can be seen that a peak at very small values of ΔZ , i.e. approximately equal-size fragments, stands out quite clearly against a rather structureless background, even though it contains only a few per cent of the yield. The background can be well accounted for by statistical considerations (e.g. it can be reproduced from artificial events constructed by sampling the fragments randomly from different events). Thus, the emerging peak cannot be of statistical origin but must be regarded as a very specific signal of the spinodal decomposition scenario. This analysis presents a powerful tool for identifying the spinodal disassembly scenario in experiments, as will be illustrated in the next section.

5.3. Isospin dependence of spinodal fragmentation

The presence of the isospin degree of freedom enriches the physics considerably and a number of studies have sought to elucidate how nuclear spinodal fragmentation depends on the neutron and proton fractions [44,130,137,257,258].

Neutron-rich nuclear system can be created in the central collision of two heavy nuclei at intermediate energies ($E_{\text{lab}} \sim 100$ MeV/A) or by bombardment of a heavy target nucleus with a light projectile at high energy ($E_{\text{lab}} \sim 1$ GeV/A). In general, the N/Z ratio of the primary fragments is

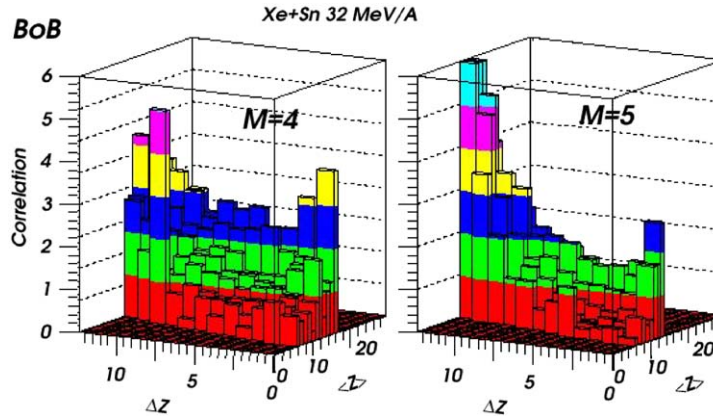


Fig. 5.16. Fragment size correlations. The IMF size correlations displayed as a two-dimensional histogram where the axes represent the average fragment charge $\langle Z \rangle$ and the associated dispersion ΔZ , as obtained with BOB simulations. The peak at very small ΔZ contains events having approximately equal-size fragments, while the background can be well reproduced by event mixing. (From Ref. [256].)

largely determined by the interplay of symmetry and Coulomb energies. As already discussed in Section 2, the spinodal decomposition process drives the system towards thermodynamic liquid–gas phase coexistence, where the high-density phase (liquid) becomes isotopically more symmetric while the low-density phase (gas) accumulates most of the excess neutrons. This effect is related to the increase of the symmetry energy with the density at subsaturation densities and is included in all realistic effective interactions.

5.3.1. Fragmentation of dilute isobars with $A = 197$

In order to elucidate the characteristic features we review here results obtained by Larionov et al. [257] for the multi-fragment break-up of systems containing $A_0 = 197$ nucleons with a variable number of protons, $Z_0 = 63, 79, 95$. The source temperature is taken as $T_0 = 3$ MeV. The systems are prepared with a density of half the saturation value and are endowed with a radial flow of 3 MeV/A (to prevent a recontraction of the source). The total excitation energy is $E_0^*/A = 8$ MeV including compression, flow, and thermal energy.

We shall discuss especially various key observables, namely charge yields, IMF ($Z \geq 3$) multiplicity distributions, N/Z ratio versus IMF charge (isotopic ratios), and seek to elucidate their sensitivity to the neutron excess of the source system (i.e. on its proton fraction $y_0 = Z_0/A_0$). We shall concentrate on the primary fragments, which are generally hot and subsequently deexcite by sequential emission of light fragments. The evolution of the fragmentation process was calculated with the stochastic mean-field (SMF) treatment [145], which represents a rough approximation to the Boltzmann–Langevin model and can be regarded as a simple version of the brownian one-body BOB model discussed above.

The radial distribution the resulting fragments at the time $t = 150$ fm/c is shown in Fig. 5.17 (left). As already seen in various earlier studies (see in particular the original study of the breakup of an expanding ^{197}Au system [150]), the fragments form a bubble-like structure where the fragments are situated at $R = 7\text{--}13$ fm, with the larger fragments being closer to the center. At this point, the

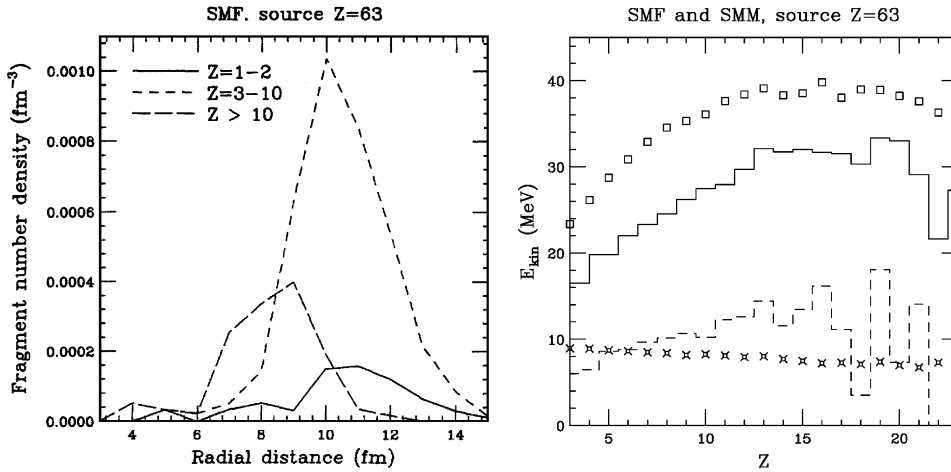


Fig. 5.17. Fragmentation of an expanding ^{197}Eu system. The fragmentation of a dilute and expanding spherical source containing 63 protons and 134 neutrons is calculated with the stochastic mean-field model. *Left*: The radial density profile of the hot fragments at the time $t=150$ fm/c. Solid, short- and long-dashed curves refer to fragments with charge numbers $Z=1-2$, $Z=3-10$ and $Z \geq 11$, respectively. *Right*: Kinetic energies as a function of the fragment charge number Z , as obtained with SMF (histograms) as well as with the statistical model SMM before (*crosses*) and after (*squares*) Coulomb acceleration. (From Ref. [257].)

dynamical evolution is stopped, the fragments are accelerated by their mutual Coulomb repulsion, and the secondary deexcitation process is carried out (see later).

The authors of Ref. [257] discussed their dynamical results relative to those obtained within a statistical model, for which they used SMM [19]. (Instructive application of SMM was also made by Botvina and Mishustin [259].) These reference results were calculated for a freeze-out density equal to one-third of the saturation value so the corresponding volume is approximately that enclosed by the bubble configuration displayed in Fig. 5.17 (*left*). Finally, the overall excitation energy is taken as $E^*/A=8$ MeV, with no radial flow. (For inclusion of radial flow into statistical multifragmentation, see Ref. [16].) It should be noted that in the dynamical treatment the source is expanding as the fragments are being formed, so once their formation is complete (i.e. they no longer feel their mutual nuclear attraction) they take up a volume larger than that of the initial unstable source.

Fig. 5.17 (*right*) shows the average IMF kinetic energy at the breakup time as a function of the fragment charge Z as obtained either dynamically or statistically, both before and after the Coulomb acceleration. The mutual Coulomb repulsion causes the fragment kinetic energies to increase with Z , except for the heavier fragments which are formed closer to the center where the Coulomb force is weaker. This effect is already visible in the dynamical spectra at the breakup time.

Since the statistical model considers fragments that are distributed uniformly within the freeze-out volume, their Coulomb interaction energy is larger than that of the dynamical fragment configurations of the same RMS size. This qualitative difference in the fragment configurations should then be reflected in the subsequent Coulomb acceleration. Indeed, from Fig. 5.17 (*right*) it can be seen that while the kinetic energy of the heavy fragments are very similar in the two treatments prior to the Coulomb acceleration, (and they are largely independent of Z), Coulomb acceleration is more

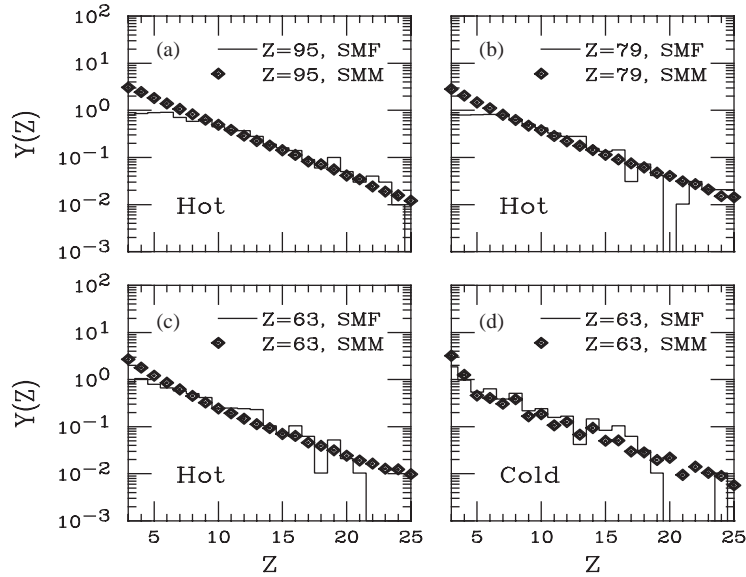


Fig. 5.18. Charge yields from various sources with $A=197$. The fragment charge yields from both hot (a,b,c) and cold (d) sources with $A=197$ and various values of Z as indicated, as obtained with either SMF (histograms) or SMM (diamonds). (From Ref. [257].)

effective for the uniform distribution of the statistical treatment than for the hollow configuration produced dynamically.

The fragment charge distributions obtained for the various sources are shown in Fig. 5.18. The results are overall very similar in the two treatments, suggesting that a high degree of equilibration occurs during the dynamical evolution. However, it is important to note that the dynamical production of primary light clusters is significantly reduced relative to the statistical yield. This characteristic feature arises because the amplification of unstable modes with short wave lengths is suppressed by the finite range of the nuclear interaction. The corresponding IMF multiplicity distributions are shown in Fig. 5.19. It is interesting to note that the statistical IMF multiplicity is roughly proportional to the charge of the fragmenting source, primarily as a consequence of the Coulomb interaction, while the dynamical IMF multiplicity is fairly constant. This latter feature can be understood from the fact that the wave lengths of the dominant unstable modes are rather independent of the proton fraction y_0 .

Furthermore, Fig. 5.20 shows the average ratio of the produced primary fragments, $\langle N/Z \rangle$, as a function of the fragment charge number Z . For the almost symmetric system having $Z=95$ (a), the fragments have practically the same N/Z . For $Z=79$ (b), the fragments have slightly lower N/Z ratio relative to the source due to the enhanced neutron loss during the multi-fragment breakup. This reduction of N/Z for the primary fragments is more pronounced for the most neutron-rich system having $Z=63$ (c). In this latter case we observe also a clear effect of the density dependence of the symmetry energy: the dynamical calculations (solid histogram) yield a decrease of N/Z with Z , for $3 \leq Z \leq 10$. Light fragments are more likely produced in regions of lower density while the heavier fragments arise from higher densities. Since low-density regions tend to be more neutron

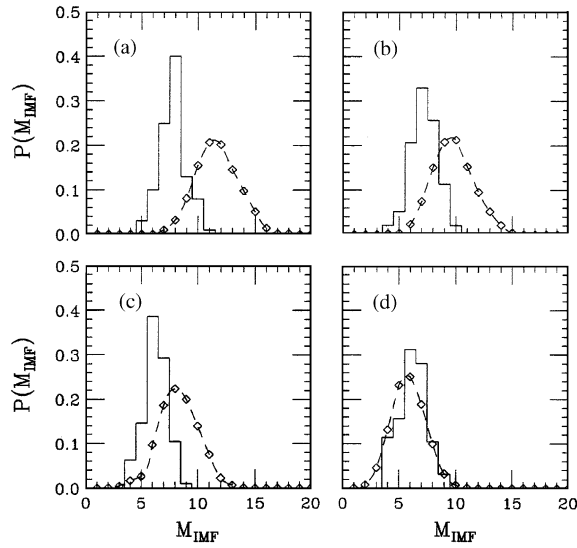


Fig. 5.19. IMF multiplicity distributions from $A = 197$. The multiplicity distributions of intermediate-mass fragments for the sources with 197 nucleons considered in Fig. 5.17, as obtained with either SMF (histograms) or SMM (diamonds). (From Ref. [257].)

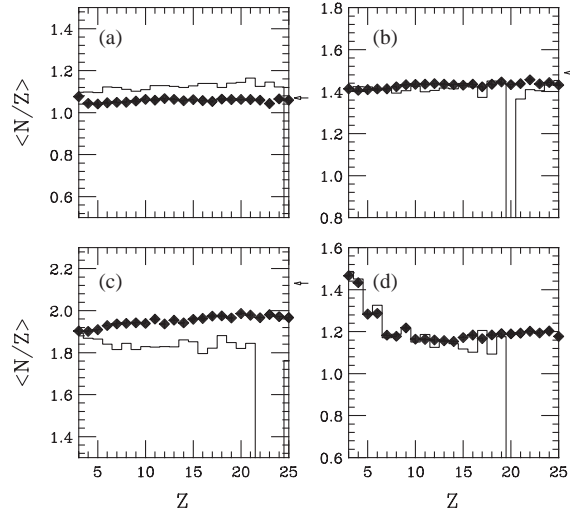


Fig. 5.20. Neutron-to-proton ratio. The average neutron-to-proton ratio $\langle N/Z \rangle$ of the primary fragments versus their charge number Z , as obtained with either SMF (histograms) or SMM (diamonds) for the same four scenarios as considered in Fig. 5.17. The arrows indicate the N/Z ratio of each source. The arrows show the N/Z ratios of initial sources. (From Ref. [257].)

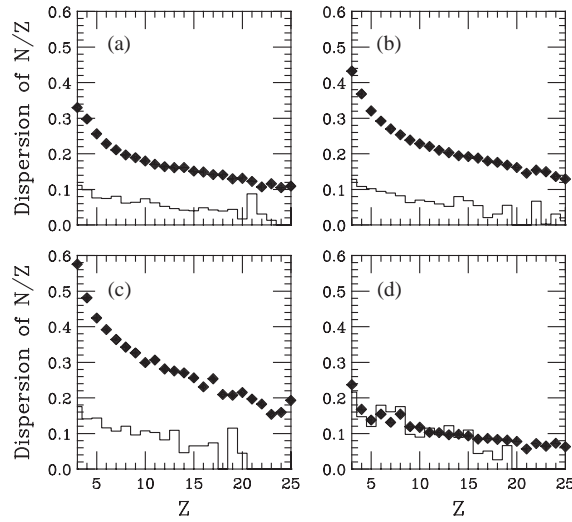


Fig. 5.21. Dispersion in N/Z . Dispersion $\sigma_{N/Z} = [\langle (N/Z - \langle N/Z \rangle)^2 \rangle]^{1/2}$ as a function of the fragment proton number Z . The cases displayed are the same as in Fig. 5.18. (From Ref. [257].)

rich (because of the isospin fractionation effect), this explains the decreasing behavior of N/Z as a function of Z .

The last observable considered is the dispersion in the N/Z ratio of the primary fragments, shown in Fig. 5.21 as a function of their charge number Z . This quantity reveals a significant difference between the two treatments at the primary stage, even when the mean values of N/Z are the same (cf. Figs. 5.20b and 5.21b). Generally, dynamically formed fragments have N/Z ratios that are closely tied to that of the source and therefore exhibit little variability, while the statistical model produces fragments whose N/Z ratios fluctuate to a degree constrained only by phase space.

As it turns out, many of the differences are washed out by the sequential de-excitation process, to which the primary fragments are subject. For example, the relative paucity of light fragments in the dynamical calculation is being largely eliminated by the feed-down from the decay of heavier fragments, while many of the additional fragments obtained in the statistical calculation are too light that their decay converts them into light particles, thus reducing the final IMF multiplicity.

Concerning the N/Z of the final products, a universal decrease of $\langle N/Z \rangle$ with Z is obtained, mostly due to a larger Coulomb barrier for the emission of light charged particles by heavier hot fragments, thus increasing neutron emission relative to charged-particle emission. The fact that the two calculations yield a similar dependence of $\langle N/Z \rangle$ on Z for the final fragments suggests that the excess neutrons of the hot fragments are very weakly bound, so they can escape from the compound nucleus at the very early stage of the deexcitation process. Such prompt neutron emission changes the excitation only little and the subsequent de-excitation steps then proceed almost unaffected. A similar smearing occurs for the N/Z dispersion. As can be seen from Fig. 5.21, the large difference present for the hot primary fragments (c) is washed out entirely by the subsequent deexcitation (d).

However, the calculations depend to some degree on structure properties of very exotic nuclei that are largely unknown, so one may expect a quite large uncertainty in the predictions of the sequential decay by the method of Ref. [19]. Nevertheless, this inherent uncertainty notwithstanding, it seems

safe to conclude that any suitable candidate signal of the spinodal nuclear fragmentation mechanism must be carefully designed to survive the eroding effects of the sequential deexcitation process.

6. Confrontation with experimental data

In recent years considerable experimental effort has been devoted to the exploration of nuclear multifragmentation with the primary focus on the possible connections between this phenomenon and the occurrence of phase transitions in nuclear matter. Of particular relevance to this issue is multifragmentation occurring in dissipative heavy ion collisions at intermediate energies. Recently developed detector arrays permit an accurate selection of events, thus enabling detailed studies of intermediate-mass fragment (IMF) production and a number of experimental findings have provided support for the occurrence of spinodal multifragmentation. This has stimulated vigorous further activity on both the experimental and the theoretical fronts.

For example, the observations have revealed a relatively sudden onset of radial expansion and an associated shortening of the disassembly time [83,260]. Furthermore, the ALADIN group [261] has reported that the nuclear caloric curve shows evidence for a phase transition at an almost constant temperature over a broad range of excitation energies and, recently, a negative specific heat was reported in the fragmentation of excited projectile-like sources [79].

In one line of research, multifragmentation data was analyzed within Fisher's droplet model [262–264] and the associated critical exponent was extracted [21,82]. In this connection, it is important to note that one expects, on the basis of studies of the various critical signals in finite systems made in exactly solvable models of the liquid–gas phase transition [62], that “critical” behavior occurs along an entire line in the phase diagram and so is compatible with a first-order phase transition.

In this section, we first review the experimental evidence for the occurrence of spinodal multifragmentation. Then we will present a detailed comparison of stochastic one-body simulations of multifragmentation events with the multifragmentation data obtained in the very central collisions studied by the INDRA collaboration [23,265].

6.1. Source characteristics: is the spinodal region reached?

When trying to evaluate the experimental evidence for spinodal fragmentation, the first issue is whether the bulk of the system really reaches conditions of density and temperature that are inside the spinodal instability region. Several different experimental observables indicate that the system may have reached these conditions: the occurrence of a radial collective flow, the size of the emitting source, the associated fragment emission time, and the temperature of the primary fragments. We shall now discuss these in turn.

6.1.1. Radial collective flow

The existence of a radial collective flow in fragmenting nuclear sources, first observed by FOPI [266], implies that the bulk of the system may reach low density values inside the spinodal region. The nuclear expansion sets in at around 5–7 MeV/A of excitation energy and the systematics is illustrated in Fig. 6.1.

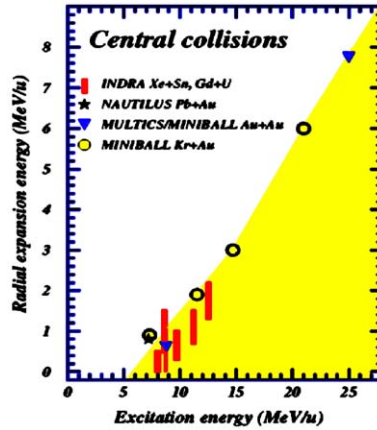


Fig. 6.1. Radial flow. A compilation of experimental data on radial flow demonstrating the onset of the nuclear explosion around 5–7 MeV per nucleon of excitation energy. (From Ref. [267].)

As a typical example, it was reported that the reaction $^{129}\text{Xe} + ^{\text{nat}}\text{Sn}$ at 50 MeV/A leads to the formation of a single isotropic source at an excitation energy of 12 MeV/A and with fragment kinetic-energy spectra indicating a fast disintegration of the system with a radial collective energy of about 2 MeV/A [268].

The value of the radial flow can be inferred from the experiment by assuming that at the freeze-out configuration consists of a number of fragments located inside a given volume and endowed with a certain amount of radial collective velocity in addition to the thermal kinetic energy. To the degree that Coulomb effects can be ignored, the radial flow can be extracted by exploiting the different dependence of the collective and the statistical energies on the fragment mass [266]. More elaborate analyses make use of statistical multifragmentation models that include Coulomb effects, such as WIX [16] or SMM [19]. The freeze-out density, which influences the interfragment Coulomb energy, and the value of the radial flow are then fitted to the observed fragment energy spectra [82,268], leading to remarkably good reproduction of the data.

6.1.2. Correlation between particles and fragments

Evidence for bulk fragmentation, which could be related to spinodal decomposition, has recently been reported in ISIS multifragmentation studies with 8–10 GeV/c π^- and p on ^{197}Au [269]. Making use of two-fragment correlation functions for events sorted in excitation energy, the authors found that the fragment emission time decreases rapidly as the excitation energy increases. In the interval $E^*/A = 2\text{--}4$ MeV the time decreases by an order of magnitude. Then above 3–4 MeV per nucleon it becomes compatible with a simultaneous production of the various fragments. The correlation can also be used to infer the volume of the emitting source which is found to increase by a factor of 3–5 in the same energy range. Moreover, it was found that the decrease in emission time is strongly correlated with the onset of multifragmentation and thermally induced radial expansion [83,260]. These findings, which are summarized in Fig. 6.2), provide strong evidence for a multifragmentation mechanism with the character of spinodal decomposition, i.e. a simultaneous breakup of the system into several IMFs.

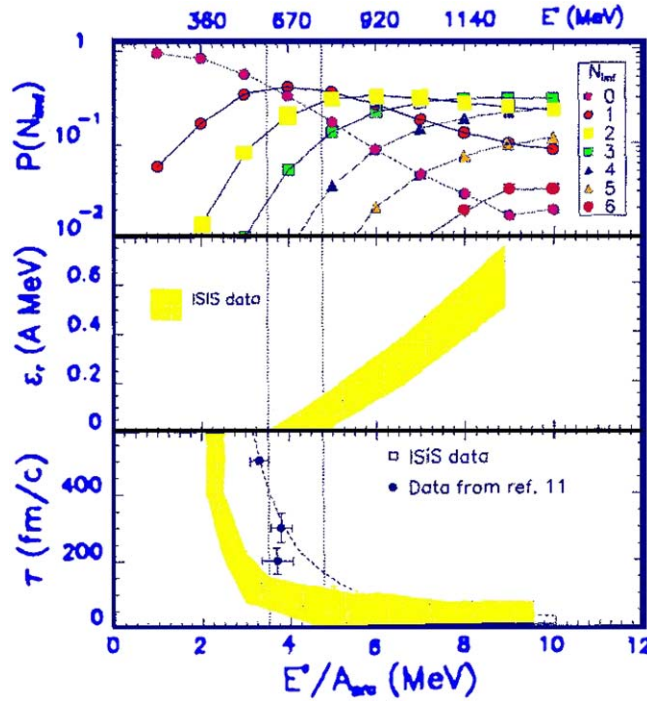


Fig. 6.2. Energy dependence of source characteristics. The dependence on the excitation energy E^*/A of the source lifetime (bottom), its thermally driven expansion energy ϵ_r (center) and the probability of observing a given IMF multiplicity (top). In the bottom panel, the shaded area indicates the range of possible space-time solutions consistent with IMF observables. The solid line is an exponential fit to the ISIS results. (From Ref. [269].)

Evidence for a transition from surface emission, akin to a gentle evaporative process, to a sudden breakup of the entire system (bulk fragmentation) was recently found also by the Medea-MultiCS collaboration [270] who observed that the production of thermal bremsstrahlung photons is in anti-coincidence with the fragment production. These photons are emitted from proton–nucleon collisions occurring in an equilibrated system and their rate increases strongly with density because of the associated increase of the Fermi speed. Therefore they can be used to measure the density reached by the system during the dynamics. An anticorrelation was then observed between IMFs and thermal photons for central collisions of Ni + Au at 45 MeV/ A , while this effect is not present for the same reaction at 30 MeV/ A . The interpretation is that the fragments arise from prompt multifragmentation during the expansion phase following the initial collisional shock, thus preventing the system from forming a compound source for thermal photons.

6.1.3. Temperature of the emitting source

Information about the temperature of multifragmenting systems was reported for example, by Marie et al. [268,271]. They applied correlation techniques to multifragmentation events of the reaction $^{129}\text{Xe} + ^{\text{nat}}\text{Sn}$ at 50 MeV/ A , thereby deducing the multiplicities of light particles (hydrogen and helium isotopes) that were emitted by the hot primary fragments, as well as their kinetic-energy spectra.

From the knowledge of the secondary light charged-particle multiplicities and kinetic energies, it is possible to reconstruct the average charges of the hot primary fragments and to estimate their mean excitation energies. In this manner, the fragment excitation energies were found to be ≈ 3.0 MeV/ A for the full IMF range, indicating a common temperature around 5 MeV. This global constancy indicates that, on the average, thermal equilibrium has been achieved at the disassembly stage of the source.

It should be noted that this value of the temperature is quite close to the value associated with the “plateau” observed in the nuclear caloric curve reported by the ALADIN collaboration [261] and in other experiments with emitting sources in the same mass range, as shown in Ref. [272]. It is also consistent with the limiting nuclear temperature imposed by the Coulomb field [273–275] as recently discussed in Ref. [276].

6.1.4. Negative specific heat

From the observations reviewed above, one may conclude that the maximum IMF production is accompanied by a dilution of the system together with a shortening of the emission times. The temperature of the hot primary fragments is found to be around 5 MeV, in the case of fragmenting sources with $A \approx 200$. These pieces of evidence are all indicating that fragmentation happens because the nuclear system enters the coexistence region of the liquid–gas phase diagram. Further evidence of multifragmentation as a process happening inside the co-existence region of the nuclear matter phase diagram is provided by the recent observation of negative specific heat in the fragmentation of excited projectile-like sources [79].

In Ref. [78] it has been proposed to use the kinetic-energy fluctuations of events having the same total energy to directly derive the ensemble heat capacity. In fact, from a classical point of view, for an ensemble at constant energy, the sharing of energy between the kinetic and the interaction parts should be governed by the respective entropies and the associated fluctuations depend upon the respective heat capacities. It is possible to show that negative heat capacity is signalled by the microcanonical kinetic-energy fluctuation becoming larger than the expected canonical limit. Hence the observation of negative specific heat indicates the presence of a first-order phase transition. However, the utility of this signal is still being debated [73].

From the experimental point of view, the total energy can readily be split into two fluctuating parts by considering the thermal agitation and fluctuation versus the partition Q -value plus the Coulomb energy. Fig. 6.3 shows the first experimental evidence of negative specific heat reported in Ref. [79].

It is interesting to note that the ISIS data [263] have been found to exhibit a Fisher-type scaling, which is typical of second order phase transitions (in infinite systems), suggesting the occurrence of critical behavior. The reason for the concurrent observation of critical behavior and negative specific heat appears to be associated with the finiteness of the nuclear system [62].

6.2. Comparison with the INDRA data

Multifragmentation events in $^{129}\text{Xe} + ^{\text{nat}}\text{Sn}$ reactions at 25–50 MeV/ A have been recently studied by the INDRA collaboration [23,256,265,278]. From 32 MeV/ A and up, compact single source events (which are associated with very central impact parameters) can be isolated making use of a flow angle selection.

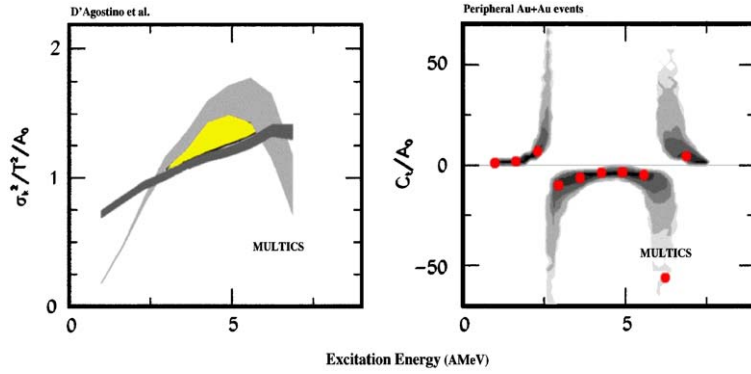


Fig. 6.3. Specific heat. The kinetic-energy fluctuation (*left*) and the specific heat (*right*), versus the excitation energy, as inferred from event-by-event energy fluctuations in quasi-projectile sources formed in peripheral Au+Au collisions at 35 MeV/A, using two different freeze-out hypotheses. (Adapted from Ref. [277].)

At 32 MeV/A, the available excitation energy per nucleon for the total system is the same as for the reaction $^{155}\text{Gd} + \text{natU}$ at 36 MeV/A, which has also been investigated with the INDRA array. Comparisons of the properties of central multifragmentation events obtained in these two reactions have revealed that the charge distribution (normalized by the average IMF multiplicity) coincide over three orders of magnitude, while the average fragment multiplicities are in the ratio 1.49, i.e. almost exactly the ratio of the total charges of the systems (156/104). Such behavior may reveal that bulk effects play a major role in the multifragmentation of these systems and suggests that spinodal decomposition may provide the onset of the disassembly of the system. Moreover, as already pointed out, the presence of radial collective flow has been experimentally observed, thus indicating that the system may expand into the unstable low-density region [279].

The kinematical properties of single-source events, as analyzed experimentally, are compatible with the assumption that, at a given point along the reaction dynamics, a freeze-out configuration is reached, i.e. the system can be described as an ensemble of hot products in thermal equilibrium, free from mutual nuclear interaction. This implies that the total system at this instant occupies a significantly larger volume than would a nucleus with the same mass, or, in other words, that it has reached a low average density.

Hence these systems are good candidates for our analysis of the possible occurrence of spinodal instabilities and for a careful comparison with the predictions of the brownian one-body (BOB) model. The model simulations show that central collisions of the two reactions considered (Xe + Sn at 32 MeV/A and Gd + U at 36 MeV/A) lead to the formation of a dense and nearly spherical composite source that subsequently expands and enters the instability region. In the BOB simulations the fluctuations are turned on already along the composite source formation path, in order to ensure that they are effective as soon as instabilities are encountered.

Table 1 lists the source properties at the time of maximum compression as well as when the bulk of the system is well inside the spinodal region, while the characteristics of the system at the end of the BOB simulations are shown in Table 2. The presence of a radial flow affects the kinematical properties of fragments and particles. As discussed above, the calculations yield several IMF's and

Table 1

For the two reactions considered, the properties of the combined system are listed at both $t = 40$ fm/c (left), when the maximum compression occurs and the radial velocity vanishes, and at $t = 100$ fm/c (right), when the bulk is well within the spinodal region (v_{max} is the radial velocity at the surface and the central temperature T is given in MeV) (from Ref. [278])

	Maximum compression				Spinodal zone				
	A	Z	ρ/ρ_0	T	A	Z	ρ/ρ_0	T	v_{max}/c
$^{129}\text{Xe} + ^{\text{nat}}\text{Sn}$	247	103	1.25	8.3	238	100	0.41	4.0	0.09
$^{155}\text{Gd} + ^{\text{nat}}\text{U}$	389	154	1.27	8.3	360	142	0.41	4.0	0.10

Table 2

Characteristics of the two systems at the end of the BOB simulations, when the de-excitation stage begins. The total mass A_{tot} and charge Z_{tot} are shared between $\langle N_f \rangle$ fragments (each having $Z \geq 5$) that have an average charge of $\langle Z_f \rangle$. The thermal and energies ε^* and ε_{rad} are in MeV per nucleon, while the Coulomb energy E_{Coul} is in MeV (from Ref. [278])

	A_{tot}	Z_{tot}	$\langle N_f \rangle$	$\langle Z_f \rangle$	$\langle \varepsilon^* \rangle$	$\langle \varepsilon_{\text{rad}} \rangle$	E_{Coul}
$^{129}\text{Xe} + ^{\text{nat}}\text{Sn}$	194.0	76.1	5.1	13.4	3.2	0.81	175.2
$^{155}\text{Gd} + ^{\text{nat}}\text{U}$	320.0	120.8	8.1	12.6	3.3	1.54	430.0

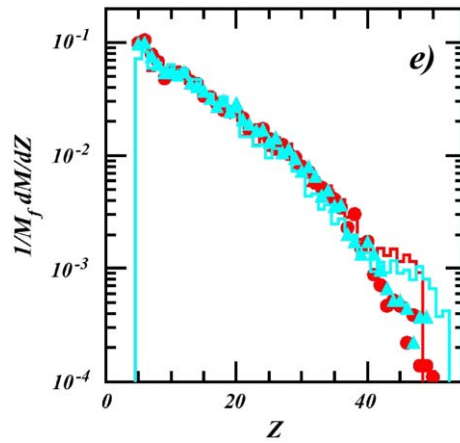


Fig. 6.4. Comparison of charge distributions. Charge distribution obtained for Xe + Sn at 32 MeV/A and Gd + U at 36 MeV/A. Experimental data are compared to the predictions of the BOB model. (From Ref. [278].)

since these are still excited, the subsequent de-excitation stage is treated using the standard code SIMON [280].

In Fig. 6.4 the charge distributions for the two systems are presented and compared with the experimental data. The calculated charge distributions are similar for the two systems and agree

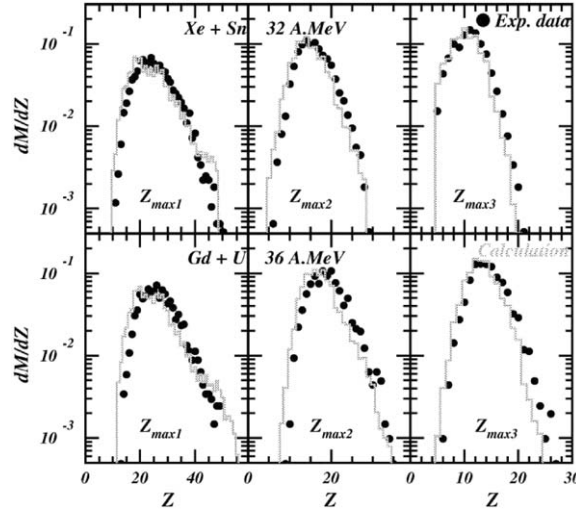


Fig. 6.5. Charge distribution of the largest fragments. Charge distributions of the three largest fragments emitted from the single multifragmenting sources formed in 32 MeV/A Xe + Sn and 36 MeV/A Gd + U, as obtained either experimentally (points) or in BOB simulations (histograms). (From Ref. [278].)

with the data. Moreover, the IMF multiplicity is close to the corresponding experimental value for both reactions. Furthermore, very light fragments are not present in the primary distributions. The rather broad charge distribution obtained for the primary fragments is due to the beating of several unstable modes and to coalescence among prefragments.

After secondary de-excitation has been taken into account, the charge distribution grows even broader as the light-mass region is being populated. A fit with a power law, $P(Z) \approx Z^{-\tau}$, will typically yield $\tau < 2$. It is interesting that a power behavior is found also in the disassembly of excited classical systems [77] (with the value τ significantly smaller than 2.2), as discussed in Section 5.2.1. Hence one may speculate that this kind of mass (or charge) distribution characterizes the disassembly of systems that are well within the spinodal region.

Fig. 6.5 shows the charge distribution of the three largest fragments detected in each event. These distributions are in excellent agreement with data, with not only the average value being well reproduced, but the entire shape as well.

The geometrical shape of the events is also well reproduced by the simulations, as one can recognize by inspecting Fig. 6.6 (left), which displays the observed isotropic ratio (which is related to the isotropy of the fragmentation events) as extracted from either the data and or the BOB events.

The comparison is less satisfactory for the fragment angular correlations, as shown in Fig. 6.6 (right). The figure represents the fragment relative angle distribution, as obtained in the simulations, divided by the distribution observed experimentally. Small relative angles occur less frequently in the simulations than in the data, in the case of Gd + U, while the occurrence of both of small and large relative angles is underestimated in the Xe + Sn case. These difference may be due to the mixing of different central impact parameters in the data, while the calculations were performed only at zero impact parameter. It would obviously be interesting to clarify this point by performing BOB simulations also for finite impact parameters.

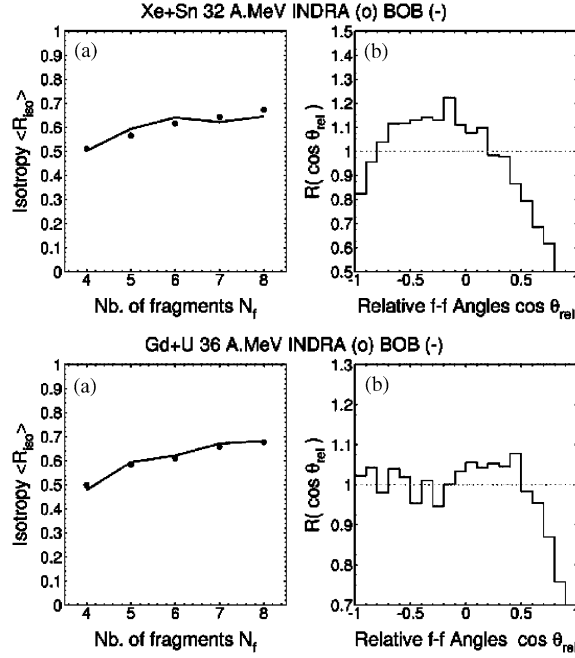


Fig. 6.6. Event geometry. The reactions 32 MeV/A Xe + Sn (*top*) and 36 MeV/A Gd + U (*bottom*) are studied either experimentally (points) or with BOB simulations (histograms). *Left*: The mean isotropic ratio of the IMF fragments versus the fragment multiplicity. *Right*: The calculated distribution of relative fragment angle, $P_{\text{BOB}}(\theta_{12})$ divided by the experimental distribution, $P_{\text{exp}}(\theta_{12})$, plotted against $\cos \theta_{12}$; equal distributions would yield unity. (From Ref. [278].)

The average kinetic energy, as a function of the fragment Z number, is compared with experimental data in Fig. 6.7. The nearly linear rise in the data for small Z may be attributed to the presence of a collective radial flow. The simulations provide a good description of the fragment energies for the Gd + U system, for which the Coulomb contribution to the radial flow is larger; for Xe + Sn the calculated energies fall within $\approx 20\%$ of the measured values. The simulations underestimate the fragment kinetic energies (and hence the radial flow), but this discrepancy is also below 20%. As indicated in the previous section, this underestimation could presumably be remedied by a quantum dynamical treatment since TDHF simulations have shown that semi-classical calculations tend to underpredict the expansion velocity by about 50%, as compared to the quantum calculations. However, considering that no parameters have been adjusted to reproduce the data, the present level of agreement is already impressive. It may thus be concluded that the BOB simulations yield a good global reproduction of the measured fragment properties, thus supporting spinodal decomposition as a candidate mechanism for the onset of multifragmentation.

6.2.1. Fragment velocity correlations

To achieve a deeper insight into the structure of the fragmentation pattern, more exclusive event-by-event analyses have been performed on both the experimental and theoretical side. Correlation functions for the relative fragment velocity are shown in Fig. 6.8 for the two INDRA reactions considered above and compared with the BOB predictions. Also shown are the statistical model

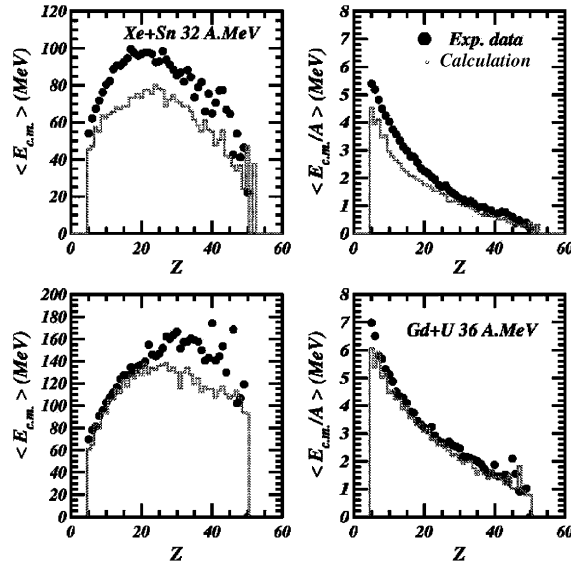


Fig. 6.7. Fragment kinetic energies. Comparison between measured (points) and calculated (histograms) average fragment kinetic energies, either total (*left*) or per nucleon (*right*), for Xe + Sn at 32 MeV/A (*top*) and Gd + U at 36 MeV/A (*bottom*). (From Ref. [278].)

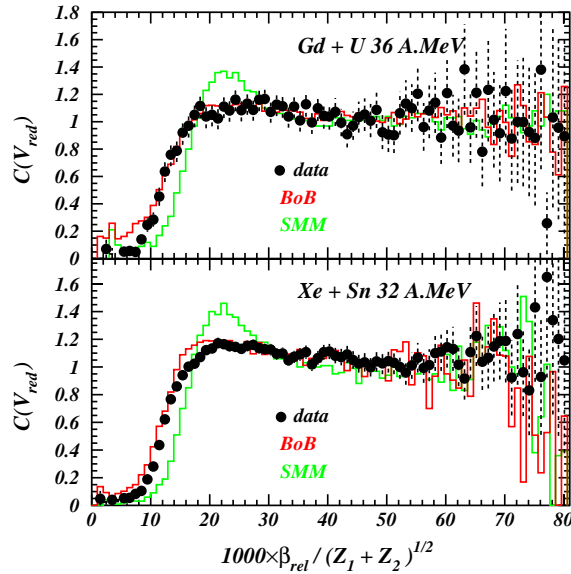


Fig. 6.8. Fragment velocity correlations. Correlation functions for the relative fragment velocity, as obtained in the INDRA data and compared with BOB and SMM predictions. (From Ref. [281].)

predictions for the disassembly of dilute and excited spherical sources under the hypothesis of statistical equilibrium.

The agreement between the data and the BOB calculations is very good. On the other hand, the comparison with SMM reveal a significant discrepancy. This seems to indicate that the dynamical simulations provide a fairly reliable description of the fragmentation geometry and the observed rather weak velocity correlation suggests that the effective freeze-out volume is relatively large. By contrast, the idealized filling of a spherical volume employed in the statistical calculation tends to overemphasize the fragment velocity correlations.

6.2.2. Partition correlations

Recently it has been investigated whether it may be possible to identify a specific signal reflecting the particular features of the early fragmentation pattern that are associated with spinodal decomposition. As extensively discussed in the previous sections, the onset of spinodal decomposition is characterized by the presence of nearly equal-sized fragments, due to the dominance of few unstable modes in the linear regime. Therefore, one may search for events that keep the memory of this initial configuration, typical of spinodal decomposition. Of course, these events are expected to appear in very small quantity, also because the experimental analysis is obviously done on the final fragment configurations. Following the analysis proposed by Moretto et al. [255], that reveals the presence of such events, even if they are very few, this study has been performed in [256], still on the INDRA data. This has revealed the presence of a few percentage of events having equal-size fragments. The striking feature is that very similar results are obtained when applying the same procedure to the BOB simulations, while statistical models do not predict at all the productions of such events [282]. As seen in Fig. 6.9, the peak at very small fluctuation ΔZ is an indication of a production of equal-size fragments, unambiguously larger than the background value, constructed considering partitions that mix randomly fragments taken from different events. This observation can be related to the particular features of the early partitions produced by the spinodal decomposition.

Given the relative weakness of the signal and its possible sensitivity to the detailed procedures (see Ref. [283]), much work has been done recently to improve the quality of the considered correlation function. In this connection, Desesquelles et al. [282] have developed a method for suppressing finite-size effects and express the correlation data relative to a purely statistical population of the phase space, thus obtaining a vastly improved representation of the physical information. Fig. 6.10 illustrates the corresponding result for the INDRA data. The spinodal signal now appears as a peak over a flat background, which is obviously much easier to interpret. These authors also showed that the fragment production in both percolation models and standard statistical multifragmentation is effectively independent, whereas the spinodal decomposition mechanism yields strong correlations characteristic of breakup into fragments of nearly equal size.

Altogether, these results provide strong evidence for the existence of a non-statistical fragmentation process leading to intermediate-mass fragments of almost equal size (the average IMF charge is $Z = 12\text{--}14$ and the dispersion is only about one charge unit). This novel event class is present within a limited range of bombarding energy and it is associated with small impact parameters. Although it represents only a few percent, it can be identified very clearly over a purely statistical background. The features of these events correspond very well to what is expected from a spinodal decomposition, as demonstrated particularly by BOB simulations which yield a quantitatively good

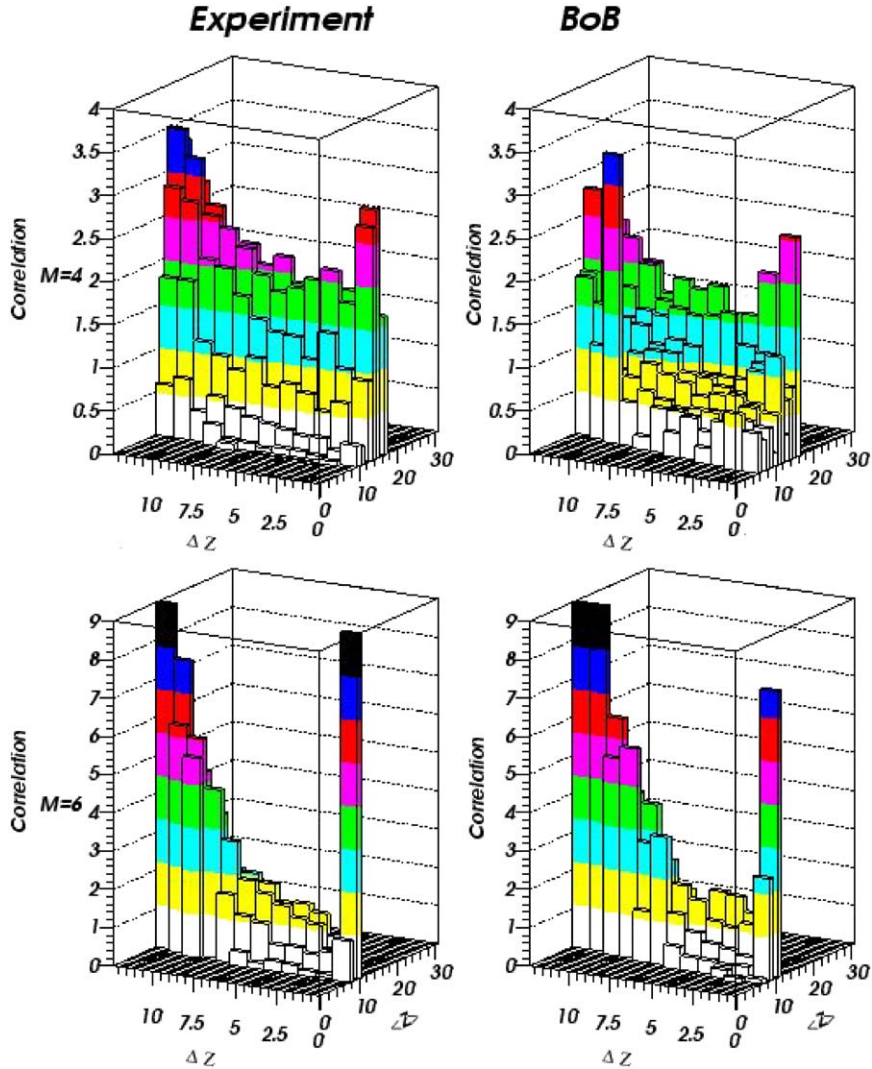


Fig. 6.9. Fragment size correlations. The IMF size correlations displayed as a two-dimensional histogram where the axis represent the average fragment charge Z and the associated dispersion σ_Z , as obtained either in the INDRA experiment or with the BOB simulations. The peak at very small σ_Z contains events having approximately equal-size fragments. (From Ref. [256].)

reproduction of the data with respect to both the small non-statistical population component and the dominant background which can be well described statistically (see below).

6.3. Discussion

From the above theoretical and experimental results it appears that the nuclear systems formed in central collisions at a suitable energy are compressed and/or heated sufficiently to ensure that their

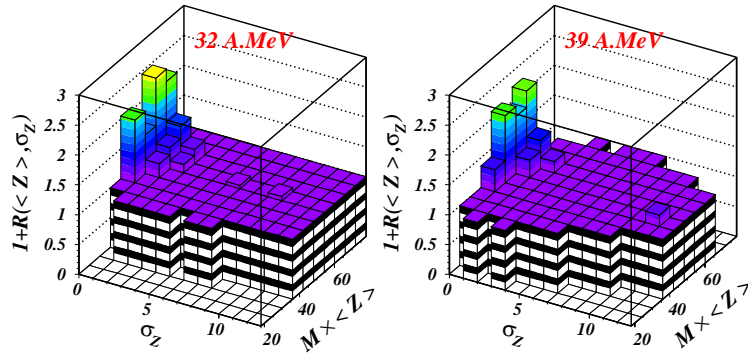


Fig. 6.10. Fragment size correlations. The IMF size correlations displayed as a two-dimensional histogram against the average fragment charge Z and the associated dispersion σ_Z , as obtained by a refined analysis of the INDRA data for two different bombarding energies. The peak at very small σ_Z contains events having approximately equal-size fragments. (From Ref. [284].)

bulk regions expand into the phase region of spinodal instability. Therefore, spinodal decomposition presents a plausible mechanism for the formation of multiple intermediate-mass fragments and, indeed, it seems that all the characteristics observed in various experiments can be understood as a result of spinodal decomposition. This is clearly illustrated by the ability of the brownian one-body dynamics (BOB) to reproduce the various data, including the multi-fragment size correlations. This success is especially remarkable in view of the fact that the calculations do not have any adjustable parameters, BOB being a well-defined approximation to the Boltzmann–Langevin equation in which the stochastic term is fundamentally related to the elementary scattering cross section in the medium.

The relation between the spinodal fragmentation mechanism and statistical multifragmentation deserves special discussion. Over the past 20 years, statistical multifragmentation models have been introduced and applied to multifragmentation data. Among these models, the most commonly employed assume that the partitions of the system are given by the statistical weights for an ensemble of hot products that are spatially confined, as would be the case if a uniform system within the liquid–gas coexistence phase region were allowed to equilibrate. (This general class of models include in particular FREESCO [14–16], MMMC [17,18], and SMM [19].) By suitable tuning of the parameters, including the freeze-out density, these models can generally be brought to render a good reproduction of the experimental inclusive fragment yields. For example, the observed INDRA IMF yields discussed above can be well reproduced by employing a freeze-out density that is one third of the saturation value and using a total excitation energy of about 6 MeV/A [285]. In fact, apart from the correlations between fragment speed and size, the statistical approaches are reproducing the various observables very well. Therefore, since the thermodynamic configurations deduced from such analyzes lie well inside the phase coexistence zone, this agreement may be considered as a further evidence for multifragmentation being associated with a first-order phase transition.

This general success of statistical models notwithstanding, it should be recognized that the underlying mechanism need not be statistical. Indeed, whenever the underlying dynamics is sufficiently complicated, one may generally expect a statistical appearance of reduced quantities, such as single-fragment observables. In particular, we have seen that a specific microscopic dynamical model,

namely the BOB approximation to the Boltzmann–Langevin equation, which contains no assumptions of thermal or chemical equilibrium (nor any tunable parameters), can fit the same single-fragment data equally well as the statistical models (and in fact does a better job for the fragment correlations), a feature noted already in the discussion of spinodal instabilities in asymmetric nuclear matter (Section 3.1.9). Thus, while it may at first seem surprising that the results of a dynamical description are so close to those of a statistical model, it should be recalled that thermodynamic equilibrium corresponds to an unbiased population of the available phase space. Therefore, one may take the similarity between dynamics and statistics as an indication that the dynamics is effective in filling the phase space during the relatively brief time available.

In the microscopic dynamical description, a fast democratic filling of the fragment partition phase space is in fact facilitated by the coupling of several important unstable modes, as discussed earlier. Thus, the spinodal decomposition mechanism provides the seeds of fragment formation and, even though this is typically a non-equilibrium process, it is possible for the single-fragment features to display a large degree of equilibration. Furthermore, the inequities in the population of the available phase space are reduced by the finiteness of the system as well as by the secondary decay processes. In this manner, the spinodal fragmentation dynamics provides justification for the application of statistical models.

However, it is to be expected that the success of the statistical models in accounting for the data depends on the degree of inclusiveness in the observables considered and that the character of the underlying dynamics may be revealed by more exclusive measurements. In particular, as the INDRA analysis of the fragment size correlations has shown, even a relatively small deviation from the statistical predictions may provide an unambiguous signal of the specific fragmentation mechanism.

In addition to accounting for the observed small non-statistical component consisting of nearly equal-mass fragments, the spinodal mechanism also provides a quantitative understanding the dominant statistical multifragmentation component as the combined result of the complex dynamics of the unstable modes, with the associated non-linearities and chaos leading to a fast population of the accessible phase space. Thus, for the vast majority of the events, their non-statistical origin in the spinodal decomposition mechanism is lost through the complicated fragmentation dynamics, while a few percent retain the spinodal characteristics to a degree sufficient for identification through correlation analysis. These can be considered as signature events for the spinodal multifragmentation mechanism.

7. Perspectives

Spinodal instability is a general phenomenon of relevance in many areas of physics. While the present review has focussed on the relationship between spinodal instability and fragmentation within the context of nuclear collisions, many of the methods and lessons are quite general and, as such, may be of utility in a broader context as well.

Within a general thermodynamic framework, we discussed in Section 2 how spinodal instability is intimately related to the occurrence of a first-order phase transition, as signalled by a convex anomaly in the thermodynamic potential. The onset of the associated spinodal decomposition was discussed in Section 3, where we saw how the onset of the phase separation can be understood by analyzing

the linear response of matter within the phase region of spinodal instability. The collective dynamics may then be described by simple feed-back equations. The associated dispersion relation identifies the modes that are amplified most rapidly and these will then tend to become dominant in the course of time. The theoretical tools for studying the further, increasingly complex, evolution were then discussed in Section 4 and we showed how the key physics is naturally contained within the Boltzmann–Langevin treatment, in which the stochastic outcome of individual two-body collisions between the constituent nucleons are propagated and amplified by the self-consistent effective one-body field. In particular, we discussed a relatively simple approximate treatment of the Boltzmann–Langevin equation, the Brownian One-Body model, in which the stochastic part of the two-body collision term is emulated by a suitably tuned stochastic one-body term, without the introduction of any adjustable parameters.

Then, in Section 5, we reviewed the applications of various dynamical treatments to nuclear fragmentation. These applications suggest that the nuclear collision zone indeed enters the spinodal phase region, under suitable conditions of bombarding energy and impact parameter. Furthermore, because the most unstable spinodal modes grow dominant, the resulting fragmentation pattern develops some regularity, leading to a significant enhancement of partitions into intermediate-mass fragments of nearly equal size, over what a purely statistical breakup would suggest.

Finally, we addressed the confrontation of these theoretical expectations with the relevant experimental data. Especially important is the INDRA observation of a small but significant non-statistical component consisting of multifragmentation events in which the intermediate-mass fragments have very similar charges. The agreement of the dynamical calculations with these data is remarkable, for the non-statistical component as well as for the dominant but featureless part of the events which can also be well accounted for statistically. Since it is hard to account for such a result by other means, it appears that spinodal decomposition is a major mechanism behind the multifragmentation phenomenon.

These intriguing findings suggest further work both experimentally and theoretically. At the breakup stage, spinodal fragmentation leads to the dominance of few fragmentation modes and an associated paucity of light fragments. However, as discussed in Section 5, these signature features may be degraded by the secondary deexcitation of the excited primary fragments. It is therefore essential to identify suitably robust observables. Even though some experimental analyzes have already been performed with the aim of extracting information about the primary fragment partitions, most notably the IMF charge partition analysis of the INDRA data, additional work still remains. Indeed, the charge correlation results are still under debate, with regard to both the definition of the uncorrelated reference that determines the normalization and the statistical significance of the extracted signal. This very important issue requires more work on the analysis methods and probably additional data with higher statistics. In addition to the need for disentangling the effect of the secondary deexcitation processes, it is important to explore the dynamical path of the fragmentation process since it is likely to depend on the specific mechanism operating. For this task new types of analysis must be developed.

Nowadays the possibility of studying fragmentation reactions with neutron-rich nuclei opens up entirely new perspectives. As discussed, the spinodal decomposition in asymmetric nuclear matter involves also a chemical component which is sensitive to the symmetry term in the nuclear matter equation of state and the fragmentation produces a corresponding chemical fractionation between the

liquid and gas phases. This type of information provides additional constraints that can be used to elucidate more precisely the multifragmentation path and thus help to test our understanding of the spinodal fragmentation process.

From the results reviewed in Section 5.3, it appears that spinodal decomposition in neutron-rich nuclei leads to isospin fractionation as a quite selective mechanism and it is encouraging that this phenomenon was recently observed [53,54]. Isospin fractionation may in fact be an even better signal of spinodal decomposition than the production of equal-size fragments, since coalescence effects and the competition between several unstable modes render the dynamical distributions rather similar to the statistical ones, apart from the deficit of light clusters in the spinodal dynamics. By contrast, the N/Z composition of the intermediate-mass fragments (which represent the liquid phase) does not depend much on the particular unstable modes involved and is therefore more robust. Thus, in the spirit of the fragment-size analysis performed on the INDRA data [23], one might seek analyses designed to reveal the N/Z values of the primary fragments. Such an approach could provide a more stringent test of spinodal decomposition and, at the same time, establish a more direct link between the observed results and the employed nuclear equation of state.

On the theoretical side, it is desirable to improve our description of spinodal decomposition dynamics. Even though the agreement between calculations and data is very good, there is a need for calculations that are theoretically more accurate. (We recall that the predictions for the INDRA case were made with the stochastic one-body model which is merely a rough approximation to the underlying Boltzmann–Langevin treatment, which itself is only a rather simplistic semi-classical model.) Only when the model is accurate and reliable can one hope that a comparison with data may yield quantitatively useful information about such key quantities as the nuclear equation of state. In this regard it seems important to go beyond the semi-classical level and take account of various quantal effects, such as memory time.

Another aspect deserving further theoretical investigation is the relation between the dynamical path and the population of the available phase space. It might be instructive to determine the degree of equilibration achieved in the course of the nuclear spinodal decomposition process and, in association with this, to identify signals reflecting the non-equilibrium features that are specific to the spinodal mechanism.

Concurrent with the advances in understanding nuclear spinodal fragmentation, discussed here in detail, there have been exciting developments on related topics, specifically regarding the occurrence of anomalies in the nuclear specific heat, which provides another phase-transition signal. This has helped stimulate renewed interest in nuclear multifragmentation as a means for probing nuclear matter away from the ordinary equilibrium. We hope that the present review will provide a valuable resource for anyone interested in this topic.

Acknowledgements

This work was supported by the Director, Office of Energy Research, Office of High Energy and Nuclear Physics, Nuclear Physics Division of the US Department of Energy under Contract No. DE-AC03-76SF00098.

Appendix A. Seyler–Blanchard model

Here we give some specific expressions for the generalized Seyler–Blanchard model, a self-consistent microscopic model based on a finite-range two-body interaction whose strength is modulated by a momentum and density dependence. When solved in the semi-classical (Thomas–Fermi) approximation it yields a good quantitative reproduction of a variety of macroscopic nuclear properties, such as the binding energies, fission barriers, and density distributions of nuclei [34,286]. In addition, for our particular parameter choice, the energy dependence of the optical potential is also quite well reproduced. Further details can be found in Ref. [35].

A.1. Basics

For spin–isospin saturated systems, the basic two-body interaction is given by

$$V(\mathbf{r}_1, \mathbf{r}_2) = -C \left[1 - \bar{\chi} \frac{p_{12}^2}{b^2} - \chi \frac{\kappa_s}{\rho_s} \left(\left(\frac{\rho(\mathbf{r}_1)}{\rho_s} \right)^{2/3} + \left(\frac{\rho(\mathbf{r}_2)}{\rho_s} \right)^{2/3} \right) \right] \frac{e^{-r_{12}/a}}{r_{12}/a}, \quad (\text{A.1})$$

where $r_{12} \equiv |\mathbf{r}_1 - \mathbf{r}_2|$ is the separation between the two nucleons, $p_{12} \equiv |\mathbf{p}_1 - \mathbf{p}_2|$ is the difference between their momenta, and $\bar{\chi} \equiv 1 - \chi$. Furthermore, ρ_s denotes the saturation value of the matter density (A.6) and κ_s is the corresponding value of the zero-temperature kinetic density (A.7). There are a total of four parameters in the model, a, b, C, χ . The first three characterize the original Seyler–Blanchard model [134], which emerges for $\chi = 0$. For those we employ the same values as in Ref. [35], $a = 0.557$ fm, $T_{\text{SB}} = b^2/2m = 89.274$ MeV, and $C = 435.1$ MeV, leading to a saturation density of $\rho_s = 0.153$ fm^{−3}, a compressibility of $K = 294.60$ MeV, and a surface-energy coefficient of $a_2 = 18.06$ MeV [35]. (For two-component systems, the strength parameter C is replaced by C_l and C_u governing the interaction strength between like and unlike nucleons, respectively [134].)

However, the energy dependence of the optical potential is then too strong, as reflected in the value $m_s^* = 0.3817m$ for the effective nucleon mass at $\rho = \rho_s$. This problem can be largely remedied by replacing part of the momentum dependence by a density dependence [34,286]. The generalized interaction (A.1) was introduced in Ref. [35] for this purpose. It has been constructed so any value of the additional parameter χ leads to the identically same results for the average nuclear properties mentioned above, at zero temperature. Furthermore, as χ is increased from zero, the effective nucleon mass m^* increases steadily and reaches its free value for $\chi = 1$. A realistic value, $m_s^* = 0.7118m$ is obtained for $\chi = 0.75$ [35].

When employing the semi-classical mean-field approximation, the motion of the individual nucleons is governed by an effective one-body Hamiltonian having a simple standard form,

$$h[f](\mathbf{r}, \mathbf{p}) = \frac{p^2}{2m^*[\rho](\mathbf{r})} + U[\rho](\mathbf{r}), \quad (\text{A.2})$$

due to the quadratic momentum dependence of V_{12} . The effective mass $m^*(\mathbf{r})$ and the effective potential $U(\mathbf{r})$ are generally functionals of the entire one-body phase-space density $f(\mathbf{r}, \mathbf{p})$, but for the particular interaction (A.1), m^* is a functional of the matter density $\rho(\mathbf{r})$ only and U is

a functional of $\rho(\mathbf{r})$ and the kinetic density $\kappa(\mathbf{r})$,

$$\frac{m}{m^*(\mathbf{r})} = 1 + \tilde{\chi} \frac{C}{T_{\text{SB}}} \tilde{\rho}(\mathbf{r}) , \quad (\text{A.3})$$

$$U(\mathbf{r}) = -C \left(\tilde{\rho}(\mathbf{r}) - \tilde{\chi} \tilde{\kappa}(\mathbf{r}) - \chi \tilde{\gamma}(\mathbf{r}) - \frac{5}{3} \chi \frac{\gamma(\mathbf{r})}{\rho(\mathbf{r})} \tilde{\rho}(\mathbf{r}) \right) , \quad (\text{A.4})$$

where we have introduced the auxiliary kinetic density $\gamma(\mathbf{r}) = (\rho(\mathbf{r})/\rho_s)^{5/3} \kappa_s$ and the tilde denotes a convolution with the normalized form factor $g(r) = \exp(r/a)/4\pi a^2 r$, $\tilde{\rho} \equiv g * \rho$, $\tilde{\kappa} \equiv g * \kappa$, and $\tilde{\gamma} \equiv g * \gamma$.

In the mean-field approximation, the state of the system is characterized by its one-particle phase-space density distribution $f(\mathbf{r}, \mathbf{p})$. We shall assume that the system is in local thermal equilibrium at a given temperature T ,

$$f(\mathbf{r}, \mathbf{p}) = [1 + e^{\beta(h(\mathbf{r}, \mathbf{p}) - \mu(\mathbf{r}))}]^{-1} = [1 + e^{p^2/2m^*(\mathbf{r})T - \alpha(\mathbf{r})}]^{-1} , \quad (\text{A.5})$$

with $\alpha(\mathbf{r}) = (\mu(\mathbf{r}) - U(\mathbf{r}))/T$. If the density $\rho(\mathbf{r})$ is specified, then the local chemical potential $\mu(\mathbf{r})$ follows. Conversely, specification of the chemical potential determines the density. This latter quantity and the associated kinetic density $\kappa(\mathbf{r})$ can be expressed in terms of the Fermi–Dirac moments $F_n(\alpha) = \int dx x^n / [1 + \exp(x - \alpha)]$,

$$\rho(\mathbf{r}) \equiv g \int \frac{d\mathbf{p}}{h^3} f(\mathbf{r}, \mathbf{p}) = F_{1/2}(\alpha(\mathbf{r})) \rho_T(\mathbf{r}) , \quad (\text{A.6})$$

$$\kappa(\mathbf{r}) \equiv g \int \frac{d\mathbf{p}}{h^3} \frac{p^2}{b^2} f(\mathbf{r}, \mathbf{p}) = \frac{2m^*(\mathbf{r})}{b^2} TF_{3/2}(\alpha(\mathbf{r})) \rho_T(\mathbf{r}) , \quad (\text{A.7})$$

with $g=4$ and $\rho_T(\mathbf{r}) = 2\pi[2m^*(\mathbf{r})T]^{3/2}/h^3$. For a given temperature T , the above system of equations can be solved self-consistently for either uniform matter [35] or for less trivial configurations, such as slabs, rods, and spheres [36].

A.2. Thermodynamics

The key thermodynamic quantity is the free energy $F = E - TS$. For the present discussion of uniform matter, it is more convenient to consider the corresponding intensive quantities, namely the densities $e = E/V$, $s = S/V$, and $f = F/V = e - Ts$,

$$e = T_{\text{SB}}\kappa - \frac{1}{2} Cn\rho + Cn\kappa_{\text{eff}} , \quad (\text{A.8})$$

$$Ts = T \left(\frac{5}{3} F_{3/2}(\alpha) - \alpha F_{1/2}(\alpha) \right) \rho_T = \frac{5}{3} T_{\text{SB}}\kappa - Cn\rho + \frac{8}{3} Cn\kappa_{\text{eff}} - \mu\rho , \quad (\text{A.9})$$

$$f = -\frac{2}{3} T_{\text{SB}}\kappa + \frac{1}{2} Cn\rho - \frac{5}{3} Cn\kappa_{\text{eff}} + \mu\rho , \quad (\text{A.10})$$

where $n \equiv 4\pi a^3 \rho$ is the number of nucleons within the interaction range. The energy per nucleon, $\epsilon \equiv e/\rho$, and entropy per nucleon, $\sigma \equiv s/\rho$, are displayed in Fig. A.1. While ϵ has a minimum for all temperatures (which moves outwards as T is increased), σ is steadily decreasing due to the decrease in the available volume.

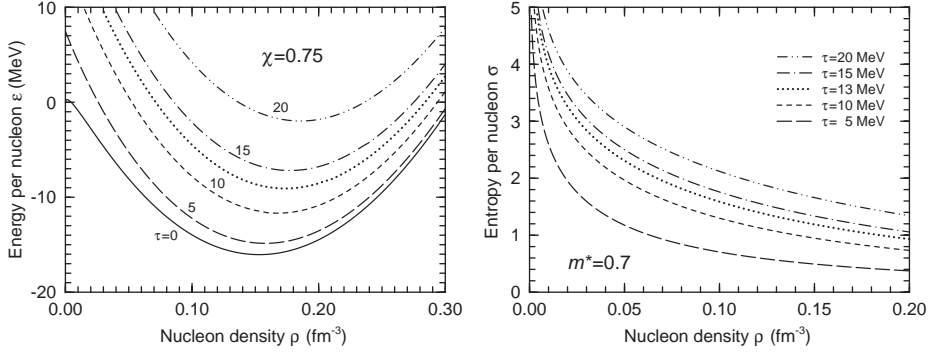


Fig. A.1. Energy and entropy of nuclear matter. The energy per nucleon $\epsilon = E/A$ (left) and the entropy per nucleon, $\sigma = S/A$ (right), in uniform isosymmetric nuclear matter as a function of the nucleon density ρ , for a range of temperatures, $T = 0, 5, 10, 15, 20$ MeV. Results are also shown for the limiting temperature $T_{\text{lim}} = 13$ MeV at which nuclear matter ceases to be self-cohesive. (From Ref. [35].)

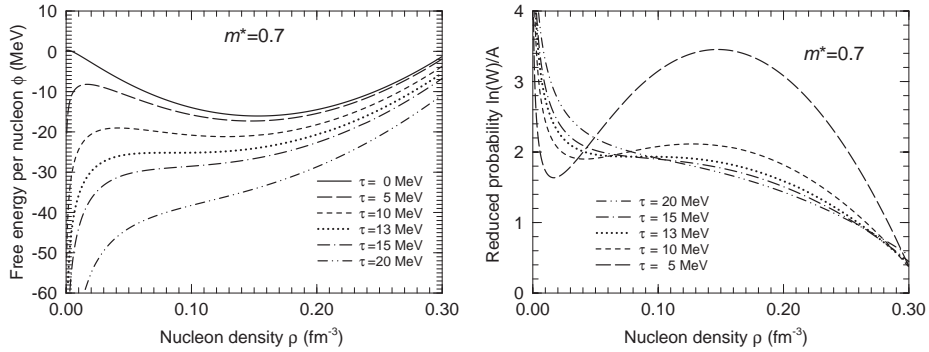


Fig. A.2. Free energy and statistical weight of nuclear matter. The free energy per nucleon $\phi = E/A$ (left) and the associated reduced statistical weight, $\omega = (1/A)\ln W = -\beta\phi = \sigma - \beta\epsilon$ (right), in uniform isosymmetric nuclear matter as a function of the nucleon density ρ for a range of temperatures. Nuclear matter ceases to be self-cohesive at the limiting temperature $T_{\text{lim}} = 13$ MeV. (From Ref. [35].)

The thermodynamic equilibrium state is determined by the free energy per nucleon, $\phi = \epsilon - T\sigma$, which is shown in Fig. A.2 (left). This quantity exhibits a minimum that moves inwards with T , since the subtraction of the entropy introduces a steady bias towards lower densities. The corresponding phase diagram, shown in Fig. 2.3, is most easily determined from the pressure, $P = -\partial_V F = \rho^2 \partial_\rho \phi$.

A.2.1. Statistical weight

For infinite matter the free energy diverges in proportion to A and the statistical weight $W[\rho]$ becomes a singular distribution sharply peaked at the most probable configuration. However, it is possible for finite systems to make excursions away from the most probable configuration. (Such systems can be studied by imposing periodic boundary conditions.) It is therefore instructive to consider the quantity $\omega = (1/A)\ln W = \sigma - \beta\epsilon$, which is the logarithm of the statistical weight divided by the number of nucleons in the system [35]. It is shown in Fig. A.2 (right).

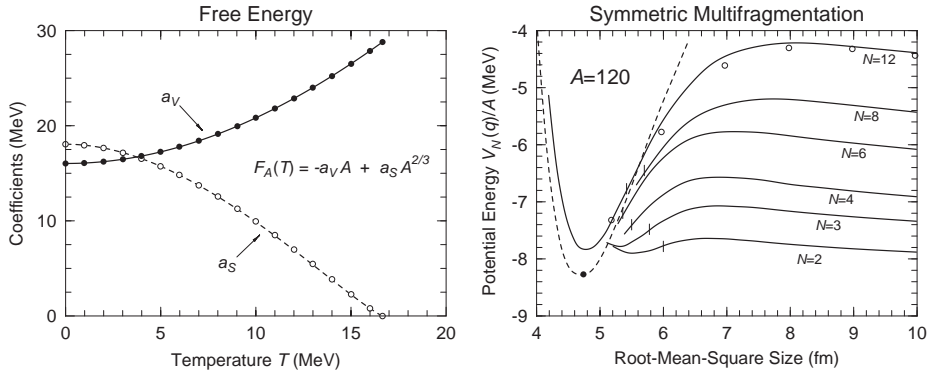


Fig. A.3. Hot nuclei and multifragmentation. *Left*: Temperature dependence of the volume and surface coefficients a_V and a_S in the liquid-drop expansion of the free energy F_A of a hot nucleus embedded in a nucleon vapor held at a given temperature T , see Eq. (A.11). *Right*: A system with 50 (charged) protons and 70 neutrons is represented as a symmetric configuration of N spherical fragments of equal size. The figure shows the energies of the corresponding N -fragment systems, as functions of the rms size of the total matter distribution, calculated at zero temperature. The vertical bars indicate the point at which the N spheres touch. For $N = 12$ the open circles are obtained for an alternate symmetric arrangement of the fragments. The dashed curve shows the result of a monopole distortion of ^{120}Sn . (Adapted from Ref. [36].)

For temperatures below the limiting value T_{lim} , the statistical weight has two peaks, reflecting the bimodal nature of the phase-coexistence equilibrium. The liquid-type peak is near the saturation density, as expected, and the most favored density shifts gradually towards more dilute values as the temperature is raised. In concert with this shift, the peak broadens and the vapor spike in the dilute region near zero density grows increasingly prominent. Thus, the system is metastable, in accordance with the fact that a nucleus held at a constant temperature will gradually disassemble into a dilute gas through sequential evaporation. When the temperature reaches a certain limiting value, there is no longer a maximum at finite density and the statistical weight increases monotonically with decreasing density, basically reflecting the increase in the entropy. This limiting temperature is thus the highest one for which a self-cohesive metastable nucleus can exist. Above T_{lim} and up to T_{crit} , metastability can be maintained only if an external pressure is applied.

A.2.2. Hot nuclei

Nuclear multifragmentation involves hot nuclei embedded a nucleon vapor [100,287,288] and the framework described above makes it possible to calculate the thermodynamic properties of such systems. In particular, the dependence of the level density parameter and the free energy on mass number and temperature can be determined [36]. For example, if only the volume and surface terms are considered, the free energy of an uncharged hot nucleus may be written on liquid-drop form,

$$F_A(T) = -a_V(T)A + a_S(T)A^{2/3}. \quad (\text{A.11})$$

The resulting volume and surface coefficients a_V and a_S are shown in Fig. A.3 (left). As the temperature is raised from zero, the volume coefficient increases steadily from its normal saturation value, $a_V(0) \approx 16.0$ MeV, until T reaches the critical temperature, $T_{\text{crit}} \approx 16.7$ MeV, above which there is only a single phase. At the same time, the surface coefficient, $a_S(T)$, decreases from its normal

value of $a_S(0) \approx 18.0$ MeV towards zero. The associated surface tension is very well reproduced by a simple analytic approximation, $\gamma(T) \approx \gamma(0)(1 + \frac{3}{2} T/T_c)(1 - T/T_c)$ [36].

A.2.3. Multifragmentation

An advantage of the treatment is that once the density distribution $\rho(\mathbf{r})$ has been specified, the associated free energy can be determined for any temperature and it yields directly the corresponding statistical weight (see above). Thus it is possible to discuss an equilibrium ensemble of different manifestations of the same system.

This is of particular interest in connection with nuclear multifragmentation where a given system may transform itself into macroscopically different configurations. As an illustration of this utility, the authors of Ref. [36] considered the breakup of a system with $A = 120$ into various multifragment channels, each one consisting of equal-size spherical fragments arranged symmetrically. The associated potential energy barrier is shown in Fig. A.3 (right). These are particularly relevant for the regular kind of fragmentation favored by the spinodal mechanism (see Sections 5.2.2 and 5.2.3) and they typically amount to a few MeV per nucleon, increasing with the number of fragments.

A.3. Landau parameters

We shall now consider small deviations from uniform matter, $\rho(\mathbf{r}) = \rho_0 + \delta\rho(\mathbf{r})$. If ρ_k denotes the Fourier component of $\delta\rho(\mathbf{r})$, the induced change in the effective Hamiltonian, $\delta h = 4\pi a^3 (\partial h / \partial \rho) * \delta\rho$, then has Fourier components of the form $h_k = (\partial h_k / \partial \rho) \rho_k$, where $\partial h_k / \partial \rho$ denotes the Fourier component of $\partial h / \partial \rho$. The Landau parameters of interest can then be readily obtained [117],

$$F_0(k, T) \equiv \phi_0 \frac{\rho_0}{T} \frac{\partial h_k}{\partial \rho} \approx \frac{m_0^*}{m} \frac{n_0 C}{T_F T_{SB}} \left[\chi T_F - \frac{3}{2} \frac{T_{SB} - 2\tilde{\chi} T_0 - 2\chi T_F}{1 + a^2 k^2} \right], \quad (\text{A.12})$$

$$F_1 \equiv 3 \left(\frac{m_0^*}{m} - 1 \right) = - \frac{3n_0 \tilde{\chi} C / T_{SB}}{1 + n_0 \tilde{\chi} C / T_{SB}}, \quad (\text{A.13})$$

with $n_0 = 4\pi a^3 \rho_0$. Furthermore, $T_F = P_F^2 / 2m \sim \rho_0^{2/3}$ is the zero-temperature Fermi kinetic energy associated with the specified average density ρ_0 , while the temperature dependent “effective Fermi energy” is $T_0 = T_{SB} \partial \kappa / \partial \rho = m_0^* \phi_1 / m \phi_0 \approx 3m_0^* T / 2m \phi_0$, with ϕ_n being the Fermi-surface moments defined in Appendix C.1. For $k, T \rightarrow 0$, corresponding to infinitely gentle density undulations in cold matter, the usual Landau parameter F_0 is recovered. For any value of the wave number k , the spinodal region is characterized by $F_0(k, T) < -1$, and within this region the system is unconditionally unstable against harmonic density distortions having a wave number smaller than k . Because of the finite range of the interaction, such instabilities can occur only for wave numbers below a certain maximum value k_0 depending on the density and temperature considered. For positive values of F_0 the system is unconditionally stable against density undulations, whereas it is subject to Landau damping for F_0 values in the interval between 0 and -1 .

The above standard Landau parameters F_0 and F_1 for cold uniform nuclear matter (i.e. $k, T = 0$) were displayed in Fig. 3.2 as functions of the density ρ , for different values of the parameter χ (which governs the effective mass at saturation, m_s^*). The dotted curves correspond to $\chi = 0$, the standard Seyler–Blanchard model in which all the modulation arises from the quadratic momentum

dependence [134]. The dashed curves are for $\chi = 0.75$, for which the effective mass has a realistic value, $m_s^* \approx 0.7m$ [35]. The solid curves show what would result if the interaction had no momentum dependence at all, $\chi = 1$, as is most often the case in effective Skyrme-type interactions. It should be noted that since all values of the parameter χ lead to the same static properties at zero temperature, all curves pass through the value $F_0 = -1$ at the same density, $\rho \approx 0.66\rho_s$, thus agreeing on the delineation of the spinodal zone at $T = 0$. Interestingly, for our preferred model having $\chi = 0.75$, the Landau parameter F_0 changes from negative to positive just below the saturation value of the density, so that all density undulations are unconditionally stable for $\rho \geq \rho_s$.

The dependence of F_0 on the wave length of the density undulations, $\lambda = 2\pi/k$, was illustrated in Fig. 3.5 (left), for zero temperature. The value of F_0 generally increases (i.e. the curve moves up) as the wave number k grows, since more rapidly changing undulations are more costly in energy. The spinodal zone then shrinks and the smallest unstable wavelength is $\lambda_{\min} \approx 3.48$ fm and occurs at $\rho \approx 0.12\rho_s$.

The temperature dependence of F_0 was illustrated in Fig. 3.5 (right) for the wave length $\lambda = 8$ fm, near which the most rapid growth occurs. It is qualitatively similar to the dependence on the wave number k , and thus F_0 grows steadily as the temperature is increased (or, conversely, the collision system becomes increasingly unstable as it expands and cools). As the temperature is increased from zero (solid curve, corresponding to the short-dashed curve in the left panel) in increments of 2 MeV up to $T = 10$ MeV (dotted curve), the value of $F_0(k, T)$ steadily increases, in accordance with the fact that the spinodal density zone shrinks as a function of the temperature.

Fig. 3.6 showed the corresponding spinodal boundaries associated with various wave lengths λ . As the wave number of the mode is increased, the region of instability shrinks. The most noticeable effects are the steady reduction of both the maximum temperature and the maximum density, whereas the minimum density only grows significantly close to the maximum unstable wave number. The standard spinodal boundary obtained in the thermodynamic analysis corresponds to $\lambda = \infty$.

A.3.1. Density ripples

We finally note that for a harmonic density distortion, $\rho(\mathbf{r}) = \rho_0(1 + c \cos \mathbf{k} \cdot \mathbf{r})$, the average free energy per nucleon is of quadratic form, $\phi = \phi_0 + \frac{1}{2} \phi_2 c^2$, for $c \ll 1$. The stiffness coefficient ϕ_2 is simply related to the Landau parameter, $\phi_2 \sim 1 + F_0$, and for zero temperature it is given by

$$\phi_2^{T=0} = \frac{1}{3} T_F \left(1 + n_0 \frac{C}{T_{SB}} \right) + \frac{n_0 C}{1 + a^2 k^2} \left(\frac{T_F}{T_{SB}} - \frac{1}{2} \right) = \frac{1}{3} T_F [1 + F_0(k, T = 0)] . \quad (\text{A.14})$$

Thus it is readily seen that the restoring coefficient ϕ_2 is a steadily decreasing function of the wavelength of the ripples, $\lambda = 2\pi/k$. Whenever it is negative, the system is unstable against infinitesimal oscillations of the specified wavelength. In the intermediate region, outside the spinodal region but still inside the region of phase coexistence, the system is stable with respect to small undulations, but there exist finite redistributions of the matter that have a more favorable statistical weight. (Indeed, as an example, the possibility of phase coexistence implies that cold uniform matter slightly below saturation prefers to condense into large separated regions of matter of normal density, interspersed with a dilute nucleon gas.) This method of analysis was employed in Ref. [35] to determine the maximum wave length for which spinodal instability exists at a given point in the ρ – T phase plane.

A.4. Collective modes in unstable nuclear matter

The phase diagram of nuclear matter exhibits a spinodal zone within which the system is mechanically unstable, so that small density irregularities may be amplified by the effective field. We apply here the formal framework described in Section 3.1.4 to the Seyler–Blanchard model in order to obtain specific quantitative results for the growth rates of the unstable collective modes in nuclear matter.

The collisionless evolution of the phase-space density $f(\mathbf{r}, \mathbf{p})$ is described by the Vlasov equation, $\partial f / \partial t = \{h[f], f\}$. We wish to consider situations in which the system exhibits small deviations from uniform matter at thermal equilibrium. The phase-space density is then of the form $f = f^0 + \delta f$, where $\delta f \ll f^0$ and $f^0(\mathbf{r}, \mathbf{p}) = [1 + \exp((h(\mathbf{r}, \mathbf{p}) - \mu)/T)]^{-1}$ is the Fermi–Dirac equilibrium distribution. For uniform matter the effective field $U(\mathbf{r})$ and the effective mass $m^*(\mathbf{r})$ are independent of position, and so f^0 depends only on the magnitude momentum. Moreover, the corresponding effective Hamiltonian is $h_0(\mathbf{r}, \mathbf{p}) = \epsilon = p^2/2m_0^* + U_0$, where the subscript 0 refers to the specified uniform density ρ_0 . To leading order in the small distortion $\delta f(\mathbf{r}, \mathbf{p})$, the temporal evolution is then governed by the following equation:

$$\frac{\partial \delta f}{\partial t} + \frac{\partial \delta f}{\partial \mathbf{r}} \cdot \frac{\partial h^0}{\partial \mathbf{p}} - \frac{\partial f^0}{\partial \mathbf{p}} \cdot \frac{\partial \delta h}{\partial \mathbf{r}} = 0. \quad (\text{A.15})$$

We note that $\partial f^0 / \partial \mathbf{p} = (\partial f^0 / \partial h_0)(\partial h_0 / \partial \mathbf{p})$ where $\partial h_0 / \partial \mathbf{p} = \mathbf{v}$. Since $\partial f^0 / \partial h_0 \approx \delta(\epsilon - \epsilon_F)$, it follows that δh needs to be evaluated only near the Fermi surface, as already anticipated in Eq. (A.12).

The corresponding equation of motion for the associated Fourier component

$$f_{\mathbf{k}}(\mathbf{p}, t) = \int \frac{d\mathbf{r}}{\sqrt{\Omega}} e^{-i\mathbf{k} \cdot \mathbf{r}} \delta f(\mathbf{r}, \mathbf{p}, t) \quad (\text{A.16})$$

is given by

$$\frac{\partial}{\partial t} f_{\mathbf{k}} + i\mathbf{k} \cdot \mathbf{v} f_{\mathbf{k}} - i\mathbf{k} \cdot \mathbf{v} \frac{\partial f^0}{\partial \epsilon} \frac{\partial h_{\mathbf{k}}}{\partial \rho} \rho_{\mathbf{k}} = 0, \quad (\text{A.17})$$

where $\partial h_{\mathbf{k}} / \partial \rho$ is given in (A.12) and $\rho_{\mathbf{k}} = (g/h^3) \int d\mathbf{p} f_{\mathbf{k}}(\mathbf{p})$.

As shown in Ref. [112], there are two collective modes for each wave number \mathbf{k} ,

$$f_{\mathbf{k}}^{\pm}(\mathbf{p}, t) = f_{\mathbf{k}}^{\pm}(\mathbf{p}) e^{\mp i\omega_{\mathbf{k}} t}, \quad (\text{A.18})$$

and inside the spinodal zone the frequencies are imaginary, so we may write $\omega_{\mathbf{k}} = i/t_{\mathbf{k}}$. The momentum dependence is given by

$$f_{\mathbf{k}}^{\pm}(\mathbf{p}) = \frac{\partial h_{\mathbf{k}}}{\partial \rho} \frac{\mathbf{k} \cdot \mathbf{v}}{\mathbf{k} \cdot \mathbf{v} \mp i t_{\mathbf{k}}^{-1}} \frac{\partial f^0}{\partial \epsilon} \approx -\frac{F_0}{\rho \phi_0} \frac{\mu}{\mu \mp i \gamma_{\mathbf{k}}} f^0 \tilde{f}^0. \quad (\text{A.19})$$

In the last relation we have used the fact that $T \partial f^0 / \partial \epsilon = -f^0 \tilde{f}^0$. Moreover, since the eigenmodes receive their support from states near the Fermi surface, we have that $\mathbf{k} \cdot \mathbf{v} \approx k V_F \mu$, so the angular and energy dependencies effectively decouple. Finally, we have introduced the dimensionless quantity $\gamma_{\mathbf{k}} = 1/k V_F t_{\mathbf{k}}$. This quantity is generally smaller than unity, being about one-third for the most rapidly amplified mode ($\lambda = 8$ fm) and at the typical temperature ($T = 4$ MeV), and it therefore provides

a meaningful expansion parameter. Expansions in terms of γ_k are especially useful near the spinodal boundary where this quantity tends to zero,

$$\left\langle \frac{\mu}{\mu - i\nu\gamma_k} \right\rangle = 1 + \left\langle \frac{i\nu\gamma_k}{\mu - i\nu\gamma_k} \right\rangle \approx -\frac{1}{F_0} \rightarrow -\frac{1}{2}\pi\gamma_k + \gamma_k^2 + \dots, \quad (\text{A.20})$$

where $\langle \cdot \rangle$ denotes the angular average over the direction $\hat{\mathbf{p}}$ of the momentum \mathbf{p} , evaluated in the Fermi surface where $p = P_F$. Thus $\gamma_k \rightarrow 0$ at the spinodal boundary where $F_0 \rightarrow -1$, i.e. the growth times diverge, $t_k \rightarrow \infty$, as one would expect.

Integration of the equation of motion (A.17) over the momentum leads to a dispersion equation from which the characteristic time t_k can be determined,

$$1 = g \int \frac{d\mathbf{p}}{h^3} \frac{\partial h_k}{\partial \rho} \frac{\mathbf{k} \cdot \mathbf{v}}{\mathbf{k} \cdot \mathbf{v} \mp i t_k^{-1}} \frac{\partial f^0}{\partial \epsilon} \quad (\text{A.21})$$

$$\approx -F_0(k, T) \left\langle \frac{\mu^2}{\mu^2 + \gamma_k^2} \right\rangle = -F_0(k, T) \left(1 - \gamma_k \arctan \frac{1}{\gamma_k} \right). \quad (\text{A.22})$$

The dispersion equation (A.21) implies that the normalization of eigenfunctions (A.19) is such that $\rho_{\mathbf{k}}^{\pm} \equiv (g/h^3) \int d\mathbf{p} f_{\mathbf{k}}^{\pm}(p) = 1$. In deriving approximation (A.22), it has been exploited that the factor $\partial f^0 / \partial \epsilon$ is peaked in the Fermi surface, and so the energy dependence of the angular average has been ignored, which is a very good approximation [117]. It should be emphasized, though, that it is important to employ an accurate value of the surface moment ϕ_0 . However, because the relevant densities are so low, the standard Sommerfeld expansion is inadequate for temperatures in excess of a few MeV and it would in fact be better to employ the rough exponential approximation $\phi_0 \sim \exp(-(\pi T/\epsilon_F)^2/12)$; at $T = 4$ MeV the fastest growth rates would then be overestimated by typically 10% and the slower ones by considerably more, and the error increases rapidly with temperature. For the results presented here, ϕ_0 is generally calculated numerically to ensure good accuracy.

Since the function $\gamma \arctan(1/\gamma)$ increases steadily from 0 to 1 as γ is changed from 0 to ∞ , it is readily seen that the above dispersion equation (A.22) has real roots $\pm\gamma_k$ when $F_0(k, T) < -1$. It is straightforward to determine γ_k by iterating the relation $\gamma^{-1} = \arctan(\gamma^{-1})F_0/(1 + F_0)$, starting from the value $\gamma = 1$, for example. It is an excellent approximation to ignore the energy average and just perform the angular average at the Fermi surface [117]. The resulting growth rates were illustrated in Fig. 3.7.

Appendix B. Boltzmann–Langevin transport treatment

In this appendix, we discuss the most important developments regarding the transport treatment of the Boltzmann–Langevin model.

We consider an ensemble of identical many-body systems, labelled by $n = 1, \dots, N$, each of which has its own reduced one-particle phase-space density, $f^{(n)}(\mathbf{r}, \mathbf{p})$. In order to facilitate the discussion, we shall, for the time being, ignore the spin–isospin degrees of freedom so that we effectively have a one-component system with a degeneracy of $g = 4$. The incorporation of spin and/or isospin is straightforward but of course makes the formulas more complicated. Moreover, it simplifies the

notation to use a single symbol to denote a location in phase space, $\mathbf{s} = (\mathbf{r}, \mathbf{p})$. It is convenient to normalize $f^{(n)}(\mathbf{s})$ so it expresses the occupancy of an elementary phase-space cell of volume h^D ,

$$g \int d\mathbf{s} f^{(n)}(\mathbf{s}) = g \int \frac{d^D \mathbf{r} d^D \mathbf{p}}{h^D} f^{(n)}(\mathbf{r}, \mathbf{p}) = \int d^D \mathbf{r} \rho^{(n)}(\mathbf{r}) = A, \quad (\text{B.1})$$

where $\rho^{(n)}(\mathbf{r})$ is the spatial density of the system n and A is the total number of nucleons in the system. It is important to note that although the physical system consists of individual nucleons (and thus has ascertain coarseness), its one-particle phase-space density appears as a continuous (and incompressible) fluid.

Assume now that the N systems have all been prepared in the same manner, so their initial one-particle phase-space densities are all equal, $f^{(n)}(\mathbf{s}, t=0) = f_0(\mathbf{s})$, while the systems generally different the many-body level. Each of the N systems now evolve independently under the combined actions of its individual self-consistent effective one-body hamiltonian (its “mean field”) and the residual interactions. Due to the stochastic nature of the residual interaction, the individual systems evolve differently at the many-body level and, generally, their reduced one-body densities will therefore also start to differ. The phase-space density of an individual system may then be written in the form

$$f^{(n)}(\mathbf{s}, t) = f(\mathbf{s}, t) + \delta f^{(n)}(\mathbf{s}, t), \quad (\text{B.2})$$

where the first term is the average density,

$$f(\mathbf{s}, t) = \prec f^{(n)}(\mathbf{s}, t) \succ = \frac{1}{N} \sum_{n=1}^N f^{(n)}(\mathbf{s}, t). \quad (\text{B.3})$$

The second term, $\delta f^{(n)}(\mathbf{s}, t)$, denotes the deviation of the individual one-body density from the ensemble-averaged density (obviously $\prec \delta f^{(n)}(\mathbf{s}, t) \succ$ vanishes).

The individual evolutions of the one-body densities $f^{(n)}(\mathbf{r}, \mathbf{p})$ will in turn cause the individual mean fields $h[f^{(n)}]$ to become different. As a result, in the abstract space of the one-body phase-space densities, the ensemble will evolve from the single initial point f_0 into a ever spreading bundle of individual trajectories $\{f^{(n)(t)}\}$. When the spread is relatively moderate, as it will be initially and as it tends to be for stable scenarios, it is useful to characterize the fluctuations of $f^{(n)}$ away from the ensemble average f by means of the correlation function for the one-particle phase-space occupancy,

$$\begin{aligned} \sigma(\mathbf{s}; \mathbf{s}') &\equiv \prec \delta f^{(n)}(\mathbf{s}) \delta f^{(n)}(\mathbf{s}') \succ = \frac{1}{N} \sum_{n=1}^N \delta f^{(n)}(\mathbf{s}) \delta f^{(n)}(\mathbf{s}') \\ &= \sigma^2(\mathbf{s}) \delta(\mathbf{s} - \mathbf{s}') + \sigma_{\text{cov}}(\mathbf{s}; \mathbf{s}'), \end{aligned} \quad (\text{B.4})$$

where $\delta(\mathbf{s} - \mathbf{s}') = h^D \delta^D(\mathbf{r} - \mathbf{r}') \delta^D(\mathbf{p} - \mathbf{p}')$. In the last line, the correlation has been decomposed into its diagonal part expressing the local variance in occupancy and the non-local remainder expressing how fluctuations at different phase-space locations are correlated. The two parts are related by unitarity, $\sigma^2(\mathbf{s}) = - \int d\mathbf{s}' \sigma_{\text{cov}}(\mathbf{s}, \mathbf{s}')$. Once the above quantity is known, then the correlation between any two one-body observables can readily be extracted.

The transport treatment makes it possible to derive a closed set of approximate equations of motion for the mean evolution of the phase-space occupancy at given points, $f(\mathbf{r}, \mathbf{p}, t)$, and the associated correlations between the fluctuations in those occupancies [204,179] (see later).

For notational convenience we note that the dynamical variable, the reduced one-particle phase-space density, can be represented by its values $\{f_i\}$ on a discrete lattice $\{s_i\}$ in phase space, $f(s) = (f_1, f_2, \dots)$.

The stochastic nature of the two-body interactions causes each individual many-body system to evolve differently. The ensuing ensemble of N dynamical histories, $\{f^{(n)}(\mathbf{r}, \mathbf{p}, t)\}$, can be described by the following (evolving) distribution of one-body phase-space densities,

$$\phi[f] = \phi(f_1, f_2, \dots) = \lim_{N \rightarrow \infty} \frac{1}{N} \sum_{n=1}^N \delta[f^{(n)} - f] = \lim_{N \rightarrow \infty} \frac{1}{N} \sum_{n=1}^N \prod_i \delta(f_i^{(n)} - f_i), \quad (\text{B.5})$$

which represents the probability density that a randomly selected system n has the specified occupancy function $f(\mathbf{r}, \mathbf{p})$.

In the Fokker–Planck approximation, the dynamical evolution of the distribution $\phi[f]$ is given by a diffusion equation,

$$\dot{\phi}[f] = - \sum_i \frac{\partial}{\partial f_i} V_i[f] \phi[f] + \sum_{ij} \frac{\partial^2}{\partial f_i \partial f_j} D_{ij}[f] \phi[f]. \quad (\text{B.6})$$

(As noted in [162], it is straightforward to carry the expansion to higher order, at the cost of significantly increased complexity, but it is not of practical interest.) The Fokker–Planck equation (B.6) contains two sets of transport coefficients, the *drift coefficients* V_i that govern the average change at the phase-space lattice site i and the *diffusion coefficients* D_{ij} that govern the degree to which the fluctuations created at two sites i and j are correlated.

In order to derive expressions for the transport coefficient functionals V and D , it is useful to note that the number of elementary transitions expected to occur during a brief time interval Δt from two given phase-space elements around $(\mathbf{r}_1, \mathbf{p}_1)$ and $(\mathbf{r}_2, \mathbf{p}_2)$ into two other given phase-space elements around $(\mathbf{r}_3, \mathbf{p}_3)$ and $(\mathbf{r}_4, \mathbf{p}_4)$ is given by

$$d\bar{v}_{12;34} = \frac{d^D \mathbf{r}_1 d^D \mathbf{p}_1}{h^D} f(\mathbf{r}_1, \mathbf{p}_1) \frac{d^D \mathbf{r}_2 d^D \mathbf{p}_2}{h^D} f(\mathbf{r}_2, \mathbf{p}_2) \delta^D(\mathbf{r}_1 - \mathbf{r}_2) \quad (\text{B.7})$$

$$\times \frac{d^D \mathbf{r}_3 d^D \mathbf{p}_3}{h^D} \bar{f}(\mathbf{r}_3, \mathbf{p}_3) \frac{d^D \mathbf{r}_4 d^D \mathbf{p}_4}{h^D} \bar{f}(\mathbf{r}_4, \mathbf{p}_4) \delta^D(\mathbf{r}_3 - \mathbf{r}_4) \quad (\text{B.8})$$

$$\times \delta^D(\mathbf{r}_1 - \mathbf{r}_3) w(\mathbf{p}_1, \mathbf{p}_2; \mathbf{p}_3, \mathbf{p}_4) \Delta t. \quad (\text{B.9})$$

It has here been used that the two-body collisions are assumed to be local in both space and time. The f factors represent the phase-space occupancies at the initial sites while the availabilities at the final sites are denoted by $\bar{f} \equiv 1 - f$. The above expression holds in any dimension D , but the elementary transition rate w depends on D , for example,

$$w(\mathbf{p}_1 \mathbf{p}_2 \leftrightarrow \mathbf{p}_3 \mathbf{p}_4) \stackrel{D=2}{=} \frac{h^4}{2m} \delta^{(4)}(p_1 + p_2 - p_3 - p_4) v_{12} \frac{d\lambda(12 \leftrightarrow 34)}{d\theta_{34}}, \quad (\text{B.10})$$

$$w(\mathbf{p}_1 \mathbf{p}_2 \leftrightarrow \mathbf{p}_3 \mathbf{p}_4) \stackrel{D=3}{=} \frac{h^6}{m^2} \delta^{(4)}(p_1 + p_2 - p_3 - p_4) \frac{d\sigma(12 \leftrightarrow 34)}{d\Omega_{34}}. \quad (\text{B.11})$$

Since the drift coefficient measures the average rate of change, it can be obtained by combining the expected changes from all the possible elementary processes,

$$V[f](s) = \bar{f}(s)W^+(s) - f(s)W^-(s) , \quad (\text{B.12})$$

where the $W^+(s)$ and $W^-(s)$ denote the rates of transition into and out of the phase-space location s , respectively,

$$\bar{f}(s)W^+(s)\Delta t = \frac{1}{2} \int d\bar{v}_{1,2;3,4} \delta(s_{1'} - s) , \quad (\text{B.13})$$

$$f(s)W^-(s)\Delta t = \frac{1}{2} \int d\bar{v}_{1,2;3,4} \delta(s_1 - s) , \quad (\text{B.14})$$

and V is just simply the difference between the rate of growth and the rate of depletion at the specified phase-space location s .

To express the diffusion coefficient, it is instructive to introduce the rates $W^{\kappa\kappa'}(s, s')$ for the joint occurrence of transitions to or from the phase-space locations s and s' ,

$$f(s)f(s')W^{--}(s, s')\Delta t = \frac{1}{2} \int d\bar{v}_{1,2;3,4} \delta(s_1 - s)\delta(s_2 - s') , \quad (\text{B.15})$$

$$\bar{f}(s)\bar{f}(s')W^{++}(s, s')\Delta t = \frac{1}{2} \int d\bar{v}_{1,2;3,4} \delta(s_{1'} - s)\delta(s_{2'} - s') , \quad (\text{B.16})$$

$$\bar{f}(s)f(s')W^{+-}(s, s')\Delta t = \frac{1}{2} \int d\bar{v}_{1,2;3,4} \delta(s_{1'} - s)\delta(s_1 - s') , \quad (\text{B.17})$$

with $W^{--}(s, s') = W^{++}(s', s)$. The off-diagonal diffusion coefficient measures the accumulated covariance between the changes at the two indicated sites and, accordingly, it can be expressed as follows,

$$\begin{aligned} D^{\text{cov}}[f](s, s') &= f(s)f(s')W^{--}(s, s') + \bar{f}(s)\bar{f}(s')W^{++}(s, s') \\ &\quad + f(s)\bar{f}(s')W^{-+}(s, s') + \bar{f}(s)f(s')W^{+-}(s, s') . \end{aligned} \quad (\text{B.18})$$

The diagonal part can be obtained by subsequently applying the unitary relation, or by simply adding the rates of growth and depletion, yielding the expected result,

$$2D^{\text{var}}[f](s) = - \int ds' D^{\text{cov}}[f](s, s') = \bar{f}(s)W^+(s) + f(s)W^-(s) . \quad (\text{B.19})$$

B.1. Expansion around the mean trajectory

The Fokker–Planck transport equation (B.6) governs the temporal evolution of the distribution $\phi[f]$ of one-body phase-space densities $f(s)$, and the expressions above makes it possible to calculate the transport coefficients for any given density $f(s)$. Generally, even when starting from a common density $f_0(s)$, the dynamics has the character of an ever widening bundle of trajectories (as illustrated in Fig. 4.4). When the trajectories are sufficiently well concentrated, as they will be at early times after a common initialization and as they may be in a stable scenario, it is useful to characterize the distribution $\phi[f]$ by its first and second moment, corresponding to the mean trajectory and the dispersion around it.

It is possible to derive a closed set of equations for these quantities [204,179]. To derive these equations of motion, one first makes a linear expansion of the drift coefficient around the average one-body density $\prec f(s) \succ$, using

$$\frac{\partial W^\kappa(s)}{\partial f(s')} = W^{\kappa-}(s, s') - W^{\kappa+}(s, s') , \quad \kappa = \pm . \quad (\text{B.20})$$

The equation of motion for the average is density is then

$$\frac{d}{dt} \prec f \succ (s) = \prec V[f](s) \succ \approx V[\prec f \succ](s) \equiv \underline{V}(s) , \quad (\text{B.21})$$

since the linear corrections average out to zero. In the last line the underscore indicates that the quantity should be evaluated on the basis of the mean density. By contrast, in the expression for the second moment the linear corrections combine with the deviations $\delta f(s')$ to produce feedback terms proportional to the width of the distribution. The resulting expression for the variance of $\phi[f]$ is then quite simple,

$$\frac{d}{dt} \sigma^2(s) = 2\underline{D}^{\text{var}}(s) - 2(\underline{W}^-(s) + \underline{W}^+(s))\sigma^2(s) . \quad (\text{B.22})$$

It can be obtained by applying unitarity to the expression for the covariance,

$$\begin{aligned} \frac{d}{dt} \sigma_{\text{cov}}(s, s') &= f(s)\underline{Z}^-(s, s') + \bar{f}(s)\underline{Z}^+(s, s') + \int ds'' [\underline{Z}(s, s')\sigma_{\text{cov}}(s'', s) \\ &\quad + \underline{Z}(s', s'')\sigma_{\text{cov}}(s, s') + \underline{Z}(s'', s')\sigma_{\text{cov}}(s, s'') + (s \leftrightarrow s')] , \end{aligned} \quad (\text{B.23})$$

where

$$Z^\kappa(s, s') = \kappa[\bar{f}(s')W^{\kappa\kappa}(s, s') - f(s')W^{\kappa\bar{\kappa}}(s, s')] , \quad (\text{B.24})$$

and $Z = Z^- + Z^+$, with $\bar{\kappa} = -\kappa$. The form of Eq. (B.22) for the variance shows that $\sigma^2(s)$ will seek to relax towards $f(s)\bar{f}(s)$ which is recognized as the equilibrium variance of the Fermi–Dirac occupancy. Moreover, once the relation $\sigma^2 = f\bar{f}$ has been obtained it will remain in effect thereafter.

B.2. Lattice simulation method

The mean-trajectory treatments have the inherent limitation of being inadequate when instabilities and bifurcations occur, such as in nuclear fragmentation. In order to make such more general processes practically tractable, a phase-space lattice simulation was developed [178,179]. It is based on the assumption that the elementary two-body scattering processes can be regarded as Markovian (though a finite memory time can be included as well). Then, within a given suitably small time interval Δt , the number of transitions actually occurring, v , is governed by the corresponding Poisson distribution having the mean given in Eq. (B.7), $d\bar{v}$. It therefore follows in particular that the variance of the number of transitions is equal to the mean number,

$$d\sigma_v^2 = d\bar{v} . \quad (\text{B.25})$$

This basic feature can be exploited for the numerical treatment.

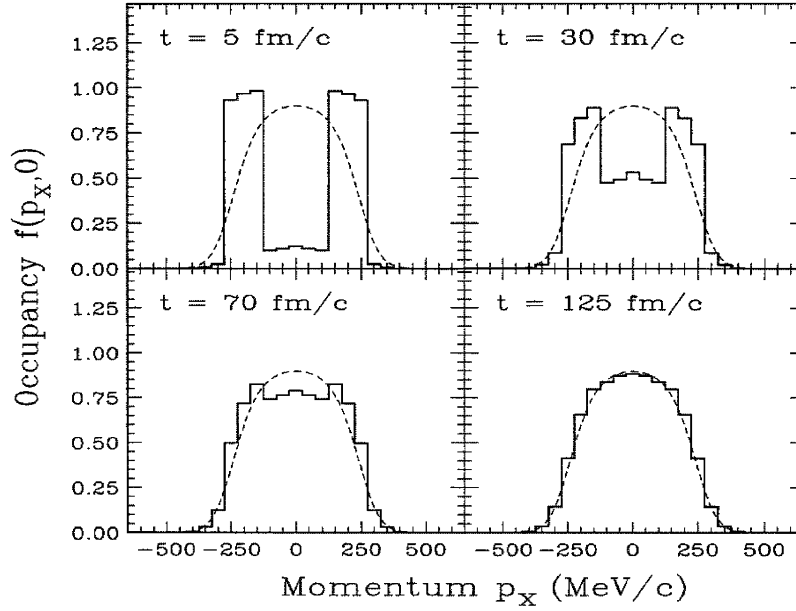


Fig. B.1. Test of the lattice simulation method: mean occupancy. The evolution of the ensemble-averaged phase-space occupancy, $f(p)$, as obtained with the lattice simulation method (histograms) for a uniform two-dimensional fermion gas prepared as a sharp hollow sphere in momentum space. The corresponding Fermi–Dirac equilibrium profile is shown by the dashed curve. (From Ref. [178].)

The lattice simulation method can now be briefly described as follows: The Vlasov evolution can readily be made on a phase-space lattice. (In practice, to achieve sufficient accuracy it is necessary to employ phase-space bins that are significantly smaller than h^D .) The two-body collisions then redistribute probability between the space–space bins. The time step Δt is chosen so that the expected number of nucleons moved in a particular elementary process, $\bar{v}_{12;34}$, is small compared to unity. The actual number of nucleons, $v_{12;34}$, moving from the two given initial bins to the two specified final bins deviates from the expectation by a stochastic amount, $\delta v_{12;34}$,

$$v_{12;34} = \bar{v}_{12;34} + \delta v_{12;34} . \quad (\text{B.26})$$

The deterministic part, \bar{v} , is obtained by integrating the expected differential change $d\bar{v}_{12;34}$ in (B.7) over the specified lattice bins, while the stochastic part, δv , is sampled from a normal distribution with the variance $\sigma_v^2 = \bar{v}$. This procedure guarantees that the resulting fluctuations have the physically correct relationship with the average changes, thus ensuring that the fluctuation–dissipation theorem is upheld. However, since the basic bin size is typically smaller than h^D , the method causes the phase-space occupancy f to make local excursions into the unphysical regions (either $f < 0$ or $f > 1$). Fortunately, this is of no import since physical observables automatically smear the information over volumes of at least h^D .

This lattice simulation method was tested for a two-dimensional gas prepared in suitable non-equilibrium states [177–179]. Fig. B.1 shows the evolution of the average phase-space

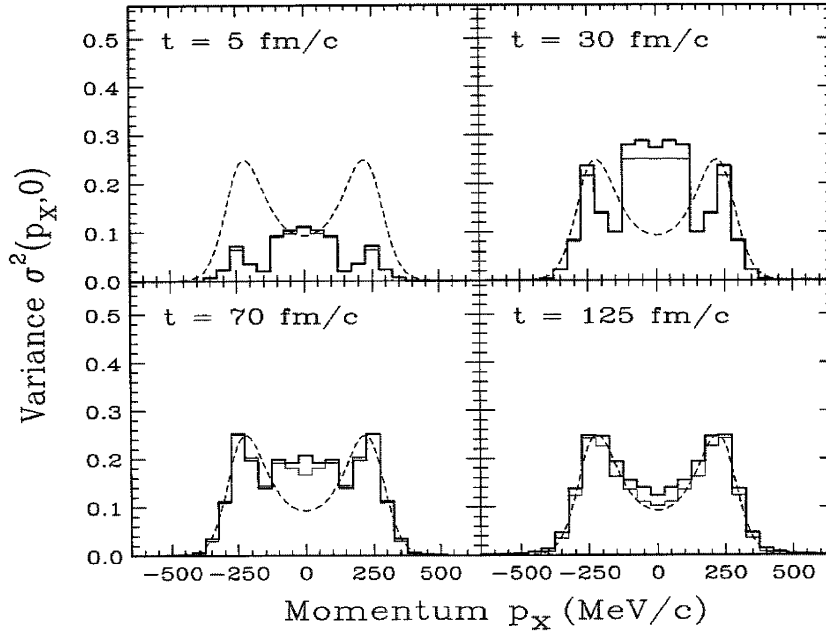


Fig. B.2. Test of the lattice simulation method: variance in occupancy. The evolution of the variance in the phase-space occupancy, $\sigma^2(p)$, as obtained with the lattice simulation method (histograms) for a uniform two-dimensional fermion gas prepared as a sharp hollow sphere in momentum space. The corresponding value of $f\bar{f}$ is shown by the thin histogram, while the dashed curve is the quantum-statistical equilibrium variance. (From Ref. [178].)

density, $\langle f(p, t) \rangle$, for a uniform gas prepared with an initially sharp hollow Fermi sphere. It is seen how the momentum profile gradually approaches the corresponding finite-temperature Fermi–Dirac distribution $f_{\text{FD}}(p)$ (which is fully determined by the initial conditions).

Fig. B.2 shows the associated variance in the phase-space occupancy, $\sigma_f^2(p, t) = \langle f(p, t)^2 \rangle - \langle f(p, t) \rangle^2$. Being initially zero, the variance in f grows initially fastest inside the hollow sphere to where most scatterings occur early on. Subsequently, it gradually evolves towards the appropriate quantum-statistical form given by $\bar{\sigma}_f^2(p) = f_{\text{FD}}(p)\bar{f}_{\text{FD}}(p)$. It is also interesting to note that the instantaneous equilibrium value, $\langle f(p, t) \rangle \langle \bar{f}(p, t) \rangle$, presents a very good approximation to the evolving non-equilibrium variance, $\sigma_f^2(p, t)$.

These and other more complicated (non-isotropic) test cases have shown that the lattice simulation method is numerically valid. Thus, in principle, it can be used to solve the Boltzmann–Langevin transport equation for general dynamical scenarios, in particular fragmentation in nuclear collisions. However, as of yet, its application for non-uniform geometries in three spatial dimensions is rather computer intensive and therefore still impractical. There is thus a need for methods that, on the one hand, provide reasonable approximations to the full lattice simulation while, on the other hand, are computationally practical.

B.3. Simplified Boltzmann–Langevin model

For the subsequent discussion it is convenient that the diffusion coefficient can be decomposed into diagonal and off-diagonal parts [289],

$$D[f](\mathbf{s}_1, \mathbf{s}_2) = [D_1^{\text{var}} \delta_{12} + D_{12}^{\text{cov}}] \delta^D(\mathbf{r}_{12}) . \quad (\text{B.27})$$

Here the subscripts provide a convenient means of indicating the momentum values and δ_{12} means $\delta^D(\mathbf{p}_{12})$. Since the diffusion coefficient is local in space, we need only be concerned with one position at a time, the coupling between different spatial points being provided by the Vlasov propagation in the effective field. It is therefore convenient to introduce the *contracted* diffusion coefficient which is obtained from the full one above by integrating over the spatial separation \mathbf{r}_{12} ; this obviously yields the expression in the bracket.

From this starting point, it is possible to develop simplified descriptions of the Boltzmann–Langevin dynamics [290,120]. In particular, adapting a method developed in connection with Fermi liquids [291,292], Randrup and Ayik [120] derived simple approximate expressions for the transport coefficients for a free Fermi–Dirac gas,

$$\text{Drift : } V_1 \approx -\frac{1}{t_0} \left[f_1 - f_1^0 - f_1^0 \bar{f}_1^0 \sum_2 C_{12} (f_2 - f_2^0) \right] , \quad (\text{B.28})$$

$$\text{Diffusion : } D_{12} \approx \frac{1}{t_0} [f_1^0 \bar{f}_1^0 \delta_{12} - f_1^0 \bar{f}_1^0 C_{12} f_2^0 \bar{f}_2^0] = D_{12}^{\text{var}} \delta_{12} + D_{12}^{\text{cov}} , \quad (\text{B.29})$$

where the local Fermi–Dirac equilibrium distribution is $f^0(\mathbf{p}) = [1 + \exp(\epsilon/T)]^{-1}$ with $\epsilon = p^2/2m$. The overall transport rate is governed by the local relaxation time t_0 ,

$$t_0^{-1} \approx \pi^2 \frac{T^2}{\epsilon_F^2} \left[1 - \pi^2 \frac{T^2}{\epsilon_F^2} \right] \rho \sigma_0 V_F , \quad (\text{B.30})$$

and the coefficient C_{12} expressing the correlation between the fluctuations induced at \mathbf{p}_1 and \mathbf{p}_2 is given by

$$\rho \phi_0 C_{12} = \frac{\epsilon_1 - \epsilon_0}{\sigma_T} \frac{\epsilon_2 - \epsilon_0}{\sigma_T} + \sum_{\ell \geq 0} \frac{\phi_0}{\phi_\ell} \left(\frac{p_1 p_2}{2m} \right)^\ell [2 - (-1)^\ell] P_\ell(\cos \theta_{12}) , \quad (\text{B.31})$$

where θ_{12} is the angle between the two momenta. Furthermore, $\sigma_T^2 \approx \frac{1}{3} \pi^2 T^2$ is the variance of the Fermi–Dirac profile function, $-T \partial f^0 / \partial \epsilon = f^0 \bar{f}^0$, and the associated energy moments (see Eq. (C.2)) are

$$\phi_n = \frac{1}{\rho} \sum_1 \epsilon_1^n f_1^0 \bar{f}_1^0 \approx \frac{D}{2} \frac{T}{\epsilon_F} \epsilon_F^n \left[1 + \frac{1}{6} \pi^2 (n-1)(n-1 + \frac{1}{2} D) \frac{T^2}{\epsilon_F^2} \right] . \quad (\text{B.32})$$

It is important to note that these approximate expressions conserve particle number, energy, and momentum exactly, as borne out by the fact that $\sum_1 V_1 F_1^\alpha$ and $\sum_2 D_{12} F_2^\alpha$ vanish, with F^α representing either the particle number A ($F_1^A = 1$), the energy E ($F_1^E = \epsilon_1$), or the momentum \mathbf{P} ($F_1^P = \mathbf{p}_1$).

Moreover, it was shown in Ref. [120] that the resulting distribution indeed relaxes towards the appropriate Fermi–Dirac equilibrium form,

$$f_1(t) \rightarrow f_1^0, \quad (\text{B.33})$$

$$\sigma_{12}(t) \rightarrow f_1^0 \bar{f}_1^0 \delta_{12} - f_1^0 \bar{f}_1^0 S_{12} f_2^0 \bar{f}_2^0, \quad (\text{B.34})$$

where S_{12} consists of the first two multipole terms in C_{12} ,

$$\rho \phi_0 S_{12} = 1 + \frac{\epsilon_1 - \epsilon_0}{\sigma_T} \frac{\epsilon_2 - \epsilon_0}{\sigma_T} + D \frac{\mathbf{p}_1 \cdot \mathbf{p}_2}{2m\epsilon_0}. \quad (\text{B.35})$$

The three terms reflect conservation of particle number, energy, and momentum, respectively.

B.3.1. Quality of the simplified model

The derived expressions for the transport coefficients provide quite reasonable approximations to those given by the full theory. To illustrate this, one may first consider the overall diffusion rate, as obtained by integrating D_1^{var} in (B.29) over \mathbf{p}_1 . Comparisons of the simple expression (B.30) with numerical evaluations of based on the exact expression (B.19) and approximation (B.29) yield agreements to within one per cent for temperatures up to 5 MeV.

One may next consider the energy dependence of D_{12}^{cov} ,

$$D(\epsilon, \epsilon') \equiv \frac{1}{\rho \phi_0 W_0} \sum_{12} \delta(\epsilon_1 - \epsilon) \delta(\epsilon_2 - \epsilon') D_{12}^{\text{cov}} \quad (\text{B.36})$$

$$\approx -\frac{f_0 \bar{f}_0}{T} \frac{f'_0 \bar{f}'_0}{T} \left(1 + \frac{\epsilon - \epsilon_0}{\sigma_T} \frac{\epsilon' - \epsilon_0}{\sigma_T} \right) \frac{\sqrt{\epsilon \epsilon'}}{\epsilon_F}. \quad (\text{B.37})$$

The first expression can be calculated by direct numerical (Monte Carlo) evaluation of the integrals in Eq. (B.18) for D_{12}^{cov} , while the approximate expression follows from the analytical approximation (B.29). The quality of the above approximations to $D(\epsilon, \epsilon')$ is illustrated in Fig. B.3.

Finally, it is also instructive to consider the angular dependence of D_{12}^{cov} ,

$$D(\theta) \equiv \frac{2}{\rho \phi_0 W_0} \sum_{12} \delta(\cos \theta_{12} - \cos \theta) D_{12}^{\text{cov}} \approx \frac{1}{2 \cos \frac{1}{2} \theta} - \frac{1}{\sin \frac{1}{2} \theta}. \quad (\text{B.38})$$

The approximate expression is implied by the approximation (B.29). Fig. B.4 shows $D(\theta)$ as obtained by numerical calculation of the rate functions in (B.18) (dots) and as given by the simple trigonometric expression (C.14) (curves). The results have been decomposed into their positive and negative parts and the approximation is seen to be quite good.

B.3.2. Minimal model

While the simple approximate expressions (B.28) and (B.29) for the Boltzmann–Langevin transport coefficients derived above may be quantitatively useful for both analytical and numerical studies of dynamical properties of Fermi liquids, such as nuclear matter, further simplification can be achieved by retaining only those correlations that are required by conservation laws.

Such extreme simplification can be achieved by discarding those terms in the expressions for the transport coefficients that have multipolarity higher than $\ell = 1$, corresponding to putting $C_{12} = S_{12}$,

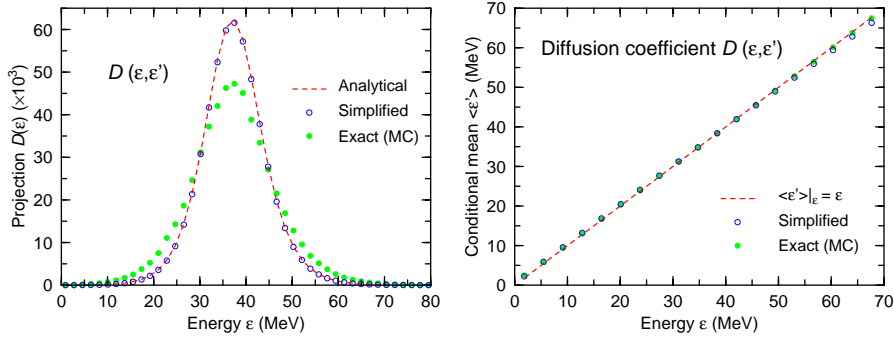


Fig. B.3. Energy dependence of the diffusion coefficient. The energy dependence of the mixed diffusion coefficient D_{12}^{cov} can be expressed by the function $D(\epsilon, \epsilon')$ defined in Eq. (B.36). This figure illustrates $D(\epsilon, \epsilon')$ for a Fermi–Dirac gas with a Fermi energy of $\epsilon_F = 37$ MeV and a temperature of $T = 4$ MeV. On the left is shown the projection $D(\epsilon)$ as obtained by integrating $D(\epsilon, \epsilon')$ over ϵ' . The solid dots results from a numerical (Monte Carlo) integration of the exact D_{12}^{cov} (given in Eq. (B.19)). The open dots follow by integrating the approximation (B.29) numerically, and the dashed curve is the simple approximation (B.37). On the right is shown the corresponding conditional mean energy $\langle \epsilon' \rangle_\epsilon$, i.e. the centroid of $D(\epsilon, \epsilon')$ considered as a function of ϵ' for a specified value of ϵ . (From Ref. [120].)

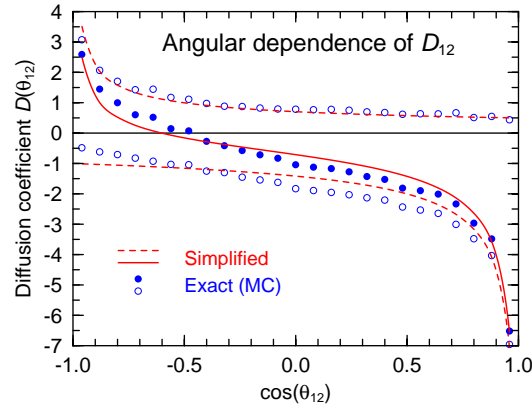


Fig. B.4. Angular dependence of the diffusion coefficient. The angular dependence of the mixed diffusion coefficient D_{12}^{cov} can be expressed by the function $D(\theta)$ defined in Eq. (B.38). This quantity is shown as a function of $\cos \theta_{12}$, where θ_{12} is the relative angle between the two specified momenta \mathbf{p}_1 and \mathbf{p}_2 , for the same case as displayed in Fig. B.3. The exact result (obtained by numerical Monte-Carlo evaluation) is shown by the solid dots, with the open dots indicating its positive and negative parts. The curves show the corresponding quantity for the trigonometric approximation included in Eq. (B.38), with the dashed curves showing separate parts. (From Ref. [120].)

yielding

$$\begin{aligned} \text{Drift :} \quad V_1 &= W_0(f_1^0 - f_1), \\ \text{Diffusion :} \quad D_{12} &= W_0[f_1^0 \tilde{f}_1^0 \delta_{12} - f_1^0 \tilde{f}_1^0 S_{12} f_2^0 \tilde{f}_2^0] = W_0 \tilde{\sigma}_{12}. \end{aligned} \quad (\text{B.39})$$

This corresponds to the simple relaxation-time approximation in which the evolution is governed by the global relaxation time $t_0 = W_0^{-1}$. The average occupancy of a given cell at s_1 then evolves

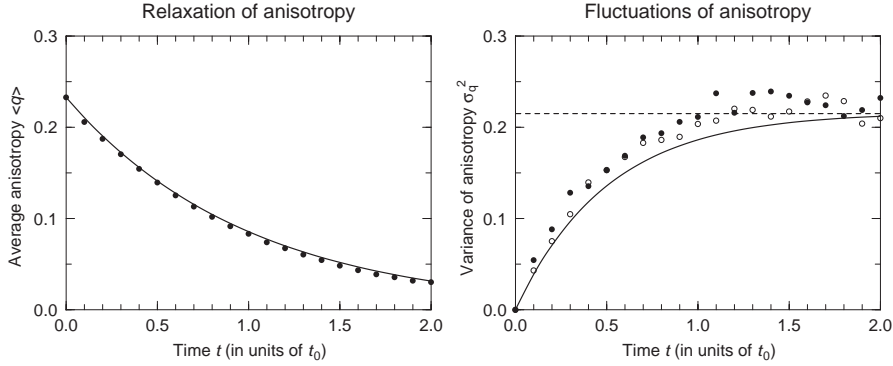


Fig. B.5. Relaxation of the quadrupole moment. *Left*: For a uniform gas of free fermions in two dimensions is shown the relaxation of the average anisotropy, $\langle q \rangle = \langle Q_{xx} - Q_{yy} \rangle / Q$, when starting from a deformed momentum distribution. *Right*: The growth of the variance of the anisotropy, σ_q^2 , for the same case as well as when starting from a Fermi–Dirac equilibrium density, which is isotropic. The corresponding analytic behaviors are indicated by the solid curves. (From Ref. [120].)

according to $\dot{f}_1 = W_0(f_1^0 - f_1)$ and so relaxes in an exponential fashion towards the appropriate Fermi–Dirac equilibrium value f_1^0 with the characteristic time constant t_0 . Moreover, since $\partial V_1 / \partial f_2 = -W_0 \delta_{12}$, the covariance matrix satisfies $\dot{\sigma}_{12} = 2W_0(\tilde{\sigma}_{12} - \sigma_{12})$ and so each element relaxes exponentially towards its proper equilibrium value $\tilde{\sigma}_{12}$ at twice that rate.

This maximally simple approximate version of the Boltzmann–Langevin transport model still contains the essential features of the full model so that it may provide a useful framework for testing numerical methods, as well as provide a quick impression of the results.

As a test illustration the methods developed, the authors of Refs. [290,120] considered the relaxation of the quadrupole moment of the momentum distribution in a uniform Fermi–Dirac gas. Results obtained with the simplified model described above are shown in Fig. B.5 and it is apparent that the stochastic simulation leads to a good reproduction of the analytical expectations for both the ensemble average distortion and the associated variance.

B.4. Memory effects

In the one-body transport treatment discussed so far, the collision term is assumed to be local in both space and time, in accordance with Boltzmann’s original treatment. This simplification is usually justified by the fact that the interaction range, as measured by the residual scattering cross section $\sigma_{NN} \approx 4 \text{ fm}^2$, is relatively small on the scale of a typical nuclear system, and the duration of a two-body collision is short on the time scale characteristic of the macroscopic evolution of the system. The resulting collective motion has then a classical character, as is the case also in TDHF. However, when the system possesses fast collective modes whose characteristic energies are not small in comparison with the temperature, then quantum effects are important and the treatment needs to be appropriately improved.

When the collision term has a non-Markovian form, then the evolution of the single-particle density matrix depends on the (recent) past. The resulting memory effects on the spreading width of

a collective state was discussed by Ayik and Dworzecka [293,294]. Deriving an extended RPA equation for the normal modes, these authors demonstrated that the memory effects in the collision term play an important role in determining the spreading width of the collective mode, in particular through the enforcement of energy conservation between the collective mode and the states responsible for its decay.

The collisional damping of collective nuclear vibrations was subsequently studied by Ayik and Boilley [295] on the basis of a Boltzmann-type transport equation with memory effects and it was shown that the incorporation of memory effects into the collision term is essential for obtaining the proper damping of small-amplitude high-frequency collective vibrations.

In a further development, Ayik [210] derived a transport equation for the single-particle phase-space density by performing a statistical averaging of the Boltzmann–Langevin equation. In analogy with Brownian motion, the fluctuating part of the collision term gives rise to a memory time in the collision kernel which, in turn, leads to a dissipative coupling between collective modes and single-particle degrees of freedom. Within this framework, Ayik et al. [296–298] have made important further advances. In particular, Ivanov and Ayik [296] showed that the coupling between mean-field fluctuations and single-particle motion provides a coherent damping mechanism which has an especially large effect on the relaxation times in the vicinity of the spinodal boundary where the equilibration rate significantly exceeds that resulting from the standard (i.e. Markovian) Boltzmann treatment.

This approach is also suitable for studying the role of memory effects on the spinodal fragmentation process and it was adapted by Ayik and Randrup [211] to nuclear matter inside the spinodal zone. As shown in Ref. [112], the (early) evolution of the collective modes is governed by the simple *Lalime* feed-back equation (4.25), in which the modes are agitated by a source term arising from the fluctuating part of the collision term and amplified exponentially by the unstable selfconsistent effective field.

The characteristic amplification time t_k corresponding to a given wave number k is determined by the associated dispersion relation. As it turns out [113,299], the fastest-growing collective modes, which are those that will become predominant, have fairly high characteristic energies $E_k = \hbar/t_k$. For example, for densities $\rho \approx 0.3\rho_0$ and wavelengths of 7–8 fm, for which the fastest amplification occurs, we have $E_k \approx 8$ MeV. This is clearly not small in comparison with the temperature in the system, which is $T \approx 4$ MeV, typically. Consequently, one must expect quantum-statistical effects to be important in the dynamics of the collective modes and the standard *BL* treatment may therefore be inadequate, since it treats the collective modes as classical. We therefore briefly recall the results obtained in Ref. [211].

The term $\delta K(\mathbf{r}, \mathbf{p}, t)$ in equation the *BL* equation is a stochastic function governed by a certain distribution function which depends on the phase-space density f , is zero on the average, and has a correlation function of the form

$$\prec \delta K(\mathbf{r}, \mathbf{p}, t) \delta K(\mathbf{r}', \mathbf{p}', t') \succ = C(\mathbf{p}, \mathbf{p}'; t - t') \delta(\mathbf{r} - \mathbf{r}') . \quad (\text{B.40})$$

In the standard *BL* model, the collisions are assumed to be instantaneous but the finite duration of a two-body collision generally modulates the corresponding frequency spectrum,

$$C(\mathbf{p}, \mathbf{p}'; t - t') = \int \frac{d\omega}{\pi} e^{-i\omega(t-t')} \tilde{C}(\mathbf{p}, \mathbf{p}'; \omega) , \quad (\text{B.41})$$

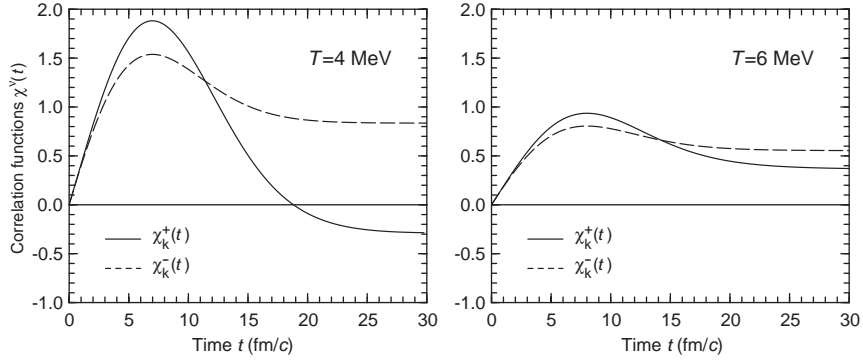


Fig. B.6. Temporal correlation functions. The collective correlation functions $\chi_k^+(t)$ (solid) and $\chi_k^-(t)$ (dashed) for an unstable mode, for either $T = 4$ MeV and $t_k = 24$ fm/c (left) or $T = 6$ MeV and $t_k = 36$ fm/c (right). (From Ref. [211].)

where

$$\tilde{C}(\mathbf{p}, \mathbf{p}'; \omega) = \tilde{C}_0(\mathbf{p}, \mathbf{p}'; \omega) \mathcal{G}(\omega t_c), \quad (\text{B.42})$$

with $\tilde{C}_0(\mathbf{p}, \mathbf{p}'; \omega)$ being the kernel entering in the standard treatment. A rough estimate of the duration time yields $t_c \approx 2a/v \approx 5\text{--}6$ fm/c which is a fairly brief length of time as compared with the typical free travel time for a nucleon, $t_{\text{mfp}} \approx \lambda/v_F \approx 20\text{--}30$ fm/c. One would therefore expect that the treatment developed in Ref. [112] will still be applicable, but with suitably modified transport coefficients. Indeed, the source terms $\mathring{D}_k^{vv'}$ responsible for the agitation of the unstable collective modes in nuclear matter may be replaced by effective coefficients of the form $\mathcal{D}_k^{vv'}(t) = \mathring{D}_k^{vv'} \chi_k^{vv'}(t)$. The modulation factor is given by $\chi_k^{vv'}(t) \equiv \chi_k^v(t) + \chi_k^{v'}(t)$, where the collective correlation functions for the given collective mode, $\chi_k^\pm(t)$, are illustrated in Fig. B.6.

It is now possible to see that when a memory time is included the collective correlation coefficients satisfy the following modified equation of motion,

$$\frac{d}{dt} \sigma_k^{vv'}(t) = 2\mathring{D}_k^{vv'} \chi_k^{vv'}(t) + \frac{v + v'}{t_k} \sigma_k^{vv'}(t). \quad (\text{B.43})$$

This equation is of the same general form as the standard Lalime equation (4.25), but it has a time-dependent diffusion coefficient, $\mathcal{D}_k^{vv'}(t) = \mathring{D}_k^{vv'} \chi_k^{vv'}(t)$, and the solution is then given by $\sigma_k^{vv'}(t) = \bar{\sigma}_k^{vv'}(t) \bar{\chi}_k^{vv'}(t)$, where the renormalization coefficients can be expressed as suitable time averages of the collective correlation functions,

$$\bar{\chi}_k^{vv'}(t) = \int_0^t dt' e^{-(v+v')\gamma_k t'} [\chi_k^v(t') + \chi_k^{v'}(t')] / \int_0^t dt' e^{-(v+v')\gamma_k t'}. \quad (\text{B.44})$$

These correction factors are illustrated in Fig. B.7.

The finite memory time introduces a certain gentleness into the source term which is reflected in the suppression of high-frequency components, as expressed by the modulation function $\mathcal{G}(\omega t_c)$. However, since $t_c \ll t_k$, this has little effect on the agitation of the collective modes. Indeed, the factor $\mathcal{G}(\omega_k t_c)$ produces a reduction of only about two per cent for the fastest mode, so it is apparent that this effect is not essential.

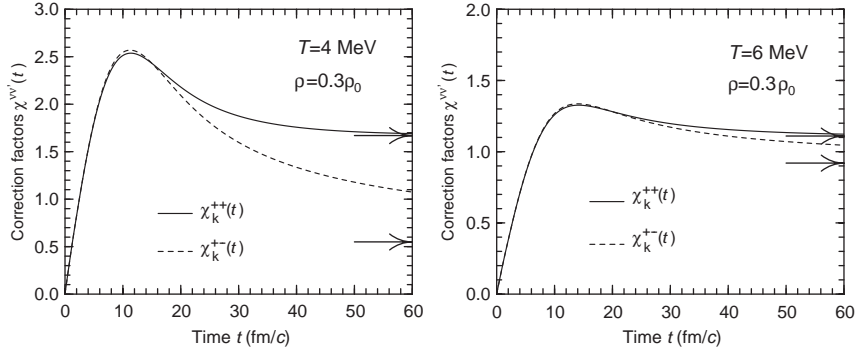


Fig. B.7. Correction for memory time. The correction factors $\tilde{\chi}_k^{vv'}$ determining the time-dependence of the covariance coefficients describing the agitation of collective modes in unstable nuclear matter, for the same two cases as in Fig. B.6. The arrows indicate the asymptotic values. (From Ref. [211].)

Much more important is the quantum-statistical enhancement expressed by the factor $\mathcal{F}_\rho(\hbar\omega/2T)$. [In the case of stable collective modes, the factor \mathcal{F} guarantees that the appropriate quantum-statistical equilibrium is approached [210], whereas the standard Boltzmann–Langevin treatment leads to a classical (Boltzmann) equilibrium occupation of the collective modes, $P_k \sim \exp(-\hbar\omega_k/T)$.] Since the characteristic energy $E_k = \hbar/t_k$ exceeds the temperature T , the factor \mathcal{F} causes a significant enhancement of the collective source terms \mathcal{D}_k and, consequently, the density undulations will grow correspondingly larger in the course of a given time interval. The effect depends strongly on the temperature T and the growth time t_k , but for the fastest mode and the most typical temperatures, the enhancement factor is 50–100%.

B.5. Relativistic formulation

The Boltzmann–Langevin model has been adapted to nuclear collisions at higher energies on the basis of Walecka-type field theory by Ayik [300]. This treatment considers spin–isospin degenerate nucleons, Δ resonances and pions and thus describes the associated one-body phase-space density distributions, $f_J(p, x)$, where $J = N, \Delta, \pi$ denotes the particular particle species and $p = (E, \mathbf{p})$ and $x = (t, \mathbf{r})$. Their dynamical evolution is governed by a set of coupled relativistic Boltzmann–Langevin equations,

$$\left(\frac{\partial}{\partial t} + \frac{\partial E_J}{\partial \mathbf{p}} \cdot \frac{\partial}{\partial \mathbf{r}} - \frac{\partial E_J}{\partial \mathbf{r}} \cdot \frac{\partial}{\partial \mathbf{p}} \right) f_J(p, x) = K_J(p, x) + \delta K_J(p, x). \quad (\text{B.45})$$

Here $K_J(p, x)$ represents the (deterministic) average effect of collisions on particles of the species J and $\langle \delta K_J(p, x) \rangle$ is the stochastic part characterized by

$$\langle \delta K_J(p, x) \delta K_{J'}(p', x') \rangle = C_{JJ'}(p, x; p', x') \delta^{(4)}(x - x'). \quad (\text{B.46})$$

The various quantities, E_J , K_J , and $C_{JJ'}$, can be evaluated in a consistent manner on the basis of Walecka-type field theory at different levels of approximation. In Ref. [300] the weak-coupling limit

was considered by including only binary collisions and the Δ decay vertex ($\Delta \leftrightarrow N\pi$) in the lowest order. The interactions are mediated by scalar and vector fields, $\phi(x)$ and $V(x) = (V_0(x), \mathbf{V}(x))$, having masses m_S and m_V . They modify the momentum, $\mathbf{p}_J^* = \mathbf{p} - g_J^V \mathbf{V}(x)$, as well as the mass, $M_J^* = M_J - g_J^S \phi(x)$, and the dispersion relation for the baryons is then

$$E_J^*(p, x) = [(\mathbf{p}_J^*)^2 + (M_J^*)^2]^{1/2}, \quad J = N, \Delta, \quad (\text{B.47})$$

while the pions remain on shell, $E_\pi^2 = p_\pi^2 + M_\pi^2$.

The resulting general Boltzmann–Langevin equation, a more complicated stochastic non-linear integro-differential equation, has not yet been implemented into a tractable form but, as an illustration, Ref. [300] considers the fluctuations of the Δ multiplicity in a spatially uniform $N\Delta$ mixture close to thermal equilibrium. It is shown that the Δ population is described by a Langevin equation and that the corresponding Fokker–Planck equation for the multiplicity distribution has an equilibrium solution of the form

$$P_{\text{equil}}(N_\Delta) \sim \frac{1}{\Gamma_\Delta} e^{-\Delta G/T}, \quad (\text{B.48})$$

where Γ_Δ is the total Δ production rate and ΔG is the difference between the free energy of the actual $N\Delta$ mixture and that of the corresponding pure nucleon gas.

As a further development of the treatment in Ref. [300], Ayik et al. [301] reduced the relativistic Boltzmann–Langevin equation to a stochastic multi-fluid model. With a view towards relativistic energies, they studied especially the case of two counter-streaming systems of nuclear matter (of the form first considered in Ref. [191]) and extracted the interflow friction force and the associated diffusion tensor.

Appendix C. Analytical approximations

In this appendix we derive a number of simple analytical expressions for the various quantities of special interest.

C.1. Fermi surface moments of higher degree

When treating the transport properties of fermion systems, it is useful to introduce the following moments,

$$\phi_n^{(k)} \equiv \frac{1}{\rho} \int \frac{d\mathbf{p}}{h^D} \epsilon^n(f(\mathbf{p})\bar{f}(\mathbf{p}))^k = \frac{2\pi}{\rho} \left(\frac{2m}{h^2}\right)^{3/2} \int_0^\infty d\epsilon \epsilon^p (f\bar{f})^k, \quad (\text{C.1})$$

where $f(\epsilon)$ is the Fermi–Dirac distribution corresponding to a given (small) temperature T . In the present investigation, the dimension of the physical space is $D = 3$, so the power of the energy is $p = n + \frac{1}{2}$. This quantity must exceed minus one in order for the moment to be finite, although the singularity at $\epsilon = 0$ is suppressed by the factor $\exp(-n\epsilon/T)$ which rapidly tends to zero for small temperatures.

For $k = 1$ these moments are those employed in Refs. [302,120] and in Eq. (B.32),

$$\phi_n^{(1)} = \phi_n \approx \frac{3}{2} \frac{T}{\epsilon_F} \epsilon_F^n \left[1 + \frac{\pi^2}{6} (n-1) \left(n + \frac{1}{2} \right) \frac{T^2}{\epsilon_F^2} \right] \approx \frac{3}{2} \frac{T}{\epsilon_F} \epsilon_F^n, \quad (\text{C.2})$$

where an expansion has been made in the (small) ratio T/ϵ_F .

In the present study we also need to consider moments of higher degrees, $k = 2, 3$. At first sight, this may appear to be a problematic task, due to the singular character of the integrand, $f\bar{f} = T\partial_\epsilon f \approx T\delta(\epsilon - \epsilon_F)$. (We use ∂_ϵ to denote $\partial/\partial\epsilon$ for brevity.) However, it is possible to evaluate these moments by elementary means, performing a suitable number of partial integrations with respect to the energy ϵ , as briefly outlined below. We are only interested in powers $n \geq -1$, for which the moments $\phi_n^{(k)}$ are well defined, and we then need not be concerned with the boundary contributions when performing the partial integrations.

First note that for an arbitrary function $F(\epsilon)$ we have

$$\int d\epsilon F f \partial_\epsilon f = \frac{1}{2} \int d\epsilon [(1 - T\partial_\epsilon)F] \partial_\epsilon f, \quad (\text{C.3})$$

by first performing a partial integration and then utilizing that $f^2 - f - f\bar{f} = f + T\partial_\epsilon f$.

Performing another partial integration, and using that $T\partial_\epsilon^2 f = 2T(\partial_\epsilon f)^2 + f\partial_\epsilon f$, we then find

$$\begin{aligned} S_n^{(2)} &\equiv T^2 \int d\epsilon \epsilon^p (\partial_\epsilon f)^2 = -\frac{T}{3} \int d\epsilon [(1 + T\partial_\epsilon)\epsilon^p] f \partial_\epsilon f \\ &= -\frac{T}{6} \int d\epsilon [(1 - T^2\partial_\epsilon^2)\epsilon^p] \partial_\epsilon f = \frac{1}{6} S_n^{(1)} - \left(n^2 - \frac{1}{4} \right) \frac{T^2}{6} S_{n-2}^{(1)}, \end{aligned} \quad (\text{C.4})$$

where the last relation has been obtained by utilizing the relation (C.3) with $F(\epsilon) = (1 + T\partial_\epsilon)\epsilon^p$. Consequently, to second order in T/ϵ_F we have

$$\phi_n^{(2)} \approx \frac{1}{4} \frac{T}{\epsilon_F} \epsilon_F^n \left[1 + \left(n + \frac{1}{2} \right) \left(\frac{\pi^2}{6} (n-1) - n + \frac{1}{2} \right) \frac{T^2}{\epsilon_F^2} \right] \approx \frac{1}{4} \frac{T}{\epsilon_F} \epsilon_F^n, \quad (\text{C.5})$$

where the last relation holds to leading order in T/ϵ_F . So to this order one may make the replacement $(f\bar{f})^2 \rightarrow \frac{1}{6} f\bar{f}$, for any dimension D .

By employing similar techniques, we can also calculate the third-degree Fermi-surface moment, $\phi_n^{(3)}$. First we perform a partial integration and find

$$S_n^{(3)} \equiv -T^3 \int d\epsilon \epsilon^p (\partial_\epsilon f)^3 = \frac{T^2}{5} \int d\epsilon [(T\partial_\epsilon + 2)\epsilon^p] f (\partial_\epsilon f)^2 + 4\epsilon^p (\partial_\epsilon f)^3, \quad (\text{C.6})$$

where it has been used that $f\partial_\epsilon(\partial_\epsilon f)^2 = (2/T)(\partial_\epsilon f)^2 - 4(\partial_\epsilon f)^3$. Using this relation again, in conjunction with a second partial integration, we find the result

$$\begin{aligned} S_n^{(3)} &= -\frac{T}{20} \int d\epsilon [(1 + T\partial_\epsilon)(2 + T\partial_\epsilon)\epsilon^p] f^2 \partial_\epsilon f \\ &= -\frac{T^2}{20} \int d\epsilon [(1 + T\partial_\epsilon)(2 + T\partial_\epsilon)\epsilon^p] (\partial_\epsilon f)^2 - \frac{T}{40} \int d\epsilon [(1 - T^2\partial_\epsilon^2)(2 + T\partial_\epsilon)\epsilon^p] \partial_\epsilon f \\ &= \frac{1}{30} S_n^{(1)} + \left(n^2 - \frac{1}{4}\right) \frac{T^2}{24} S_{n-2}^{(1)} + \dots, \end{aligned} \quad (\text{C.7})$$

where we have again used that $f^2 = T\partial_\epsilon f + f$ and relation (4.39) with $F = (1 + T\partial_\epsilon)(2 + T\partial_\epsilon)\epsilon^p$. Consequently, we have

$$\phi_n^{(3)} \approx \frac{1}{20} \frac{T}{\epsilon_F} \epsilon_F^n \left[1 + \left(n + \frac{1}{2}\right) \left(\frac{\pi^2}{6}(n-1) - \frac{5}{4} \left(n - \frac{1}{2}\right) \right) \frac{T^2}{\epsilon_F^2} \right] \approx \frac{1}{20} \frac{T}{\epsilon_F} \epsilon_F^n. \quad (\text{C.8})$$

For any dimension D , and to leading order in T/ϵ_F , we may then make the replacement $(f\bar{f})^3 \rightarrow \frac{1}{30} f\bar{f}$.

The approximate expressions (C.2), (C.5), and (C.8) help to simplify the treatment considerably, both in the present context and for a variety of other problems. The second-order approximations are quite accurate for $k=1,2,3$ and in the temperature range of interest, leading to slight overestimates. For $n=0$, which is the moment needed in the present investigation, the error is well below one per mille at the standard temperature of $T=4$ MeV, and it has grown to only 1–2% at $T=10$ MeV. In the same temperature range the lowest-order expressions, which are the ones employed throughout the present study, have errors growing from about 1% to 6–8%.

C.2. Angular averages

In this appendix we derive a number of simple analytical expressions for the various quantities of special interest, utilizing the dispersion relation,

$$1 = g \int \frac{d\mathbf{p}}{h^3} \frac{\partial h_k}{\partial \rho} \frac{\mathbf{k} \cdot \mathbf{v}}{\mathbf{k} \cdot \mathbf{v} \mp it_k^{-1}} \frac{\partial f^0}{\partial \epsilon} \quad (\text{C.9})$$

$$\approx -F_0(k, T) \left\langle \frac{\mu^2}{\mu^2 + \gamma_k^2} \right\rangle = -F_0(k, T) \left(1 - \gamma_k \arctan \frac{1}{\gamma_k} \right), \quad (\text{C.10})$$

and taking advantage of the fact that the temperature is (assumed to be) small relative to the Fermi energy. Since the integrals over momentum space contain the modulation factor $\partial f^0/\partial \epsilon$, the integrands are confined to a relatively narrow interval around the Fermi surface so, consequently, the energy integration effectively decouples from the directional average. We can then readily obtain the following angular averages,

$$-\frac{1}{F_0} \approx \left\langle \frac{\mu}{\mu - iv\gamma_k} \right\rangle = 1 + \left\langle \frac{iv\gamma_k}{\mu - iv\gamma_k} \right\rangle = 1 - \frac{\pi}{2} \gamma_k + \gamma_k^2 + \dots, \quad (\text{C.11})$$

which follow directly from the dispersion relation. The expansion in terms of γ_k shows the behavior near the spinodal boundary where $F_0 \rightarrow -1$ so γ_k tends to zero. Moreover, the auxiliary quantities $g_n \equiv \langle (\mu^2 + \gamma_k^2)^{-n} \rangle$ can also be evaluated, yielding $\gamma_k^2 g_1 = \gamma_k \arctan(1/\gamma_k) = 1 + 1/F_0$ and $2\gamma_k^2 g_2 = g_1 + 1/(1 + \gamma_k^2)$.

We can then evaluate the following angular averages,

$$\left\langle \frac{\mu}{\mu + i v \gamma_k} \frac{\mu}{\mu - i v' \gamma_k} \right\rangle = \left\{ \frac{1 - \gamma_k^2 g_1}{1 - 3\gamma_k^2 g_1 + 2\gamma_k^4 g_2} \right\} = -\frac{1}{F_0} - \left(\frac{1}{F_0} + \frac{1}{1 + \gamma_k^2} \right) \delta_{\bar{v}v'}, \quad (\text{C.12})$$

$$\left\langle \frac{1}{\mu - i v \gamma_k} \frac{1}{\mu + i v' \gamma_k} \right\rangle = g_1 + (v v' - 1) \gamma_k^2 g_2 = \frac{1 + F_0}{\gamma_k^2 F_0} \delta_{vv'} - \frac{1}{1 + \gamma_k^2} \delta_{\bar{v}v'}, \quad (\text{C.13})$$

$$\left\langle \left\langle \frac{\mu_1}{\mu_1 + i v \gamma_k} \mu_{12} \frac{\mu_2}{\mu_2 - i v' \gamma_k} \right\rangle \right\rangle = \left\langle \frac{\mu_1^2}{\mu_1 + i v \gamma_k} \right\rangle \left\langle \frac{\mu_2^2}{\mu_2 - i v' \gamma_k} \right\rangle = v v' \frac{\gamma_k^2}{F_0^2}, \quad (\text{C.14})$$

where $\bar{v} \equiv -v$. In the last quantity the directional average is with respect to both $\hat{\mathbf{p}}_1$ and $\hat{\mathbf{p}}_2$ and we have used the trigonometric relation $\mu_{12} \equiv \cos \theta_{12} = \cos \theta_1 \cos \theta_2 + \sin \theta_1 \sin \theta_2 \cos \phi_{12}$. Since $\langle \phi_{12} \rangle$ only the first term contributes which effectively allows the replacement $\mu_{12} \rightarrow \mu_1 \mu_2$ and thus causes the two integrations to decouple.

C.2.1. Legendre expansion

It is instructive for the analysis, as well as computationally helpful, to evaluate the angular averages by performing multipole expansions of the functions involved and we indicate here the most important relations.

We first note that the directional part of the dual basis functions can be expanded in terms of the Legendre polynomials $P_n(\mu)$,

$$q_k^v(\mathbf{p}) \approx \mathcal{N}_k \frac{i v}{\mu + i v \gamma_k} = \mathcal{N}_k \sum_{n \geq 0} (2n + 1) q_n^v P_n(\mu), \quad (\text{C.15})$$

where the expansion coefficients are given by $q_n^v = -i v Q_n(-i v \gamma_k)$ [303]. The complex Legendre polynomials $Q_n(z)$ satisfy the same recursion relation as the ordinary Legendre polynomials,

$$(n + 1) Q_{n+1}(z) = (2n + 1) z Q_n(z) - n Q_{n-1}(z), \quad (\text{C.16})$$

starting from $Q_0 = -i v \phi$ and $Q_1 = -\gamma_k \phi - 1$, where $\phi = \arctan(\gamma_k)$. We note that $(q_n^v)^* = q_n^{\bar{v}} = (-)^n q_n^v$.

The expansion for the eigenfunctions is equally simple,

$$f_{\mathbf{k}}^v(\mathbf{p}) \approx \frac{F_0}{\rho \phi_0} f_0 \bar{f}_0 \sum_{n \geq 0} (2n + 1) f_n^v P_n(\mu), \quad (\text{C.17})$$

where $f_n^v = \delta_{n0} - q_n^{\bar{v}}$, since $\mu/(\mu - i v \gamma_k) = 1 + i v/(\mu - i v \gamma_k)$. The elements of the overlap matrix are then given by

$$(o_k^{-1})^{vv'} \approx \frac{1}{6} \frac{F_0^2}{\rho \phi_0} \sum_{n \geq 0} (2n + 1) (f_n^v)^* f_n^{v'}. \quad (\text{C.18})$$

It follows from the symmetry properties that the terms are all positive for the diagonal elements, whereas they alternate in sign for the off-diagonal elements.

The above relations suffice for calculating the variance part of collective source terms, as well as the covariance part in the minimal model where the coupling term C_{12} contains only monopole and dipole terms.

In the more general case, the covariance part can be evaluated by taking advantage of the simple multipole expansion derived in Ref. [120], $C_{12} \sim \sum_{\ell} c_{\ell} P_{\ell}(\mu_{12})$. The key relation is

$$\begin{aligned} & \left\langle \left\langle \frac{-iv}{\mu_1 - iv\gamma_k} P_{\ell}(\mu_{12}) \frac{iv'}{\mu_2 + iv'\gamma_k} \right\rangle \right\rangle \\ &= \sum_{nn'} (2n+1)(2n'+1)(q_n^v)^* q_{n'}^{v'} \int \frac{d\omega_1}{4\pi} \frac{d\omega_2}{4\pi} P_n(\omega_1) P_{\ell}(\omega_{12}) P_{n'}(\omega_2) = (q_{\ell}^v)^* q_{\ell}^{v'} . \end{aligned} \quad (\text{C.19})$$

C.3. Overlap matrix and dual basis

The eigenfunctions $f_{\mathbf{k}}^v(\mathbf{p})$ are not orthogonal in momentum space. It is therefore of interest to consider the 2×2 overlap matrix o_k^{-1} between the collective modes. It has the elements

$$(o_k^{-1})^{vv'} \equiv \int \frac{d\mathbf{p}}{h^3} f_{\mathbf{k}}^v(\mathbf{p})^* f_{\mathbf{k}}^{v'}(\mathbf{p}) \approx -\frac{F_0}{6\rho\phi_0} \left\{ 2 + \frac{1}{1 + \frac{F_0}{\gamma_k^2}} \right\} \rightarrow \frac{1 + \frac{\pi}{2}\gamma_k\delta_{vv'}}{6\rho\phi_0} . \quad (\text{C.20})$$

We have here used the above formula (C.12) and also employed the expression (C.5) which effectively replaces $(f^0 \bar{f}^0)^2$ by $\frac{1}{6} f^0 \bar{f}^0$. On the right is indicated the behavior as the spinodal boundary is approached. The overlaps may also be evaluated by means of a Legendre expansion, which is sometimes instructive. We note that the overlaps are positive and both tend to $1/(6\rho\phi_0)$ at the spinodal boundary.

It was shown in Ref. [208] that the functions

$$q_{\mathbf{k}}^v(\mathbf{p}) \equiv \sum_{v'} o_k^{vv'} f_{\mathbf{k}}^{v'}(\mathbf{p}) = \frac{ivkV_F \mathcal{N}_k}{\mathbf{k} \cdot \mathbf{v} + ivt_k^{-1}} \quad (\text{C.21})$$

form the dual basis, $\langle q_{\mathbf{k}}^v | f_{\mathbf{k}}^{v'} \rangle = \delta_{vv'}$, with the normalization constant \mathcal{N}_k given by

$$\mathcal{N}_k^{-1} \approx -\frac{1}{\gamma_k} \left[1 + \frac{F_0}{1 + \gamma_k^2} \right] = \frac{\pi}{2} + \left(\frac{\pi^2}{4} - 2 \right) \gamma_k + \dots . \quad (\text{C.22})$$

The normalization coefficient \mathcal{N}_k remains fairly constant, exceeding its limiting value of $\pi/2$ by at most about 7%, while the inclusion of the next term in the expansion (C.22) brings the accuracy within 1%, except for the most rapidly amplified modes at zero temperature, where γ_k is largest.

In the above definition (C.21) the summation extends over *all* the states v , not merely the collective ones. The original treatment in Ref. [112] corresponds to including only the two collective modes in the expansion (C.21) of the dual basis, leading to the approximate dual states $\tilde{q}_{\mathbf{k}}^{\pm}(\mathbf{p})$ [208].

C.4. Source terms

The 2×2 matrix of the collective source terms $\mathcal{D}_k^{vv'}$ can be obtained by projecting the diffusion coefficient onto the dual basis given in Eq. (C.21) [208]. This yields

$$\mathcal{D}_k^{vv'} \approx \frac{\rho\phi_0}{t_0} \mathcal{N}_k^2 \left[\frac{1+F_0}{\gamma_k^2 F_0} \delta_{vv'} + \frac{\delta_{\bar{v}v'}}{1+\gamma_k^2} - \left(\frac{1+F_0}{\gamma_k F_0} \right)^2 - \frac{3vv'}{F_0^2} \right]. \quad (\text{C.23})$$

The first two terms arise from the variance part of the diffusion coefficient, $\hat{D}^{\text{var}}(\mathbf{p}_1, \mathbf{p}_2)$, while the two last terms are the odd and even contributions from the covariance part, $\hat{D}^{\text{cov}}(\mathbf{p}_1, \mathbf{p}_2)$. We note that $\mathcal{D}_k^{vv} \sim \gamma_k^{-1}$ near the spinodal boundary, while the mixed source term remains finite (see Ref. [208]). The initial growth rate of collective density undulations having the wave number k is then proportional to

$$\mathcal{D}_k \equiv \sum_{vv'} \mathcal{D}_k^{vv'} \approx \frac{2\rho\phi_0}{t_0} \left[1 + \frac{F_0}{1+\gamma_k^2} \right]^{-2} \left[\frac{\gamma_k^2}{1+\gamma_k^2} - \frac{(1+F_0)(2+F_0)}{F_0^2} \right] \rightarrow \frac{4}{\pi} \frac{\rho\phi_0}{t_0} \frac{1}{\gamma_k}, \quad (\text{C.24})$$

where the behavior near the boundary has been indicated.

By similar means it is possible to derive expressions for the approximate source terms employed in Ref. [112]. In that initial analysis, the source term was written as a matrix product, $\tilde{\mathcal{D}}_k = o_k \Delta_k o_k$, where $o_k^{vv'}$ are the elements of the inverse overlap matrix (C.20), where the inverse overlap matrix is given by

$$o_k^{vv'} = 6vv' \frac{\rho\phi_0}{F_0} \left[\left(1 + \frac{F_0}{1+\gamma_k^2} \right) \left(3 + \frac{F_0}{1+\gamma_k^2} \right) \right]^{-1} \left(1 + \left(1 + \frac{F_0}{1+\gamma_k^2} \right) \delta_{\bar{v}v'} \right) \rightarrow \frac{6vv'}{\pi\gamma_k} \rho\phi_0. \quad (\text{C.25})$$

In deriving this result, we have employed the formula (C.8) which makes it possible to replace $(f^0 \bar{f}^0)^3$ by $\frac{1}{30} f^0 \bar{f}^0$ in the integrand. Moreover,

$$\Delta_k^{vv'} \equiv \int \frac{d\mathbf{p}}{h^D} \int \frac{d\mathbf{p}'}{h^D} f_k^v(\mathbf{p}')^* \hat{D}(\mathbf{p}, \mathbf{p}') f_k^{v'}(\mathbf{p}') \approx \frac{1}{5t_0} (o_k^{-1})^{vv'} - \frac{1+3vv'\gamma_k^2}{36t_0\rho\phi_0}. \quad (\text{C.26})$$

It then follows that

$$\tilde{\mathcal{D}}_k^{vv'} = \frac{o_k^{vv'}}{5t_0} - \frac{\rho\phi_0 F_0}{t_0} \left[\left(3 + \frac{F_0}{1+\gamma_k^2} \right)^{-2} + vv' \left(1 + \frac{F_0}{1+\gamma_k^2} \right)^{-2} \right]. \quad (\text{C.27})$$

The term containing o_k arises from the variance part of \hat{D} , and it diverges as γ_k^{-1} . The two last terms are the even and odd contributions from the covariance part, respectively. Near the spinodal boundary the latter quantity diverges as γ_k^{-2} . However, these singularities cancel when the various collective contributions are combined,

$$\tilde{\mathcal{D}}_k \equiv \sum_{vv'} \tilde{\mathcal{D}}_k^{vv'} \approx -\frac{\rho\phi_0}{t_0} \frac{2}{3 + \frac{F_0}{1+\gamma_k^2}} \left[\frac{6}{5} \frac{1}{F_0} + \frac{2}{3 + \frac{F_0}{1+\gamma_k^2}} \right] \rightarrow \frac{1}{5} \frac{\rho\phi_0}{t_0}, \quad (\text{C.28})$$

so the collective density fluctuations remain regular at the spinodal boundary. It should also be noted that the covariance terms are of the same order of magnitude as the variance part (their relative magnitudes being approximately 5:6), but of opposite sign, so a significant degree of cancellation occurs when the various contributions are all combined.

Appendix D. Expanding bulk matter

Since the systems for which spinodal fragmentation occur are generally in a state of expansion, it is important to ascertain how this complication may affect the character of the process. The effect of expansion on spinodal fragmentation was investigated in [126] and we summarize the results here. This study treated a macroscopically uniform system (with periodic boundary conditions) within the framework of the self-consistent Vlasov equation. Since the geometry of the space is that of a multidimensional torus, the overall expansion can be introduced by prescribing a suitable time dependence of the torus radii. Although such a rescaling can readily be done in each dimension separately, a single common scaling factor is employed in order to describe an isotropic uniform expansion of nuclear matter.

D.1. Comoving variables

It is convenient to replace the usual position and momentum variables (\mathbf{q}, \mathbf{p}) by the corresponding angle and action variables (\mathbf{Q}, \mathbf{P}) ,

$$\mathbf{Q} = \frac{\mathbf{q}}{R(t)}, \quad (\text{D.1})$$

$$\mathbf{P} = R(t)\mathbf{p} - m\dot{R}(t)\mathbf{q}, \quad (\text{D.2})$$

where the common torus radius has a prescribed time dependence, $R(t)$. The single-particle Hamiltonian of the expanding system then acquires a standard form,

$$h(\mathbf{q}, \mathbf{p}) = \frac{1}{2m} \left[\mathbf{p} - m \frac{\dot{R}(t)}{R(t)} \mathbf{q} \right]^2 + u(\mathbf{q}) = \frac{P^2}{2M(t)} + U(\mathbf{Q}, t) = H(\mathbf{Q}, \mathbf{P}), \quad (\text{D.3})$$

where the mass is the associated moment of inertia, $M(t) \equiv mR(t)^2$, and the potential energy is $U(\mathbf{Q}, t) \equiv u(\mathbf{q} = R(t)\mathbf{Q})$. Consequently, the Vlasov equation retains its familiar form,

$$\frac{\partial f(\mathbf{Q}, \mathbf{P}, t)}{\partial t} = \frac{\partial U(\mathbf{Q}, t)}{\partial \mathbf{Q}} \cdot \frac{\partial f(\mathbf{Q}, \mathbf{P}, t)}{\partial \mathbf{P}} - \frac{\mathbf{P}}{M(t)} \cdot \frac{\partial f(\mathbf{Q}, \mathbf{P}, t)}{\partial \mathbf{Q}}. \quad (\text{D.4})$$

To obtain the physical matter density from the above phase-space distribution of the angle-action variables, one must take account of the increased volume,

$$\rho(\mathbf{q}, t) = R(t)^{-D} \varrho(\mathbf{Q}) = \frac{g}{R(t)^D} \int \frac{d^D \mathbf{P}}{h^D} f(\mathbf{Q}, \mathbf{P}, t). \quad (\text{D.5})$$

Furthermore, if the effective potential is generated by convoluting the density with a smearing function of a physical range a , a correspondingly smaller range $A(t) = a/R(t)$ must be employed when working only with the stretched variable \mathbf{Q} .

It is instructive to note that the above Vlasov equation has the following solution,

$$f_0(\mathbf{Q}, \mathbf{P}, t) = \left[1 + \exp \left(\beta(t) \left(\frac{P^2}{2M(t)} - \mu(t) \right) \right) \right]^{-1}, \quad (\text{D.6})$$

where $\beta(t) = \beta(0)/\lambda(t)^2$ and $\mu(t) = \mu(0)/\lambda(t)^2$, with $\lambda(t) \equiv R(t)/R(0)$ being the expansion factor. When written in terms of the physical variables,

$$f_0(\mathbf{q}, \mathbf{p}, t) = \left[1 + \exp \left(\beta(t) \left(\frac{1}{2M(t)} \left(\mathbf{p} - m \frac{\dot{R}(t)}{R(t)} \mathbf{q} \right)^2 - \mu(t) \right) \right) \right]^{-1}, \quad (\text{D.7})$$

this solution is recognized as a Fermi–Dirac distribution boosted by the local comoving frame and that the Hubble-type expansion causes the temperature $T = 1/\beta$ and the chemical potential μ to decrease in time as $\sim \lambda(t)^{-2}$.

D.2. Linear response

We now adopt the above Fermi–Dirac solution as the background distribution and obtain the RPA equation for the small disturbance $\delta f(\mathbf{Q}, \mathbf{P}, t) = f(\mathbf{Q}, \mathbf{P}, t) - f_0(\mathbf{P}, t)$,

$$\frac{\partial \delta f}{\partial t} + \frac{\partial \delta f}{\partial \mathbf{Q}} \cdot \mathbf{V} - \frac{\partial \delta f}{\partial \mathbf{P}} \cdot \frac{\partial U[\varrho(\mathbf{Q})](t)}{\partial \varrho(\mathbf{Q})} \frac{\partial \delta \varrho(\mathbf{Q})}{\partial \mathbf{Q}} = 0, \quad (\text{D.8})$$

where $\mathbf{V}(t) \equiv M(t)\mathbf{P}$. For the Fourier transform,

$$f_{\mathbf{K}}(\mathbf{P}, t) = \int \frac{d\mathbf{Q}}{2\pi} e^{-i\mathbf{K} \cdot \mathbf{Q}} f(\mathbf{Q}, \mathbf{P}, t), \quad \varrho_{\mathbf{K}}(\mathbf{Q}) = g \int \frac{d\mathbf{P}}{h^D} f_{\mathbf{K}}(\mathbf{P}, t), \quad (\text{D.9})$$

the RPA equation then reads as follows,

$$i \frac{\partial}{\partial t} f_{\mathbf{K}}(\mathbf{P}, t) = \mathbf{K} \cdot \mathbf{V} \left(f_{\mathbf{K}}(\mathbf{P}, t) + \frac{\partial f_0}{\partial \varepsilon(t)} \frac{\partial U_{\mathbf{K}}(t)}{\partial \varrho} \varrho_{\mathbf{K}}(t) \right), \quad (\text{D.10})$$

where we have introduced the kinetic energy $\varepsilon(t) = P^2/2M(t)$. This equation can be recast,

$$i \frac{\partial f_{\mathbf{K}}(\mathbf{P}, t)}{\partial t} = g \int \frac{d\mathbf{P}'}{h^D} \mathcal{K}_{\mathbf{K}, \mathbf{K}'}(\mathbf{P}, \mathbf{P}', t) f_{\mathbf{K}'}(\mathbf{P}', t), \quad (\text{D.11})$$

where the RPA kernel \mathcal{K} is diagonal in the mode index \mathbf{K} ,

$$\mathcal{K}_{\mathbf{K}\mathbf{K}'}(\mathbf{P}, \mathbf{P}', t) = \delta_{\mathbf{K}\mathbf{K}'} \mathbf{K} \cdot \mathbf{V} \left(\frac{h^D}{g} \delta(\mathbf{P} - \mathbf{P}') - \frac{\partial f_0}{\partial \varepsilon(t)} \frac{\partial U_{\mathbf{K}}(t)}{\partial \varrho} \right). \quad (\text{D.12})$$

This kernel is time dependent since the inertia, the potential, the temperature and the chemical potential are evolving with time. However, it can be easily seen that at a given time it corresponds to the linear response kernel of the static expanded system. Therefore, the instantaneous eigenfrequencies of this kernel are not affected by the expansion. However, in order to study properties such as the stability of the system, one needs to follow the propagation of δf over a finite time t . Since \mathcal{K} is

diagonal, this problem can be solved independently for each \mathbf{K} ,

$$f_{\mathbf{K}}(t) = \hat{T} e^{-i \int_0^t dt' \mathcal{K}(t')} f_{\mathbf{K}}(0) \equiv \mathcal{M}_{\mathbf{K}}(t) f_{\mathbf{K}}(0) , \quad (\text{D.13})$$

where \hat{T} is the time-ordering operator. The monodromy matrix $\mathcal{M}_{\mathbf{K}}$ propagates $f_{\mathbf{K}}$ from 0 to t and the time evolution can thus be studied by considering its eigenvalues $E_{\mathbf{K}}^v$ and eigenfunctions $f_{\mathbf{K}}^v$,

$$f_{\mathbf{K}}^v(t) = \mathcal{M}_{\mathbf{K}}(t) f_{\mathbf{K}}^v(0) = e^{i E_{\mathbf{K}}^v(t)t} f_{\mathbf{K}}^v(0) . \quad (\text{D.14})$$

In the usual case of a non-expanding system, where the kernel \mathcal{K} is independent of time, the solutions of Eq. (D.14) are the eigenstates of the RPA kernel and the eigenfrequencies $\Omega_{\mathbf{K}}$ are obtained from the associated dispersion relation (3.26). In the case of an expanding system, applying the Magnus transformation [304], it is possible to rewrite Eq. (D.13) as follows,

$$f_{\mathbf{K}}(t) = e^{\mathcal{B}(t) - i \int_0^t dt' \mathcal{K}(t')} f_{\mathbf{K}}(0) , \quad (\text{D.15})$$

where \mathcal{B} is a sum of integrals depending on the two-time commutators of the RPA kernel. For relatively slow expansion speeds, or for a very short time interval t , one may retain only the first term of (D.15) so that it is possible to express the time dependence of $f_{\mathbf{K}}(t)$ as in Eq. (D.14) where $E_{\mathbf{K}}(t)$ is now given by new dispersion relation,

$$1 = g \int \frac{d\mathbf{P}}{h^D} \frac{\mathbf{K} \cdot \bar{\mathbf{V}}}{\mathbf{K} \cdot \bar{\mathbf{V}} + E_{\mathbf{K}}(t)} \frac{\partial f_0}{\partial \varepsilon(t)} \frac{\partial \bar{U}_{\mathbf{K}}(t)}{\partial \varrho} , \quad (\text{D.16})$$

where we have introduced the time-averaged inertial parameter,

$$\bar{M}^{-1}(t) = \frac{1}{t} \int_0^t dt' M^{-1}(t') \quad (\text{D.17})$$

and the time-averaged potential,

$$\bar{U}_{\mathbf{K}}(t) = \frac{\bar{M}(t)}{M(t)} \frac{1}{t} \int_0^t dt' U_{\mathbf{K}}(t') , \quad (\text{D.18})$$

and $\bar{\mathbf{V}}(t) \equiv \mathbf{P}/\bar{M}(t)$.

The dispersion equation (D.16) shows that the expanding scenario is very similar to the familiar static case. Indeed, if we introduce a renormalized Landau parameter,

$$\bar{F}_0^{\mathbf{K}}(t) = - \frac{\partial \bar{U}_{\mathbf{K}}(t)}{\partial \varrho} g \int \frac{d\mathbf{P}}{h^D} \frac{\partial f_0}{\partial \varepsilon(t)} , \quad (\text{D.19})$$

and a renormalized free response function $\bar{\xi}$,

$$\bar{\xi}(E_{\mathbf{K}}, t) g \int \frac{d\mathbf{P}}{h^D} \frac{\partial f_0}{\partial \varepsilon(t)} = g \int \frac{d\mathbf{P}}{h^D} \frac{\mathbf{K} \cdot \bar{\mathbf{V}}}{\mathbf{K} \cdot \bar{\mathbf{V}} + E_{\mathbf{K}}(t)} \frac{\partial f_0}{\partial \varepsilon(t)} , \quad (\text{D.20})$$

then the dispersion equation can be recast into the standard form,

$$\bar{\xi}(E_{\mathbf{K}}(t), t) = -\bar{F}_0^{\mathbf{K}}(t)^{-1} . \quad (\text{D.21})$$

D.3. Discussion

The above analysis shows that during a given time, over which the commutator between the RPA kernel taken at the time t and the initial one is small compared with the eigenvalues of any of these two kernels, the system follows the standard phenomenology and so it will present instabilities, provided that $\bar{F}_0^K(t) < -1$. In such a case the expansion of Fermi liquids will lead to a modification of the sound velocity associated with long wave lengths.

For short wave lengths we know that the range of the force associated with the potential U is reducing or even suppressing the instability by effectively introducing an ultraviolet cut-off. The simplest way to include these effects is to expand the Fourier transform of the potential in powers of \mathbf{K} and consider only the lowest orders,

$$U_{\mathbf{K}}(t) = U(t)(1 - \frac{1}{2} K^2 \sigma_Q^2(t)) , \quad (\text{D.22})$$

where σ_Q is related to the range of the interaction in the variable \mathbf{Q} and therefore is inversely proportional to $R(t)$. In such a case \bar{U} becomes

$$\bar{U}_{\mathbf{K}}(t) = \bar{U}(t)(1 - \frac{1}{2} K^2 \bar{\sigma}_Q^2(t)) , \quad (\text{D.23})$$

with the renormalized range being given by

$$\bar{\sigma}_Q^2(t) \int_0^t dt' U(t') = \sigma_Q^2(t) \int_0^t dt' U(t') \lambda^2(t) \lambda^2(t') . \quad (\text{D.24})$$

If we consider only the first order terms in the expansion, $\lambda \approx 1$, we obtain

$$\bar{\sigma}_Q^2(t) \approx \sigma_Q^2(t) \lambda(t) . \quad (\text{D.25})$$

The associated interaction range in the \mathbf{q} variable evolves according to the same equation. Thus the expansion mimics a force with a longer range. This can be understood by considering that particles being too far apart to interact at the time t might have been initially closer and so in interaction. Therefore, the memory of this interaction enlarges the effective range, as described in Eq. (D.25).

From this study of expanding matter, one can conclude that the main effect of the expansion can be taken into account by introducing time-averaged inertia and Landau parameters as well as the rescaled interaction range. Thus spinodal instabilities are present also in expanding systems and follow the same phenomenology.

Just as this review was being completed, a paper appeared in which density fluctuations in expanding matter was studied within a one-body model augmented by a stochastic field constrained by the fluctuation–dissipation theorem for the expanding medium [127]. An analysis of the coupling between the evolving fluctuations and the expanding fluid yielded the distribution of the liquid domains resulting from the spinodal decomposition and the associated fragment size distribution compared favorably with the experimental multifragmentation data.

Appendix E. Spinodal fragmentation in FMD

The occurrence of spinodal fragmentation is a general feature of first-order phase transitions and not merely an artifact associated with the use of mean-field treatments. In order to illustrate how spinodal fragmentation occurs in many-body approaches as well, we summarize here a study made

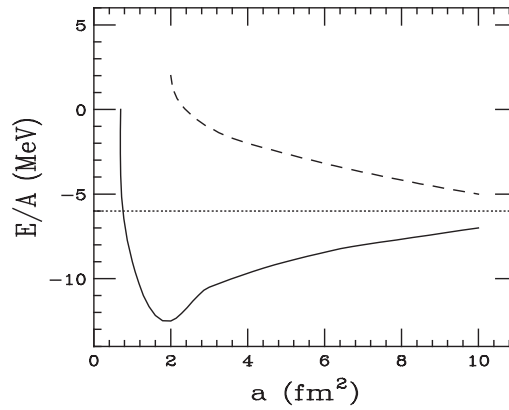


Fig. E.1. FMD energy. Energy per nucleon as a function of a , variance of the Gaussian width parameter, for a two-dimensional stationary system having a lattice mesh of $d = 5$ fm for a system with (solid curve) and without (dashed curve) α packaging. The dotted line shows the binding energy of the uniform system, which is approached when a grows large. (From Ref. [305].)

with in the framework of fermionic molecular dynamics (FMD) [305]. For studies of spinodal fragmentation within classical molecular dynamics, see Refs. [108,109,220].

E.1. Static properties

We consider idealized two-dimensional nuclear matter at zero temperature (using periodic boundary conditions). The nucleons are represented by Gaussian wave packets and they interact through a Skyrme potential having $t_0 = -243.5 \text{ MeV fm}^2$ and $t_3 = 846 \text{ MeV fm}^4$ [162]. Since the effective interaction is independent of spin and isospin, the single-particle wave functions have a four-fold degeneracy at zero temperature and this symmetry is preserved along the entire time evolution.

The wave packets form initially a regular lattice and two cases are considered: (1) each lattice site has a four-fold degeneracy or (2) each site has only one nucleon whose spin and isospin alternate (to achieve the same density, the mesh size d should then be halved). Fig. E.1 shows how the corresponding energy depends on the width parameter a , the variance of the Gaussian wave packet. When the width is large, the system resembles uniform matter and the energy value approaches the value expected at the considered density, $\rho = 4d^{-2} = 0.16 \text{ fm}^{-2}$ (the saturation density is $\rho_s = 0.55 \text{ fm}^{-2}$ for this force). Since the system may gain energy by forming α clusters, the spin–isospin saturated system has optimum width minimizing the energy, $a_0 = 2 \text{ fm}^2$. Such a minimum is observed for all dilute systems and the corresponding density has bumps at the lattice sites. By contrast, when the spin–isospin symmetry is broken by *fiat*, energy is gained only by spreading, as the uniform limit is approached.

To study the phase diagram and the possible coexistence of two phases, and at the same time to learn about the fragmentation dynamics, one may perturb the initially uniform system and follow its response. In this way one may see whether instabilities occur (and hence define the spinodal region) and, at the same time, one may study the most important features of the early fragment formation.

E.2. Early fragmentation dynamics in dilute systems

For a given Hamiltonian H , the equations of motions for the various parameters may be derived from the time dependent variational principle (see [247,248]). Since, to a good approximation, the early dynamics is described by a linear response treatment, we summarize an RPA study of fermionic molecular dynamics [305].

We use s_n to denote the four complex Gaussian wave packet parameters (the three phase-space centroids and the complex variance a) for the nucleon located at the lattice site n . By linearizing the equations of motion [247] around a stationary solution, $s_n = \dot{s}_n + \delta s_n$, we obtain the equations of motion [305],

$$\sum_{n'} A_{nn'} \cdot \delta \dot{s}_{n'}^* = \sum_{n'} \left[\frac{\partial^2 \mathcal{H}}{\partial s_n \partial s_{n'}} \cdot \delta s_{n'} + \frac{\partial^2 \mathcal{H}}{\partial s_n \partial s_{n'}^*} \cdot \delta s_{n'}^* \right], \quad (\text{E.1})$$

The matrix multiplying the time derivative $\delta \dot{s}_{n'}^*$ is defined as

$$A_{nn'} = \frac{\partial^2 \mathcal{L}_0}{\partial s_n \partial \dot{s}_{n'}^*} - \frac{\partial^2 \mathcal{L}_0}{\partial \dot{s}_n \partial s_{n'}^*}, \quad (\text{E.2})$$

where $\mathcal{L}_0 = \mathcal{L} + \mathcal{H}$, with \mathcal{L} being the Lagrange function for the system and $\mathcal{H} = \langle \hat{H} \rangle$.

The centroids of the Gaussian wave packets are placed on a lattice of a given mesh d , so that the index n runs over the lattice sites. Due to the imposed translational symmetry of the unperturbed system, the above relations do not depend on the specific lattice site n . The imaginary part of the centroid position (proportional to the momentum) vanishes in the unperturbed stationary state, as does the imaginary part of the width parameter. Furthermore, due to the isotropy of the system, we need to consider perturbations $\delta \mathbf{z}$ along only one of the lattice directions, but we shall give the general form of the equations. The above linear equation (E.1) then yields two coupled equations of motion,

$$\sum_{n'} A_{nn'} \cdot \delta \dot{s}_{n'}^* = \sum_{n'} B_{nn'} \cdot \delta s_{n'} + C_{nn'} \cdot \delta s_{n'}^*, \quad (\text{E.3})$$

where

$$B_{nn'} = \frac{\partial^2 \mathcal{H}}{\partial s_n \partial s_{n'}} \quad , \quad C_{nn'} = \frac{\partial^2 \mathcal{H}}{\partial s_n \partial s_{n'}^*}. \quad (\text{E.4})$$

Taking the Fourier transform with respect to time and considering the plane wave representation, $\delta s_n = \sum_k \delta s_k e^{ikdn}$, we obtain the dispersion equation [305],

$$i\omega_k A_k \cdot \delta s_{-k}^* = B_k \cdot \delta s_k + C_k \cdot \delta s_{-k}^*. \quad (\text{E.5})$$

Information about the evolution of the system is given by determining eigenvalues and eigenvectors of this system of complex equations. The four eigenvalues come in pairs of solutions with opposite sign, so that there are two independent solutions for ω_k . Negative solutions for ω_k^2 signal the presence of instabilities. Moreover, the value of ω_k informs us about the early dynamical development of the perturbation introduced in the system and hence on the path towards fragmentation.

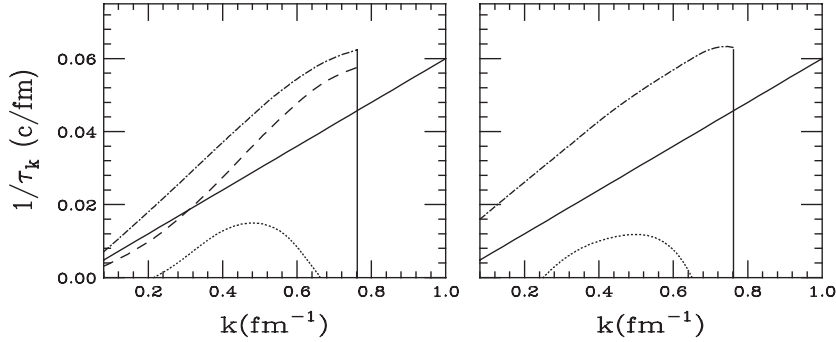


Fig. E.2. FMD dispersion relations. Dispersion relations obtained within AMD (*left*) or FMD (*right*), using several values of the wave packet variance: $a = 2 \text{ fm}^2$ (dot-dashed), $a = 4 \text{ fm}^2$ (dashes), $a = 7 \text{ fm}^2$ (dots). Also shown is the result obtained with linearized TDHF (solid). (From Ref. [305].)

E.2.1. AMD framework

Let us first consider the case where the Gaussian widths are kept fixed, as in AMD calculations [246]. The only time-dependent parameter is then the Gaussian centroid. The electric isoscalar modes are defined by the unique complex equation for the displacement of the centroid positions of the wave functions, $\delta \mathbf{z}_n = (\delta x_n, \delta y_n, \delta z_n, 0)$,

$$i\omega_k \mathbf{A}_k \cdot \delta \mathbf{z}_{-k}^* = \mathbf{B}_k \delta \mathbf{z}_k + \mathbf{C}_k \delta \mathbf{z}_{-k}^* \quad (\text{E.6})$$

Then only two opposite solutions appear, $\pm\omega_k$, for each wave vector \mathbf{k} .

For example, let us consider a mesh having $d = 3.8 \text{ fm}$ corresponding to an average density of $\rho_0 = \frac{1}{2}\rho_s$. In this case, ω_k^2 may be negative and the system is then unstable. The resulting growth time $t_k \equiv |\omega_k|^{-1}$ is shown in Fig. E.2 (*left*) for various values of the width a , to which it is very sensitive. For values of around $a \approx 2 \text{ fm}^2$ the growth times are close to those predicted by linearizing the quantal mean-field treatment TDHF (quantal RPA) (solid curve). However, in such a case, due to the small width, the observed instabilities can be understood as spinodal instabilities of a gas of α particles.

When the width of the Gaussians is increased, the instabilities are being quenched. In particular, in the case of a uniform initial density (large values of the width), the instabilities are almost fully suppressed, in contrast to the quantal RPA calculations (see Fig. E.2). This effect originates from the fact that the forces acting on the wave packet centroids are very weak due to the smoothing resulting from the large widths. Then the motion of the centroids is inhibited and so are the instabilities. The vertical cutoff seen in Fig. E.2 arises because modes with wave-lengths shorter than twice the lattice mesh cannot be represented on the lattice.

Conversely, in a full TDHF calculation sound waves can be propagated by the co-operative contribution of several single-particle wave functions, which are not constrained to have any particular form. However, the RPA dispersion relation also yields a cutoff, but at larger wave numbers, $k > 2 \text{ fm}^{-1}$, due to quantal effects [105].

When the width is kept fixed, as in AMD, it is well-known that particles can experience a spurious dynamics, due to conflicts between the fixed width of the wave packets and the need to have anti-symmetric Slater determinants. In particular, particles of the same type exhibit spurious

scattering. This problem, which could affect the results presented above, is removed in calculations of the FMD type, where also the widths of the wave packets evolve.

E.2.2. FMD framework

In the FMD case, we consider a mesh size of $d = 3.8$ fm, which is typical. The initial stationary state then has minimal energy when the width value $a = 2$ fm² is employed. We shall also discuss a nearly uniform case having $a = 7$ fm², which is approximately stationary since the derivative of the energy is small for large width values (see Fig. E.1). Large widths mimic also stationary states for more disordered systems (where the spin–isospin symmetry is explicitly broken).

With the width as a time-dependent parameter, one obtains two independent solutions for ω_k . They are associated with different coupled motions of the centroids and the widths. In Fig. E.2 (right) we display the solution that most corresponds to a displacement of the centroid positions. The inclusion of the width as a dynamical parameter slightly modifies the dispersion relation only slightly from its AMD form. Hence also in the framework of FMD calculations, instabilities are suppressed when the stationary width is large.

In the case of a nucleon gas (i.e. when the spin–isospin symmetry is broken), the minimum energy is reached asymptotically for large values of the width a (see the dashed line in Fig. E.1). Therefore, one can conclude that in an excited situation, where the α -package is broken, the natural tendency of the nucleons will be to present a large width. This is in fact the well-known effect related to the wave packet spreading. Then, according to the previous discussion about dispersion relations, one should expect an important quenching of the spinodal instabilities when the width is considered as a dynamical variable (FMD).

From this study it follows that when the α packing is broken the FMD evolution of a nuclear reaction allows clusterization to happen only at the dense stage, when correlations among the particles are strong and the value of the width is still close to the initial one. This, of course, would not correspond to spinodal decomposition. Conversely, in approaches using a fixed width, spinodal decomposition may happen if the system enters low density regions, even in the absence of α packing [306]. Furthermore, for appropriate values of the width, one may obtain features similar to those obtained in stochastic mean field treatments as well as in classical systems interacting through long-range forces [39].

E.3. Phase transitions in finite systems

In the context of FMD dynamics, it has been shown that, for systems of interacting nucleons in the field of an external-container, it is possible to observe a liquid–gas phase transition of first order [307]. Nuclei in their ground state and confined by an external field are excited by displacing all wave packets randomly from their ground-state positions. The system then relaxes into a coexistence between large clusters (the liquid phase) and very light particles (the vapor phase). As the excitation energy is increased, a first-order phase transition appears, as inferred from the analysis of the associated caloric curve (temperature versus excitation energy). Increasing the amplitude of the external field (which can be considered as an external pressure acting on the system), the plateau in the caloric curve finally disappears and one can in this manner identify the critical temperature. For ¹⁶O nuclei, the value of the critical temperature obtained is $T_c = 8$ MeV. From this analysis, together with the analysis made above, one can deduce that the coexistence between liquid and gas

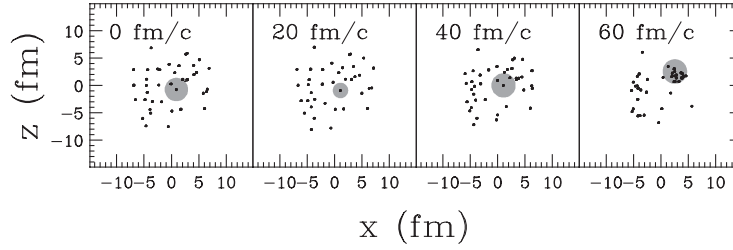


Fig. E.3. FMD fragmentation pattern. Fragmentation pattern exhibited by a dilute system of 160 nucleons with α symmetry enforced. (From Ref. [305].)

phases may be due to the resilience of the α -like structure present in the ground state of the finite nuclei considered. In fact, we have seen that, in absence of the α packing, the width acquires large values when the density is low and cluster formation is inhibited.

E.4. Dynamical evolution of excited and dilute finite systems

To illustrate the dynamical evolution of excited finite systems, we discuss 3D simulations for 160 nucleons based on the FMD approach [305]. The parameters chosen for the Skyrme-like force are $t_0 = -1033 \text{ MeV fm}^3$ and $t_3 = 14687.5 \text{ MeV fm}^6$. To account for finite-range effects (important when surfaces are presents), the one-body density has been convoluted with a Gaussian of width $g = 0.4 \text{ fm}$. The system is initialized as a piece of a 3D lattice at half normal density, using the α packing. The α clusters are then perturbed randomly around their initial positions to allow possible amplification of unstable modes. The widths of the wave packets are also perturbed. It is seen that the dynamical evolution induces oscillations of the widths around the equilibrium value (2 fm^2) for α particles. When these oscillations are sufficiently small, so that the widths remain small during the entire evolution, one observes the formation of “fragments” (clusters of α particles), as illustrated in Fig. E.3. As discussed before, this mechanism resembles the spinodal decomposition of a gas of α particles. (It should be noted that if the widths were kept fixed (as in AMD) at a rather small value (like $a = 2 \text{ fm}^2$), the occurrence of instabilities and cluster formation would have been observed as well.)

Another case worth considering is the nucleon gas. Here the 160 nucleons are initially placed randomly within a sphere of radius $R = 8 \text{ fm}$ (the average density is then $\frac{1}{2}\rho_s$) and the system is endowed with a small self-similar expansion. Two cases are considered for the initial widths: $a = 2 \text{ fm}^2$ (corresponding to an energy of $2 \text{ MeV}/A$) and $a = 4 \text{ fm}^2$ (corresponding to $E/A = -2 \text{ MeV}$). The time evolution of these systems are shown in Fig. E.4.

In both cases the early dynamics is dominated by an increase of the width. This is the behavior expected for a disordered system since the minimum energy is obtained for large widths (see Fig. E.1). The more excited system undergoes a vaporization into individual nucleons, while the other system collapses into a single source, evaporating few nucleons from its surface. Almost no clusterization is observed. This absence of spinodal instabilities in the simulations confirms the conclusion drawn from the linear response treatment. Because of the appearance of large widths the residual interaction between centroids is smoothed out so that spinodal instabilities are suppressed.

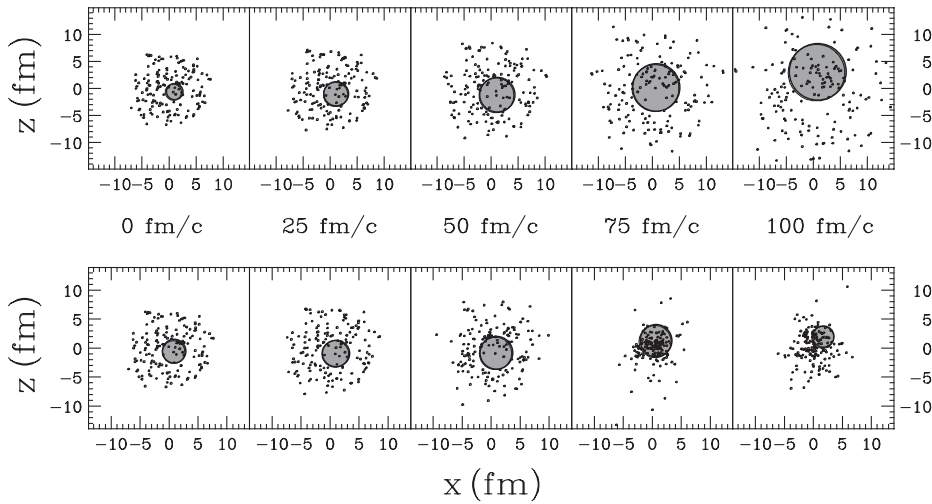


Fig. E.4. FMD evolution. Time evolution of a nucleon gas initialized at half the saturation density, for two different values of the excitation energy. (From Ref. [305].)

However it should be noticed that clusterization could occur also in the case of a nucleon gas if the width is kept fixed, as in AMD calculations.

E.5. Further developments of molecular dynamics

We finally briefly recall certain further developments of molecular dynamics that appear to provide an improved framework for understanding nuclear dynamics. In particular, in order to alleviate problems associated with the use of a fixed wave packet, various forms of stochastic branching have been introduced into many-body approaches of the FMD and AMD type. The resulting extended treatments have been applied to nuclear fragmentation, though the specific spinodal fragmentation mechanism has yet to be investigated with these refined approaches.

In order to take account of the energy fluctuations in a system described by a wave packet [308], Ohnishi and Randrup [309,310] augmented the AMD propagation by a stochastic term, leading to the *Quantum Langevin* model. The Langevin term enables the Gaussian wave packet system to explore its entire energy spectral distribution, rather than being restricted to its average value. In this manner, it is ensured that the system relaxes towards the appropriate quantum-statistical equilibrium, contrary to what happens in the usual deterministic FMD and AMD treatments. The inclusion of quantum fluctuations via the Langevin term improves the nuclear equation of state and influences the outcome of nuclear reactions [311]. (This general quantum mechanical effect also plays a role for the critical properties of noble gases [312].)

In particular, the quantum Langevin term is significant in nuclear multifragmentation, as was demonstrated by the investigation of Au+Au collisions at 100–400 MeV per nucleon [313]. It appears that the inclusion of quantum fluctuations enhances the average multiplicity of IMF, especially in central collisions, with respect to standard QMD or AMD simulations, thus improving the

agreement with experimental data. This is mainly because the fragment excitation energies are reduced due to the effect of quantum fluctuations.

A different approach was taken by Ono and Horiuchi [314], who augmented the AMD model with a stochastic incorporation of the Vlasov equation, yielding the *AMD-Vlasov* model. During given time intervals, the system is propagated according to the mean-field transport equation for the one-body density and a branching of trajectories is considered, each of them having the Gaussian wave packet structure.

Multifragmentation in Au+Au collisions has also been studied within this approach [315]. In these simulations, probably due to the Vlasov corrections, a composite system may survive until it enters low-density regions. Then fragmentation might be considered to happen as a consequence of the occurrence of bulk instabilities, though this was not directly investigated in Ref. [315]. In this case the fragmentation pattern should resemble the results obtained in the stochastic mean-field approximation. This would be an interesting issue to pursue.

References

- [1] L.G. Moretto, G.J. Wozniak, *Ann. Rev. Nucl. Part. Sci.* 43 (1993) 379.
- [2] G.C. Bonsignori, et al. (Eds.), in: *Bologna 2000: Structure of the Nucleus at the Dawn of the Century*, Vol. I: Nucleus–Nucleus Collisions, Sections II–V, World Scientific, Singapore, 2001.
- [3] G.F. Bertsch, P.J. Siemens, *Phys. Lett. B* 126 (1983) 9.
- [4] P.J. Siemens, *Nature* 305 (1983) 410.
- [5] J. Richert, P. Wagner, *Phys. Reports C* 350 (2001) 1.
- [6] A. Bonasera, M. Bruno, C.O. Dorso, P.F. Mastinu, *Rev. Nuovo Cim.* 23 (2000) 1.
- [7] O. Lopez, *Nucl. Phys. A* 685 (2001) 246.
- [8] Ph. Chomaz, in: E. Norman, et al. (Eds.), *Intl. Nucl. Phys. Conf. 2001*, AIP (2002) 167.
- [9] L.G. Moretto, et al., in: E.B. Norman, et al., (Eds.), *Intl. Nucl. Phys. Conf. 2001*, AIP, New York, 2002, p. 182.
- [10] W.A. Friedman, W.G. Lynch, *Phys. Rev. C* 28 (1983) 16.
- [11] J.A. López, J. Randrup, *Nucl. Phys. A* 503 (1989) 183.
- [12] C. Dorso, J. Randrup, *Phys. Lett. B* 301 (1993) 320.
- [13] W.A. Friedman, *Phys. Rev. C* 42 (1990) 667.
- [14] J. Randrup, S.E. Koonin, *Nucl. Phys. A* 356 (1981) 223.
- [15] G. Fai, J. Randrup, *Nucl. Phys. A* 381 (1982) 557.
- [16] J. Randrup, *Comp. Phys. Comm.* 77 (1993) 153.
- [17] D.H.E. Gross, *Rep. Prog. Phys.* 53 (1990) 605.
- [18] D.H.E. Gross, et al., *Phys. Rep. C* 279 (1997) 119.
- [19] J.P. Bondorf, et al., *Phys. Rep. C* 257 (1995) 133.
- [20] T.S. Biro, J. Knoll, J. Richert, *Nucl. Phys. A* 459 (1986) 692.
- [21] J.B. Elliott, et al., *Phys. Rev. Lett.* 85 (2000) 1194.
- [22] M.E. Fisher, *Physics* 3 (1967) 255.
- [23] B. Borderie, *J. Phys. G* 28 (2002) R217.
- [24] B. Diu, C. Gutmann, D. Lederer, B. Roulet, *Élément de Physique Statistique*, Hermann, Paris 1989, ISBN 2-7056-6065-8.
- [25] B. Friedman, V.R. Pandharipande, *Nucl. Phys. A* 361 (1981) 502.
- [26] P. Ring, P. Shuck, *The Nuclear Many-Body Problem*, Springer, New York, 1980.
- [27] T.H.R. Skyrme, *Phil. Mag.* 1 (1956) 1043.
- [28] T.H.R. Skyrme, *Nucl. Phys.* 9 (1959) 615.
- [29] G.Q. Li, *Comm. Theo. Phys.* 13 (1990) 457.
- [30] R. Ogul, *Int. J. Mod. Phys. E* 7 (1998) 419.

- [31] F.S. Zhang, *Z. Phys. A* 356 (1996) 163.
- [32] G. Sauer, H. Chandra, U. Mosel, *Nucl. Phys. A* 264 (1976) 221.
- [33] R.G. Seyler, C.H. Blanchard, *Phys. Rev.* 124 (1961) 227.
- [34] W.D. Myers, W.J. Swiatecki, *Ann. Phys.* 204 (1990) 401.
- [35] J. Randrup, E. de Lima Medeiros, *Nucl. Phys. A* 529 (1991) 115.
- [36] E. de Lima Medeiros, J. Randrup, *Phys. Rev. C* 45 (1992) 372.
- [37] C. Dorso, J. Randrup, *Phys. Lett. B* 232 (1989) 29.
- [38] W.I. Goldburg, J.S. Huang, NATO Advanced Study Institute on Fluctuations, Instabilities, and Phase Transitions, Geilo, Norway, Vol. 87, Plenum Press, New York, 1975.
- [39] B. Jacquot, A. Guarnera, Ph. Chomaz, M. Colonna, *Phys. Lett. B* 386 (1996) 23.
- [40] M. Barranco, J.R. Buchler, *Phys. Rev. C* 22 (1980) 1729.
- [41] N.K. Glendenning, *Phys. Rev. D* 46 (1992) 1274.
- [42] H. Müller, B. Serot, *Phys. Rev. C* 52 (1995) 2072.
- [43] B.A. Li, C.M. Ko, *Nucl. Phys. A* 618 (1997) 498.
- [44] V. Baran, M. Colonna, M. Di Toro, A.B. Larinov, *Nucl. Phys. A* 632 (1998) 287.
- [45] D. Catalano, G. Giansiracusa, U. Lombardo, *Nucl. Phys. A* 681 (2001) 390.
- [46] S.J. Lee, A.Z. Mekjian, *Phys. Rev. C* 63 (2001) 44605.
- [47] V. Baran, M. Colonna, M. Di Toro, V. Greco, *Phys. Rev. Lett.* 86 (2001) 4492.
- [48] J. Margueron, Ph. Chomaz, *Phys. Rev. C* 67 (2003) 041602.
- [49] B.D. Serot, *Rep. Prog. Phys.* 55 (1992) 1855.
- [50] B.D. Serot, J.D. Walecka, *Int. J. Mod. Phys. E* 6 (1997) 515.
- [51] M. Colonna, Ph. Chomaz, S. Ayik, *Phys. Rev. Lett.* 88 (2002) 122701.
- [52] Ph. Chomaz, F. Gulminelli, *Phys. Lett. B* 447 (1999) 221.
- [53] H.S. Xu, et al., *Phys. Rev. Lett.* 85 (2000) 716.
- [54] H.S. Xu, et al., *Phys. Rev. C* 65 (2002) 061602.
- [55] G. Verde, et al., *Nucl. Phys. A* 681 (2001) 299c.
- [56] M.B. Tsang, et al., *Nucl. Phys. A* 681 (2001) 323c.
- [57] M.B. Tsang, et al., *Phys. Rev. Lett.* 86 (2001) 5023.
- [58] W. Thirring, *Z. Phys. A* 235 (1970) 339.
- [59] M.S.S. Challa, J.H. Hetherington, *Phys. Rev. Lett.* 60 (1988) 77;
Phys. Rev. A 38 (1988) 6324.
- [60] M.K. Kiessling, J.K. Percus, *J. Stat. Phys.* 78 (1995) 1337.
- [61] A.C. Hernandez, S. Velasco, *Am. J. Phys.* 66 (1998) 928.
- [62] F. Gulminelli, Ph. Chomaz, *Phys. Rev. Lett.* 82 (1999) 1402.
- [63] Ph. Chomaz, V. Duflot, F. Gulminelli, *Phys. Rev. Lett.* 85 (2000) 3587.
- [64] Ph. Chomaz, F. Gulminelli, V. Duflot, *Phys. Rev. E* 64 (2001) 046114.
- [65] F. Gulminelli, P. Chomaz, in: I. Iori (Ed.), XXXVI Winter Meeting on Nuclear Physics, Bormio, Italy, 1998, p. 404.
- [66] D.H.E. Gross, E. Votyakov, *Europhys. J. B* 15 (2000) 115.
- [67] D.H.E. Gross, *Nucl. Phys. A* 681 (2001) 366.
- [68] D.H.E. Gross, *Chaos, Solitons and Fractals* 13 (2002) 417.
- [69] F. Calvo, *Ann. Phys. Fr.* 24 (1999) 1.
- [70] D. Lynden-Bell, XXth IUPAP International Conference on Statistical Physics, Paris, July 20–24, 1998.
- [71] P. Labastie, R.L. Whetten, *Phys. Rev. Lett.* 65 (1990) 1567.
- [72] S.J. Lee, A.Z. Mekjian, *Phys. Rev. C* 56 (1997) 2621.
- [73] L.G. Moretto, J.B. Elliott, L. Phair, G.J. Wozniak, *Phys. Rev. C* 66 (2002) 041601(R).
- [74] G. Peilert, J. Randrup, H. Stöcker, W. Greiner, *Phys. Lett. B* 260 (1991) 271.
- [75] J. Aichelin, H. Stöcker, *Phys. Lett. B* 176 (1986) 14.
- [76] C. Dorso, S. Duarte, J. Randrup, *Phys. Lett. B* 188 (1987) 287.
- [77] S. Pratt, C. Montoya, F. Ronning, *Phys. Lett. B* 349 (1995) 261.
- [78] Ph. Chomaz, F. Gulminelli, *Nucl. Phys. A* 647 (1999) 153.
- [79] M. D’Agostino, et al., *Phys. Lett. B* 473 (2000) 219.

- [80] R. Bougault, et al., in: I. Iori (Ed.), *Proceedings of the 38th Winter Meeting on Nuclear Physics*, Bormio, Italy, 2000, p. 404.
- [81] N. Leneindre, Ph.D. Thesis, University of Caen, France, 1999; LPCC-T-9902.
- [82] M. D’Agostino, et al., *Nucl. Phys. A* 650 (1999) 329.
- [83] T. Lefort, et al., *Phys. Rev. C* 64 (2001) 64603.
- [84] M. Schmidt, et al., *Phys. Rev. Lett.* 86 (2001) 1191.
- [85] M. Hillert, *Acta Met.* 9 (1961) 525.
- [86] J.W. Cahn, M. Hillert, *J. Chem. Phys.* 28 (1958) 258.
- [87] J.W. Cahn, *Acta Met.* 9 (1961) 795.
- [88] J.W. Cahn, *Acta Met.* 10 (1962) 179.
- [89] J.W. Cahn, *Acta Met.* 14 (1966) 1685.
- [90] J.W. Cahn, *Trans. Metl. Soc. AIME* 242 (1968) 166.
- [91] H.E. Cook, *Acta Met.* 18 (1970) 297.
- [92] J.S. Langer, M. Bar-on, *Ann. Phys.* 78 (1973) 421.
- [93] J.S. Langer, M. Bar-on, H.D. Miller, *Phys. Rev. A* 11 (1975) 1417.
- [94] J.S. Langer, in: C. Gorréche (Ed.), *Solids Far From Equilibrium*, Cambridge University Press, Cambridge, 1992, p. 330.
- [95] J.D. Gunton, M. San Miguel, P.S. Sahni, *Phase Transitions and Critical Phenomena*, Vol. 8, Academic Press, New York, 1983.
- [96] G. Holzwarth, G. Eckart, *Nucl. Phys. A* 325 (1979) 1.
- [97] M. Brack, C. Guet, H.B. Håkansson, *Phys. Rep. C* 123 (1985) 275.
- [98] S. Ayik, E. Suraud, J. Strijewski, M. Belkacem, *Z. Phys. A* 337 (1990) 413.
- [99] B. Jacquot, Ph.D. Thesis, University of Caen, France, 1996; GANIL Report No. T-96-05, 1996.
- [100] P. Bonche, S. Levit, D. Vauterin, *Nucl. Phys. A* 427 (1984) 278.
- [101] G. Fabbri, F. Matera, *Phys. Rev. C* 58 (1998) 1345.
- [102] L.D. Landau, *Sov. Phys. JEPT* 3 (1957) 920.
- [103] L.D. Landau, E.M. Lifshitz, *Statistical Physics*, Pergamon Press, Oxford, 1958.
- [104] C.J. Pethick, D.G. Ravenhall, *Ann. Phys.* 183 (1988) 131.
- [105] S. Ayik, M. Colonna, Ph. Chomaz, *Phys. Lett. B* 353 (1995) 417.
- [106] H. Heiselberg, C.J. Pethick, D.G. Ravenhall, *Phys. Rev. Lett.* 61 (1988) 818.
- [107] H. Heiselberg, C.J. Pethick, D.G. Ravenhall, *Ann. Phys.* 223 (1993) 37.
- [108] J.A. López, G. Lübeck, *Phys. Lett. B* 219 (1989) 215.
- [109] J.A. Lopez, *Rev. Mexicana Fisica* 48 (1992) 95.
- [110] B.L. Friman, J. Niskanen, E.M. Nyman, *Nucl. Phys. A* 383 (1982) 285.
- [111] D. Kiderlen, H. Hofmann, *Phys. Lett. B* 332 (1994) 8.
- [112] M. Colonna, Ph. Chomaz, J. Randrup, *Nucl. Phys. A* 567 (1994) 637.
- [113] M. Colonna, Ph. Chomaz, *Phys. Rev. C* 49 (1994) 1908.
- [114] P. Pines, D. Noziers, *The Theory of Quantum Liquids*, Vol. 1, Addison-Wesley, 1989.
- [115] J. Ventura, A. Polls, X. Vinas, S. Hernandez, M. Pi, *Nucl. Phys. A* 545 (1992) 247c.
- [116] J. Ventura, A. Polls, X. Vinas, S. Hernandez, *Nucl. Phys. A* 578 (1994) 147.
- [117] J. Randrup, Report LBL-35848 (1994).
- [118] D. Idier, B. Benhassine, M. Farine, B. Remaud, F. Seville, *Phys. Rev. C* 48 (1993) R498.
- [119] P. Božek, *Phys. Lett. B* 383 (1996) 121.
- [120] J. Randrup, S. Ayik, *Nucl. Phys. A* 572 (1994) 489.
- [121] A.B. Larionov, I.N. Mishustin, *Phys. At. Nucl.* 57 (1994) 636.
- [122] E.S. Weibel, *Phys. Rev. Lett.* 2 (1959) 83.
- [123] S. Mrówczyński, *Phys. Rev. C* 49 (1994) 2191.
- [124] S. Mrówczyński, *Phys. Lett. B* 393 (1997) 26.
- [125] J. Randrup, St. Mrówczyński, *Phys. Rev. C* in press; nucl-th/0303021.
- [126] M. Colonna, Ph. Chomaz, A. Guarnera, B. Jacquot, *Phys. Rev. C* 51 (1995) 2671.
- [127] F. Matera, A. Dellafiore, G. Fabbri, *Phys. Rev. C* 67 (2003) 34608.
- [128] W. Cassing, V. Metag, U. Mosel, K. Niita, *Phys. Rep. C* 188 (1990) 363.

- [129] P. Haensel, Nucl. Phys. A 301 (1978) 53.
- [130] M. Colonna, M. Di Toro, A.B. Larinov, Phys. Lett. B 428 (1998) 1.
- [131] F. Matera, V.Yu. Denisov, Phys. Rev. C 49 (1994) 2816.
- [132] C.F. von Weizsäcker, Z. Phys. 96 (1935) 432.
- [133] H.A. Bethe, R.F. Backer, Rev. Mod. Phys. 8 (1936) 82.
- [134] W.D. Myers, W.J. Swiatecki, Nucl. Phys. 81 (1966) 1.
- [135] G. Baym, H.A. Bethe, C.J. Pethick, Nucl. Phys. A 175 (1971) 225.
- [136] H. Krivine, J. Treiner, O. Bohigas, Nucl. Phys. A 336 (1990) 155.
- [137] B.A. Li, A.T. Sustich, M. Tilley, B. Zhang, Nucl. Phys. A 699 (2002) 493.
- [138] E. Ramakrishnan, et al., Phys. Rev. C 57 (1998) 1803.
- [139] S.J. Lee, Phys. Lett. B 263 (1991) 141.
- [140] B. Jacquot, S. Ayik, Ph. Chomaz, M. Colonna, Phys. Lett. B 383 (1996) 247.
- [141] V.M. Kolomietz, S. Shlomo, Phys. Rev. C 60 (1999) 044612.
- [142] W. Nörenberg, G. Papp, P. Rozmej, Eur. Phys. J. A9 (2000) 327.
- [143] W. Nörenberg, G. Papp, P. Rozmej, Eur. Phys. J. A14 (2000) 43.
- [144] Ph. Chomaz, M. Colonna, A. Guarnera, J. Randrup, Phys. Rev. Lett. 73 (1994) 3512.
- [145] A. Guarnera, M. Colonna, Ph. Chomaz, Phys. Lett. B 373 (1996) 267.
- [146] A. Guarnera, Ph. Chomaz, M. Colonna J. Randrup, Phys. Lett. B 403 (1997) 191.
- [147] R. Donangelo, A. Romanelli, H. Schultz, A.C. Sicardi-Schifino, Phys. Rev. C 49 (1994) 3182.
- [148] R. Donangelo, A. Romanelli, A.C. Sicardi-Schifino, Phys. Rev. C 53 (1996) 1873.
- [149] L.P. Csernai, J. Nemeth, G. Papp, J. Heavy Ion Phys. 3 (1996) 17.
- [150] G. Batko, J. Randrup, Nucl. Phys. A 563 (1993) 97.
- [151] W. Bauer, G.F. Bertsch, H. Schultz, Phys. Rev. Lett. 69 (1992) 1888.
- [152] E. Norbeck, Q.Z. Luo, Y.W. Cheng, P. Pogodin, F.D. Ingram, Nucl. Phys. A 607 (1996) 105.
- [153] B. Borderie, B. Remaud, M.F. Rivet, F. Seville, Phys. Lett. B 302 (1993) 15.
- [154] D. Vautherin, M. Veneroni, Proceedings of the First International Spring Seminar on Nuclear Physics, Sorrento, Italy, 1986.
- [155] B. Jacquot, M. Colonna, S. Ayik, Ph. Chomaz, Nucl. Phys. A 617 (1997) 356.
- [156] E. Chabanat, et al., Nucl. Phys. A 627 (1997) 710.
- [157] E. Chabanat, et al., Nucl. Phys. A 635 (1997) 231;
Erratum: Nucl. Phys. A 643 (1998) 441.
- [158] M. Tabor, Chaos and Integrability in Non Linear Dynamics, Wiley, New York, 1989.
- [159] E. Ott, Chaos in Dynamical Systems, Cambridge University Press, Cambridge, 1993.
- [160] R. Donangelo, A. Romanelli, A.C. Sicardi-Schifino, Phys. Lett. B 263 (1991) 342.
- [161] V.G. Kartavenko, K.A. Gridnev, W. Greiner, Int. J. Mod. Phys. E 3 (1994) 1219.
- [162] G.F. Burgio, Ph. Chomaz, J. Randrup, Phys. Rev. Lett. 69 (1991) 885.
- [163] D.H.E. Gross, B.A. Li, A.R. De Angelis, Ann. Phys. 1 1 (1992) 467.
- [164] G. Fai, J. Randrup, Nucl. Phys. A 404 (1983) 551.
- [165] S.E. Koonin, J. Randrup, Nucl. Phys. A 471 (1987) 355c.
- [166] J.P. Bondorf, Nucl. Phys. A 488 (1988) 31c.
- [167] X. Campi, Nucl. Phys. A 495 (1989) 259c.
- [168] A. Bonasera, V. Latora, A. Rapisarda, Phys. Rev. Lett. 79 (1995) 3434.
- [169] M. Belkacem, V. Latora, A. Bonasera, Phys. Rev. C 52 (1995) 271.
- [170] T. Srokowski, M. Ploszajczak, Phys. Rev. Lett. 75 (1995) 209.
- [171] M. Baldo, E.G. Lanza, A. Rapisarda, Chaos 3 (1993) 691.
- [172] M. Baldo, G.F. Burgio, A. Rapisarda, Phys. Rev. C 51 (1994) 198.
- [173] P. Božek, Phys. Lett. B 386 (1996) 1.
- [174] C.H. Dasso, M. Gallardo, M. Saraceno, Nucl. Phys. A 549 (1992) 265.
- [175] B. Jacquot, M. Colonna, Ph. Chomaz, A. Guarnera, Phys. Lett. B 359 (1995) 268.
- [176] M. Colonna, G.F. Burgio, Ph. Chomaz, M. Di Toro, J. Randrup, Phys. Rev. C 47 (1993) 1395.
- [177] G.F. Burgio, Ph. Chomaz, M. Colonna, J. Randrup, Nucl. Phys. A 581 (1995) 356.
- [178] Ph. Chomaz, G.F. Burgio, J. Randrup, Phys. Lett. B 254 (1991) 340.

- [179] G.F. Burgio, Ph. Chomaz, J. Randrup, Nucl. Phys. A 529 (1991) 157.
- [180] G.F. Burgio, M. Baldo, A. Rapisarda, Phys. Lett. B 321 (1994) 307.
- [181] S. Chattopadhyay, Phys. Rev. C 53 (1996) R1065.
- [182] A. Atalmi, M. Baldo, G.F. Burgio, A. Rapisarda, Phys. Rev. C 53 (1996) 2556.
- [183] A. Atalmi, M. Baldo, G.F. Burgio, A. Rapisarda, Phys. Rev. C 58 (1998) 2238.
- [184] B. Jacquot, A. Guarnera, Ph. Chomaz, M. Colonna, Phys. Rev. C 54 (1996) 3025.
- [185] K.A. Snover, Ann. Rev. Nucl. Part. Sci. 42 (1992) 483.
- [186] J.J. Gårdhøje, Ann. Rev. Nucl. Part. Sci. 42 (1992) 483.
- [187] M. Colonna, A. Bonasera, Phys. Rev. E 60 (1999) 444.
- [188] G.F. Bertsch, S. Das Gupta, Phys. Rep. C 160 (1988) 190.
- [189] L.W. Nordheim, Proc. R. Soc. London A 119 (1928) 689.
- [190] E.A. Uehling, G.E. Uhlenbeck, Phys. Rev. 43 (1933) 552.
- [191] J. Randrup, Nucl. Phys. A 314 (1979) 429.
- [192] G.F. Bertsch, H. Kruse, S. Das Gupta, Phys. Rev. C 29 (1984) 673.
- [193] J. Knoll, B. Strack, Phys. Lett. B 149 (1984) 45.
- [194] B. Strack, J. Knoll, Z. Phys. A 315 (1984) 249.
- [195] J. Knoll, J.S. Wu, Nucl. Phys. A 481 (1988) 173.
- [196] M. Colonna, M. Di Toro, A. Guarnera, V. Latora, A. Smerzi, Phys. Lett. B 307 (1993) 273.
- [197] M. Colonna, M. Di Toro, A. Guarnera, Nucl. Phys. A 580 (1994) 312.
- [198] Y. Abe, S. Ayik, P.G. Reinhard, E. Suraud, Phys. Rep. 275 (1996) 49.
- [199] M. Bixon, R. Zwanzig, Phys. Rev. 187 (1969) 267.
- [200] M.H. Ernst, E.G.D. Cohen, J. Stat. Phys. 25 (1981) 153.
- [201] S. Ayik, Z. Phys. A 298 (1980) 83.
- [202] S. Ayik, C. Gregoire, Phys. Lett. B 212 (1988) 269.
- [203] S. Ayik, C. Gregoire, Nucl. Phys. A 513 (1990) 187.
- [204] J. Randrup, B. Remaud, Nucl. Phys. A 514 (1990) 339.
- [205] P.G. Reinhard, E. Suraud, S. Ayik, Ann. Phys. 213 (1992) 204.
- [206] P.G. Reinhard, E. Suraud, Ann. Phys. 216 (1992) 98.
- [207] P.G. Reinhard, E. Suraud, Nucl. Phys. A 545 (1992) 59c.
- [208] S. Ayik, Ph. Chomaz, M. Colonna, J. Randrup, Z. Phys. 355 (1996) 407.
- [209] D. Kiderlen, Nucl. Phys. A 589 (1995) 320.
- [210] S. Ayik, Z. Phys. A 350 (1994) 45.
- [211] S. Ayik, J. Randrup, Phys. Rev. C 50 (1994) 2947.
- [212] W. Wen, P. Chau Huu-Tai, D. Lacroix, Ph. Chomaz, S. Ayik, Nucl. Phys. A 637 (1998) 15.
- [213] W. Bauer, G.F. Bertsch, S. Das Gupta, Phys. Rev. Lett. 58 (1987) 863.
- [214] F. Chapelle, G.F. Burgio, Ph. Chomaz, J. Randrup, Nucl. Phys. A 540 (1992) 227.
- [215] S. Ayik, E. Suraud, M. Belkacem, D. Boilley, Nucl. Phys. A 545 (1992) 35c.
- [216] M. Colonna, M. Di Toro, A. Guarnera, S. Maccarone, M. Zielinska-Pfabé, H.H. Wolter, Nucl. Phys. A 642 (1999) 449.
- [217] F. Matera, A. Dellafiore, Phys. Rev. C 62 (2000) 044611.
- [218] D.H. Boal, Nucl. Phys. A 447 (1986) 479.
- [219] D.H. Boal, J.N. Glosli, Phys. Rev. C 37 (1988) 91.
- [220] D.H. Boal, J.N. Glosli, Phys. Rev. C 42 (1990) 502.
- [221] H. Schulz, H. Reinhardt, B. Kämpfer, Ann. Phys. 45 (1988) 258.
- [222] G. Papp, W. Nörenberg, J. Heavy Ion Phys. 1 (1995) 241.
- [223] K. Morawetz, Phys. Rev. C 62 (2000) 044606.
- [224] K. Snepken, X. Vinet, Nucl. Phys. A 480 (1988) 342.
- [225] B.A. Li, D.H.E. Gross, Nucl. Phys. A 554 (1993) 257.
- [226] M. Colonna, N. Colonna, A. Bonasera, M. DiToro, Nucl. Phys. A 541 (1992) 295.
- [227] M. Colonna, P. Roussel-Chomaz, N. Colonna, M. Di Toro, L.G. Moretto, G.J. Wozniak, Phys. Lett. B 283 (1992) 180.
- [228] D. Cussol, C. Gregoire, M. Pi, E. Suraud, Nuovo Cim. A 104 (1991) 611.

- [229] E. Suraud, M. Pi, P. Schuck, B. Remaud, F. Seville, *Phys. Lett. B* 229 (1989) 359.
- [229a] E. Suraud, D. Cussol, C. Gregoire, D. Boilley, M. Pi, P. Schuck, B. Remaud, F. Seville, *Nucl. Phys. A* 495 (1989) 73.
- [230] C. Fuchs, P. Essler, T. Gaitanos, H.H. Wolter, *Nucl. Phys. A* 626 (1997) 987.
- [231] D. Lacroix, Ph. Chomaz, *Nucl. Phys. A* 636 (1998) 85.
- [232] M. Belkacem, V. Latora, A. Bonasera, *Phys. Lett. B* 326 (1994) 21.
- [233] L.G. Moretto, K. Tso, N. Colonna, G.J. Wozniak, *Phys. Rev. Lett.* 69 (1992) 1884.
- [234] H.S. Xu, et al., *Phys. Rev. C* 48 (1993) 933.
- [235] L. Wilets, E.M. Henley, M. Kraft, A.D. Mackellar, *Nucl. Phys.* 282 (1977) 341.
- [235a] L. Wilets, Y. Yariv, R. Chestnut, *Nucl. Phys.* 301 (1978) 359.
- [236] D.H. Boal, J.N. Glosli, *Phys. Rev. C* 38 (1988) 1870.
- [237] C. Dorso, J. Randrup, *Phys. Lett. B* 215 (1988) 611.
- [238] S. Drozd, J. Okolowicz, M. Ploszajczak, *Phys. Lett. B* 109 (1982) 145.
- [239] E. Caurier, B. Grammaticos, T. Sami, *Phys. Lett. B* 109 (1982) 150.
- [240] W. Bauhoff, E. Caurier, B. Grammaticos, M. Ploszajczak, *Phys. Rev. C* 32 (1985) 1915.
- [241] J. Aichelin, *Phys. Rep. C* 202 (1991) 233.
- [242] G. Peilert, et al., *Phys. Rev. C* 39 (1989) 1402.
- [243] T. Maruyama, et al., *Phys. Rev. C* 57 (1998) 655.
- [244] S. Chikazumi, T. Maruyama, S. Chiba, K. Niita, A. Iwamoto, *Phys. Rev. C* 63 (2001) 024602.
- [245] R. Nebauer, et al., *Nucl. Phys. A* 658 (1999) 67.
- [246] A. Ono, H. Horiuchi, T. Maruyama, A. Ohnishi, *Phys. Rev. Lett.* 68 (1992) 2898.
- [247] H. Feldmeier, *Nucl. Phys. A* 515 (1990) 147.
- [248] H. Feldmeier, K. Bieler, J. Schnack, *Nucl. Phys. A* 586 (1995) 493.
- [249] E. Suraud, S. Ayik, M. Belkacem, J. Stryjewski, *Nucl. Phys. A* 542 (1992) 141.
- [250] E. Suraud, S. Ayik, M. Belkacem, F.S. Zhang, *Nucl. Phys. A* 580 (1994) 323.
- [251] F.S. Zhang, E. Suraud, *Phys. Lett.* 319 (1993) 35.
- [252] F.S. Zhang, E. Suraud, *Phys. Rev. C* 51 (1995) 3201.
- [253] M. Colonna, Ph. Chomaz, A. Guarnera, *Nucl. Phys. A* 613 (1997) 165.
- [254] A. Guarnera, Ph.D. Thesis, University of Caen, France, 1996; GANIL Report No. T-96-01.
- [255] L.G. Moretto, et al., *Phys. Rev. Lett.* 77 (1996) 2634.
- [256] B. Borderie, et al., *Phys. Rev. Lett.* 86 (2001) 3252.
- [257] A.B. Larionov, A.S. Botvina, M. Colonna, M. Di Toro, *Nucl. Phys. A* 658 (1999) 375.
- [258] V. Baran, M. Colonna, M. Di Toro, V. Greco, M. Zielinska-Pfabé, H. Wolter, *Nucl. Phys. A* 703 (2002) 603.
- [259] A.S. Botvina, I.N. Mishustin, *Phys. Rev. C* 63 (2001) 061601(R).
- [260] T. Lefort, et al., *Phys. Rev. C* 62 (2000) R31604.
- [261] J. Pochodzalla, et al., *Phys. Rev. Lett.* 75 (1995) 1040.
- [262] M. Mahi, et al., *Phys. Rev. Lett.* 60 (1988) 1936.
- [263] J.B. Elliott, L.G. Moretto, L. Phair, G.J. Wozniak, *Phys. Rev. Lett.* 88 (2002) 042701.
- [264] J.B. Elliott, et al., *Phys. Rev. C* 67 (2003) 024609.
- [265] J.D. Frankland, et al., *Nucl. Phys. A* 689 (2001) 940.
- [266] S.C. Jeong, et al., *Phys. Rev. Lett.* 72 (1994) 3468.
- [267] D. Durand, E. Suraud, B. Tamain, Institute of Physics, 2000, ISBN: 0750305371.
- [268] N. Marie, et al., *Phys. Lett.* 391 (1997) 15.
- [269] L. Beaulieu, et al., *Phys. Rev. Lett.* 84 (2000) 5971.
- [270] R. Alba, et al., *Nucl. Phys. A* 681 (2000) 339c.
- [271] N. Marie, et al., *Phys. Rev. C* 58 (1998) 256.
- [272] J.B. Natowitz, et al., *Phys. Rev. C* 65 (2002) 34618.
- [273] J. Besprosvany, S. Levit, *Phys. Lett. B* 217 (1989) 1.
- [274] P. Bonche, S. Levit, D. Vauterin, *Nucl. Phys. A* 436 (1985) 265.
- [275] S. Levit, P. Bonche, *Nucl. Phys. A* 437 (1985) 426.
- [276] J.B. Natowitz, K. Hagel, Y. Ma, M. Murray, L. Qin, R. Wada, J. Wang, *Phys. Rev. Lett.* 89 (2002) 212701.
- [277] M. D'Agostino, et al., *Nucl. Phys. A* 699 (2002) 795.

- [278] J.D. Frankland, et al., Nucl. Phys. A 689 (2001) 905.
- [279] M.F. Rivet, et al. (INDRA Collaboration), Phys. Lett. B 430 (1998) 217.
- [280] D. Durand, Nucl. Phys. A 541 (1992) 266.
- [281] G. Tăbăcaru, et al., in: G.C. Bonsignori, et al. (Eds.), Bologna 2000: Structure of the Nucleus at the Dawn of the Century, World Scientific, Singapore, 2000, p. 321.
- [282] P. Désesquelles, Phys. Rev. C 65 (2002) 034604.
- [283] J.L. Charvet, et al., nucl-ex/0212012.
- [284] G. Tăbăcaru, et al., Eur. J. Phys. (in press); nucl-ex/0212018.
- [285] S. Salou, Ph.D. Thesis, University of Caen, France, 1997; GANIL Report No. T-97-06.
- [286] W.D. Myers, W.J. Swiatecki, Ann. Phys. 211 (1991) 292.
- [287] P. Bonche, S. Levit, D. Vauterin, Nucl. Phys. A 428 (1984) 95.
- [288] G. Fai, J. Randrup, Nucl. Phys. A 487 (1988) 397.
- [289] N.G. van Kampen, Stochastic Processes in Physics and Chemistry, North-Holland, New York, 1981.
- [290] B. Benhassine, M. Farine, E.S. Hernandez, D. Idier, B. Remaud, F. Sebillé, Nucl. Phys. A 545 (1992) 81c.
- [291] P. Morel, P. Nozières, Phys. Rev. 126 (1962) 1909.
- [292] G. Baym, C.J. Pethick, in: K.H. Bennemann, J.B. Ketterson (Eds.), The Physics of Liquid and Solid Helium, Part II, Wiley, New York, 1976, p. 1.
- [293] S. Ayik, M. Dworzecka, Phys. Rev. Lett. 54 (1985) 534.
- [294] S. Ayik, M. Dworzecka, Nucl. Phys. A 440 (1985) 424.
- [295] S. Ayik, D. Boilley, Phys. Lett. B 276 (1992) 263; *ibid.* A284 (1992) 482E.
- [296] Y.B. Ivanov, S. Ayik, Nucl. Phys. A 593 (1995) 233.
- [297] S. Ayik, Phys. Lett. B 493 (2000) 47.
- [298] S. Ayik, Y. Abe, Phys. Rev. C 64 (2001) 024609.
- [299] J. Randrup, Nucl. Phys. A 583 (1995) 329.
- [300] S. Ayik, Phys. Lett. B. 265 (1991) 47.
- [301] S. Ayik, Y.B. Ivanov, V.N. Ruuskikh, W. Nörenberg, Nucl. Phys. A 578 (1994) 640.
- [302] J. Randrup, in: J. Misquich, G. Pelletier, P. Schuck (Eds.), Statistical Description of Transport in Plasma, Astro-, and Nuclear Physics, Nova Science Publishers, New York, 1993, p. 353.
- [303] M. Abramowitz, I.A. Stegun, Handbook of Mathematical Functions, Dover, New York, 1970 (Eq. (8.8.3)).
- [304] W. Magnus, Comm. Pure Appl. Math. 7 (1956) 649.
- [305] M. Colonna, Ph. Chomaz, Phys. Lett. B 436 (1998) 1.
- [306] D. Kiderlen, P. Danielewicz, Nucl. Phys. A 620 (1997) 346.
- [307] H. Feldmeier, Nucl. Phys. A 681 (2001) 398.
- [308] A. Ohnishi, J. Randrup, Nucl. Phys. A 565 (1994) 474.
- [309] A. Ohnishi, J. Randrup, Phys. Rev. Lett. 75 (1995) 596.
- [310] A. Ohnishi, J. Randrup, Ann. Phys. 253 (1997) 279.
- [311] Y. Hirata, A. Ohnishi, Y. Nara, T. Harada, J. Randrup, Nucl. Phys. A 639 (1998) 389.
- [312] A. Ohnishi, J. Randrup, Phys. Rev. A 55 (1997) 3315.
- [313] A. Ohnishi, J. Randrup, Phys. Lett. B 394 (1997) 260.
- [314] A. Ono, H. Horiuchi, Phys. Rev. C 53 (1996) 2958.
- [315] A. Ono, Phys. Rev. C 59 (1999) 853.